MODELING OF A 1" DIAMETER AIR-WATER CYLINDRICAL HYDROCYCLONE

by

Bijan Aminnejad

A thesis submitted to the Faculty of Engineering in partial fulfilment of the requirements for the degree of Doctorate of Philosophy

Major Subject
Mining Engineering (Physical Separation)

at

DALHOUSIE UNIVERSITY

Halifax, Nova Scotia, Canada

February 2004

Your file Votre référence
ISBN: 0-612-93281-8
Our file Notre référence
ISBN: 0-612-93281-8

DALHOUSIE UNIVERSITY

To comply with the Canadian Privacy Act the National Library of Canada has requested that the following pages be removed from this copy of the thesis:

Preliminary Pages
- Examiners Signature Page
- Dalhousie Library Copyright Agreement

Appendices
- Copyright Releases (if applicable)

Dedicated to:

This thesis would be incomplete without a mention of the support provided to me by my wife, *Maryam*, to whom this thesis is dedicated.

ABSTRACT

A small diameter cylindrical hydrocyclone has been designed, constructed and modeled to separate air from an air-water two-phase flow. The model is capable of predicting significant variables such as bubble cut-size and pressure drop. The prototype is a separator that may be used in a fast flotation system, to remove gas from liquid phase and or remove small amounts of free or emulsified oil from water. An extensive experimental program was conducted. Feed flow rates of 50-70 litres per minute, and pressure 200-350 kPa were used with a mean bubble size between 25-100 μm. The air-water separation was determined at low air dispersion hold-ups. Bubble generation and sizing was carried out in a turbulent unit, which consisted of an orifice plate mounted in a 2.54 cm diameter PVC flange. Bubble size and volume distribution in the feed and hydrocyclone streams were measured using laser scattering techniques and statistically analyzed using a Rosin-Rammler distribution. Empirical models were used to predict the small diameter cylindrical hydrocyclone performance. Hydrocyclone separation efficiency was also examined. Gas-liquid separation was calculated based on air-phase hold-ups and mass balance calculations. Experimental data was compared with model predicted results and variance was found particularly in the overflow stream. A computer code, in Java language, incorporating adopted and modified models that predict pressure drop, separation efficiency and cut-size have been developed.

TABLE OF CONTENTS

LIST OF TABLES

LIST OF FIGURES

NOMENCLATURE

Symbol	Units	Brief Definition
α	g	Field of acceleration
α	°	Inclination angle
α	g	Acceleration of turbulent spectrum.
α	-	Entrance constriction coefficient
$\alpha_1, \alpha_2, \alpha_3$	0.45	Constants
β	-	Orifice ratio
β		Hydrocyclone cone angle
γ_w	kg/m^3	Specific gravity of water
Δ_γ	°	Specific gravity differences
$\Delta\rho$	kg/m^3	Density differences
Δ_x	m	Characteristic length proportional to D_o
Δp	kPa	Pressure drops.
ε_a	m^2/s^3	Turbulent kinetic energy dissipation rate
ε_o^{loc}	W/kg	Local value of energy dissipation in a unit mass
θ	°	Hydrocyclone cone angle
θ	-	Circumfrential direction
η_o	%	Separation efficiency
θR	m	Arch length
λ	m	Wavelength of the max interface perturbation
μ	Nsm^{-2}	Fluid viscosity @ 20 C ($gcm^{-1}s^{-1}$)
μ_c	Nsm^{-2}	Viscosity of continues phase
μ_o	Nsm^{-2}	Suspended material viscosity
μ_t		Turbulent Eddy Viscosity(rate of dissipation per unit kinetic energy)
ν	m/s	Superficial velocity in the cyclone's body

ξ	mV	Zeta potential
ξ	-	b/R
ρ_c	kg/m^3	Density of continuous phase
ρ_l	kg/m^3	Density of the liquid
ρ_o	kg/m^3	Organic phase density
ρ_p	kg/m^3	Particle density
ρ_{ph}	kg/m^3	Density of the dispersed Phase
ρ_s	kg/m^3	Solid Particle density
ρ_w	kg/m^3	Specific gravity of water.
σ	mN/m	Surface energy at the interface
σ_t	1	Diffusion rate
σ_ε	1.217	Diffusion rate
τ	s	Particle relaxation Time
τ_c	$dyne/cm^2$	Shear stress at the core region τ =F/A
τ_w	$dyne/cm^2$	Wall shear stress
υ	m^2/sec	Kinematic viscosity of the fluid mixture
υ_r	m/s	Radial velocity
υ_t	m/s	Tangential velocity
υ_z	m/s	Axial velocity
υ_w	m^2/s	Kinematic viscosity of water.
ϕ		Frictional losses
θ_R	m	Arch length
ϕ_v	%	Volume fraction of solid particles
ψ	-	Shape coefficient of a bubble
λ_{max}		Maximum interface perturbation
Ω	-	Swirl density
A	m^2	Interfacial area
A_s	m^2	Cross sectional area of hydrocyclone.

a	-	Constant
a	m	Ellipsoid axes
a	m	Thickness of inlet slot.
A_{in}	m^2	Inlet cross sectional area
A_{is}	m^2	Inlet slot cross sectional area
Ar^{-n}		Overflow tangential velocity profile.
A_R	m^2	Total inside area of the cyclone
b	m	Minor axis of ellipsoid
b	m	Width of the cyclone inlet
B		Peak tangential velocity radius factor
Br^{-m}		Underflow tangential velocity
C	-	Critical value of Weber number
C	0.025	Empirical constant
C	-	Hydrocyclone pressure drop constant
Ca		Cavitation number $Ca = P - P_v / 0.5\rho v^2$
C_μ	0.09	Empirical constant
C_0	%	Dispersed phase hold-up
C_0	1.15	Flow velocity coefficient.
C_D	--	Drag coefficient $C_D = \frac{g(\rho_p - \rho_w)}{\rho_p . V^2}$
C_f	-	Skin friction coefficient
C_i	m^3	Mass fraction of inlet solids (by Volume)
C_o	-	Critical value in orifice
C_o	m^3	Mass fraction of overflow solids (by volume)
C_o	Kgm^{-3}	Mass ratio liquid/gas
c_w	%	Concentration of solids by weight
C_μ	-	Empirical Constant
$C^k{}_{\alpha\beta}$	-	Interface transformers for turbulent kinetic energy.
$C^\varepsilon{}_{\alpha\beta}$	-	Interface transformers for turbulent diffusion.

Cy_{50}	-	Characteristic cyclone number (constant)
d	μ	Diameter of the particle (droplet) under consideration
d_o	m	Overflow droplet size
d_i	m	Inflow droplet size
D	m	Hydrocyclone reference diameter
D	m	Hydrocyclone major diameter
d_{50}	%	50% cutsize
d_{50}		Cut-size (the particle drop size at 50% migration probability), size of separation
d_{75}		particle drop size at 75 % migration probability
d_b	μm	Diameter of bubble
D_c	m	Hydrocyclone inside diameter
d_c	m	Diameter of cylindrical feed inlet
Dc	m	Characteristic diameter of the GLCC
D_c	m	Core diameter
d_g		Mass median of soild size distribution.
D_i	m	Mean inlet droplet size
D_i	mm	Cyclone's inlet diameter
d_{max}	μm	Max diameter of a drop that can survive a stress without breaking-up
D_n	m	Diameter of second cone
D_o	m	Overflow orifice diameter
D_o	m	Vortex finder diameter
D_p	μm	Diameter of particle
D_p	m	Pipe diameter
D_s	m	Cyclone cylindrical part diameter
D_t	m^2	Feed inlet area
D_u	m^2	Underflow orifice area
D_z	m	Axial diameter

E	%	Efficiency
e	m	Ellipsoid axes
E_u	$Eu = CP = \frac{\Delta p}{\frac{1}{2}\rho v^2}$	Euler number (Pressure coefficient CP)
f	-	Fraction break-up
f	-	Total friction factor
F	%	Split ratio
F_{buoy}	$kgms^{-2}$	Buoyancy force $F_{buoyancy} = \rho_l.g.V_{solid}$
F_{cf}	N	Centrifugal force
F_D	N	Drag force
F_r	N	Resistance force
F_r	-	Froude number
G	kg/s	Quantity of dispersed phase entering to the hydrocyclone in unit time
H		Total Head
H	m	Cyclone length
H_{lo}	%	Liquid hold-up
g	m/s^2	acceleration of gravity
g_l	kg/s	The quantity of solid phase of the dispersion located at a certain radius r_l of the hydrocyclone
g_u	%	Solid recovery in the underflow
h	m	Height of the separation zone
I	-	Hydrocyclone inlet factor
J_{in}	ms^{-1}	Inlet fluid velocity
K	-	Particle inertia parameter
K		Resistance coefficient for elbow or tee
K_a	m^2/s^2	Turbulent kinetic energy per unit mass
K_d	-	Correction factor
k_f		Resistance coefficient
k	m^2/s	Thermal diffusivity

K_i	%	Feed Water concentration (volume based %)
K_o	%	Overflow water concentration
L	m	Height of the separation chamber
L	m	Hydrocyclone length
l	m	Hydrocyclone cylindrical section
L_c	m	Length of hydrocyclone
L_i	m	Interface length
L_{in}	m	Inclined inlet length
L_{ll}	m	Liquid length in location l
L_{lw}	m	Level of liquid at the wall
Lo	m	Vortex finder length
L_s	m	Cyclone cylindrical part length
LZVV	-	Locus of zero vertical velocity
m	-	Exponent of correction factor
m	kg	Mass
m_l	kg	Mass of a particle in a particular size
M_t		Momentum flux at the inlet slot
M_T		Axial momentum flux at the characteristic diameter position
n	-	Number of samples
n	0.8	Empirical constant
n	--	Exponent for tangential velocity
N_{Re}	-	Reynolds number
PDR		Split pressure drop ratio
P_{in}	kPa	Inlet pressure (feed pressure)
P_o	kPa	Overflow pressure
$Pr = C_p . \mu/k$	Dimensionless	Prandtl number
P_{rej}	kPa	Reject flow pressure
P_u	kPa	Underflow pressure
q	m^3/s	Inlet flow rate

Q	m^3	Volumetric flow-rate
Q_0		Total capacity of the hydrocyclone
Q_b	m^3	Concentration of the mixture emerging through the bottom outlet
$Q_w^c Q_g^i$	m^3	Clean underflow water rate
Q_w^i	m^3	Inlet flow rate
Q_g^c	m^3	Clean underflow gas flow rate
Q_g^i	m^3	Inlet gas flow rate
Q_{inlet}	m^3/s	Total flow rate at the inlet
$Q_{overflow}$	m^3/s	Total flow rate at the upper outlet
Q_t	m^3	Concentration of the mixture emerging through the top outlet
r	m	Running value of the radius
r		Radial coordinate
R	m	Radii of the cylindrical part of the hydrocyclone
R	mm	Radius of the inlet centre.
r	mm	Hydrocyclone radius
r	mm	Radial position
Rc		Radius at characteristic location
r_c	mm	Air core radius.
R^{cr}	mm, inch	Critical radius
R_o^i	μm	Radius of the equivalent spherical bubble
Re	-	Reynolds number $\mathrm{Re} = \frac{\rho v L}{\mu}$
R_{in}	m	Inlet radius
Re_{in}	-	Inlet Reynold number
Re_p	-	Particle Reynolds number
Re_z	-	Reynolds number in axial position.
R_f	%	Split ratio

R_s	m	superficial radius
R_m	m	Geometric mean radius
R_x	m	Vortex finder diameter
R_z	m	Radius in axial position
s	--	Swirl number
S	m	Length of vortex finder
S_i		The amount of withdrawal of solid phase
Stk	--	Stokes number
StK_{50}	--	Stokes' number for cut-size d_{50}
T	°C	Temperature
t	s	Time
t_l	s	Mean residence time of solid phase particles
U	m/s	Radial velocity of bubbles
U	m/s	Reference velocity
U_{avz}		Average axial velocity
u	m/s	Velocity component
u'	m/s	Velocity fluctuation
U_d	m/s	Settling velocity
u_i	m/s	Time average velocity component
U_r	m/s	Radial Velocity
U_t	m/s	Terminal settling velocity
U_u	m/s	Under-flow average axial velocity
v_x	m/s	Superficial axial velocity in vortex finder
U_z	m/s	Axial velocity
V^2/r	g	Gravitational acceleration
V	m^3	Volume
V'		Velocity of water pulsation.
v	m/s	Velocity
$V\varphi$	m/s	Tangential component of the flow velocity
V_q		Rotational velocity.

V_φ	m/s	Tangential component of the viscosity of the descending liquid flow
V_0	m^3	Useful volume of the vessel
v_{at}	m^2s^{-1}	Kinematic turbulent viscosity
V_g	cm^3	Volume of gas
V_{go}	m/s	Velocity of gas at zero net location of the hydrocyclone
v_{in}	m/s	Fluid velocity at the feed inlet
$\bar{V}_i$	m/s	Average feed velocity
V_{in}	m/s	Feed fluid velocity
V_{is}	m/s	Average inlet velocity
Vr	m/s	Radial velocity
V_{sg}	m/s	Superficial gas velocity
V_t	m/s	Tangential velocity
$V_t(r)$	m/s	Tangential velocity in the radius of r.
V_{tis}	m/s	Tangential velocity in the inlet slot
$v_{\theta CS}$	m/s	Internal spin velocity (inner core velocity)
$v_{\theta m}$	m/s	Geometrical mean rotational velocity
$v_{\theta W}$	m/s	Wall velocity just after inlet
v_z	m/s	Characteristic velocity
v_{zw}	m/s	Wall axial velocity
W	m/s	Axial velocity
W(z)	m/s	Mean axial velocity at level z
We	---	Weber number $We = \frac{\rho v^2 L}{\sigma}$
W_z	m/s	Mean axial velocity
x	%	% Recovery in each sample
X	kg	Mass Dryness Fraction
x	m	Coordinate direction
x_g	m	Mass median of the solid size

x_i, x_j		Coordinate direction
x_t	%	Volume fraction of the heavy phase in the top
z	m	Axial radius
z_t		Axial tangent

Subscripts:

Symbol	Definition
η	Separation efficiency
θ	Tangential
^{o}	Temperature degree
0	Zero liquid flow
50	Cut-size
a	Annular
av	Average
b	Bubble
body	In the cyclone body
c	Core
CS	In the surface CS
cyc	Cyclone
fact	Factor
g	Gas
i, j	Coordinate direction
in	Inclined inlet
is	Inlet slot
l	Liquid
m	Mixture
m	Mixture density
of	Overflow

p	Particle
r	Radial
r	Radial position
rCS	Radial gas velocity component in the surface CS
t	Tangential or turbulent
uf	Underflow
w	Wall
w	Wall
x	Gas inlet tube or vortex finder
z	Axial

Superscripts

$\bar{}$	Average

ACKNOWLEDGEMENTS

The author wishes to thank the following persons and entities for their support and guidance.

- Dr. Ian. M. Flint for his inspiration, advice, support and encouragement for this work.
- Guiding committee members, Drs H. Hancock and P. Yuet for their advice, constructive recommendations and participating in my guiding committee.
- My wife Maryam, son Houman and daughter Homa and my parents Mr. Vali Aminnejad and Mrs. Moazzameh Farjadi for their support and encouragement to achieve and succeed.
- The author also wants to thank to Mr. D. Adams and Mr. R. Dube for assistance in building the experimental set-up and prototype hydrocyclone.
- Mr Ryan Perkins, co-op student, for writing the Java codes.

NEW KNOWLEDGE

The new knowledge, obtained in this thesis, is summarized in the following four points:

1. Design of 1" inch gas-liquid cylindrical hydrocyclone.

2. Development of recycled batch mode cylindrical de-gassing hydrocyclone test method.

3. Development of a rapid turbulent de-gassing system including orifice plate bubble generator, and cylindrical hydrocyclone.

4. Development of empirical models to predict pressure drop, separation efficiency and cut-size (d_{50}) in the underflow and overflow streams of the air-water cylindrical hydrocyclone.

1. INTRODUCTION

The principle and basic design of conventional hydrocyclones is almost 100 years old. Its first application was in the mineral processing industry, but lately it has been used in both the chemical and petroleum industries as an alternative to gravity based conventional separators. Conventional separators, such as the free water knock out drum (FWKO) or American Petroleum Institute Separators (API), need a large area, are of heavy weight, and have high capital, maintenance and operating costs. These disadvantages have motivated the oil and gas industry to develop hydrocyclone based separators for gas-liquid and liquid-liquid phase separations which are light weight and low cost. Recent developments in liquid-liquid and gas-liquid separation, starting from about 1980, show that the new generation of hydrocyclones can separate oil, or gas, from water. Colman, Thew and Corney (1980) designed and constructed a conical hydrocyclone, with a specific geometry, that has become standard for de-oiling hydrocyclones. The use of a longer cone (smaller angle) and proper design of the inlet area have allowed hydrocyclones, of standard design, to separate oil and gas from "produced" water efficiently. The concentrated light phase is removed through the overflow, usually called "reject", while the treated water flows out the under-flow. The low-density difference between the organic and aqueous phases and the possibility of dispersed-phase drop breakage instead of drop coalescence make this separation, and the modeling of this separation, more difficult.

There has been significant research done on liquid-liquid and gas-liquid conical and multi conical shape hydrocyclones. However, only a few papers are available concerning the small diameter cylindrical hydrocyclone.

Behaviours of the gas-phase in the hydrocyclone, including nucleation, growth, breakage and coalescence, are not understood well and there has not been a reliable method developed to calculate de-gassing hydrocyclone performance.

This work concentrates on modeling a small diameter (2.54 cm) cylindrical hydrocyclone (**Figure 1**) in combination with orifice plates for possible application in bubble, selective solids or organic phase separations from water. To this end, a model was developed that predicts performance and operating characteristics under various operating conditions. Conical hydrocyclones are also discussed to provide a theoretical background. The hydrocyclone was tested only in the context of continuous flow of the dispersed gas.

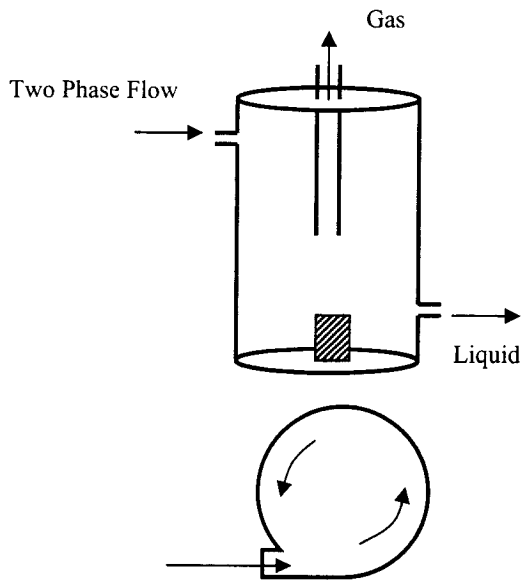

Figure 1: 2.54 cm diameter gas liquid cylindrical hydrocyclone configuration

The air-water feed flowing into the hydrocyclone through the tangential inlet produces a swirling motion and centrifugal vortex region that causes disengagement of the phases. The heavy water phase is forced toward the cyclone wall and is discharged from the underflow tangential outlet. The light air phase moves to the low pressure central core and flows through to the overflow via the vortex finder.

Experiments were conducted only in a batch-recycled mode. The test results were used to determine cyclone-modeling parameters. Triton ×100, a non-ionic surfactant dilute in tap water was used to stabilize the bubble sizes – no other chemical reagents were tested. Both the testing and model are limited to air - water separations only.

These existing works by previous researchers is used, whenever possible, and modified or adjustmented when necessary.

The computer codes included in the appendix can be used to predict pressure drop and bubble cut-sizes in underflow and overflow streams.

2. BACKGROUND AND THEORY

2.1 Introduction

Little information is available on the design and modeling of the small diameter gas-liquid cylindrical hydrocyclone. No models are available that can accurately predict all the significant variables in a cylindrical type hydrocyclone. Most of information in the literature on hydrocyclones concerns liquid-liquid and gas-liquid conical hydrocyclones. Studies published have focused on conical and double conical de-oiling applications or conical solid particle separation applications. Researchers at the University of Tulsa have designed and developed CFD models for a single- and two-phase flow in gas-liquid large diameter cylindrical hydrocyclones. (Erdal, 1996; Arpandi, 1995; and Motta, 1997)

The reason for choosing the cylindrical cyclone is that the geometry is more amenable to mathematical treatment than a conical shape while still being capable of air removal.

2.2 How Liquid-Liquid and Gas-Liquid Hydrocyclones Work

D. Bradley (1965) attempted to use hydrocyclones for liquid-liquid separation. He stated that "the separation of immiscible liquids in the hydrocyclone is as feasible as the separation of solid from liquid". However difficulties, arise because of the following:

- Density differences are generally smaller,
- Shear force can cause droplet breakage or coalescence,
- Conventional hydrocyclones have design deficiencies when applied to liquid-liquid and gas-liquid separations,
- Tangential velocity and residence time need to be increased but not to the point that the droplets or bubbles are sheared.

2.3 De-Oiling Hydrocyclones

H. U. Regehr (1968) attempted to design a hydrocyclone for the separation of light dispersions. A small diameter hydrocyclone was used to achieve a high acceleration field while avoiding excessive inlet pressure. The feed material was oil and plastic beads. The cyclone body was extended to maintain adequate residence time (L/D >10). These designs have not been commercially developed by the oil industry.

D. A. Colman et. al. (1979) studied hydrocyclone geometry for de-oiling hydrocyclones. At the same time, I. C. Smyth and M. T. Thew (1980) reported success on separation of kerosene from water using a different geometry hydrocyclone. In 1984, D. A. Colman et. al. developed a unique de-oiling hydrocyclone characterized by its dual conicity. This type of hydrocyclone consists of a cylindrical swirl chamber with a tangential inlet and a conical acceleration chamber followed by a long cone of very low conicity and a cylindrical tube. The long thin cone and the straight tube help maintain the tangential velocity, reduce the distance a droplet has to travel and provide an increased residence time. The vortex finder was replaced by a simple hole of small diameter.

The offshore oil industry first used Thew's de-oiling hydrocyclones for the treatment of "produced" water in 1984. They are now the standard method for "produced" water treatment both offshore and onshore. The first permanent installations began in 1983-1984 in the North Sea and the Bass Strait (Tasmania, Australia).

De-oiling hydrocyclones are an alternative to induced gas flotation, dissolved gas flotation and gravity separation methods such as American Petroleum Institute Separator (API) and Corrugated Plate Interceptor (CPI). De-oiling hydrocyclones are about 10% the size and weight of earlier types of conventional hydrocyclones and have a residence time usually less than two seconds. This vessel is not sensitive to motion or orientation, very rarely uses chemicals, and the organic phase hold-up in the feed is usually less than two percent. An example of de-oiling hydrocyclone performance derived from different oil fields (North Sea) is provided in **Table 1**.

Table 1: De-oiling hydrocyclone performance, Colman D.A., et. al. (1984).

Diameter	Feed Pressure	Feed Temp.	Inlet oil conc.	Overflow oil
mm	kPa.	(°C)	mg/l	conc. mg/l
120	700	90	400-600	25-30
70	500	90	400-600	20-25
120	1000	85	500-700	30
70	2100	50	150-375	30-60
70	2200	90	40-80	8-10

D.A. Colman et. al. (1980) have empirically defined the hydrocyclone efficiency of removal as **Equation 1.**

$$E(d)=100\left\{1-e^{-\left[1.8\left(\frac{d}{d_{75}}-0.19\right)\right]}\right\} \qquad \text{Equation 1}$$

This formula predicts the separation efficiency for a known droplet size distribution given the hydrocyclone nominal diameter and operating conditions. In **Equation 1,** "d" is particle size, recovery percent and "d_{75}" is 75% cut-size.

2.3.1 Cylindrical De-oiling Hydrocyclones

The ARCO oil company developed a cylindrical hydrocyclone with spiral vane internals (Auger Separator). This cyclone was tested in selected Alaskan oil fields and achieved gas carry-under of between 2% and 18%.

B. C. Millington and M.T. Thew (1987) reported that the vortex has a tangential velocity structure caused by the flow conditions (laser doppler anemometry- L.D.A). D. Farchi (1990) in his MSc. thesis conducted tangential velocity measurements with a static Pitot tube. Farchi's measurements confirmed that a "forced" vortex (intensified vortex) occurs in the cyclone.

A forced vortex occurs within the core region close to the hydrocyclone axis. Farchi used a transparent cylindrical vessel, which enabled the free vortex to be clearly seen when water leaves the centrally positioned orifice outlet. The profile of this vortex was determined experimentally. The fluid inlet to the vessel was through two tubes set at a precise angle. This arrangement gave an initial swirling motion to the fluid at the periphery with a subsequent enlargement of the flow profile. The definition of the free and vortex flow is shown in **Figure 2**.

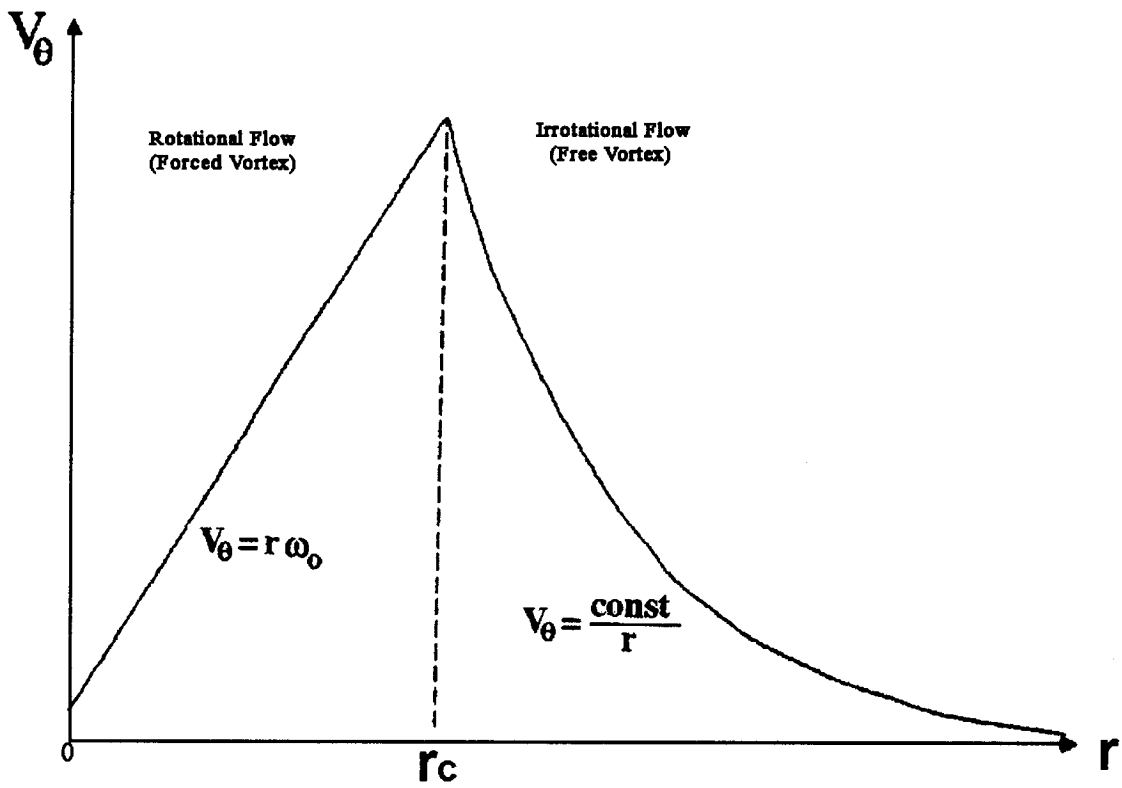

Figure 2: Rotational vs. irrotational flow (Kleinstreuer, C, 1997).

In this figure ω_o is initial angular velocity, V_θ is tangential velocity, r_c is radius of the core, r is a radial position, c/r is ratio of core radius to cyclone radius.In a forced vortex flow, radial velocity is close to zero and tangential velocity; $V_\theta = f(r) = c/r$.

G. H. Kimber and M. T. Thew (1974) designed and studied de-oiling cylindrical hydrocyclones for the separation of finely divided oil from water. This design (**Figure 3**)

resulted in 90% of the oil being removed from the over-flow, or reject stream, using a 50 mm hydrocyclone (200 litres per minutes, up to 1000 ppm of Esso Roxstone 90; a lubricating oil of relatively high density and viscosity). These tests indicated that a cylindrical hydrocyclone, of their design, was inadequate for commercial application. They reported that multiple inlets and axial outlets achieved a linear oil core more efficiently than single inlets and tangential outlets.

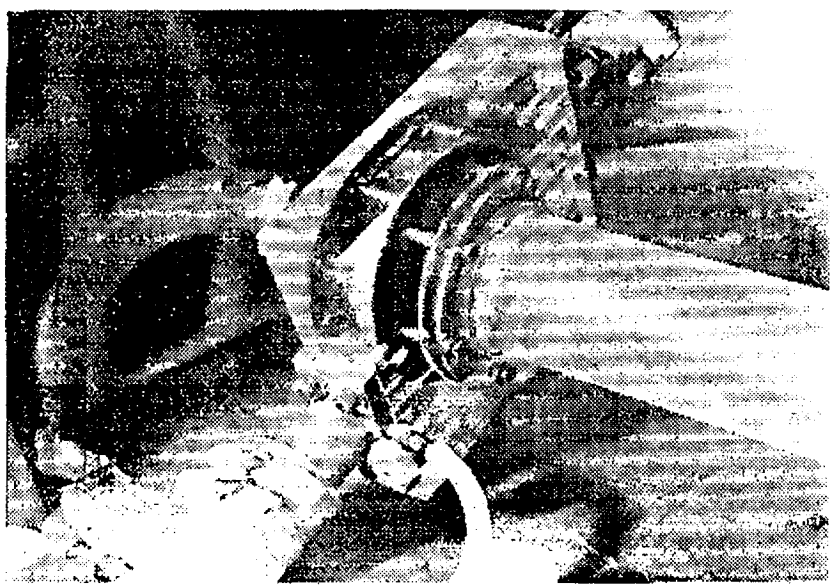

Figure 3: Kimber G.H. and Thew M.T. (1974) two-point inlet cylindrical hydrocyclone.

2.3.1.1 Effect of Solids

G. H. Kimber and M. T. Thew (1974) reported that oil-water separation is hindered by the presence of solid particles, such as silt, sand or rust, which agglomerate with oil.

2.3.1.2 Effect of Geometry

G. H. Kimber and M.T. Thew (1974) designed a cylindrical hydrocyclone according to the following criteria:

- Ease of construction,
- Convenient for assembly in parallel flow installations,
- Allows a simple change in L/D ratio,
- Twin tangential inlet: aids vortex symmetry and helps maintain a linear core,

- Twin tangential outlets: creates a clean smooth, outlet flow,
- Two axial outlets for outlet enriched flow (overflow),
- A larger diameter hydrocyclone needs a higher inlet pressure to maintain an adequate acceleration field (region of high swirl flow),
- A smaller diameter requires a more complex manifold and has a greater risk of port blockage.

The Thew cyclone is shown schematically in **Figure 4**.

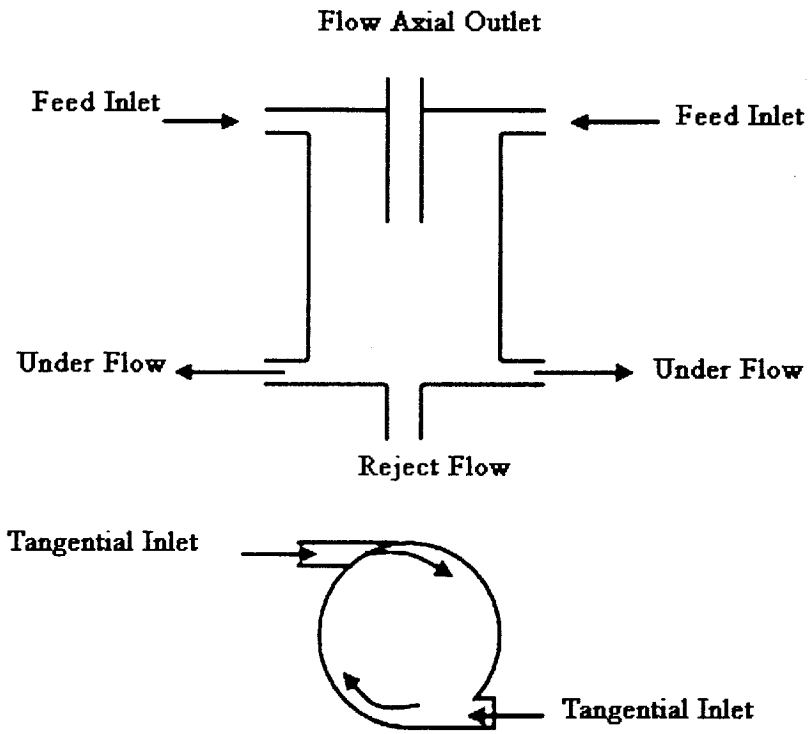

Figure 4: Dual inlet cylindrical hydrocyclone schematic (Kimber and Thew; 1974).

2.3.1.3 Length to Diameter (L/D) Ratio

The L/D ratio has a large effect on droplet residence time and also on how much the velocity profile, near the downstream end, differs from that at the inlet. The smaller the hydrocyclone diameter, the greater the centrifugal forces developed and, consequently, the smaller the size particle that may be separated.

2.3.1.4 Length of Hydrocyclone

G. H. Kimber and M. T. Thew (1974) state that cyclone length does not have a major effect on its performance and speculate that L/D <10 would be disadvantageous. Sufficient length is necessary for separation residence time. However, H. U. Regehr (1968) determined the best L/D ratio to be in the range of 15 to 20.

A. C. Hoffman (2001) studied the effect of cyclone length on separation performance. He stated increasing the hydrocyclone length up to less than 5.5 times of the cyclone diameter would reduce the pressure drop and increase the separation efficiency. When this ratio exceeds 5.5, the separation efficiency of the hydrocyclone dramatically decreases. In long hydrocyclones the swirl flow collapses that is somewhere near the bottom of hydrocyclone (at the natural vortex end; L_n).

This is also reported by R. Alexander (1949), who states that the vortex flow suddenly stops at the natural vortex length (L_n) in the lower point of the cyclone body.

W. Barth (1956) states that excessive length of the hydrocyclone increases the residence time and friction in cyclone wall and eventually the tangential velocity; V_θ, will decrease.

2.3.1.5 Down Stream Outlet

A small outlet area produces a large pressure drop across the cyclone that may causes cavitations in the outlet flow orifice. G. H. Kimber and M. T. Thew (1974) reported that in tests using 9.5-mm diameter outlets and high flow rates, gas liberation (separation of gas and liquid) could be seen at the outlet orifice.

2.3.1.6 Axial Outlet (Reject Flow)

Axial outlets are necessary for oil-enriched flow. In conventional solid-liquid hydrocyclones, the axial outlet adjacent to the tangential inlet (vortex finder) will carry about 90% of the outflow **(Figure 4)**. This vortex finder is designed to avoid a large short circuit flow. In de-oiling hydrocyclones, this reject ratio is between 5-10% of the

flow and thus a relatively smaller diameter outflow is required. If a high proportion of the inflow were removed through the axial outflow, the flow through the radial outflow stream may reverse, thus, defeating the objective of minimal water in the oil-enriched stream.

D. A. Colman and M. T. Thew (1980) reported that the addition of a small taper angle, as low as 1-2°, made a radical difference to the flow field. This design, when compared to the large cylindrical geometry, gave a more stable, smaller diameter reversed flow core and permitted operation with an extremely small diameter overflow exit port. Stable split ratios; "F", as low as 0.2% of feed were achieved. The best results were achieved without a vortex finder. An integral part of this design was a long cylindrical tailpipe and axially reversed core in which the smallest droplets migrate.

2.3.2 Factors Influencing Separation Performance (All Kinds of Cyclones)

Oil-water separation in a hydrocyclone can be characterized using Stokes' Law -- performance is impacted by variables such as dispersed phased sizes; "d", differential density (ρ_w is the water density, ρ_o is oil density), water viscosity; "μ" [g /cm/s], and gravitational, or in the case of cyclone centrifugal acceleration. This relationship is shown in **Equation 2**.

$$v = \frac{\left(\rho_w - \rho_p\right) g d_p^2}{18\mu} \qquad \text{Equation 2}$$

The separation velocity; "v" [cm/s] is directly proportional to the separation efficiency. According to Stokes' Law, the driving force for separation is the density difference between the continuous and dispersed phases.

Performance is impacted by the inlet flow rate, reject rate, temperature, differential density, chemical treatment, oil and solids content, and the free and dissolved air content. The oil droplet size also plays an important role in this separation. For each application,

most of these factors will remain constant. Operating variables, including feed composition and rate, along with pressure drop, generally dictate efficiency. The pressure drop between the inlet and each outlet is also key to performance.

N. Meldrum (1988) tested a Vortoil hydrocyclone and proposed the function shown in **Equation 3** for de-oiling liquid-liquid hydrocyclone oil-removal efficiency (E). In this relationship, the Reynolds number; "Re", density difference "$\Delta\rho$" and droplet size "d" are significant.

$$E = f\left[\left(\frac{4Q\rho_w}{\pi d\mu} = \mathrm{Re}\right)\frac{\bar{d}}{d}, \frac{\Delta_l}{\rho_w}\right] \qquad \text{Equation 3}$$

In Equation 3, "Q" [$cm^3 s^{-1}$], is the flow rate, "ρ_w" [$g\ cm^{-3}$] is the water density, "d" [cm] is droplet diameter, "$\bar{d}$" [cm] is the average droplet size; μ [$g\ cm^{-1}s^{-1}$] is viscosity and $\Delta\rho$ is the density difference between continuous and dispersed phases.

2.3.2.1 Effect of Slurry Density

The slurry density; ρ_m can be calculated using **Equation 4.**

$$\rho_m = \frac{100}{\frac{c_w}{\bar{\rho}_p} + \frac{100 - c_w}{\bar{\rho}_l}} \qquad \text{Equation 4}$$

In **Equation 4**, c_w is the solid particle concentration by weight in percent, ρ_m is the density of the dispersion, ρ_p is the density of solid particles and ρ_l is the liquid density.

2.3.2.2 Effect of Slurry Viscosity

The presence of particles or droplets invariably increases the slurry viscosity to a value greater then the fluid itself, and in many cases results in a slurry which is non-Newtonian in character.

A. Einstein (1906) conducted a theoretical analysis and proposed a viscosity equation **(Equation 5)** for dilute suspensions in laminar flow where the particles have no interaction with each other.

$$\frac{\bar{\mu}_m}{\bar{\mu}_o} = 1 = 2.5\phi_v \qquad \text{Equation 5}$$

In **Equation 5** " $\bar{\mu}_m$" is viscosity of suspension, " $\bar{\mu}_o$" is the viscosity of suspending medium and "ϕ_v" is the volume fraction of solid particles. The viscosity of more concentrated suspensions must take into account the various types of particle interactions that may occur.

2.3.2.3 Droplet Size Effect

Separation velocity is a function of droplet size -- this velocity increases with droplet size meaning that the larger droplets move more rapidly toward the central core. Very small droplets can form oil-in-water emulsions that hinder separation.

C. Gomez et. al. (2001) reported that oil separation efficiency increases with droplet size, and that larger droplets coalesce faster than the smaller droplets. They found that the droplet sizes in the under-flow are smaller than in the inlet-flow due to the break-up of droplets in the liquid-liquid hydrocyclone (LLHC).

D. A. Flanigan et. al. (1992) used a Vortoil de-oiling hydrocyclone. They studied the effect of droplet size in oil removal efficiency (**Figure 5**). They found that the oil removal efficiency increases dramatically when the reject ratio (over-flow) approaches one and that at ratios higher than one the separation efficiency was constant. A summary of their results are shown in **Figure 6** and **Figure 7**.

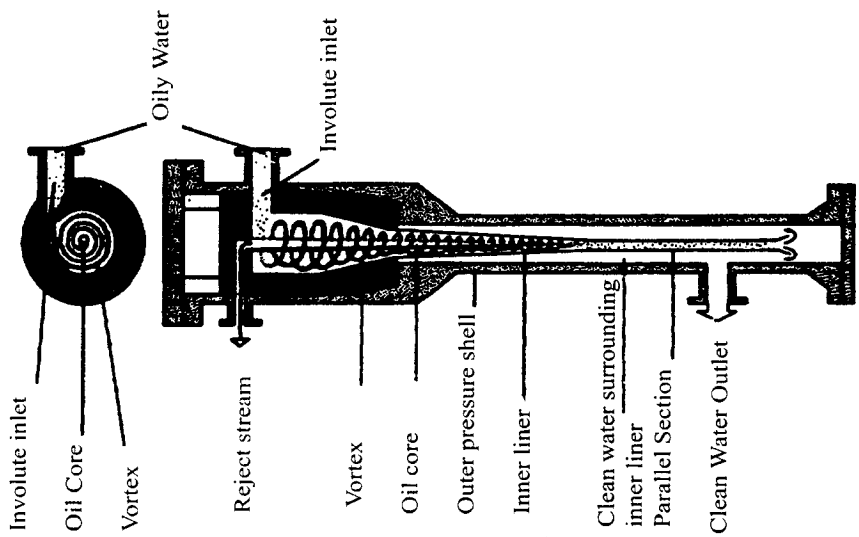

Figure 5: Vortoil de-oiling hydrocyclone as used by Flanigan D. A., et al. (1992).

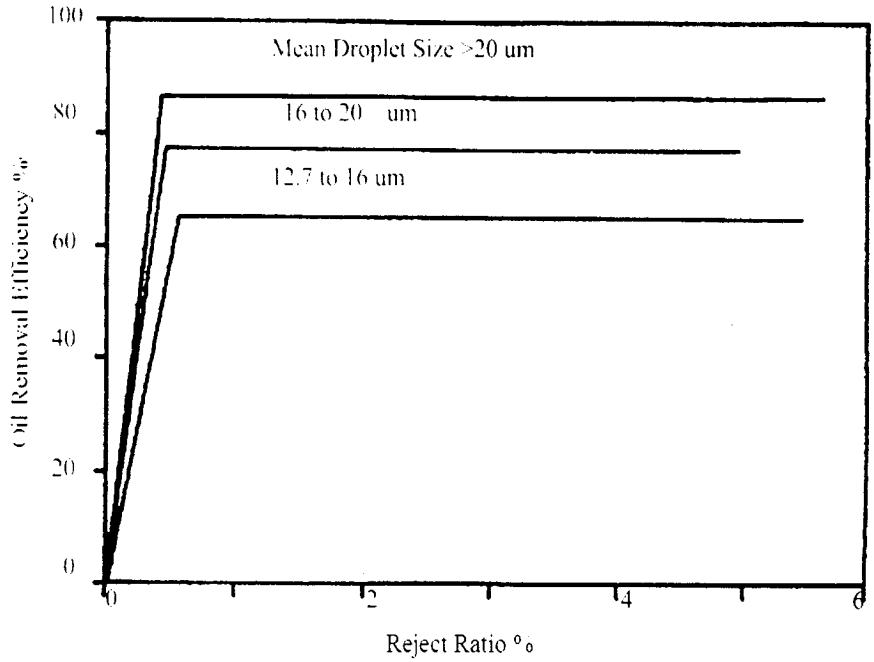

Figure 6: Effect of droplet size on oil removal efficiency for 60 mm and 35 mm de-oiling hydrocyclone from Flanigan D.A., et al. (1992).

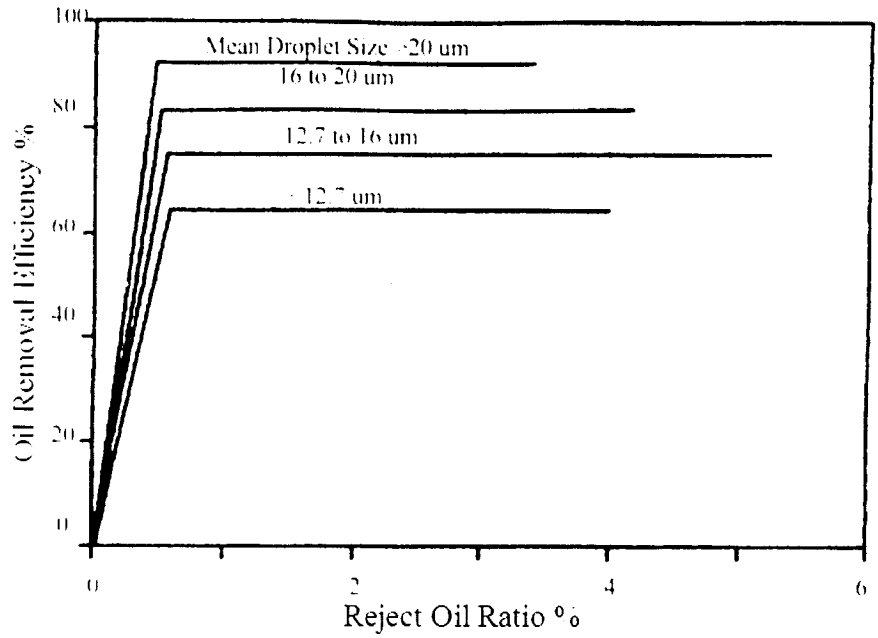

Figure 7: Effect of droplet size on oil removal efficiency for 60 mm and 35 mm de-oiling hydrocyclone from Flanigan D.A., et al. (1992).

A. C. Hoffman, et al. (2001) found that larger particles or droplets separate more easily than smaller one.

2.3.2.4 Effect of Chemicals

Some chemicals such as de-foamers, de-scalers, corrosion inhibitors and de-mulsifiers are commonly added to oil, particularly lube oil. K. M. Simms et. al. (1992) used Terra Nova crude oil and reported a 2-3% separation improvement in the performance of hydrocyclones (de-oilers). They used different oil pumps to make the dispersion with different droplet size distributions. Their results are plotted in **Figure 8**.

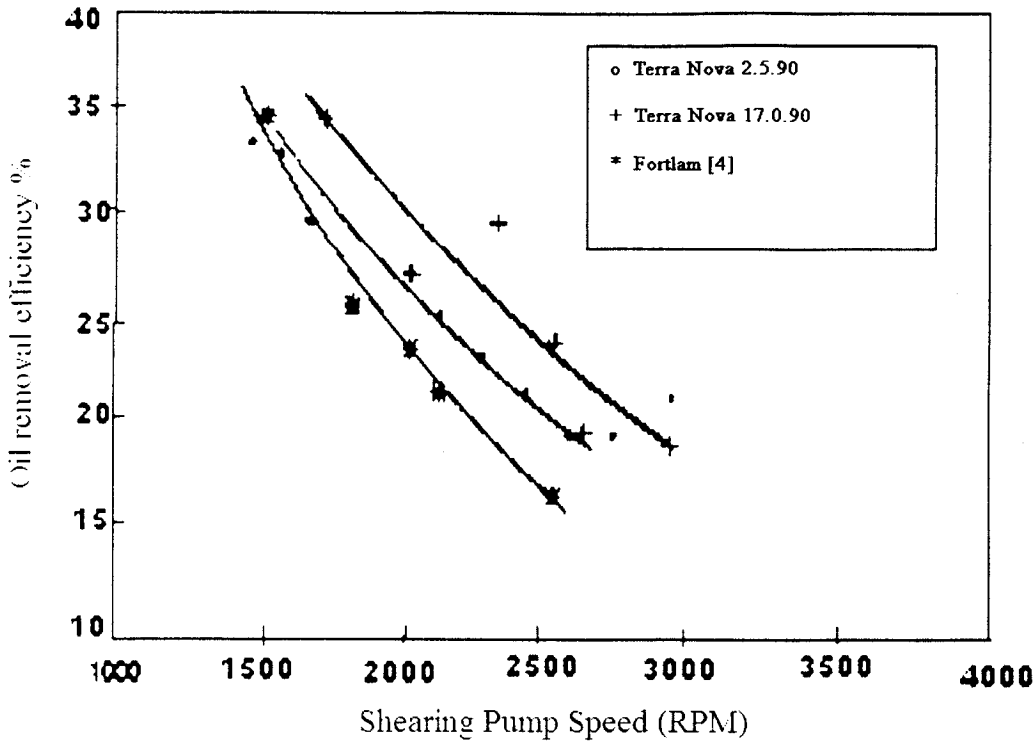

Figure 8: Feed drop size vs. shearing pump speed (Simms K. M., 1992).

K. M. Simms et. al. reported that the oil droplet size decreased when the pump speed increased. Coagulants and flocculants, chemicals such as Alum, $Al_2(SO_4)_3$ and $FeCl_3$, have been used in some North Sea production units.

Surfactants, in high concentration, affect the interfacial properties and emulsion stability of oil-in-water droplets and decrease separation efficiency.

2.3.2.5 Effect of Flow Rate

Low flow rates cause insufficient swirl. Inlet Reynolds number and the fluid turbulence inside the cyclone (**Equation 6**) influence oil removal efficiency.

$$\mathrm{Re} = \frac{J_{in} D_c}{v} \qquad \text{Equation 6}$$

In **Equation 6**, "Re" is the inlet Reynolds number, "D_c" is the diameter of the feed inlet port, "J_{in}" is the fluid velocity at the feed inlet, and "ν" is the fluid kinematic viscosity [cm^2/s].

Low Reynolds' number and flow-rate cause low swirl which is needed for cyclonic separation. Droplet breakage occurs when the Reynolds' number is high – this is not desired for cyclonic two-phase flow separation.

K. M. Simms et. al. (1992) observed a progressive increase in separation efficiency with feed flow rate (**Figure 9**).

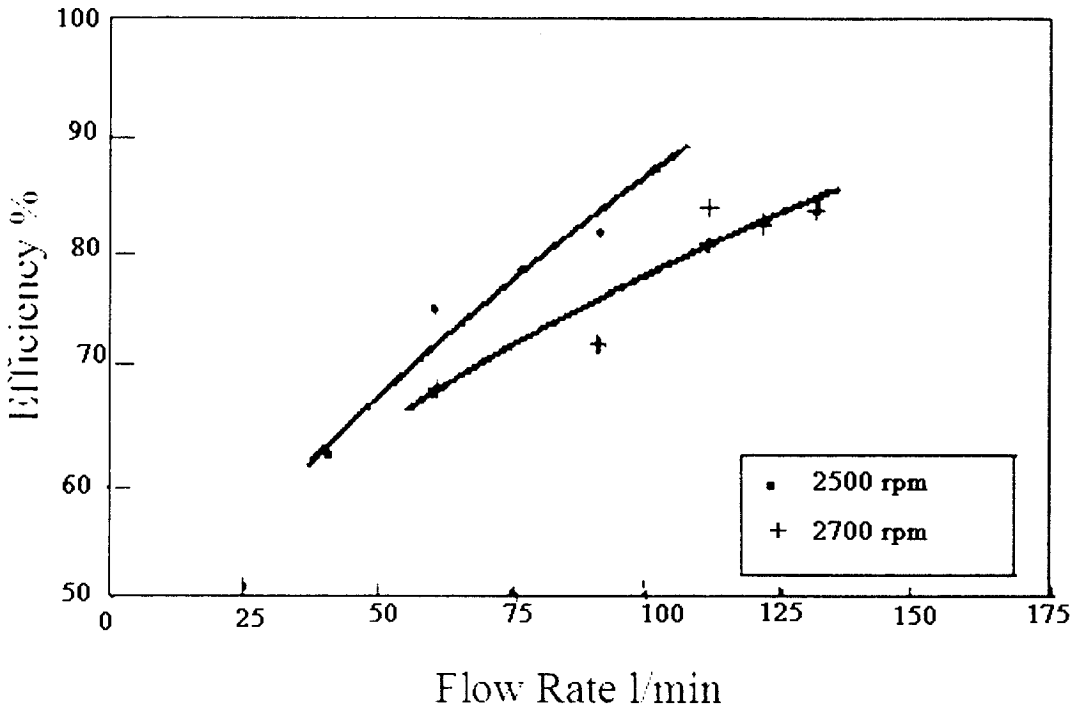

Figure 9: Separation efficiency vs. flow rate (500 ppm, 25°C) after Simms K.M. (1992).

Figure 9 shows that feed flow rate is proportional to pump speed -- feed flow rate provides the necessary kinetic energy for conversion to centrifugal force, which is necessary for cyclonic separations.

N. Meldrum (1988) reported that as flow rate increases the efficiency of separation to an optimum (**Figure 10**). Further increases in flow cause a sharp drop in efficiency. A certain minimum flow rate is necessary to set-up the vortex motion and establish centrifugal force separation. N. Meldrum (1988) emphasizes that high flow rate causes droplet breakage and increases core pressure. As this pressure approaches atmospheric, the available pressure to drive the reject stream is reduced. This situation inhibits the rejected flow rate resulting in little or no separation.

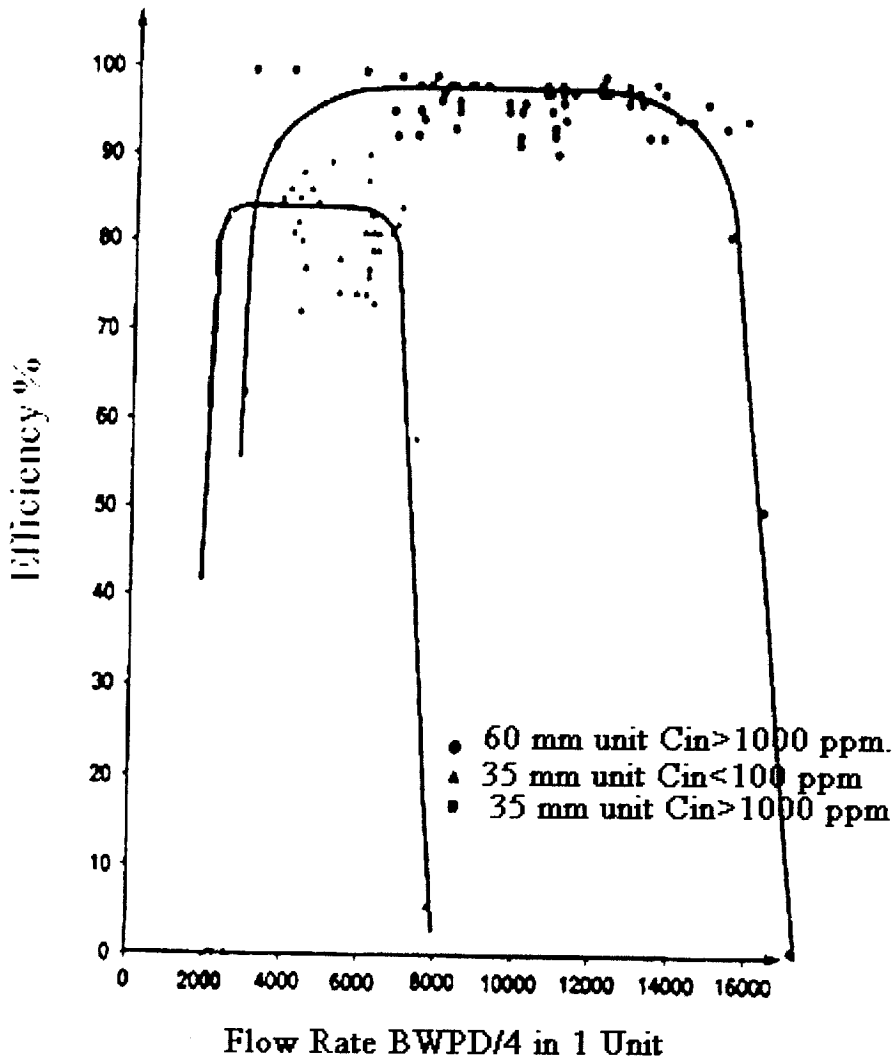

Figure 10: Hydrocyclone efficiency vs. flow rate from Meldrum N. (1988).

2.3.2.6 Effect of Temperature

Temperature influences separation performance by altering the water and organic phase viscosities. Furthermore, a small change in differential density also occurs. Temperature increase usually improves a hydrocyclones' performance by reducing the water viscosity.

2.3.2.7 Split Ratio

The split ratio is an important operational parameter defined as the ratio of overflow to inlet volumetric flow rates **(Equation 7).**

$$F = \frac{Q_{overflow}}{Q_{inlet}} \qquad \text{Equation 7}$$

In **Equation 7**; "F" is the split ratio, "$Q_{overflow}$" is the total flow rate at the upper outlet of the liquid-liquid hydrocyclone (LLHC) and "Q_{inlet}" is the total inlet flow rate.

G. R. Kimber and M. T. Thew (1974) reported that cyclone efficiency increases to an optimum with the split ratio as shown in **Figure 11**.

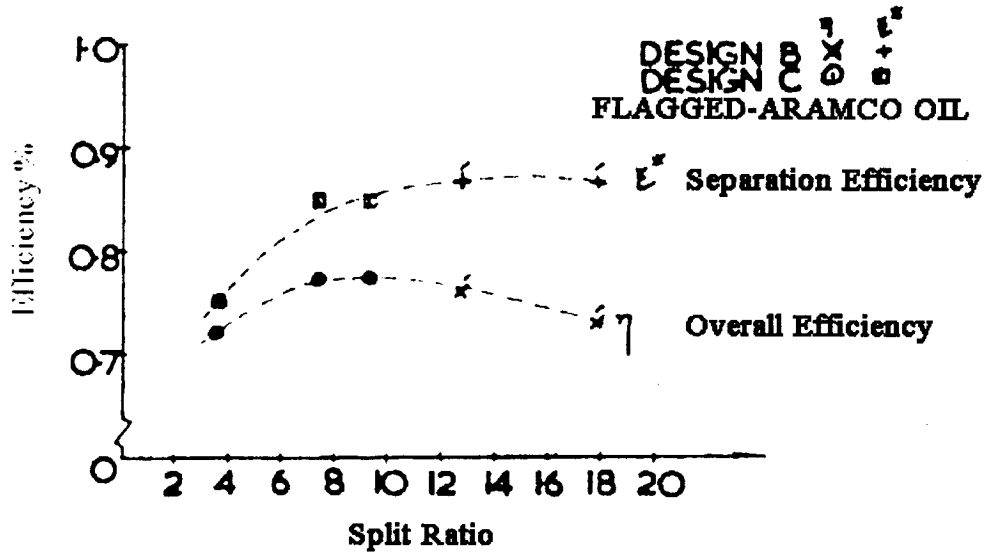

Figure 11: Variation of separation with split ratio (Kimber G. R and Thew M. T. 1974).

2.3.2.8 Effect of Operating Pressure and Pressure Drops.

The pressure drops between the inlet and each outlet are critical for successful hydrocyclone operation. For a given flow rate, a minimum inlet pressure is required to generate the vortex. When the minimum inlet driving force is reached, inlet to underflow "ΔP_1", and inlet to overflow "ΔP_2", differential pressures give an indication of the hydrocyclone performance. The upper-flow ratio is defined as the ratio of over- to inlet-flow and may be expressed as a percentage. Hydrocyclone operation below the optimum upper flow ratio results in a low dispersed phase removal efficiency because a small volume of that phase reaches the central core and is removed with the overflow stream. Operating above the optimum overflow ratio does not impair removal, but adds water volume of the overflow stream. Typical operating overflow ratios range from 0.5% to 3%.

L. Svarovsky (1984) reported that with increasing pressure drop the efficiency of separation increases; the typical operating pressure of large cyclones is usually between 100 and 200 kPa.

G.R. Kimber and M.T. Thew (1974) emphasized that pressure drop through the cyclone is proportional to inflow squared (**Figure 12**). Figure 12 illustrates the results of two-cyclone geometry's: A and B.

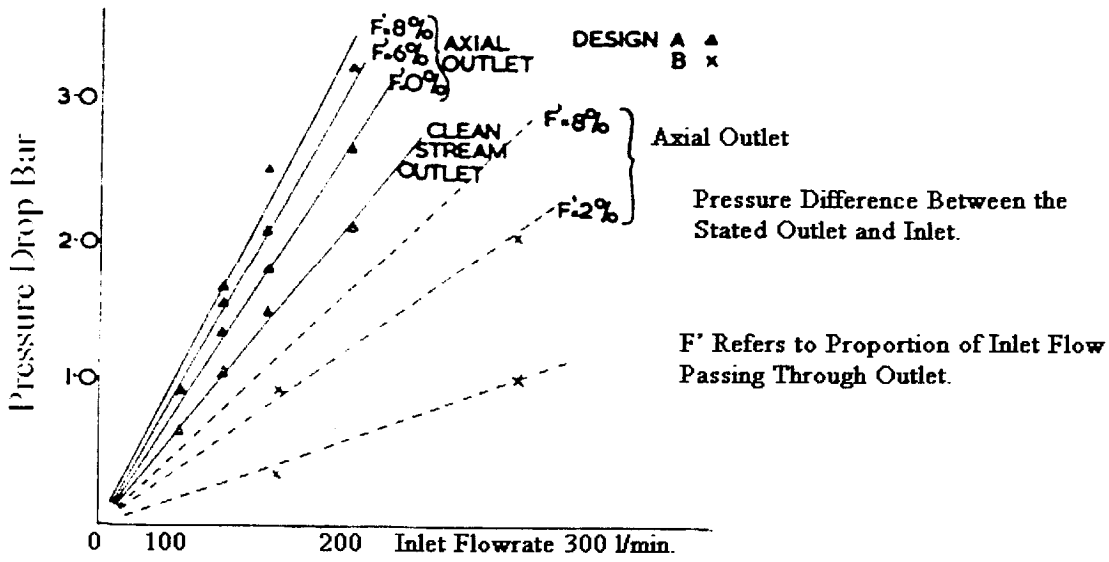

Figure 12: Pressure drops - flow rate from Kimber G.R and Thew M.T. (1974).

C. Gomez, et. al. (2001) modified Bernoulli's equation to calculate the pressure drop from the inlet to the under-flow outlet **(Equation 8).**

$$P_{in} + \frac{1}{2}\rho_c V_{in}^2 = P_u + \frac{1}{2}\rho_c U_u^2 + \rho_c \left(h_{cf} + h_f\right) + \rho_c g \sin\theta \qquad \text{Equation 8}$$

In Equation 8 "ρ_c" is the continuous phase density; "P_{in}" and "P_u" are the inlet and outlet pressures respectively; "V_{in}" is the average inlet velocity; "U_u" is the underflow average axial velocity; "θ" is the angle of the liquid-liquid hydrocyclone axis with the horizontal and "h_{cf}" and "h_f" correspond to the centrifugal force and frictional losses expressed as a "head" or height.

N. Meldrum (1988) notes that under normal operating conditions, there are two distinct pressure drops across the hydrocyclone separator. The first, the pressure drop between the inlet-flow and the under-flow, is shown in **Equation 9 -- Figure 13** and the second, the pressure drop between inlet-flow and the over-flow, is shown in **Equation 10 -- Figure 14.**

$$\Delta p_1 = p_{in} - p_{out}$$ Equation 9

$$\Delta p_2 = p_{in} - p_{rej}$$ Equation 10

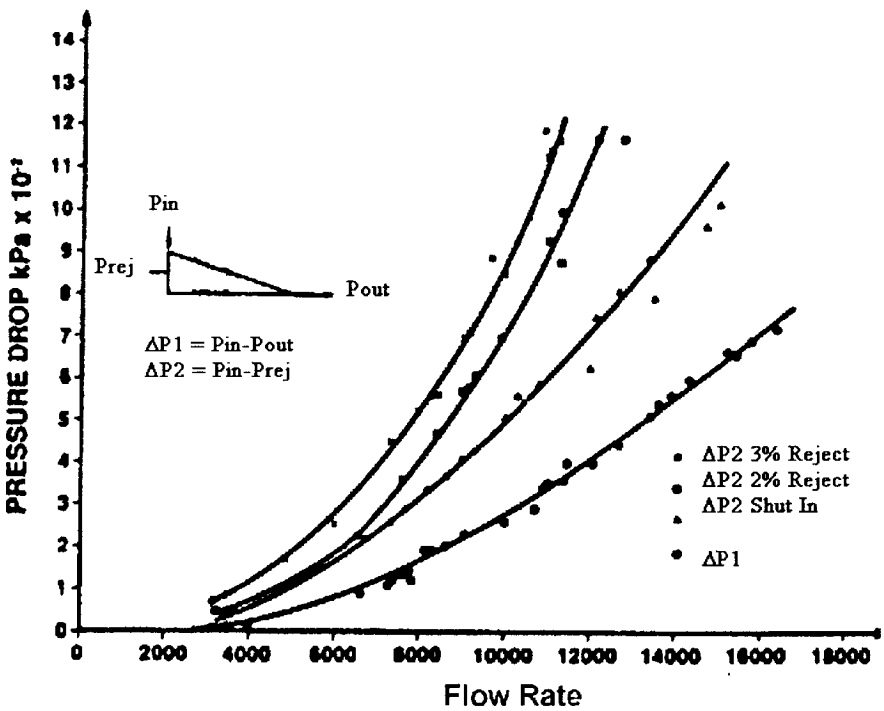

Figure 13: 60-mm hydrocyclone pressure drop vs flow rate from Meldrum N. (1988).

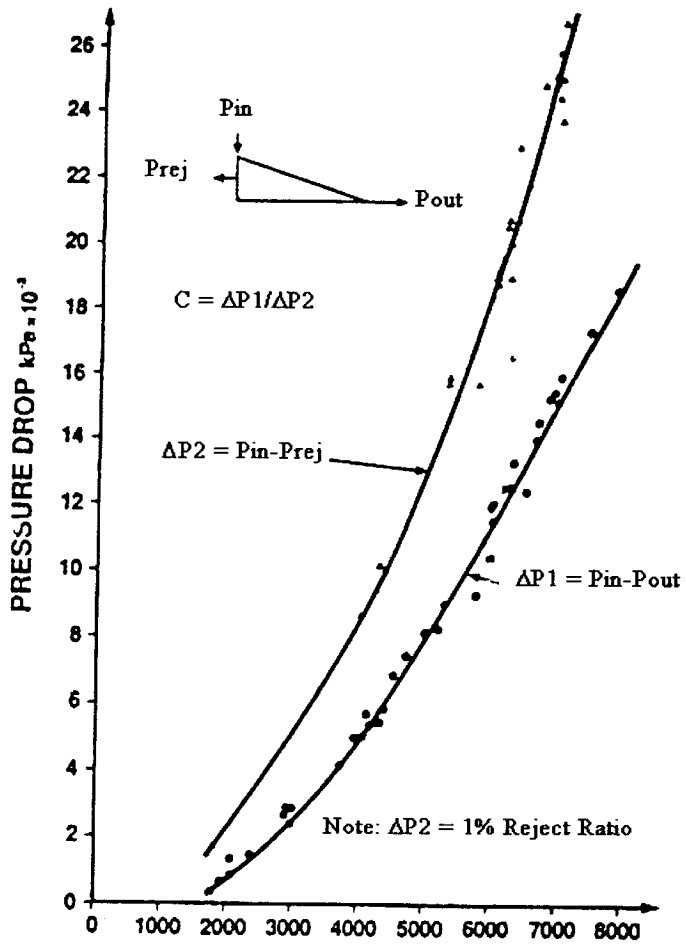

Figure 14: 35-mm hydrocyclones pressure drop vs flow rate from Meldrum N. (1988).

In hydrocyclone separation performance, the most significant pressure drop is between the feed inlet and overflow streams. This pressure drop determines hydrocyclone capacity and may be used for control purposes. N. Meldrum (1988) has proposed the relationships shown in **Equation 11** and **Equation 12** to predict hydrocyclone pressure drop.

$$C = \frac{P_{in} - P_{over}}{P_{in} - P_{under}} = \frac{\Delta P_2}{\Delta P_1}$$ Equation 11

$$P_{rej} = P_{in} - C(P_{in} - P_{out})$$ Equation 12

In **Equation 11** and **Equation 12**, "C" is a constant, "P_{in}" is the inlet-flow pressure; "P_{rej}" is the upper-flow pressure and "P_{out}" is the under-flow stream pressure.

2.3.2.9 Effect of Feed Concentration

L. Svarovsky (1984) reported that as feed concentration increases the efficiency of separation falls. Hydrocyclones are therefore operated with dilute feeds whenever high total mass recoveries are sought -- this may be acceptable in solid - liquid separations. In the case of oil separation, higher inlet oil concentrations increase the probability of coalescence, which in turn gives rise to an increased mean droplet size. Care is needed to control and minimize shear upstream of the hydrocyclone in order to prevent droplet breakage.

G. R. Kimber and M.T. Thew (1974) reported that the overall efficiency of a cyclone is almost independent of inlet oil concentration (**Figure 15**).

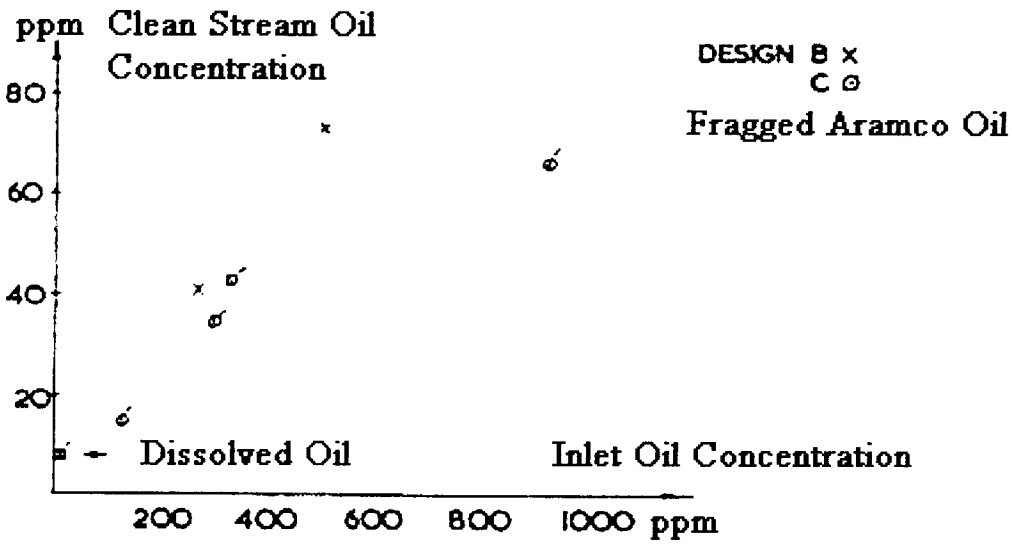

Figure 15: Variation of separation with oil inlet concentration (Kimber G.R and Thew M.T; 1974).

K. M. Simms et. al. (1992) investigated the effect of oil concentration in the Vortoil de-oiling hydrocyclone using inlet oil concentrations from 50 to 5000 ppm. They reported that the organic-phase hold-up has a much greater effect on the degree of dispersion than either shearing pump speed or temperature, particularly above 1000 mg/l. The authors achieved a discharged level of 40 mg/l (EPA discharge guideline) with feed oil concentrations up to 350 ppm.

C. Gomez et. al, (2001) reported that increasing oil content improves separation -- probably because the larger oil droplets coalesce faster than the smaller ones. The authos stated that this finding is also true for bubble coalescence.

2.3.3 Particle - Liquid Interactions in Low Concentrations

At concentrations of less than about 0.5%, by volume, the individual particles are on average so far apart that they do not affect each other as they move through the fluid. Particle separation can be achieved by applying force to the particles. The magnitude of this force can usually be easily expressed. The drag force, however, is more difficult to establish. Drag force; F_D, can be written as **Equation 13**.

$$F_D = C_D A \frac{\rho u^2}{2} \qquad \text{Equation 13}$$

In **Equation 13,** "u" [m/s] is the relative velocity between the fluid and the particle, "ρ" [kg/m^3] is the fluid density, "A" is the projected area of the particle, and "C_D" [N] is the drag coefficient. For coarse particles, the drag coefficient is constant and dependent upon the particle Reynolds number (**Equation 14** and **Figure 16**).

$$\mathrm{Re}_p = \frac{u_p d_p \rho_l}{\mu_l} \qquad \text{Equation 14}$$

In **Equation 14**, "Re_p" is particle Reynolds number; "u_p" [cm s^{-1}] is particle-settling velocity, and "ρ_l" [g cm^{-3}] and "μ_l" [g $cm^{-1}s^{-1}$] are the liquid density and viscosity respectively.

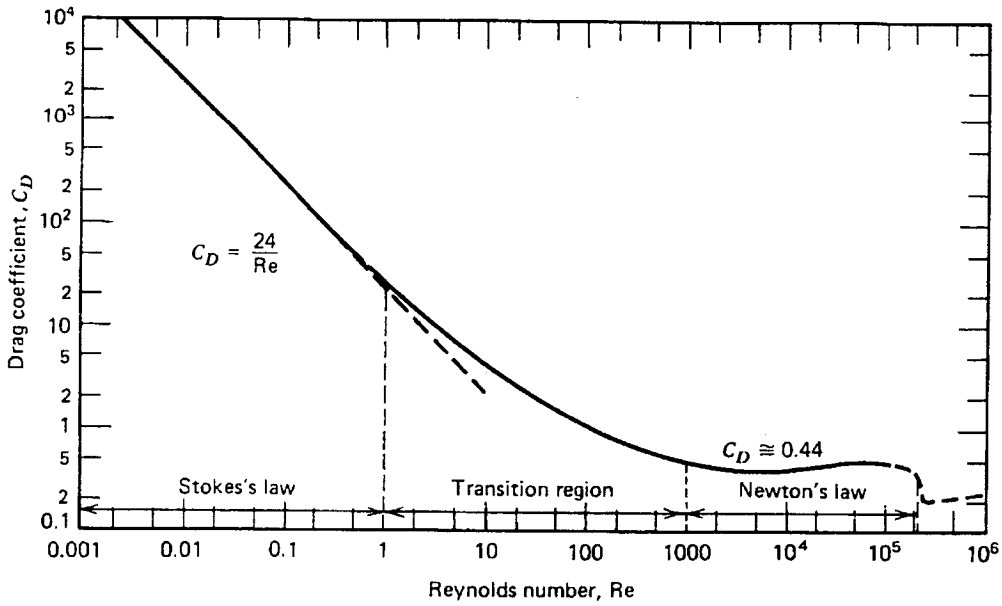

Figure 16: Drag coefficient versus particle Reynolds number for spherical particles (Vennard, J. K, 1982).

At low Reynolds' number, under laminar flow conditions where viscous forces prevail "C_D" can be determined theoretically from the Navier-Stokes' equations. The solution is known as Stokes' law (**Equation 15**).

$$u_p = \frac{g d_p^2 (\Delta\rho)}{18\mu_l} \qquad \text{Equation 15}$$

For Reynolds number below 0.2 the drag force can be written as **Equation 16**.

$$C_D = \frac{24}{Re_P} \qquad \text{Equation 16}$$

"Re_p", which characterizes the flow around the particles, is given by **Equation 14**. For Reynolds' numbers greater than 1000 (Newtonian region) the flow is fully turbulent, with inertial forces prevailing, and C_D becomes a constant equal to about 0.44.

For a particle of mass "m" under the influence of a field of acceleration "a", the equation of the motion is **Equation 17**.

$$m\frac{du}{dt} = ma\left(1-\frac{\rho_l}{\rho_s}\right) - F_D \qquad \text{Equation 17}$$

Where "ρ_s" is solid density, "ρ_l" is liquid density, du/dt is derivative of velocity to time and "F_D" is the drag force.

In hydrocyclone applications concerned with the separation of fine particles the Reynolds number is low "<0.2" due to the low value of "d_p" and "u_p"; therefore, it is reasonable to assume Stokes' law.

The terminal settling velocity; "U_t", can be expressed as **Equation 18.**

$$U_t = \tau a \qquad \text{Equation 18}$$

In **Equation 18**, "τ" [s] is the particle relaxation time and "*a*" [cm/s^2] is the acceleration. Particle relaxation time, τ [s] can be determined by using **Equation 19**.

$$\tau = \frac{\rho_s d_p^2}{18\mu_l} \qquad \text{Equation 19}$$

In **Equation 16** "ρ_s" is dispersed phase density, "d_p" particle diameter, and μ_l is liquid viscosity.

The radial velocity in a hydrocyclone, "u_r" [cm/s] due to the centrifugal acceleration, can be expressed as **Equation 20**.

$$u_r \approx \frac{\tau \upsilon^2}{D_c} \qquad \text{Equation 20}$$

In **Equation 20,** D_c [cm] is cyclone diameter and υ [cm/s] is feed velocity.

2.3.4 Stokes' Number

Stokes' number; "Stk", is a dimensionless number that relates the inertial forces and hydrodynamic forces and is calculated using **Equation 21**. This number deals with the dynamics of particles, droplets and bubbles and is an important parameter in fluid particle flow. A small Stokes' number; < 1, indicates that particles follow the streamlines almost perfectly and collision between the particles are rare.

$$Stk = \frac{\tau v^2}{D_c} \qquad \text{Equation 21}$$

2.3.5 Reynolds Number

The fluid Reynolds number is a ratio of inertial force to viscous force. "Re" can be determined by **Equation 22**.

$$\mathrm{Re} = \frac{v d_p \rho_l}{\mu_l} \qquad \text{Equation 22}$$

In **Equation 22,** "v" is the settling velocity, "d_p" is the particle diameter, and "ρ_l" and "μ_l" are the liquid density and kinematic viscosity (m^2s^{-1}) respectively. Kinematic viscosity is a variable, which describes the diffusion of momentum $\mu = \eta/\rho$, η is dynamic viscosity and ρ is density.

2.3.6 Euler Number

Another important dimensionless group characterizing the performance of hydrocyclones is the resistance coefficient, defined as the static pressure drop; "Δp", across the hydrocyclone inlet and outlet divided by the dynamic pressure calculated from the characteristic velocity, "v". The resistance coefficient is called the Euler number; "Eu" and can be calculated using **Equation 23**.

$$Eu = \frac{2\Delta p}{\rho v^2}$$ Equation 23

In **Equation 23**, Δp is pressure drop, ρ is density and v is velocity of the medium.

2.4 Modeling Theory

2.4.1 Introduction and Background of Hydrocyclone Modeling.

Theoretical studies of hydrocyclone flow are, in general, based on the Navier-Stokes' equations.

Multi-phase flow enters the hydrocyclone through a tangential inlet(s). The inflow is directed into a vortex without disrupting the reverse flowing core. As the feed is forced down the liner, it flows in a helical form along the liner walls. The flow accelerates in the concentric reducing section of conical hydrocyclones **(Figure 17)** and this velocity creates a strong centrifugal force that promotes rapid separation.

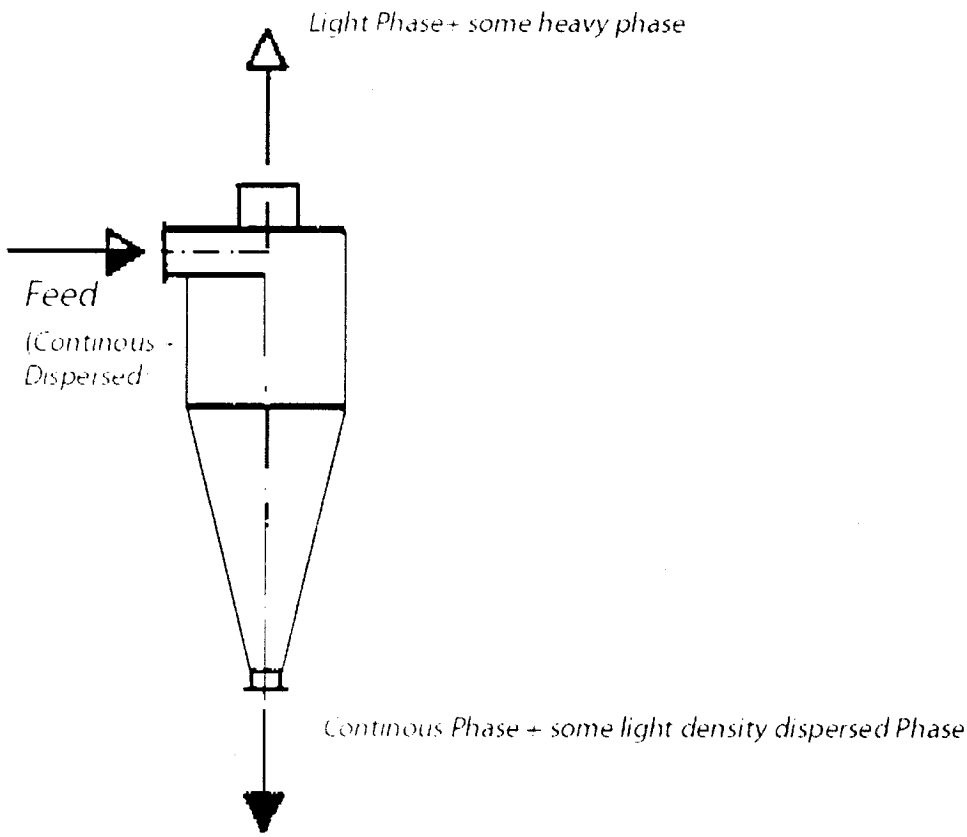

Figure 17: Multi-phase flow hydrocyclone from Svarovsky L. (1984).

The denser phase (water) moves to the walls of the hydrocyclone and down to the outflow (bottom). The lighter phase (organic or air) is drawn into the low-pressure core and removed from the upstream outlet orifice (reject flow). The vortex and reverse flowing core extends down into the tail or conical section of the hydrocyclone. The tail increases the residence time and allows smaller droplets to migrate into the core. The total residence time in a hydrocyclone is usually less than two seconds.

Centrifugal forces in a hydrocyclone may be on the order of 1000 times that of gravity; therefore, this vessel is insensitive to motion, orientation or vibration.

The relationship between hydrocyclone geometries; such as diameter, inlet size, and the dimensions of the reject and outflow orifices, affect the range of inlet concentrations and oil droplets sizes that can be separated, as well as the flow capacities at a given pressure drop.

De-oiling hydrocyclones are capable of splitting dispersions of up to 30% organic-phase hold-up with droplet sizes greater than 10 μm. The organic dispersed phase must be immiscible and have a density difference with the continuous phase; "$\Delta\rho$", > 0.05 g/cm^3 at the operational temperature. The continuous-phase must have a lower viscosity; while the gas or vapour dispersed, phase content should be less than 20% by volume.

2.4.2 Theories of Hydrocyclone Separation

2.4.2.1 Introduction

This section compares hydrocyclones separation process models developed models by several investigators.

2.4.2.2 Equilibrium Orbit Theory

L. R. Plitt (1976) presents fundamental equations which estimate the separation size based on the equilibrium orbit theory. At some point in the cyclone, it is assumed that

the "d_{50}" particle size is at equilibrium with respect to the two principal forces acting on it -- fluid drag force and centrifugal force, as shown in **Figure 18** and **Figure 19.** In these figures "F_c" is centrifugal force, "F_d" is drag force, "V" is tangential component of fluid velocity and "W" is radial component of fluid velocity.

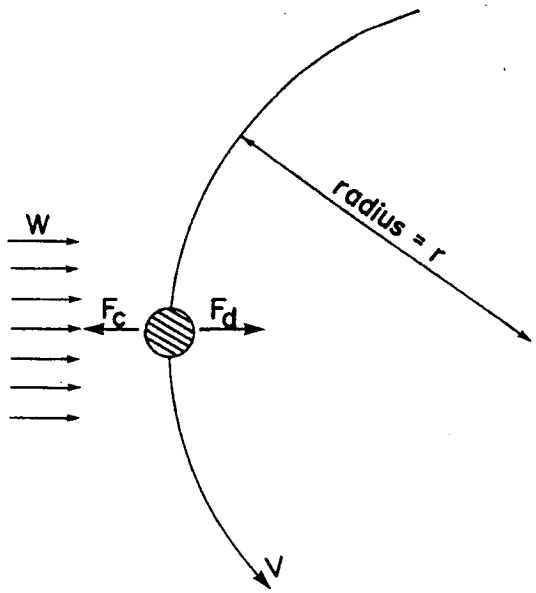

Figure 18: Force acting on an orbiting particle in a hydrocyclone from Plitt L. R. (1976).

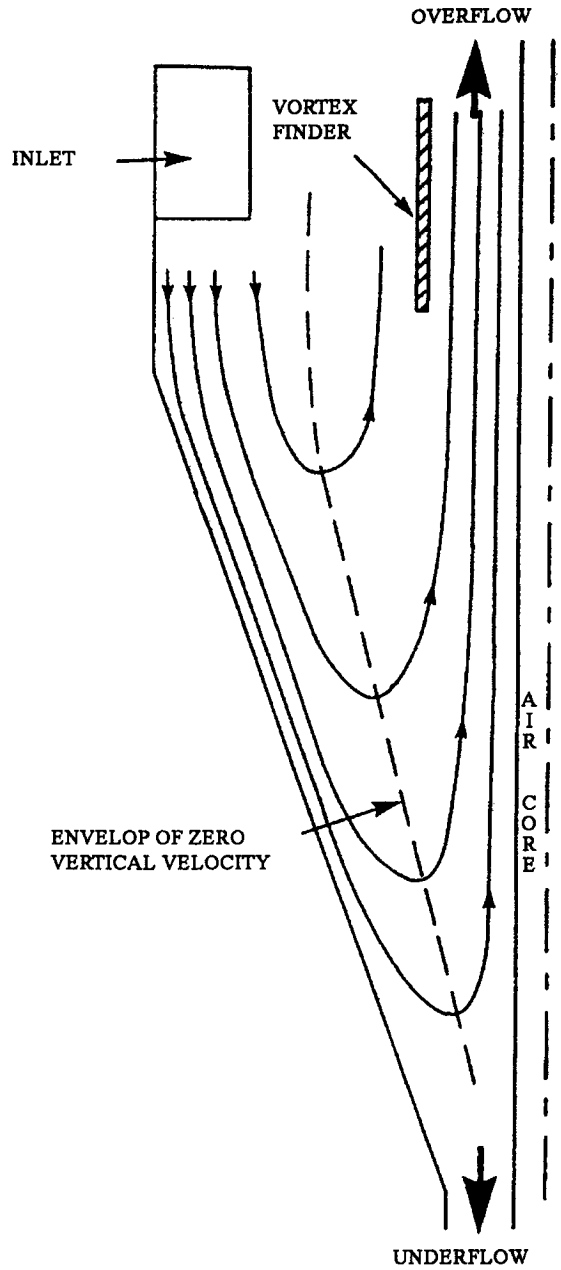

Figure 19: Distribution of the vertical and radial velocities from L. R. Plitt (1976).

The best-known approach to the equilibrium orbit theory is that of D. Bradley and D. J Pulling (1959). This theory is based on the fact that, for solid-liquid separation, the solid usually has a higher specific gravity than the liquid and the radial fluid velocity and settling velocity are of opposite sign. The authors developed a model based on the placement of a flow control mantle. Proper placement of the mantle has shown that inward radial velocity does not occur in the region immediately below the vortex finder.

D. Bradley and D. J. Pulling (1959) assume that separation only occurs across the conical surface below the mantle as shown in **Figure 20**.

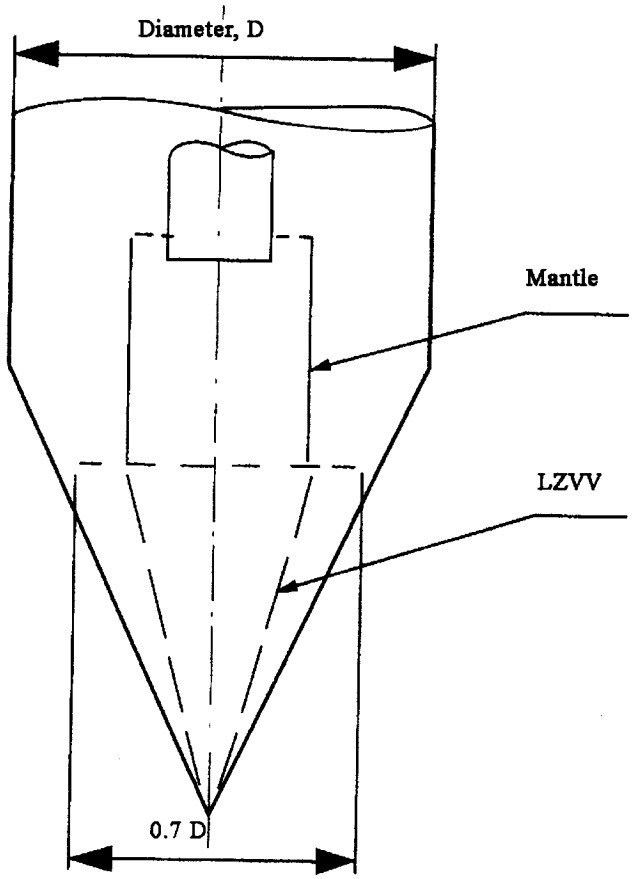

Figure 20: Conical surface and mantle below the vortex finder, Bradley D and Pulling D.J (1965).

M. G. Driessen (1939) developed the equilibrium orbit theory based on the concept of equilibrium radius. According to this concept, particles of a given size attain an equilibrium radial orbit in the cyclone where their terminal settling velocity; "U_r", is equal to the radial velocity of the liquid "v_r". Particles are elutriated by the inward radial flow according to the balance of the centrifugal and drag forces as shown in **Equation 24**.

$$u_r = \tau \frac{v_t^2}{r} \qquad \text{Equation 24}$$

In **Equation 24,** "τ" [s] the particle residence time, "r" is the cyclone radius and "v_t" is the tangential velocity.

N. Yoshioka and Y. Hotta (1955) carried out a series of tests using 50 to 150 mm hydrocyclones with dilute slurries and developed the empirical relationship shown in **Equation 25.**

$$\bar{d}_{50} = \frac{48.8 D^{0.1} D_i^{0.6} D_o^{0.8} - \mu^{-0.5}}{Q^{0.5} \left(\bar{\rho}_s - \bar{\rho}_l \right)^{0.5}} \qquad \text{Equation 25}$$

In **Equation 25** "d_{50}" [m] is the particle median split size, "ρ_s" [kg/m^3] is dry solid density, "ρ_l" [kg/m^3] is liquid density, "D" [m] is cyclone diameter, "D_i" [m] is the inlet diameter, D_o [m] is overflow diameter, Q [m^3/s] is feed volume rate and μ is the continuous-phase viscosity [kg m/s].

This size relationship assumes that the locus of zero vertical velocity (LZVV) is in the form of an imaginary cone that coincides with the apex of the cyclone and its base is at the bottom of the vortex finder (**Figure 20**). The radial liquid velocity remains constant over the whole LZVV. N. Yoshioka and Y. Hotta (1955) developed the general dispersed-phase separation relationship shown in **Equation 26.**

$$Stk_{50} = \frac{0.154}{Eu} \left(\frac{D_c}{D_o} \right)^{0.3} \qquad \text{Equation 26}$$

In this equation, "Stk_{50}" is the Stokes number (for cut-size "d_{50}") found using **Equation 27.**

$$Stk_{50} = \frac{d_{50}^2 (\rho_s - \rho_l) v}{18 \mu D_c} \qquad \text{Equation 27}$$

In these equations, "Eu" is the Euler number, "D_c" is the hydrocyclone body diameter, "D_o" is the cyclone overflow diameter, μ is viscosity and "v" is the superficial velocity in the cyclone body; the characteristics velocity, as calculated by **Equation 28.**

$$v = \frac{4Q}{\pi D_c^{\,2}} \qquad \text{Equation 28}$$

The experimental particle removal correlation of N. Yoshioka and Y. Hotta (1955), for a 150-mm diameter cyclone, resulted in the Euler number as shown in **Equation 29**.

$$E_u = 54.3\left(\frac{D}{D_i}\right)^{1.2}\left(\frac{D}{D_o}\right)^{1.9} \qquad \text{Equation 29}$$

In **Equation 29,** "D" is the cyclone diameter, "D_i" is the inlet equivalent diameter and "D_o" is the diameter of overflow.

D. Bradley and D. J. Pulling (1965) demonstrated the feasibility of liquid-liquid separations in a hydrocyclone but also underlined the difficulty of separations with low differential densities and possible droplet breakage -- the tangential velocity and residence time need to be increased to raise efficiencies under these conditions. A longer cone of smaller angle and proper inlet area has allowed standard design hydrocyclones to separate oil from "produced" water efficiently. By using a backpressure arrangement (overflow pressure), oil may be removed as a concentrated phase at the overflow (reject), while cleaned water flows through the underflow.

D. Bradley and D.J. Pulling (1959) developed their model based on theoretical constants that were adjusted slightly to fit the experimental results. Their model for a 38 mm hydrocyclone is shown in **Equation 30.** The authors derived "Eu" from the centrifugal static head as shown in **Equation 31**.

$$Stk_{50} = \frac{2(0.38)^{2n}}{Eu\pi n}\left(1 - R_f\right)\tan\frac{\theta}{2}\left[\left(\frac{D}{D_o}\right)^{2n} - 1\right] \qquad \text{Equation 30}$$

$$Eu = \left(\frac{D}{D_i}\right)^4 \frac{\alpha^2}{n}\left[\left(\frac{D}{D_o}\right)^{2n} - 1\right] \qquad \text{Equation 31}$$

In **Equation 30** and **Equation 31,** θ is cone angle, D is cyclone diameter, D_i is diameter of the cyclone inlet, and D_o is the diameter of the vortex finder.

Referring to **Equation 30** and **Equation 31**, "R_f" is underflow-to-feed-ratio (flow ratio), "n" and "α" depend on the cyclone design and the fluid properties ("α" is also dependent on "Q"). For the given cyclone design D. Bradley and D.J. Pulling (1959) found that α = 0.45 and n = 0.8. According to D. Bradley and D.J. Pulling (1959), "Stk_{50}" does not depend on the inlet diameter except for a possible affect on "n". Some investigators have criticized this theory because it:

- does not take into account the residence time of the particle in the cyclone.
- does not take in account the turbulence as it might affect particle separation.
- can not be applied when the dispersed phase has a lower specific gravity than the continuous phase.

2.4.2.3 Residence Time Theory

The residence time theory was developed by K. Rietema (1961). This model uses the decantation theory based on hydrocyclone particle residence time and radial displacement (calculated assuming non-equilibrium conditions). The theory assumes a homogenous distribution of all particles across the inlet. The author developed this model based on the wall migration concept. In his model, he relates hydrocyclone tangential velocity, V_θ and hydrocyclone pressure drop (Δp) to determine cut-size. The cut-size will be the size of particle, which, if entering precisely in the center of the inlet pipe, just reaches the wall

after residence time "T". Mathematically, this means that the particle radial settling velocity, integrated with time, should be equal to half the inlet diameter – as shown in **Equation 32.**

$$\int_0^T u_r dt = \frac{D_i}{2} \qquad \text{Equation 32}$$

Predicted velocity "u_r", is calculated from tangential fluid velocity; "v_t", using **Equation 33** (K. Rietema; 1961).

$$u_r = \frac{d_{50}^2 \Delta\rho}{18\mu} \frac{v_t^2}{r} \qquad \text{Equation 33}$$

In this model, the residence time is related to cyclone dimensions and axial fluid velocity; "v_z", defined in **Equation 34** as the change in vertical distance with time.

$$v_z = \frac{dz}{dt} \qquad \text{Equation 34}$$

The authors combined **Equation 33** and **Equation 34** with an expression for a static pressure drop to obtain the relationship found in **Equation 35**, and **Equation 36.**

$$Stk_{50} = \frac{\pi Cy_{50} D}{36 Eu L} \qquad \text{Equation 35}$$

$$\Delta p = \rho_w \int_0^R \frac{v_t^2}{r} dr \qquad \text{Equation 36}$$

"Cy_{50}" is a characteristic cyclone number for the well-designed hydrocyclone and is calculated by the relationship shown in **Equation 37.**

$$Cy_{50} = \frac{d_{50}{}^2 \Delta\rho}{\mu} L \frac{(\Delta p)_t}{\rho Q}$$ Equation 37

In this equation, "L" [cm] is the length of the hydrocyclone, "D" is the hydrocyclone diameter, "ρ_w" is the liquid density, "v_t" [cm/s] is the tangential velocity, "R" is the radius of the inlet center, "v_i" is the velocity of liquid in inlet, "r" is cyclone diameter, Δp_t is total pressure loss necessary to operate the cyclone, μ is liquid viscosity and "Q" [cm^3/s] is the suspension feed flow rate in hydrocyclone.

The author rearranged **Equation 37** and included geometrical variables to give **Equation 38**.

$$\frac{d_{50}^2 \Delta\rho L \Delta p}{\mu\rho Q} = \frac{36 v_z R}{\pi v_i D_i}$$ Equation 38

A. B. Holland-Batt (1982) developed a newer version of residence time theory, the so-called "Bulk Model"; that considers radial flow. The residence time of the liquid in the cyclone was used as residence time and average radial fluid velocity. The author assumes a narrow cone angle and "l" equal to length of the cylindrical section (**Equation 39**).

$$Stk_{50} = \frac{1}{4Eu}\left(\frac{1}{\frac{L}{D}+\frac{l}{D}} + \frac{3\ln 2}{\frac{L}{D}+\frac{2l}{D}}\right)$$ Equation 39

Equation 39 does not include the effects of the inlet and vortex finder diameters.

H. F. Trawinski (1980) developed another theoretical approach to cut-size prediction that can be considering a version of the residence time theory. This relationship is found in **Equation 40**.

$$Stk_{50} = \frac{1}{8Eu}\frac{D}{(L-l)}\frac{D}{D_o}$$ Equation 40

The author uses Stokes' Law to calculate the cut-size and proposes a rather simplistic correlation for the pressure drop, flow rate relationship where the Euler number apparently does not depend on Reynolds number.

2.4.2.4 Crowding Theory

This is a mechanistic theory that postulates that the behaviour of a hydrocyclone is the result of an ordered process that is independent of its dimensions (D. A. White, 1991). The main variables that describe the process are the fraction of feed solids and water that are rejected from the under-flow.

The crowding theory was first suggested by P. H. Fahlstrom (1963) who proposed that the cut-size is primarily a function of the capacity of the underflow orifice and of the feed particle size distribution. He states that the crowding effect, hindered discharge through the apex, can swamp the primary interaction to the extent that the cut-size can be estimated from the mass recovery to the underflow.

P. H. Fahlstrom (1963) reported that cut-size was dependent upon the feed density and pulp characteristics. He stated that hydrocyclone dimensions and feed flow rate had no effect on the relationship.

2.4.2.5 Turbulent Two-Phase Flow Theory

The effect of turbulence on separation in hydrocyclones has been of concern to researchers. K. Rietema (1961) studied this issue and estimated the turbulent viscosity; "ε", with the aid of tangential velocity profiles measured by D. F. Kelsall (1952). K. Rietema (1961) uses the dimensionless parameter; "λ", as calculated in **Equation 41**.

$$\lambda = \frac{v_r R}{\varepsilon}$$ Equation 41

In **Equation 41,** "v_r" is the cyclone radial velocity, "R" is the cyclone radius and "ε" is the turbulent viscosity.

H. Schubert and T. Neese (1980a) proposed a separation model based on turbulent two-phase flow. They assume a homogenous, stationary turbulent field, with particles moving under Stokes' Law, a particle size smaller than the smallest eddy and low concentrations. They derived two general models for turbulent cross-flow classification depending on the way the underflow and overflow streams are removed (**Equation 42**).

$$Stk_{50} = \frac{0.5676 k_d^2}{\sqrt{E_u}} \frac{\ln\left[0.91\left(\frac{D_o}{D_u}\right)^3\right]}{(1-c)^3\sqrt{\rho}}$$ Equation 42

In **Equation 42,** "c" is feed solid concentration, "k_d" is correction factor determined using **Equation 43**.

$$k_d = [220 d_g (\frac{\Delta\rho}{D})^{0.5}]^m$$ Equation 43

In **Equation 43,** "m" is the exponent of the correction factor and "d_g" is the mass median of the solids size distribution. The exponent "m" has the following values: m = 5D for D < 0.1m and m = 0.5 for D ≥ 0.1m.

2.4.2.6 Comparison of Theories of Separation

The equilibrium orbit theory and residence time theory are well suited to solid-liquid separations, but appear to be less attractive for liquid-liquid separation within de-oiling or gas-liquid separation hydrocyclones (low-density differences and droplet breakage).

Furthermore, the equilibrium orbit theory assumes that the Stk_{50} number and Euler number are constant for the family of geomechanically similar hydrocyclones – this may not be the case.

2.4.3 Mechanistic Separation Modeling

2.4.3.1 Introduction

Mechanistic models are an intermediate approach between an empirical and the exact solution that are capable of predicting separation efficiency, pressure drops, and tangential, radial and axial velocities of certain hydrocyclones. Hydrodynamic flow behaviour in the hydrocyclone and the tangential, radial and axial velocities are factors that can be investigated in order to model hydrocyclone flow and separation performance. One of the most popular solutions for the flow in conical and cylindrical hydrocyclones is a simplified form of the Navier – Stokes' equations.

A. Arpandi et. al. (1996) developed a mechanistic model for two-phase flow in gas-liquid cylindrical hydrocyclone (GLCC) separators capable of predicting the hydrodynamic flow behaviour, including the equilibrium liquid level, gas liquid interface, zero net liquid hold-up, the onset of liquid carry-over by annular mist flow, bubble trajectory, liquid and velocity distributions and the total pressure drop across the GLCC. This type of hydrocyclone is shown in **Figure 21**.

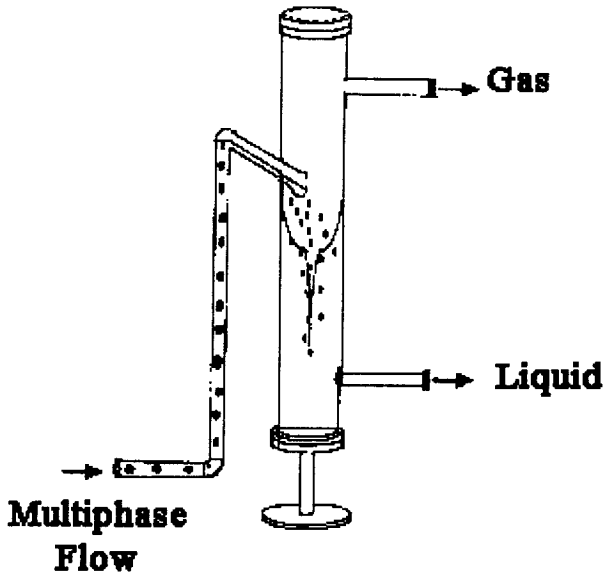

Figure 21: Gas-liquid cylindrical hydrocyclone configuration by Kouba G. E. (1995).

A. Arpandi et. al. (1995) modified the mechanistic models developed by G. E. Kouba (1995). He designed, constructed and tested an 8.64 cm inside diameter (ID) GLCC **(Figure 22).**

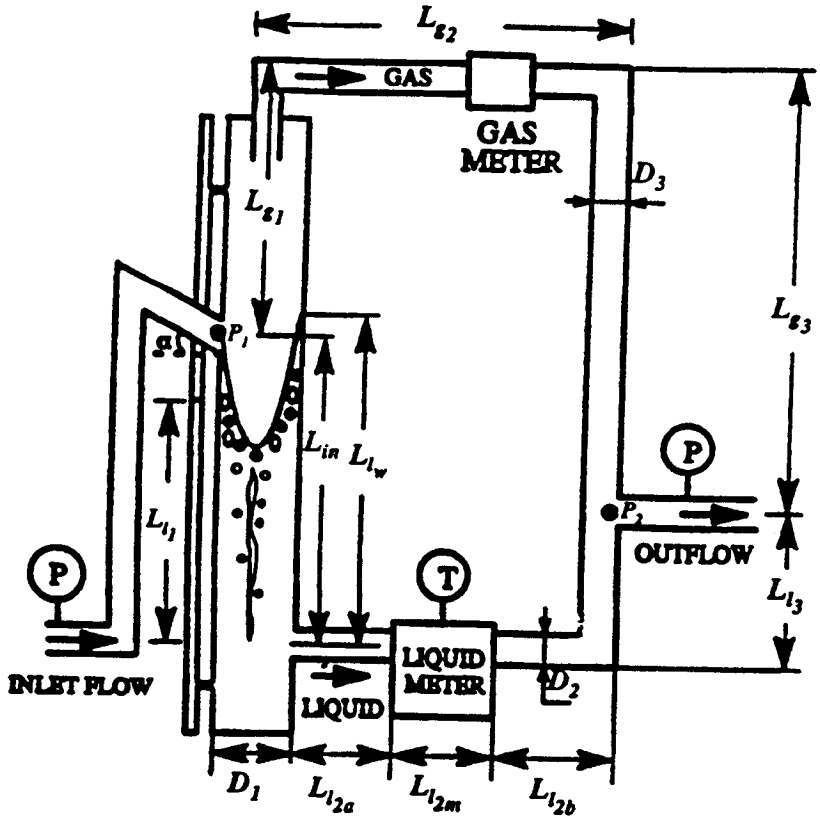

Figure 22: GLCC loop nomenclature for mechanistic model after Arpandi, A. (1995).

A. Arpandi et. al. (1995) also developed a mechanistic model capable of predicting equilibrium liquid level in the cylindrical hydrocyclone. This relationship is shown in **Equation 44**.

$$L_{l_1} = \frac{\Phi_l - \Phi_g + \rho_l g L_{l_3} - \rho g\left(L_{in} + L_{g_1} - L_{g_3}\right)}{g\left(\rho_l - \rho_g\right) - \left[\frac{\rho_l v_{l_1}}{2}\frac{f_{l_1}}{D_1}\right]}$$

Equation 44

In this model "L_{l1}" is liquid length in location 1, "Φ" is the frictional losses, "f" is a friction factor, "g" is gas, "l" is liquid, "L_{in}" is the inclined inlet length (Figure 22), "g" is the acceleration due to gravity, "v" is velocity and "D" is the hydrocyclone diameter. lg_1, lg_2 and lg_3 are distances shown in **Figure 22**.

The author also modeled the gas-liquid interface shape between points 1 to 4 **(Figure23 and Figure 24)**.

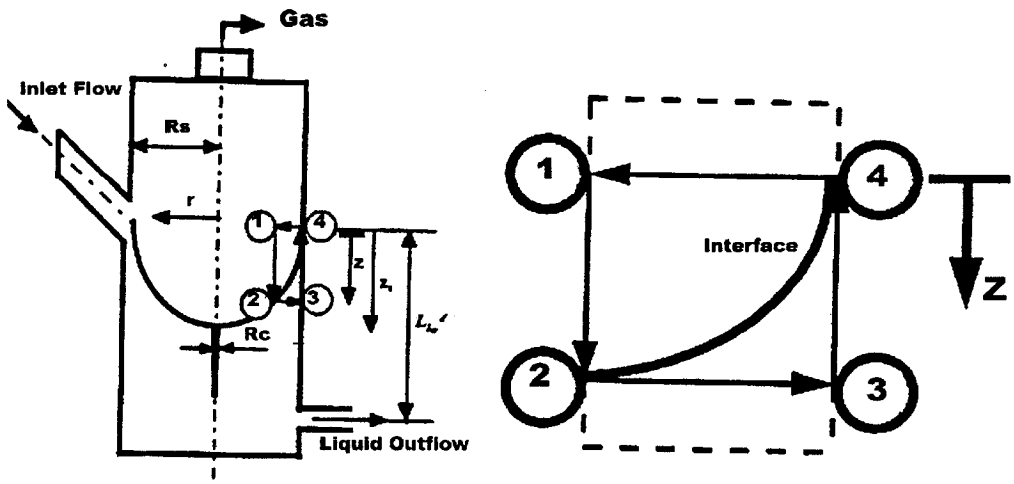

Figure23: Gas- liquid interface geometry, model Kouba G. E. (1995).

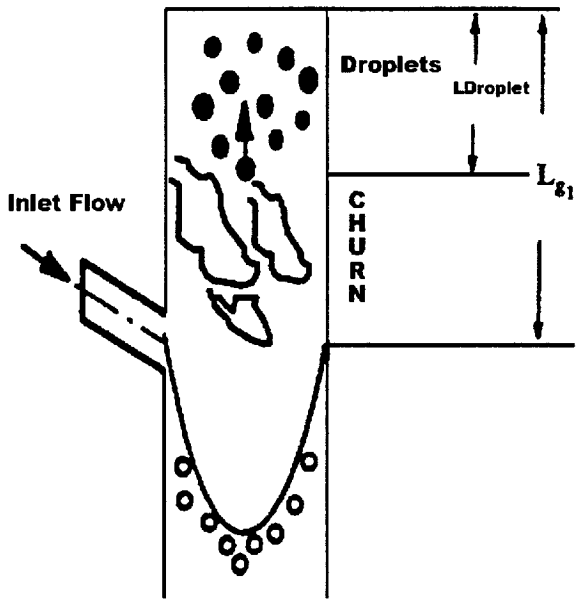

Figure 24: Zero-net liquid flow phenomenon in the upper part of the GLCC, Kouba G. E. (1995).

A. Arpandi et. al. (1995) developed a model to predict the tangential velocity distribution for flow in a vortex as shown in **Equation 45**.

$$v_t(r) = v_{tis}\left[\frac{r}{R_s}\right]^n \qquad \text{Equation 45}$$

In **Equation 45** "$v_t(r)$" is the tangential velocity in the radius "r", "v_{tis}" is the tangential velocity in the inlet slot, "r" is radial co-ordinate, "R_s" is GLCC superficial radius **(Figure23).**

A. Arpandi et. al. (1995) states that the tangential velocity in the inlet slot, "v_{tis}" can be found using **Equation 46.**

$$v_{tis} = vl_{in}\frac{A_{in}}{A_{is}}\cos(\alpha) \qquad \text{Equation 46}$$

In **Equation 46** "A_{in}" is inclined inlet cross sectional area, "l_{in}" is a length of the inclined inlet, v is velocity, "A_{is}" is inlet slot cross sectional area and "α" is inclination angle (α = 27°).

A. Arpandi assumed a churn/slug flow in the upper part of the gas liquid cylindrical hydrocyclone. He modified the Taylor bubble rise velocity "v_{g0}" equation as shown in **Equation 47**.

$$v_{g0} = C_0 v_{sg} + \sqrt{0.35 g D_s\left[\frac{\rho_l - \rho_g}{\rho_l}\right]} \qquad \text{Equation 47}$$

In **Equation 47**, "C_0" is a flow velocity coefficient, "v_{sg}" is the superficial gas velocity, "D_s" is the diameter of hydrocyclone, "g" is the gravitational acceleration. A. Arpandi et. al. (1995), based on the data collected for a low-pressure air-water system, found "C_0" to be 1.15.

The authors also calculated the total liquid volume displaced by the gas vortex and gas core filament using the interface location z(r). This relationship is shown in **Equation 48.**

$$V_g = \int_{R_c}^{R_s} 2\pi r z(r) dr + \frac{\pi}{4} D_c^2 \left(L_{lw} - z_t \right)$$ Equation 48

In **Equation 48,** "V_g" is the volume of gas, "R_s" and "R_c" are radius of hydrocyclone and radius of the core, "r" is the radial coordinate, "z" is the axial distance, "D_c" is the core diameter, "L_{lw}" is the level of liquid at the wall and "z_t" is the axial tangent **(Figure23).**

The highest point of the liquid phase, where the interface touches the GLCC wall (vortex crown), can be calculated by the following **Equation 49**.

$$L_{l_w} = L_{l_1} + \frac{V_g}{A_s}$$ Equation 49

In **Equation 49,** "A_s" is the cross sectional area of hydrocyclone, "L_{lw}" the highest level of liquid phase and "V_g" is the gas volume. The author also modeled the zero-net liquid flow hold-up using **Equation 50**.

$$H_{l0} = 1 - \left[\frac{v_{sg}}{v_{g0}} \right]$$ Equation 50

In **Equation 50** "H_{l0}" is the liquid hold-up, "v_{sg}" is the superficial gas velocity and "v_{g0}" is velocity of gas at zero net location of the hydrocyclone.

C. Gomez et. al. (2001) have developed a mechanistic model for a 2" diameter liquid-liquid hydrocyclone. The main input parameters for this model are LLHC geometry, fluid properties, inlet droplet size distribution, and operational conditions. This model is

capable of predicting the LLHC hydrodynamic flow field, namely the axial, tangential, and radial velocity distribution of the continuous phase and oil-water separation efficiency.

The L. E. Gomez et. al. (1999) model for swirl intensity (ratio of the local tangential momentum flux to total momentum flux) is a modification of models proposed by I. F. Erdal et al. (1998b) based on CFD simulation of F. Erdal (2001). In this model Ω can be found using **Equation 51**. Swirl density is the ratio of the rate of tangential flux to the total momentum flux.

$$\Omega = 0.49\,\mathrm{Re}^{0.118}\left(\frac{M_t}{M_T}I^2\right)^{0.93}\left(1+1.2\tan(\beta)^{0.15}\right)EXP\left[-\left(\frac{1}{2}\right)\left(\frac{M_t}{M_T}I^4\right)^{0.35}\left(\frac{1}{\mathrm{Re}_z}\right)^{0.16}\left(\frac{z}{Dc}\right)^{0.7}\left(1+2\tan(\beta)^{0.12}\right)\right] \quad \text{Equation 51}$$

In **Equation 51** "Ω" is swirl density, "M_t" is the momentum flux at the inlet slot (pressure has the same units as momentum per unit time per unit area, which is the momentum *flux*: the rate momentum is transported across unit area, [kg m s^{-1}][s^{-1} m^{-2}]), "M_T" is the axial momentum flux at the characteristic diameter position, "I" is the inlet factor, "Re_z" is the Reynolds number in axial position, "D_c" is the characteristic diameter of the liquid-liquid hydrocyclone (measured where the angle changes from the reducing section to the tapered section in the Colman and Thew's design, and the top diameter of the 3 tapered section of the Young's design), "z" is the axial position starting from "Dc" and "β" is the cone angle.

In this model Reynolds, number was defined in the same way as pipe flow -- with the caution that it refers to a given axial position. This is calculated using **Equation 52**.

$$\mathrm{Re}_z = \frac{\rho_c U_{avz} D_z}{\mu_c} \quad \text{Equation 52}$$

In **Equation 52**, "Re_z" is Reynolds number in axial position, "U_{avz}" average axial velocity, "μ_c" is the viscosity of continuous phase and "D_z" is the axial diameter.

Referring to **Equation 51,** the inlet factor "I" defined by F. Erdal (2001) is shown in **Equation 53**.

$$I = 1 - EXP\left[-\frac{n}{2}\right] \qquad \text{Equation 53}$$

Where "n" is 1.5 for dual inlets and 1 for involuted single inlet devices.

2.4.3.2 Tangential Velocity

B. Gomez et. al. (2001) modeled tangential velocity. They confirmed experimentally that there is a forced vortex near the hydrocyclone axis and a "free like" vortex in the outer wall region. **Equation 54** can be used to describe tangential velocity when the effect of the wall boundary layer is neglected.

$$\frac{w}{U_{avc}} = T_m \frac{R_c}{r}\left\{1 - EXP\left[-B\left[\frac{r}{R_C}\right]^2\right]\right\} \qquad \text{Equation 54}$$

In **Equation 54,** "w" is the continuous-phase local tangential velocity, "U_{avc}" is the average bulk axial velocity, "B" is the peak tangential velocity radius factor, "r" is the radial position, "R_c" is the characteristic location radius (**Figure23**). For a single inlet, $T_m = \Omega$ and $B = 55.7\Omega^{-1.7}$.

2.4.3.3 Axial Velocity

B. Gomez et. al. (2001) developed the mechanistic model shown in **Equation 55** for axial velocity. Positive values of axial velocity represent downward flow near the wall and the negative values represent upward reverse flow near the hydrocyclone axis.

$$u(r) = a_1 r^3 + a_2 r^2 + a_3 r + a_4$$ Equation 55

In **Equation 55**, "a_1" through "a_4" are constants, "r" is the radial position and "u(r)" is the liquid velocity at the radius "r".

2.4.3.4 Radial Velocity

B. Gomez et. al. (2001) states that the radial velocity of the continuous-phase; "v", is small and can be neglected. Radial velocity is a function of the axial velocity and geometrical parameters. In the cylindrical section of the hydrocyclone, where tan (θ) is equal to zero, the radial velocity is equal to zero. The authors used the equation developed by D.F. Kelsall (1952) and D. Wolbert, et. al. (1995) (**Equation 56**) to estimate the radial velocity profile in liquid-liquid hydrocyclones.

$$v = \frac{r}{R_z} u \tan(\theta)$$ Equation 56

In **Equation 56** "u" is continuous-phase local axial velocity, "v" is the radial velocity, "R_z" is radius at an axial elevation, θ is inclination angle and "r" is radial position.

D. Wolbert et. al. (1995) studied the efficiency of de-oiling hydrocyclones using D. A. Colman and M. T. Thew's hydrocyclone shown in **Figure 25**.

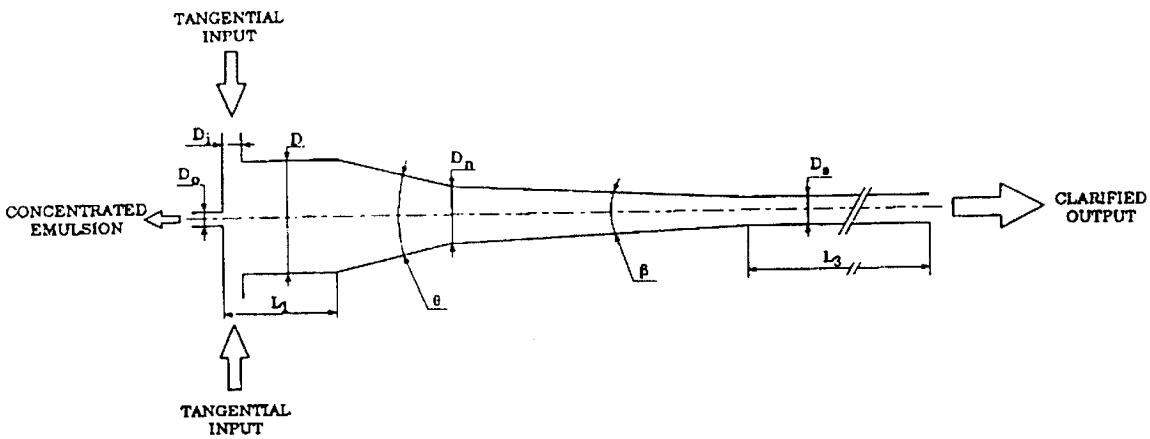

Figure 25: D. A. Colman and M. T. Thew's (1984) hydrocyclone design.

D. Wolbert et. al. (1995) states that the fluid velocity in a hydrocyclone has three components: tangential; V, axial; W, and the radial; U. After experimental studies he concludes that two types of vortices occur: a forced vortex in the core and a semi-free vortex region where the tangential velocity is usually defined by the modified Helmholz law (**Equation 57**).

$$C = Vr^n \qquad \text{Equation 57}$$

In **Equation 57**, "r" is the radial coordinate, "V" is tangential velocity, "C" is a constant and "n" ranges between -1 (forced vortex) and 1 (free vortex). The values of "n" ranged from 0.5 and 0.9 and can be obtained from the inlet velocity. The tangential velocity near the wall is equal to the inlet velocity; thus **Equation 57** becomes **Equation 58**.

$$Vr^n = \alpha \bar{V}_i \left(\frac{D}{2}\right)^n = \alpha \bar{V}_i D_n^n \qquad \text{Equation 58}$$

In this equation, "V" is the tangential velocity, "$\bar{V}_i$" [ms^{-1}] is the average feed velocity in the hydrocyclone, "α" is related to the ratio "D_i/D" ("D" is the cyclone diameter and "D_i" is the inlet diameter) and "D_n" is the diameter of the second cone (**Figure 25**). The authors estimated axial velocity, in Thew-type de-oiling hydrocyclones, using **Equation 59**.

$$\frac{W}{W(z)} = -3.33 + 12\frac{r}{R_z} - 8.63\left(\frac{r}{R_z}\right)^2 + 1.19\left(\frac{r}{R_z}\right)^3 \qquad \text{Equation 59}$$

In **Equation 59,** "W" is the axial velocity, "W(z)" is the mean axial velocity at level "z" in the lower cone angle section if there is no concentrated emulsion output as determined using **Equation 60**.

$$W_z = \frac{Q}{\pi R_z^2}$$ Equation 60

In **Equation 60,** "Q" is volumetric flow rate and "R_z" is the radius of the wall at level "z" and "R_z" is given by **Equation 61**.

$$R_z = \frac{D_n}{2} - z\tan\left(\frac{\beta}{2}\right)$$ Equation 61

In **Equation 61,** "D_n" is second cone diameter and "β" is the angle of the lower cone section.

The axial velocity distribution of D. Wolbert et al. (1995) is presented in **Figure 26.**

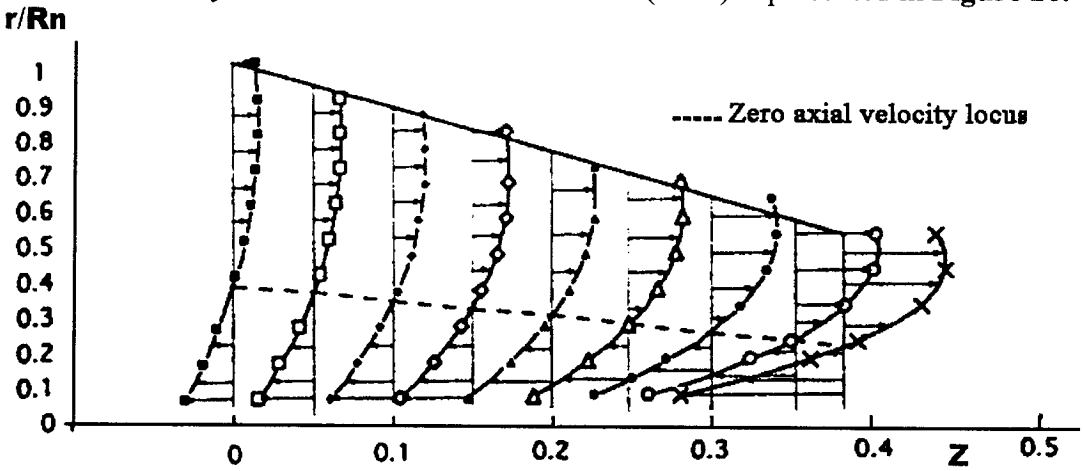

Figure 26: Axial velocity distribution by Wolbert D., et al. (1995).

D. Wolbert et. al. (1995) used the radial velocity relationship of D. F. Kelsall (1952) presented here as **Equation 62.**

$$U = -\frac{r}{R_z} W \tan\left(\frac{\beta}{2}\right)$$ Equation 62

In **Equation 62** "β" is the angle of the lower cone angle section, "W" is axial velocity and "U" is radial velocity.

In the dispersed-phase, the droplet settling velocity is usually given by Stokes' law, provided the droplet Reynolds number is less than one. This is usually the case in a liquid-liquid hydrocyclone. **Equation 63** shows Stokes' law where gravitational acceleration is replaced by centrifugal acceleration.

$$v = \frac{\Delta\rho d^2 \frac{V^2}{r}}{18\mu}$$ Equation 63

In **Equation 63,** "v" is settling velocity, "μ" is viscosity, "r" is radial coordinate, "d" is droplet diameter and "$\frac{V^2}{r}$" is the normal or centrifugal acceleration.

2.4.4 Computational Fluid Dynamics (CFD) Models

F. Motta et. al. (2001) developed a simplified, dedicated, computational fluid dynamics (CFD) model for rotational two-phase turbulent flow in gas-liquid cylindrical hydrocyclone separators. This model calculates the turbulent eddy viscosity, provides estimates of the complex tangential and axial velocities and the void fraction distributions. The author compared the predictions of this model to the experimental results of D. Farchi (1990) that used liquid and gas mass flow rates of 2.66 and 0.002 kg/s.

F. M. Erdal (2001) conducted cylindrical cyclone separator CFD simulations using one- and two-phase flows. These simulations where based on the equipment show in **Figure 21**.

The F.M. Erdal et. al. (1996) study verified that axisymmetric simulation gives good results when compared to three-dimensional simulations. They developed an expression for the ratio of inlet tangential velocity to average axial velocity and the relationship ratio between and hydrodynamic flow behaviour. For single-phase flow, it was assumed that turbulent flow could be represented as a complex, unsteady, laminar flow. CFD was used to solve this flow using the Navier-Stokes equations (high Reynolds number k-ε turbulence model where, "k" is turbulent kinetic energy per unit mass, m^2/s^2 and "ε" is dissipation rate of turbulent kinetic energy, m^2/s^3). When incompressible steady and fully turbulent flow is assumed, the Navier - Stokes equation takes the form of **Equation 64** and **Equation 65**.

$$\frac{\partial u_i}{\partial x_i} = 0 \qquad \text{Equation 64}$$

$$u_j \frac{\partial u_i}{\partial x_j} = -\frac{1}{\rho}\frac{\partial p}{\partial x_i} + \frac{1}{\rho}\frac{\partial}{\partial x_i}\left[\mu\left(\frac{\partial u_i}{\partial x_j} + \frac{\partial u_j}{\partial x_i}\right) - \rho u_i' - \rho u_j'\right] \qquad \text{Equation 65}$$

In these equations, "u_i" is the time-averaged velocity component, "x_i" and "x_j" are coordinate directions, "p" is the pressure, "ρ" is the density, "u'" is the velocity fluctuation (u') is the ratio of mixing length to mixing time used for dynamic behaviour of bubbles in the cyclone and "μ" is the viscosity.

In this axisymmetric model, three-dimensional flow is introduced into the hydrocyclone tangentially from the inlet all around the cyclone, as shown in **Figure 27**.

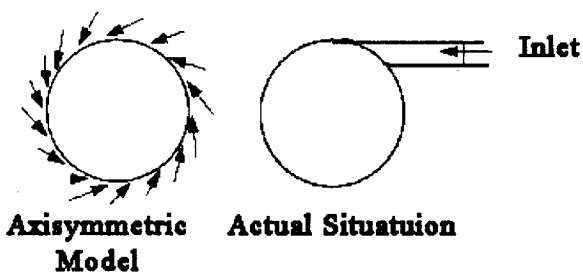

Figure 27: Equivalent tangential velocity concept for axisymmetric model (Erdal F. M. et. al. 1996).

A mechanistic model was developed to determine the inlet tangential velocity decay in the inlet region. The cyclone was separated into two layers, namely, the core and shear layer, as shown schematically in **Figure 28**.

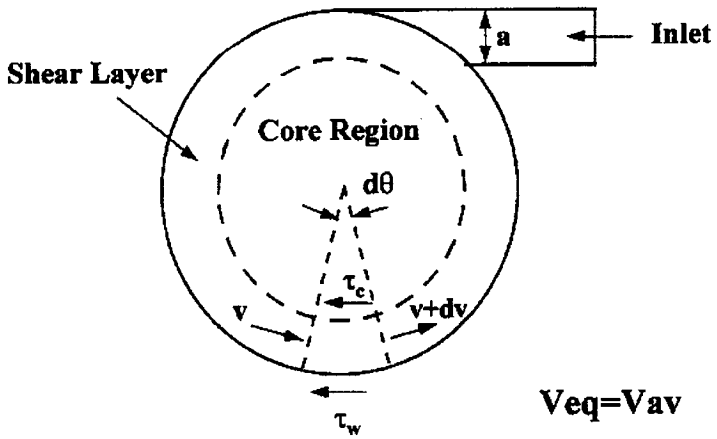

Figure 28: Control volume for the tangential velocity decay model (Erdal F.M., 1996).

In **Figure 28**, "a" is the width of inlet slot and shear layer, "v" is the magnitude of velocity vector, "θ" is the circumferential direction in radians, "τ_w" is the wall shear stress, and "τ_c" is the shear stress at the core region.

The change in the tangential velocity; "dV_t", is obtained as a function of the circumferential angle; "θ", the wall shear stress; "τ_w", and the shear stress at the core region; "τ_c" using **Equation 66**.

$$dV_t = -V_t + \sqrt{V_t^2 - \frac{d\theta}{\rho a}\left[\tau_w R + \tau_c (R-a)\right]} \qquad \text{Equation 66}$$

In **Equation 66**, "R" is the hydrocyclone radius and "a" is the inlet slot width. The wall shear stress; "τ_w" of **Equation 66** can be determined using **Equation 67**.

$$\tau_w = \frac{1}{2}\rho V_t^2 C_f$$ Equation 67

In **Equation 67,** "C_f" is a dimensionless skin friction coefficient that is calculated using **Equation 68**.

$$C_f = 0.0592\,\mathrm{Re}^{-1/5}$$ Equation 68

In **Equation 68**, the Reynolds number is calculated using **Equation 69.**

$$\mathrm{Re} = \frac{\rho_l V_t \theta R}{\mu_l}$$ Equation 69

In **Equation 69,** "θR" is the arc length measured from the inlet.

Referring to **Equation 66,** the shear stress at the core; "τ_c", is calculated using **Equation 70**.

$$\tau_c = \mu_t \frac{V_t}{R}$$ Equation 70

In **Equation 70,** μ_t is the eddy viscosity calculated using **Equation 71**.

$$\mu_t = C\rho V_t R$$ Equation 71

In **Equation 71,** "C" is an empirical constant equal to 0.025.

An example of the tangential velocity decay predicted by **Equation 66** is shown in **Figure 29.**

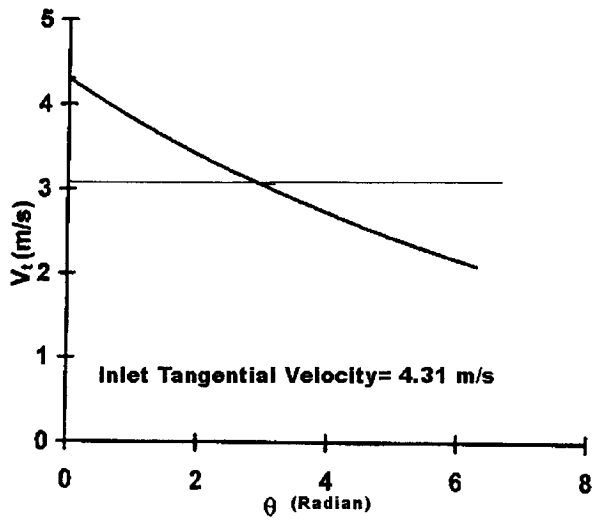

Figure 29: Predicted tangential velocity decay at the inlet plane of the GLCC by (Erdal F. M., 1996).

M. F. Erdal et. al. (1998b) found that grid spacing is important in the radial and circumferential directions for three-dimensional simulations. Two examples of this are shown in **Figure 30.**

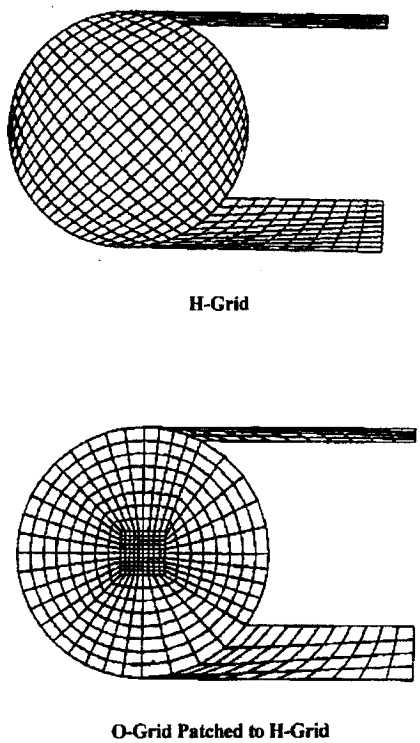

Figure 30: Two available griddling options in CFX software (Erdal., F. M, 1996).

M. F. Erdal et. al. (1998) carried out three-dimensional simulations, for single-phase flow, using CFD; the geometry and typical grid configuration used are shown in **Figure 31** and **Figure 32**.

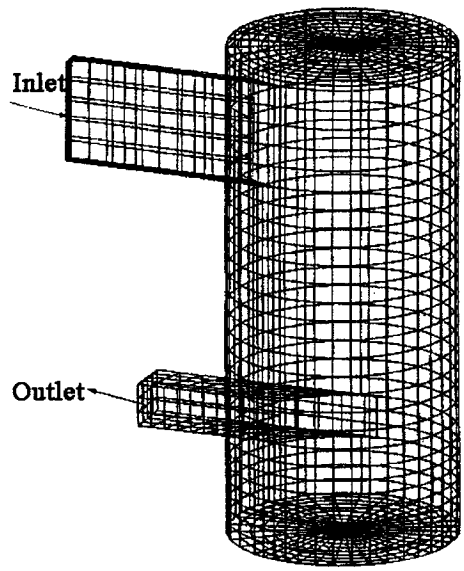

Figure 31: Geometry and grid configuration by Erdal F. M. (1998).

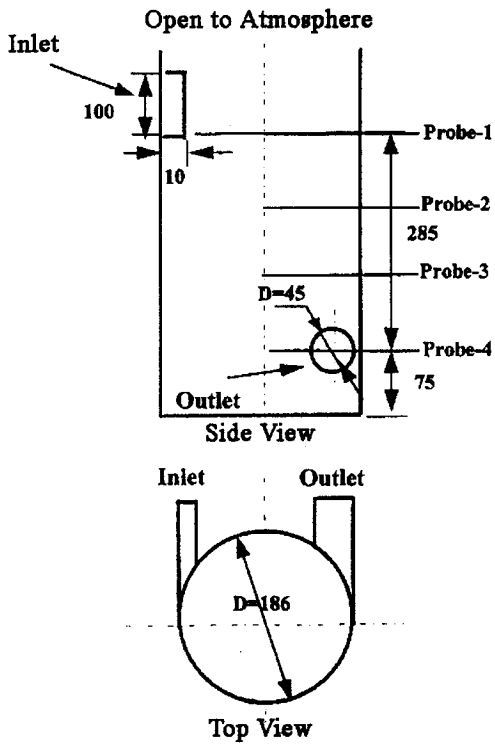

Figure 32: Gas-liquid separator geometry used by Frat D., (1990) all dimensions in mm.

F. M. Erdal et. al. (1998b) compared the simulation results with the available experimental data of D. Farchi (1990) and found a good agreement as shown in **Figure 33**.

F. M. Erdal et. al. (1996) proposed a mechanistic model using CFD for two-phase turbulent flow. The definition for the kinematic turbulent viscosity for each phase is the algebraic equation shown in **Equation 72**.

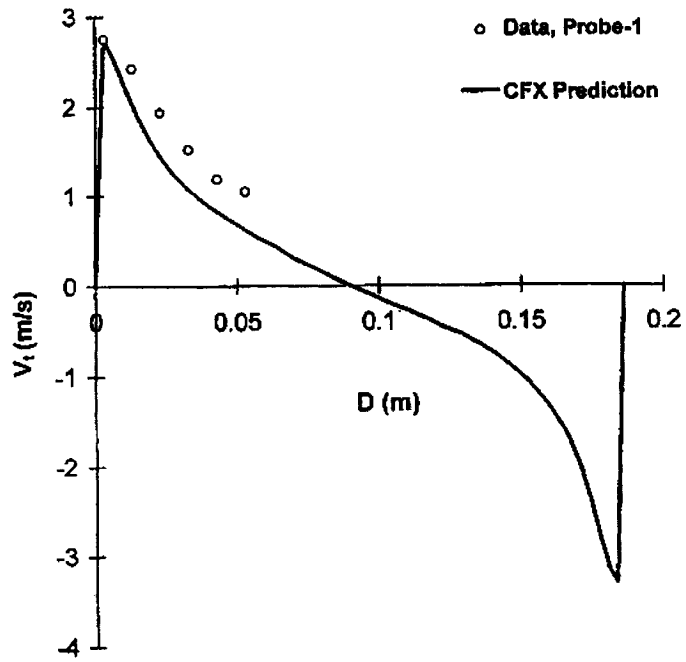

Figure 33: Tangential velocity prediction vs. data obtained from Farchi D., (1990).

$$\nu_{at} = c_{\mu} \frac{k_{\alpha}^2}{\varepsilon_{\alpha}} \qquad \text{Equation 72}$$

In **Equation 72** "ν_{at}" is the kinematic turbulent viscosity, "c_{μ}" is an empirical constant, "k_a" [m^2/s^2] is the turbulent kinetic energy per unit mass and "ε_a" [m^2/s^3] is the turbulent kinetic energy dissipation rate. The transport equations for "k" and "ε", in a phase, which is defined as turbulent, take the form of the k-ε model shown in **Equation 73**.

$$\frac{Dr_\alpha k_\alpha}{Dt} = \frac{\partial}{\partial x_j}\left(r_\alpha \frac{v_{\alpha t}}{\sigma_t}\frac{\partial k_a}{\partial x_j}\right) + v_{\partial t} r_\alpha \frac{\partial u_{\alpha i}}{\partial x_j}\left(\frac{\partial u_{\alpha i}}{\partial x_j} + \frac{\partial u_{aj}}{\partial x_i}\right) - r_\alpha \varepsilon + c^k_{\alpha\beta}\left(k_\beta - k_\alpha\right) \quad \text{Equation 73}$$

In some two-phase flows, the dispersed phase can be defined as laminar as shown in **Equation 74**.

$$\frac{Dr_\alpha \varepsilon_\alpha}{Dt} = \frac{\partial}{\partial x_j}\left(r_\alpha \frac{v_{\alpha t}}{\sigma_\varepsilon}\frac{\partial \varepsilon_a}{\partial x_j}\right) + c_1 v_{\alpha t} r_\alpha \frac{\varepsilon_\alpha}{k_a}\frac{\partial u_{\alpha i}}{\partial x_j}\left(\frac{\partial u_{\alpha i}}{\partial x_j} + \frac{\partial u_{aj}}{\partial x_i}\right) - c_2 r_\alpha \frac{\varepsilon_\alpha^2}{k_\alpha} + c^\varepsilon_{\alpha\beta}\left(\varepsilon_\beta - \varepsilon_\alpha\right) \quad \text{Equation 74}$$

In **Equation 74** the subscript "α" stands for gas and "β" for liquid, "σ" is the Prandtl number, "σ_t" and "σ_ε" represent the diffusion rates of "k" and "ε". In this two-phase k-ε model the value of the empirical constants are shown in **Table 2**.

Table 2: The value of constants in the k-ε turbulence model Erdal F. M., (1996).

C_μ	C_1	C_2	σ_t	σ_ε
0.09	1.44	1.92	1	1.217

Also in Equation 74 "$c^k_{\alpha\beta}$" and "$c^\varepsilon_{\alpha\beta}$" are interface transfers terms for turbulent kinetic energy and turbulent diffusion, respectively; Erdal et. al. (1998b) considered these two values equal to zero.

M.A.Z. Coelho, and R.A. Medronho, (2001) reported that CFD gives a good understanding of the strongly swirling turbulent flow inside the hydrocyclone. High swirl induces anisotropic turbulence. The "k-ε" model assumes isotropic turbulence, thus, it usually gives an incorrect prediction of the flow patterns (M.A.Z. Coelho and R. A. Medronho, 2001) CFD may misrepresent the flow structure and separation performance of the hydrocyclone.

2.4.5 Empirical Models

Most empirical models use a large number of coefficients that can be obtained only by direct experiments conducted in the separation between the solid-, liquid- and gas-phases with a particular cyclone design. These models describe separation performance in terms of split ratio, pressure drop and cut-size. They are capable of fitting well with their original data but the equation constants must be recalculated for each new data set.

2.5 The Behavior of Gas Bubbles in a Hydrocyclone

2.5.1 Introduction

The production quality of numerous technological processes depends on the presence or absence of gas bubbles. An understanding of nucleation, growth and motion of bubbles under centrifugal forces is needed in order to apply hydrocyclones to the task of controlling bubbles in industrial fluids.

Dissolved gas bubbles are nucleated in a liquid upon an abrupt pressure drop. Coalescence or fragmentation of these bubbles may occur within a hydrocyclone. Knowledge of bubble generation and their behaviour in a hydrocyclone are important to understand phase engagement and stability of the lighter phase. Some papers related to this subject are reviewed and summarized in this section.

V.G. Levich (1959) reported that the mechanism of bubble fragmentation might be different according to the hydrodynamic conditions. V.G. Levich (1959) stated that when bubbles move into a liquid, the gas that makes the atmosphere of the bubble is entrained by that liquid, which results in a vortex flow of gas within the bubble. The author reported if the dynamic head of the gas is higher than the excess pressure, after formation of the bubble, then liquid bursts into the bubble and the bubble collapses. Levich proposed a model for calculation of the critical radius; "R^{cr}", at which the bubble collapses. The relationship is shown in **Equation 75**.

$$R^{cr} \approx \left(\frac{3}{K_f}\right)^{1/3} \frac{\sigma}{V^2 \sqrt[3]{\rho_g \rho_l^2}}$$ Equation 75

In **Equation 75** "V" is the velocity of the bubble in liquid, "K_f" is the resistance coefficient, "ρ_g" and "ρ_l" are the densities of the gas and liquid, and "σ" is the surface tension at the interface.

S. A. Kondrat' ev (1987) proposed fragmentation of bubbles by a wave mechanism. The liquid flowing around the bubble causes an intrinsic perturbation at the bubble surface. The curvature of the bubble surface at the wave trough of this perturbation can attain a critical value, at which the liquid pressure approaches the gas pressure in the bubble or even exceeds it. Liquid bursts into the bubble in the form of a jet, the bubble is destroyed, and a spectrum of smaller bubbles is created. The size of the formed bubbles depends on the wavelength and magnitude of the interface perturbation and on the size of the parent bubble.

If Rayleigh-Taylor or Kelvin-Helmholtz instabilities (S.A. Kondrat'ev 1987) are developed at the bubble surface then the wavelength of the maximum interface perturbation can be calculated using **Equation 76**.

$$\lambda_{max} = \frac{6\pi\sigma}{\left(\rho_g^2 V^4 + 3\sigma\alpha\rho_l\right)^{1/2} + \rho_g V^2}$$ Equation 76

In **Equation 76** "α" is the acceleration of the turbulent formation "σ" is surface tension and "V" is the velocity of the liquid behind the wave, which is taken to be equal to the velocity of the bubble in the liquid.

The Rayleigh-Taylor instability occurs any time a dense, heavy fluid is being accelerated by a light fluid; such as two different density liquids or gas and liquid systems. The dense fluid falls under the influence of gravity and bubbles of light fluids rise up on the

sides. Two completely plane-parallel layers of fluid are stable, but the slightest perturbation leads to tangential (Lateral) acceleration. In other words, the instability of superimposed fluids of differing densities across an interface, driven by gravity, leads to mixing if the higher density layer is greater than the lower density phase. (Y. Jayalakshmi and D. Beysens 1995).

Kelvin-Helmholtz instability (R. Krasny, 1986) results from velocity shears between two media. These media need not be of different densities. Any time there is a non-zero curvature, the flow of one fluid around another will lead to a small centrifugal force, which in turn leads to a change in pressure thereby amplifying the ripple. A flat vortex sheet of constant strength separates two streams of fluid moving in opposite directions. When the sheet is given a small perturbation, it rolls up to form an array of spiral vortices as shown in **Figure 34**.

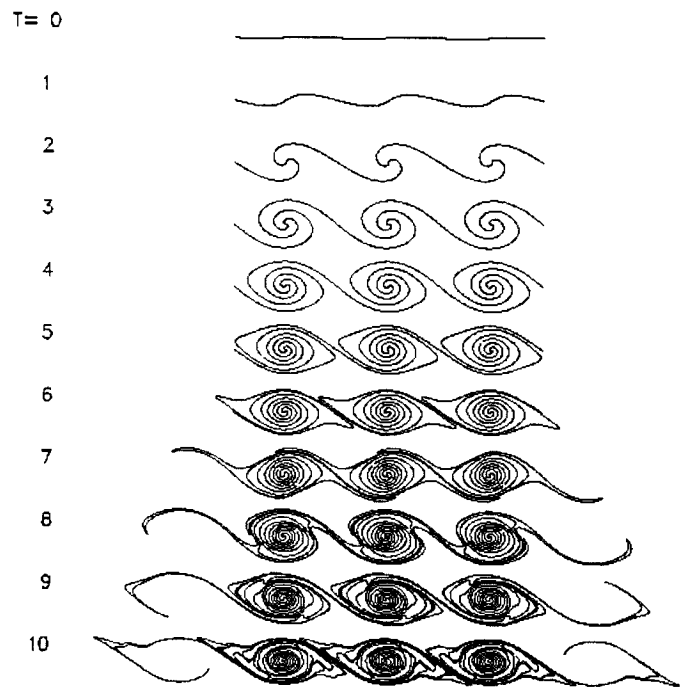

Figure 34: Kelvin- Helmholtz instability array of spiral vortices (Krasny, R 1986).

S. A. Kondrat' ev. (1987) reported that in a turbulent liquid flow, bubble fragmentation is also associated with a wave of interface perturbation. The velocity and acceleration of the liquid are functions of location and time. Viscous force should be taken into account for small bubble fragmentation. The acceleration of a turbulent spectrum is found using

Equation 77. The turbulent spectrum is characteristic of the "inertial sub-range", the frequency range in which large eddies break into smaller eddies which break into even smaller eddies

$$\alpha = 6\left(\frac{\varepsilon^2}{l}\right)^{1/3} \qquad \text{Equation 77}$$

In **Equation 77** "ε" is the power dissipated in a unit mass of liquid per unit time and "l" is the maximum size of a turbulent formation from the inertial sub-region of the turbulence spectrum. The size of a turbulent formation should not exceed the size of the bubble.

2.5.2 Velocity of Flow around the Bubble in Turbulent flow

Bubbles within a specific range of sizes can take part in the turbulent formation motion. The time of gas bubble acceleration to the turbulent formation velocity is short. Velocity around a bubble can be written as **Equation 78** (S. A. Kondrat' ev 1987).

$$V = C(\varepsilon l)^{1/3} \qquad \text{Equation 78}$$

Where "l" is the maximum size of a turbulent formation (turbulent intensity) from the inertial sub-region of the turbulence spectrum, "ε" is the power dissipated in a unit mass of liquid per unit time and "C" is a coefficient.

2.5.3 Gas Bubble Time of Acceleration

S.A. Kondrat' ev (1987) proposed that the gas bubble time of acceleration may be equal to the lifespan of the turbulent formation, by virtue of the fact that the structure of the latter is vortical (described by **Equation 79**).

$$\tau = \frac{1}{\sqrt{6}}\left(\frac{l^2}{\varepsilon}\right)^{1/3}$$ Equation 79

In **Equation 79** "l" is the size of the turbulent formation with which the gas bubble moves and "τ" is the time of acceleration.

2.5.4 Kolmogorov- Obukhov Bubble Fragmentation Theory

Another model of bubble fragmentation is based on the Kolmogorov- Obukhov theory of local isotropic turbulence. According to this theory, the difference in dynamic heads, that deforms and fragments a bubble in turbulent flow, is caused by small-scale pulsations in velocity. The deformation of a bubble under the action of turbulent pulsations results in growth of its surface. When the surface area of the deformed bubble exceeds the sum of the surface area of two or more bubbles with the same total volume, the existence of the single bubble becomes energetically disadvantageous, and the bubble splits (M.G. Lagutkin and A.P. Kilmov, 1993).

M.G. Lagutkin. and A.P. Kilmov, (1993) used this theory of local isotropic turbulence, and experimental data obtained from other investigators, to develop a model that estimates bubble size in a rotating turbulent flow. This empirical relationship is shown in **Equation 80**.

$$d_b \approx 3.5\left(\sigma / \rho_l\right)^{0.6}\left(\varepsilon_0^{loc}\right)^{-0.4}$$ Equation 80

In **Equation 80** "ε_0^{loc}" is the local value of energy dissipation in a unit mass of the liquid [Watt per kilogram (W/k_g)], "ρ_l" is the liquid density, "σ" is the surface energy at the interface and "d_b" is size of the bubble.

O.V. Voinov and A.G. Petrov (1976) experimentally found that large air bubbles quickly split into smaller ones in a turbulent flow of water at Re ≈ 10^5 and a critical Weber

number. This Weber number is calculated by the root-mean square velocity; $V^{'}$, of water pulsations beyond which the bubble splits (**Equation 81**).

$$We = \frac{\left(V^{'}\right)^2 d_b \rho_l}{\sigma} \qquad \text{Equation 81}$$

V.A. Kireev (1975) calculates the radius of the largest stable bubble in the hydrocyclone (hydrocyclone tested by the author) at about 10^{-4} m. The critical size of a bubble, calculated by N. I. Gel'Perin et. al. (1975) is about 10^{-3} m, which is much higher than yielded by other methods.

M.G. Lagutkin and A.P. Klimov (1993) reported that the main forces acting on a gas bubble in a hydrocyclone, at a distance "r" from the axis and at the liquid rotation velocity; "V_φ" are as follows:

- The centrifugal force; "F_{cf}" directed along the radius; "r", from the center of the hydrocyclone to its wall where "$V\varphi$" is the rotational velocity and "R_0" is the spherical bubble radius . This relationship is shown in **Equation 82**.

$$F_{cf} = \frac{4}{3}\pi R_0^3 \rho_g \frac{V_\varphi^2}{r} \qquad \text{Equation 82}$$

- The buoyancy force; "F_{buoy}", directed to the hydrocyclone axis (**Equation 83**).

$$F_{buoy} = \frac{4}{3}\pi R_0^3 \rho_l \frac{V_\varphi^2}{r} \qquad \text{Equation 83}$$

- The resistance force; "F_r", of the viscous incompressible liquid flow on the bubble, which is deformed in the direction perpendicular to the direction of this flow (**Equation 84**).

$$F_r = 12\pi\mu R_0' U$$ Equation 84

In **Equation 84**, "R_0'" is the radius of the equivalent spherical bubble and "U" is the radial velocity of the bubble relative to the liquid.

$$R_0' = \frac{(4/3)C_0}{\lambda_0 - (\lambda_0^2 - 1)a\tan\lambda_0}$$ Equation 85

In **Equation 85,** $\lambda_0 = b/C_0$ Where "C_0" is found using **Equation 86**.

$$C_0 = \sqrt{e^2 - b^2}$$ Equation 86

In **Equation 86** "e" and "b" are the major and minor axes of the ellipsoid.

M.G. Lagutkin and A.P. Klimov (1991) presented the equation of motion for a bubble of mass "m" in a viscous incompressible liquid at moderate Reynolds number of the hydrocyclone as **Equation 87**.

$$ma = F_{cf} - F_{buoy} - F_r$$ Equation 87

The authors presented **Equation 88** for the case of the quasi-stationary motion of gas bubbles in the rotating flow at a certain distance "r" from the center.

$$\frac{4}{3}\pi R_0^2 \rho_l \frac{V_\varphi^2}{r} = 16\pi U\psi\mu$$ Equation 88

Where "ψ" is the shape coefficient of the bubble as determined by **Equation 89**.

$$\psi = \frac{C_0 / R_0}{\lambda_0 - \left(\lambda_0^2 - 1\right) a \tan \lambda_0}$$ Equation 89

The authors developed a model to predict the velocity of the gas bubble in the case of quasi-stationary motion along the hydrocyclone radius when 1< Re < 600. This relationship is shown in **Equation 90**.

$$U = \frac{R_0^2 \rho_l V_\varphi^2}{12 \psi \mu r}$$ Equation 90

2.6 Air Core Diameter Prediction

M.R. Davidson (1995) developed a model to predict the air core diameter in a two outlet cylindrical hydrocyclone, using the physics of uniform density and inviscid flow at each outlet, modified by an empirical factor to account for these viscous effects. The author mentioned that accurate predictions for the size of the air core in both hydrocyclones and vortex chambers could be achieved using the model developed. Tangential velocity profiles were used of the form "Ar^{-n}" and "Br^{-m}" at the overflow and underflow. Ar^{-n} is the tangential velocity at overflow (annulus) and Br^{-m} is the tangential velocity at underflow ($n \leq 1$). m and n are exponent in expression for O/F and U/F tangential velocity. Davidson applied the Bernoulli equation on the air core boundary separately at both outlets (**Equation 91 and Equation 92**).

$$u_o = (2H - A^2 r_c^{-2n})^{0.5}$$ Equation 91

$$u_u = (2H - B^2 r_c^{-2m})^{0.5}$$ Equation 92

The total volumetric flow rate through the hydrocyclone can be calculated using **Equation 93**.

$$Q = \pi\left(r_o^2 - r_c^2\right)\left(2H - A^2 r_c^{-2n}\right)^{0.5} + \pi\left(r_u^2 - r_c^2\right)\left(2H - B^2 r^{-2m}\right)^{0.5} \qquad \text{Equation 93}$$

In **Equation 91** through **Equation 93,** r_c is air core radius and H is total head.

Davidson applied the condition expressed in **Equation 94** to maximize "Q" with respect to "r_c" for a fixed "H", and multiplied the resultant expression for "r_c" by $(\nu_w/\nu)^k$ to account the viscosity effects. The developed model (**Equation 95**) estimates the air core size.

$$\frac{\partial Q}{\partial r_c} = 0 \qquad \text{Equation 94}$$

$$r_c = \left(\frac{n r_o^2 u_u w_{co}^2 + m r_u^2 u_o w_{cu}^2}{u_u (2u_o^{2+} n w_{co}^2) + u_o (2u_u^2 + m w_{cu}^2} \right)^{0.5} \left(\frac{\upsilon_w}{\upsilon} \right)^k \qquad \text{Equation 95}$$

In **Equation 91**, through Equation 95, "A" is a constant used in the expression for O/F tangential velocity, "B" is a constant used in the expression for U/F tangential velocity, "H" is the total head, "m" is the exponent in expression for U/F tangential velocity, "n" is the exponent in expression for O/F tangential velocity, "r" is the radial coordinate, "r_c" is the air core radius, "r_o" is the O/F radius, "r_{un}" is the U/F radius, "u" is the axial velocity, "u_o" is the magnitude of O/F axial velocity, "u_u" is the magnitude of U/F axial velocity, "w" is the tangential velocity, "W_c" is the tangential velocity at the air core boundary, "Q" is the volumetric flow rate, "ν_w" is the kinematic viscosity of water, and "ν" is the kinematic viscosity of the fluid (mixture).

2.7 Adopted Empirical Models

2.7.1 Introduction

This section provides background information on hydrocyclone modelling, including information on batch recycled tests, and significant variables including bubble cut-size, pressure drops and separation efficiency. The feed is composed of gas bubbles, possible organic droplets, possible solid particles, and water. Each of these is affected differently by the cyclone. In order to characterise cyclone performance the separation effects on each of these populations must be quantified. This study is focuses on the separation of gas bubbles.

Hydrocyclone modelling can be used to help understand the separation process, optimise process control and to minimise experimental and capital costs. Most hydrocyclone models are simplified, or depend on empirical correlation. Intensive experimental data is necessary to validate any empirical model and the model must fit the experimental data. In this study, models are based on the fundamentals of cyclonic separation, pre-existing models, and the experimental data.

Experimental models were used to predict separation performance in terms of pressure drop, bubble cut-size and efficiency. These methods are applicable for conventional hydrocyclones. Few studies exist for a small diameter cylindrical hydrocyclones (Hoffman, 2002). Existing models for the three key performance indicators for hydrocyclone: separation efficiency, pressure drop and cut-size (d_{50}) are outlined in this section.

2.7.2 Models for Prediction of Cut-Size (d_{50})

2.7.2.1 Muschelknautz Model

Muschelknautz developed an empirical model to predict bubble cut-point size in the hydrocyclone. This relationship is found in **Equation 96**. The Muschelknautz predicted cut-size data is shown in **Appendix V**. The model predicted cut-size; "d_{50}", using the

equipment and test conditions of this study, ranged from 20-26.3 μm. A schematic diagram of the hydrocyclone is shown in **Figure 35** and **Figure 36**.

$$d_{50} = x_{fact}\sqrt{\frac{18\mu(0.9Q)}{2\pi(\rho_p - \rho)v_{\theta CS}^2(H-S)}} \qquad \text{Equation 96}$$

In **Equation 96**, "x_{fact}" is a correction factor that may be applied for fitting the experimental results to the model, Q is flow rate, ρ_p, particle density, ρ continuous phase density, S vortex finder length and H is cyclone length. In **Equation 96** all parameters and variables are know except the inner core tangential velocity "$v_{\theta CS}^2$" of the gas. In order to calculate "$v_{\theta CS}^2$"**Equation 97** is used.

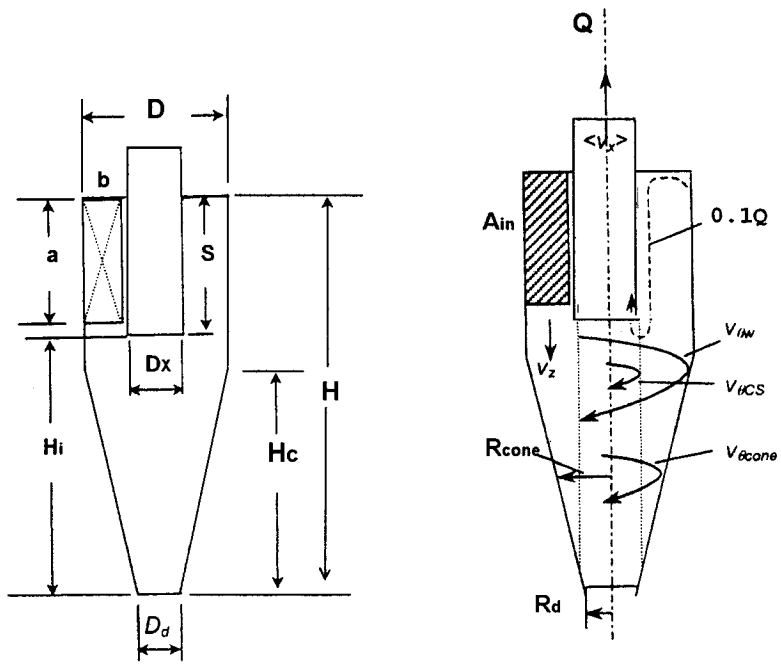

Figure 35: The schematic diagram showing the various dimensional notations (Hoffman, A, 2002).

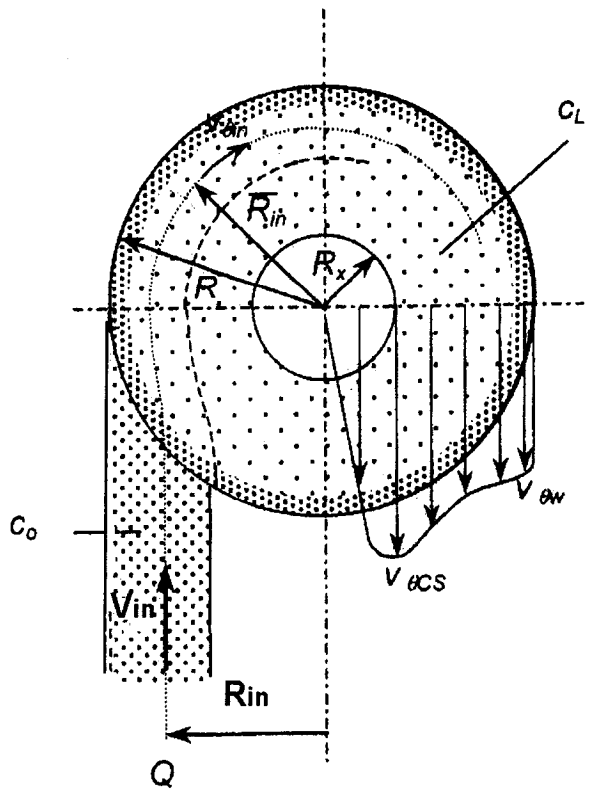

Figure 36: Plan view of the hydrocyclone showing the additional notation (Hoffman, A, 2002).

$$v_{\theta CS} = \frac{v_{\theta W}\left(\frac{R}{R_x}\right)}{\left[1+\frac{fA_R v_{\theta W}\sqrt{\frac{R}{R_x}}}{2Q}\right]}$$

Equation 97

In **Equation 97** "A_R" is the total inside area of the cyclone ($A_R = A_{roof} + A_{barrel} + A_{vt}$, A_{vt} is the area of vortex tube, A_{barrel} is the area of the cylindrical body and A_{roof} is the area of the top part of the cylinder); "$v_{\theta W}$" is wall velocity just after the inlet; "R" is the radius of the hydrocyclone; "R_x" is radius of the vortex finder; *"f"* is friction factor and "Q" is the volumetric feed inlet.

Total friction factor; *"f"* is predicted by Muschelknautz using **Equation 98 and Equation 99.**

$$f = f_{air} + 0.25\left(\frac{R}{R_x}\right)^{-0.625}\sqrt{\frac{\eta c_o Fr_x \rho}{\rho_{str}}}$$ Equation 98

$$f = f_{air} + f_{water} = 0.005\left(1+3\sqrt{c_o}\right)$$ Equation 99

In these equations "ρ_{str}" is the density of the strand of solids (an string of particles twisted together), "η" is the overall cyclone collection efficiency (0.9-0.99), "Fr_x" is the Froude number for the flow out the vortex tube and "c_o" is the mass fraction of solids in the feed. The predicted friction factor for the test given hydrocyclone and feed was 0.005.

The Froude number; "Fr" in the vortex finder (used in Equation 98) can be calculated using **Equation 100**.

$$Fr_x = \frac{v_x}{\sqrt{2R_x g}}$$ Equation 100

In **Equation 100** "v_x" is superficial axial velocity through the inlet section of the vortex tube.

The Froude number is the ratio of inertial force to gravitational force and indicates the effect of gravity on hydrocyclone performance. It can be used to quantify the type of flow:

Fr < 1 .....Sub-critical Flow (Tranquil Flow)
Fr =1 .....Critical Flow
Fr >1 .....Rapid Flowing Supercritical Flow

In large diameter hydrocyclones the effect of gravitational force on separation performance is significant.

In this research, the calculated Froude number ranged from 2.8 - 9.8 and characterised a supercritical flow regime.

Another independent variable is the characteristic velocity; "v", inside the hydrocyclone. This can be calculated using **Equation 101.**

$$v = \frac{4Q}{\pi D_c^2} \qquad \text{Equation 101}$$

In **Equation 101** "Q" [m^3/s] is volume inflow rate, "D_c" is the hydrocyclone inside diameter (2.45 cm).

The characteristic velocity of the flow across the hydrocyclone ranged between 1.4 and 2.8 m/s. This data is summarized in **Appendix N**.

Inner core velocity in the vortex finder; "$v_{\theta cs}$", used in equation 96, can be predicted using **Equation 102.**

$$v_{\theta cs} = \left(\frac{v_{zw}}{v_{\theta m}} \right)^2 \qquad \text{Equation 102}$$

In the **Equation 102**, "v_{zw}" is wall axial velocity, and "$v_{\theta m}$" is geometrical mean rotational velocity.

In this study, the predicted inner core velocity ranged from 3.7-7.3 m/s (**Appendix T**).

Geometrical mean rotational velocity ($v_{\theta W}$) of the flow inside the hydrocyclone can be predicted using **Equation 103** and substitution into **Equation 102** gives the inner core velocity (Hoffman, 2002).

$$v_{\theta m} = \sqrt{v_{\theta w} v_{\theta CS}}$$ Equation 103

Reynolds number is a dimensionless number that defines the inlet feed flow regime of the hydrocyclone. This number can be calculated using **Equation 104**.

$$\mathrm{Re} = \frac{VD\rho}{\mu}$$ Equation 104

In **Equation 104**; "V" is the characteristic velocity [m/s]; "D" is cyclone diameter [0.0254 m]; ρ is the density of water [1000 Kg/m^3] and μ is water viscosity [0.001 kg/m/s].

Cyclone body Reynolds number (Re_R) represents the flow regime across the hydrocyclone. Muschelknautz and Trefz (1990) developed **Equation 105** to calculate this dimensionless number.

$$\mathrm{Re}_R = \frac{R_{in} R_m v_{zw} \rho}{H\mu\left(1 + \left(\frac{v_{zw}}{v_{\theta m}}\right)^2\right)}$$ Equation 105

In **Equation 105** "ρ" and "μ" are the gas-phase density and absolute viscosity, "$v_{\theta m}$" is geometrical mean rotational velocity based on the spin velocity near the wall "$v_{\theta w}$", "$v_{\theta CS}$" is internal spin velocity (inner vortex), "μ" is absolute viscosity, "R_m" is geometric mean radius and "H" cyclone length.

This equation is good for Reynolds numbers greater than 2 000. Predicted hydrocyclone Reynolds numbers ranged from 57-100. These results are summarized in **Appendix R**. Calculated cyclone body Reynolds numbers ranged from 963- 1642 and feed Reynolds number was greater than 35 000, which means that the flow regime was turbulent. These results are detailed in **Appendix R.**

The geometric mean radius of the cyclone used in equation 105 and can be calculated using **Equation 106.** In **Equation 106** "R_x" is vortex diameter and "R" is the cyclone diameter.

$$R_m = \sqrt{R_x R} \qquad \text{Equation 106}$$

According to Muschelknautz, the wall axial velocity; "V_{ZW}", of equation 105, can be predicted using **Equation 107**. Predicted data in this study was ranged from 2.4-5 m/s.

$$V_{zw} = \frac{0.9Q}{\pi(R^2 - R_m^2)} \qquad \text{Equation 107}$$

The mean gas velocity in tangential inlet "v_{in}" can be estimated using **Equation 108.**

$$v_{in} = \frac{Q}{A_{in}} = \frac{Q}{ab} \qquad \text{Equation 108}$$

In **Equation 108**, "a" and "b" are the height and wide of the cyclone inlet, "Q" is the volumetric flow rates [ms^{-1}], "A_{in}" is area of tangential inlet and $R_{in} = R\text{-}R_x$. The mean gas inlet velocity in this study ranged from 6.5 to 14 m/s using **Equation 108.** These results are shown in **Appendix Q**. Fluid velocity across the wall of the hydrocyclone "$v_{\theta w}$" can be predicted using **Equation 109.**

$$v_{\theta w} = \frac{v_{in} R_{in}}{\alpha R} \qquad \text{Equation 109}$$

In **Equation 109**, "$v_{\theta w}$" is the wall velocity, "v_{in}" is the mean gas velocity inlet and "R_{in}" is the inlet radius. The predicted wall velocity of the fluid in the hydrocyclone ranged between 2.6 and 5.6 m/s. This data is detailed in **Appendix Q**.

The constriction coefficient of the hydrocyclone; "α" used in equation 109 can be predicted using **Equation 110** and **Equation 111.**

$$\alpha = \frac{1}{\xi}\left\{1 - \sqrt{1+4\left[\left(\frac{\xi}{2}\right)^2 - \frac{\xi}{2}\right]}\sqrt{1 - \frac{\left(1-\xi^2\right)\left(2\xi-\xi^2\right)}{1+c_o}}\right\} \qquad \text{Equation 110}$$

$$\xi = b/(\frac{1}{2}D) = \frac{b}{R} \qquad \text{Equation 111}$$

In **Equation 110** and **Equation 111**, "α" is the constriction coefficient, "c_o" is the ratio of incoming solids to incoming gas masses in the stream feeding the cyclone, "b" is the width of the cyclone inlet, "D" is the cyclone diameter, "R" is the radius of the cyclone, and "ξ" = b/R.

2.7.2.2 Barth Cut-Size Model

The Barth (1956) model for calculation of cut point across the hydrocyclone is shown in **Equation 112**. The Barth predicted cut-size data is shown in **Appendix O.** The Barth model predicted cut-size (d_{50}) ranged from 24-31 μm. The inner core velocity, "$v_{\theta CS}$" is calculated using **Equation 97.**

$$d_{50} = \sqrt{\frac{v_{rCS}\,9\mu D_x}{\rho_p v_{\theta CS}^2}} \qquad \text{Equation 112}$$

The radial velocity of the flow inside the hydrocyclone "v_{rcs}" calculated using **Equation 113**.

$$v_{rCS} = \frac{Q}{\pi D_x H_{cs}} \qquad \text{Equation 113}$$

In **Equation 113,** "Q" is the volumetric flow-rate through the cyclone, "D_x" is the diameter of the vortex finder, and "H_{cs}" is the height of the vortex finder.

There are only minor differences between the Muschelknautz and Barth cut-size models.

2.7.3 Efficiency Models

2.7.3.1 Introduction

Gas – liquid separation in the hydrocyclone occurs in two different areas. Most of the light, dispersed phase, separates in the vortex due to the centrifugal action. Separation may also occur in the hydrocyclone inlet. The system is subjected centrifugal forces that causes a radial settling velocity of "$w_{s,z}$". This settling velocity is created by an axial flow component v_{ax}. The higher density phase, with the high settling velocity, will reach the cyclone wall and the light dispersed phase (bubbles) will be dragged to the low pressure inner vortex core (**Figure 37**). Bubbles may break or coalesce during this process.

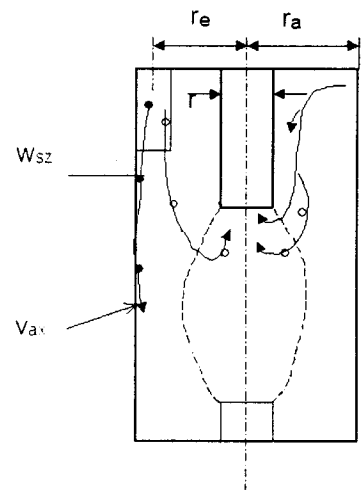

Figure 37: Axial and radial velocity of droplets and bubbles on a two-phase flow through a hydrocyclone, Klett, A (2001).

Klett, A (2001) studied hydrocyclonic separation and reported that the separation of the heavy phase at the wall of the hydrocyclone depends on the differential between feed

flow and overflow, and the cyclone length. In the case of air-water separation, a large amount of water is removed at the wall (Hoffman, 2002). Assuming "K" is the volume fraction reporting to the overflow and the settling velocity of the continuous phase, which can be calculated using **Equation 114**. K value is around 0.9.

$$w_{s,50} = \frac{0.5KQ}{A_w} \qquad \text{Equation 114}$$

In **Equation 115** "$w_{s,50}$" is the settling velocity of a particle, which is separated in the zone of downward flow, "Q" is inlet flow rates and "A_w" is the clarification area.

The author assumed Stokes' law is valid for a cut-size, at the cyclone's separation zones, Aw can be used as function of density differential ($\Delta\rho$) between phases and viscosity (μ). The validity of the Stokes' law for a certain cut-size at the separation zone is as a function of viscosity (μ) and density differences between phases ($\Delta\rho$) and can be write as an **Equation 115.**

$$d_{50} = \sqrt{w_{s,50}\frac{18\mu}{\Delta\rho\bar{z}}} \qquad \text{Equation 115}$$

In **Equation 115** mean centrifugal acceleration $\bar{z}$ can be calculated using **Equation 116.**

$$\bar{z} = \frac{v_\theta^2}{r} \qquad \text{Equation 116}$$

The author found that the d_{50} distribution across the vortex finder could be calculated using **Equation 117**.

$$1-Q(d)=\exp\left(-\left(\frac{d}{1.3d_{50}}\right)^{1.2}\right)$$ Equation 117

In equation 117, Q(d) is the particle size distribution in cyclone entrance. Separation efficiency is an indication of the separation of bubbles from the feed into the product streams. In efficiency studies two parameters are significant; namely bubble cut-size (d_{50}) and the slope of the efficiency curve.

The overall separation efficiency of a hydrocyclone; "η", can be calculated as the volume fraction of the feed gas sent to the overflow **(Equation 118).**

$$\eta=\frac{V_o}{V_f}=1-\frac{V_u}{V_f}=\frac{V_o}{V_o+V_u}$$ Equation 118

In equation 118, "η" is overall separation efficiency, "V_o", "V_u" and " V_f" are overf;ow, underflow and feed flow volume fraction.

In this section efficiency and overall separation efficiency models (mass fraction of the feed captured by the cyclone) developed by Muschelknautz; Dirgo-Leith; and Ebbenhorst-Tenbergen and Rietema are discussed with reference to (Hoffman, 2002).

2.7.3.2 Muschelknautz Hydrocyclone Efficiency Model (1990)

Overall separation efficiency; "η", is the mass fraction of the feed solids, droplets or bubbles captured by the hydrocyclone and does not consider the size or density of the dispersed phase. There is a separation efficiency for each particle size. The ideal efficiency curve is a S shape (if the separation was sharp the curve would be a vertical line at d_{50}) that changes under the influence of turbulence, agglomeration and coalescence. The definition and description of separation efficiencies is summarized in **Table 3**.

Table 3: Relationship between efficiency and cut-size

Efficiency	Cut-size
$\eta \rightarrow 0$	$d \rightarrow 0$
$\eta \rightarrow 1$	$d >> d_{50}$
$\eta = 0.5$	$d = d_{50}$

The efficiency curve (EC) is normally defined with two parameters x_i using a known d_{50} and the slope (m). The Muschelknautz model computes an efficiency curve (S shape curve) and an overall separation efficiency at low inlet solids ($C_o < C_{oL}$).

A variety of equations have been proposed to represent $\eta(d_{50}, m)$. On such relationship is found in **Equation 119** (Muschelknautz 1980).

$$\eta_i = \frac{1}{1+\left(\frac{d_{50}}{d_i}\right)^m}$$ Equation 119

In equation 119, "η_i" is efficiency, "d_{50}" is mean particle cut-size, "d_i" is diameter of particular particles and "m" is an empirical value. The efficiency prediction, based on the experimental data of the research, is shown in **Appendix W** and **Appendix Y**.

2.7.3.3 The Dirgo and Leith (1985) Hydrocyclone Efficiency Model

Dirgo and Leith developed an empirical model to calculate hydrocyclone efficiency that is shown in **Equation 120**. This equation represents a functional form for the efficiency curve.

$$\eta(d) = \frac{1}{1+\left(\frac{d_{50}}{d}\right)^{6.4}}$$ Equation 120

In **Equation 120** "m" is 6.4 – this is the slope of the lineralized efficiency curve ($1/\eta(x)-1$ vs. d/d_{50}) and is used to evaluate the sharpness of that curve. A low value of "m" indicates a poorly designed hydrocyclone.

The efficiency and overall efficiency prediction based on the experimental data of the research is shown in **Appendix Y**.

2.7.3.4 Ebbenhorst-Tenbergen and Rietema Model for overall Efficiency η

In the case of liquid-liquid and gas-liquid separations, a cyclone does not produce completely separated phases. A portion of light and heavy phase will present in both product streams. Ebbenhorst-Tenbergen and Rietema developed a universal definition for overall efficiency that is shown in **Equation 121** (Kimber and Thew 1974). This model takes no account of size distribution.

$$\eta = \left| \frac{Q_w^c}{Q_w^i} - \frac{Q_g^c}{Q_g^i} \right| \qquad \text{Equation 121}$$

In equation 121, "Q_w^c" is the clean underflow water rate, "Q_w^i" is the inlet water flow rate, "Q_g^c" is the clean underflow gas flow rate and "Q_g^i" is the inlet gas flow rate.

The Muschelknautz and Dirgo-Leith models predict separation efficiency curves and Ebbenhorst-Tenbergen model predict overall separation efficiency.

2.7.4 Pressure Drop over the Hydrocyclone

2.7.4.1 Introduction

Pressure drop across the hydrocyclone is an important factor for separation performance. The pressure drop across a cyclone; "Δp", is proportional to the square of the volumetric flow rate. In dimensionless form, pressure drop is often known as the "Euler number" as shown in **Equation 122,** where $\langle v_z \rangle$ is the mean axial velocity in the cyclone body). The

Euler number is a pressure loss factor used in fluid friction and momentum transfer. In turbulent flow, it is the pressure force to inertial force ratio.

$$E_u \equiv \frac{\Delta p}{\frac{1}{2}\rho < v_z >^2}$$ Equation 122

The pressure drop that occurs in the entry point is negligible. However, in the separation space or body of the cyclone and the vortex finder significant pressure drops occur.

2.7.4.2 Pressure drop in Vortex Finder

The Barth and Muschelknautz (1970) pressure drop model predict the pressure drop from the decay of pressure in the inlet, hydrocyclone body and vortex finder areas. This model states that the pressure loss in vortex finder area (Δp_x) is much greater than the pressure drop in inlet and hydrocyclone body.

2.7.4.3 Vortex Finder Models

Barth estimated the loss in the vortex finder by a semi-empirical approach. His semi-empirical model is shown in **Equation 123**.

$$\frac{\Delta p_x}{\frac{1}{2}\rho v_x^2} = \left(\frac{v_{\theta CS}}{v_x}\right)^2 + K\left(\frac{v_{\theta CS}}{v_x}\right)^{\frac{4}{3}}$$ Equation 123

Here "K" is an empirical value (3.41 - 4.4). The predicted Barth pressure drop across the vortex finder ranged 45 from 138 kPa under different operational conditions (**Appendix AA**).

Muschelknautz developed a model and predicts the loss in the core and in the vortex finder. This relationship is found in **Equation 124**.

$$\Delta p_x = \left[2 + \left(\frac{v_{\theta CS}}{v_x} \right)^2 + 3 \left(\frac{v_{\theta CS}}{v_x} \right)^{\frac{4}{3}} \right] \frac{1}{2} \rho v_x^2$$

Equation 124

This model's predicts pressure drop across the vortex finder ranged from 41 to 115 kPa under different operational conditions. This data is summarized in **Appendix AA**.

Pressure drop across the vortex finder is significant and can be predicted by the model shown in **Equation 125**. In this model, "v_x" is the flow velocity in vortex finder. Muschelknautz also developed **Equation 125** for vortex finder pressure drop prediction.

$$Eu_x = \frac{\Delta p}{\frac{1}{2} \rho v_x^2}$$

Equation 125

The predicted Euler number, as a pressure drop factor in vortex finder, ranged from 41 to 152 kPa. This data is summarized in **Appendix AA**.

2.7.5 Comparison of the Pressure Drop Models

The data given by the Barth and Muschelknautz models showed a good correlation between themselves and both models predicted the same range of the pressure drop in the vortex finder.

2.7.6 Pressure Drop in Hydrocyclone Body

2.7.6.1 Barth, W (1956)

Barth states that inlet losses could be effectively avoided by design. The author reported that "the pressure loss in the body as the decrease in dynamic pressure at this imagined friction surface", i.e. he considered the decrease in total pressure to arise from the loss of swirl velocity at the friction surface. This relationship is found in **Equation 126.**

$$\frac{\Delta p_{body}}{\frac{1}{2}\rho v_x^2} = \frac{D_x}{D}\left[\frac{1}{\left[\frac{v_x}{v_{\theta cs}} - \frac{(H-S)}{0.5D_x} f\right]^2} - \left(\frac{v_{\theta cs}}{v_x}\right)^2\right]$$

Equation 126

In **Equation 126**, "D_x" is the vortex finder diameter, "D" is the body diameter, "ρ" is the gas density, "v_x" is the vortex finder gas velocity, "$v_{\theta CS}$" is the vortex finder tangential velocity, "H" is the cyclone height, "S" is the vortex finder length, *"f"* ($f = f_{air} + f_{water}$), is the friction factor and "$v_{\theta CS}$" is the internal spine velocity.

The Barth model predicts pressure drop across the hydrocyclone that ranges from 16 to 102 kPa for different operational conditions.

2.7.6.2 Muschelknautz, E (1980)

According to the Muschelknautz model, the wall loss, or the loss in the cyclone body, is given by **Equation 127**.

$$\Delta p_{body} = \frac{f A_R \rho \left(v_{\theta w} v_{\theta CS}\right)^{1.5}}{2 \times 0.9 Q}$$

Equation 127

The Muschelknautz model predicts pressure drop across the hydrocyclone that ranges from 10 to 50 kPa for different operational conditions. This data is presented in detail in **Appendix EE**.

2.7.7 Pressure Drop in Hydrocyclone Inlet

2.7.7.1 Shepherd and Lapple (1940)

This model (**Equation 128**) is valid for slot inlet hydrocyclones – as such it is applicable to this study, and incorporate only the dimensions of the gas inlet and outlet. In equation

128 "*a*" and "b" are width and length of the tangential inlet and "D_x" is the diameter of the vortex finder.

The pressure drop across the inlet is low with a predicted inlet Euler number of 12.22 (**Appendix EE**).

$$Eu_{in} = \frac{16ab}{D_x^2}$$ Equation 128

2.7.7.2 Casal, J and Martinez-Benet, JM (1983)

Casal and Martinez-Benet developed the purely empirical model for prediction of pressure drop across the hydrocyclone that is shown in **Equation 129 and Equation 130**. This model incorporates only the dimensions of the gas inlet and outlet.

$$Eu_{in} = 3.33 + 11.3\left(\frac{ab}{D_x^2}\right)^2$$ Equation 129

$$Eu_{in} = \left(\frac{\Delta p}{\rho v_{in}^2}\right)$$ Equation 130

In these equations, "a" is the inlet area, "b" is the outlet area and "D_x" is the gas exit tube diameter. The predicted inlet Euler number for the test equipment using this calculation is 9. This data is detailed in **Appendix EE**.

2.8 Dimensionless Numbers

2.8.1 Stokes' number for cut-size d_{50} (StK_{50})

Stokes' number is often used in cyclone models. The Stokes' number for the cut-size d_{50} can be calculated using **Equation 131.**

$$StK_{50} = \frac{d_{50}^2(\rho_l - \rho_g)v}{18\mu D_c}$$ Equation 131

In **Equation 131** , "d_{50}" [μm] is the cut-size; "μ" is the viscosity of water; "ρ_l" is the density of water, "ρ_g" is the density of air, and "v" is the characteristic velocity.

2.8.2 Swirl Number (S)

The swirl number represents the intensity of swirl in annular flow and can be expressed as **Equation 132**.

$$S = \frac{Tangential\ momenta}{Axial\ momenta} = \frac{Tangential\ Velocity}{Axial\ Velocity} = \frac{m/s}{m/s}$$ Equation 132

The predicted swirl number data for the test hydrocyclone and vortex finder is detailed in **Appendix GG.** Swirl number in vortex finder ranged from 3 to 5 and in the body of the hydrocyclone ranged from 3.1 to 3.2. This indicates a high swirl flow regime which is typically a good environment for air - water separations. Generally, $S < 0.5$ is considered weak to moderate and above 0.5 is high.

2.9 Conclusions of Literature Review

Navier-Stokes equations are a good starting point to model the vortex flow (radial, axial and tangential) in liquid-liquid and air-water hydrocycloes. In these types of separators, the radial velocity is dependent upon the axial velocity. In hydrocyclone modelling, axial velocity is a significant parameter. The effect of geometry, feed physical properties and pressure drop on the hydrodynamics of multiphase flow are also significant.

Development of a mechanistic model is a reasonable compromise between the simplicity of empirical, and complexity of CFD models.

3. INSTRUMENT and APPARATUS

3.1 Introduction

In this chapter, the experimental set-up and its components are presented including details of each part of the circuit used such as pumps, valves and piping, air addition, creation of bubbles, and the hydrocyclone. Along with this, a description of experimental procedure is given.

Experiments were carried out using the facilities of the Dalhousie Mineral Engineering Centre. This cyclone circuit is shown in **Figure 38**. This test circuit (a modified Mozely system) was designed to gather data on the performance of an air-water cylindrical hydrocyclone. Bubble size measurement on various streams was carried out using a Malvern 2600-C particle size analyser.

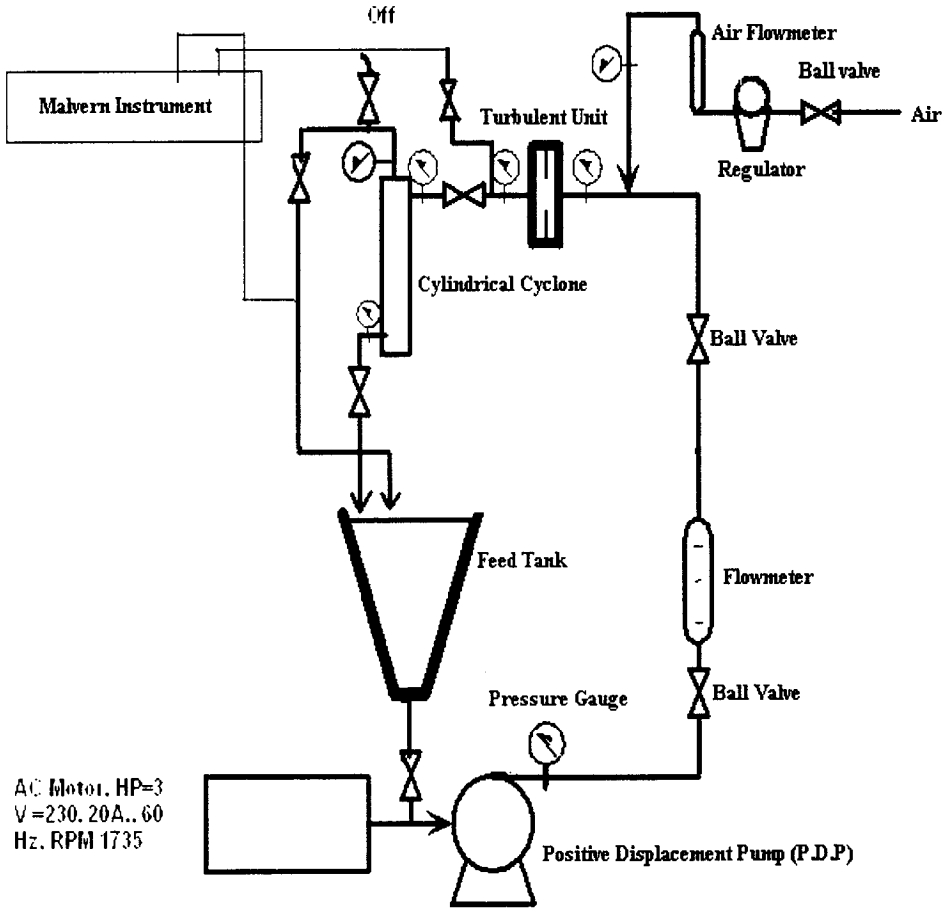

Figure 38: Schematic Diagram of the Experimental Set-up.

The equipment used in this circuit included a fixed speed positive displacement pump (PDP), bypass valves that controlled the feed flow rate to the cyclone, and a PVC conical mixer tank. Pressure gauges were mounted at the feed inlet and outlet of both the collision promoter and hydrocyclone.

Preliminary mixing of the continuous-phase, tap water, and the dispersed-phase, dry house air was performed in the positive displacement pump. Direction of flow was controlled by a check valve on the 2.54 cm ID pipe. Additional air was introduced prior to the orifice plate through a 5 mm plastic tube inserted to the centre-line of the fixed pipe. The dispersion investigated was composed of less then one percent air by volume.

Bubbles entering the orifice plate were strongly deformed by the turbulent eddies generated. The high shear rates caused bubble breakage resulting in a decrease in average bubble size. Turbulence, which caused the breakage, was monitored by the pressure drop across the orifice plate.

The separation vessel was a 2.54 cm diameter cylindrical aluminium hydrocyclone. The two-phase output from the orifice plate was used to feed the hydrocyclone for the bubble separation.

Water and air flow rates were adjusted using control valves and flow meters with known accuracies. The feed flow rate ranged between 50-75 l/m yielding a Reynolds number of approximately 10,000 and a swirl number ranged 7-8.

3.2 Components of the Experimental Set-up

3.2.1 Storage and Metering

3.2.1.1 Feed Tank

Feed water was stored in a PVC tank of 200 litre of capacity. This tank was connected to the positive displacement pump (PDP).

3.2.1.2 Flow Meters

The feed fluid was metered using a Dwyer flow meter with a 2.54 cm inline connection, 0-75 litre per minute capacity and ±2% accuracy. This flow meter was equipped with control valve, a check valve and a pressure gage.

The airflow rate was controlled using a Dwyer air flow meter and with a range of 10-100 SCFH or 50 litre per minute and an accuracy of ± 2%.

3.2.1.3 Piping

2.54 cm, 1.9 cm and 1.27 cm inside diameter high pressure PVC pipes and fittings were used in this work.

3.2.1.4 Pump

The source of kinetic energy required for creation of the air-in-water dispersion and the centrifugal force inside the cylindrical hydrocyclone, was a Mono Merlin positive displacement pump (**Figure 39**). This pump delivered up to 30 m^3 per hour of feed at pressures up to 550 kPa. The general specification of this pump is summarized in **Table 4**.

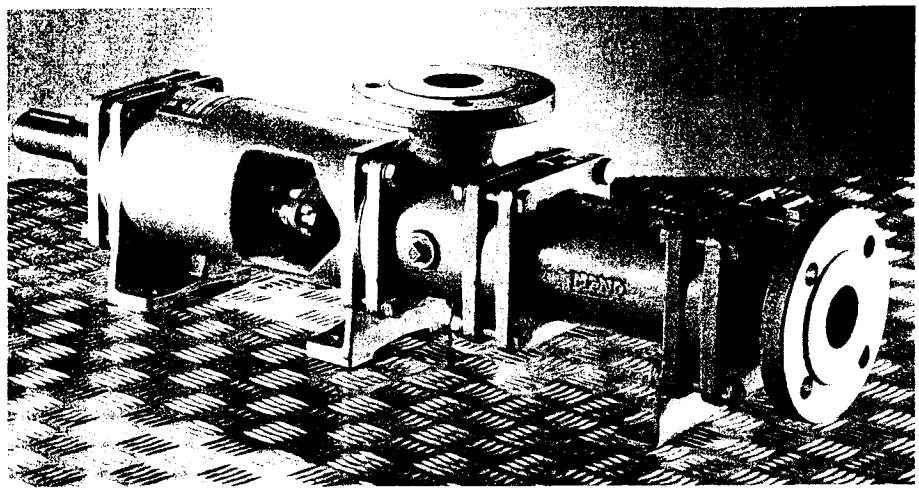

Figure 39 : Mono-Merlin positive displacement pump (courtesy to Mono-Merlin Company).

Table 4: General specifications of the used Mono-Merlin pump.

Pump	Type	Power	RPM	Voltage	Hertz	Amper
Mono Merlin	CAF 12G 1B4	HP		V	Hz	mA
		7.5	1735	230	60	20

3.2.1.5 Air Compressor

An air pump (compressor) manufactured by Campbell Housfield, supplied air at pressures up to 690 kPa.

3.2.1.6 Gauges

Pressure gauges on the 2.54 cm feed line where located before and after the orifice flange to measure pressure drop across the orifice plate. The range of these gauges was between 0-690 kPa (Model BII, Error ± 5%).

3.2.2 Turbulent Unit (Collision Promoter)

There are many methods that can be used for air-water contact. These include mechanically agitated tanks, pumps, static mixers, and orifice plates. In this research an orifice plate and/or a pump was used. The advantage of the orifice system was that it is adjustable, turbulence can be controlled and small bubble sizes can be generated with a

narrow size distribution. In this work, water and gas were injected through the orifice (**Figure 40**) in order to generate bubbles. The bubble size increased with gas rate and decreased with water rate, frother concentration, and turbulent intensity.

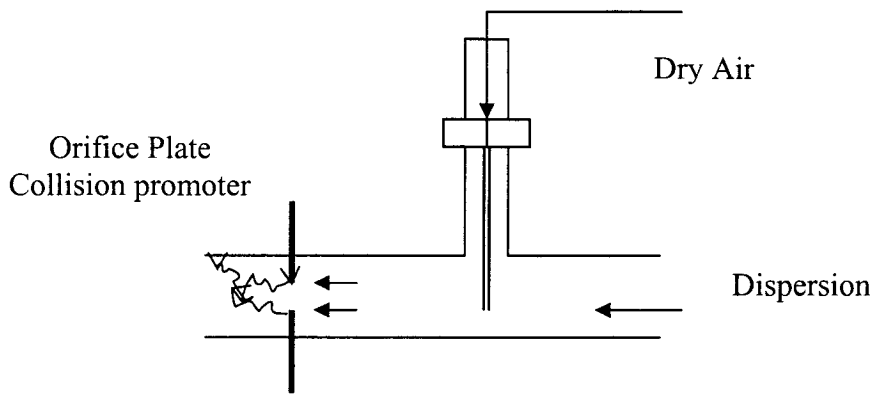

Figure 40: The Schematic diagram of the bubble generator and collision promoter.

In this design, air was injected through a 0.5 cm diameter tube into the centre-line of the 2.54 cm ID dispersion pipe, 5 cm before the orifice plate. Orifice plates were mounted in 2.54 cm inside diameter orifice flanges. The β ratio (Diameter of orifice/ diameter of pipe) ranged between 0.2-0.6 (**Figure 41**)

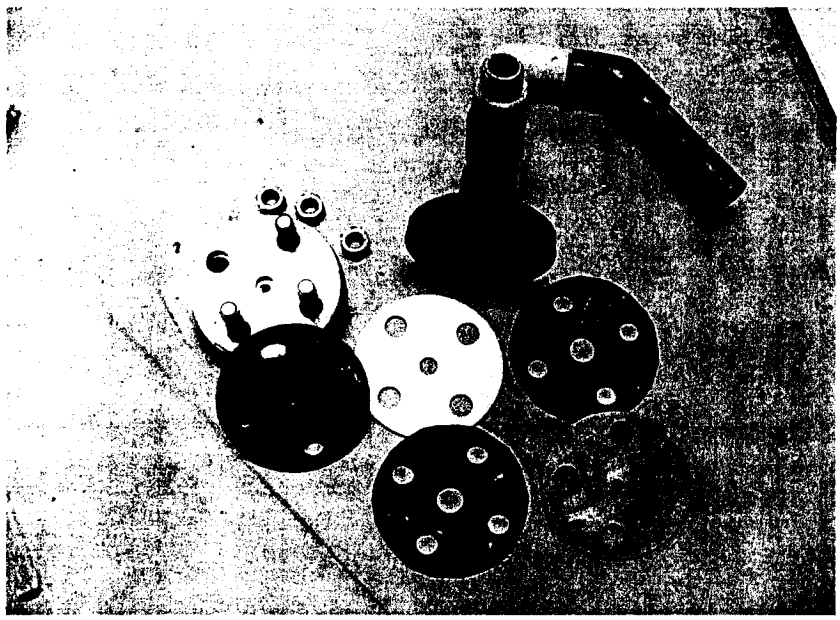

Figure 41: Orifice plates and orifice flange.

3.2.3 Cylindrical Hydrocyclone

3.2.3.1 Introduction

The hydrocyclone used was an aluminium cylinder with an inside diameter of 2.54 cm and inside length of 40.64 cm. The inlet and under-flow ports were tangentially located at opposite ends of the cylindrical body. Both were rectangular slots with a length of 2.54 cm and width of 0.635 cm. The flow rate in all streams of the hydrocyclone could be modified using ball valves. The pedestal was mounted at the bottom of the hydrocyclone to minimize two-phase bubbly flow to the under-flow. **Figure 42** shows the top part of the cylindrical hydrocyclone prototype including the inlet port.

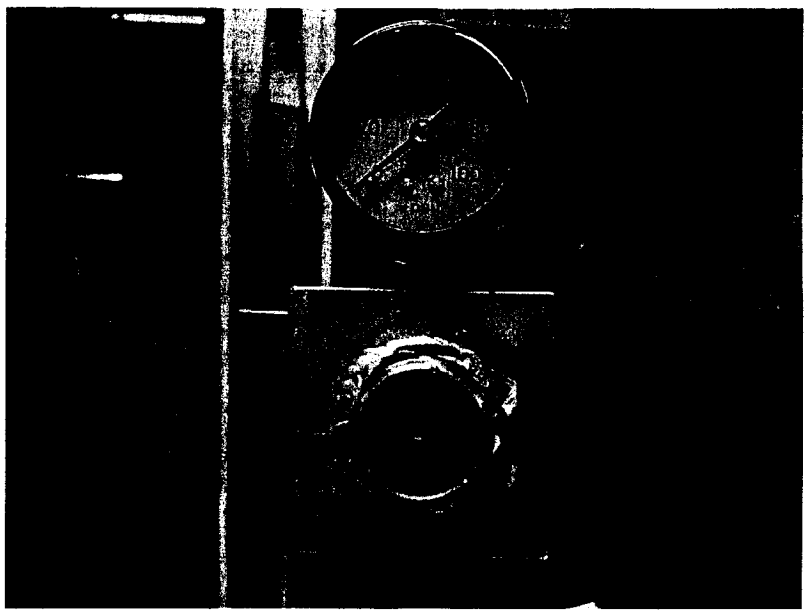

Figure 42: peripheral inlet of the 2.54 cm de-oiling cylindrical hydrocyclone.

3.2.3.2 Over-flow Port Dimensions (axial outlet)

The diameter of the over-flow (reject stream) exit port was 0.5 cm. The flow through this port could be controlled using a ball valve mounted above the hydrocyclone (valve dismantled when the picture was taken) as shown in **Figure 42**.

3.2.3.3 Tangential Port Dimensions (Inlet and Underflow Outlet)

The lower flow exit port was a rectangular slot with dimensions of 2.54 cm long and 0.5 cm (1/15 of the cyclone circumference) wide tangentially mounted to the cylindrical body. The dimensions of the tangential inlet- and under-flow tangential outlets were 2.54×0.5 cm (area of 1.27 cm^2).

3.2.3.4 Vortex Finder

The vortex finder was mounted in the top cap of the hydrocyclone and connected to the axial outlet port. The inside diameter of the vortex finder was 1.27 cm and the length was 25.4 cm. The main purpose of the vortex finder was to prevent a short circuit within the hydrocyclone and help to stabilize the air and water core **(Figure 43).**

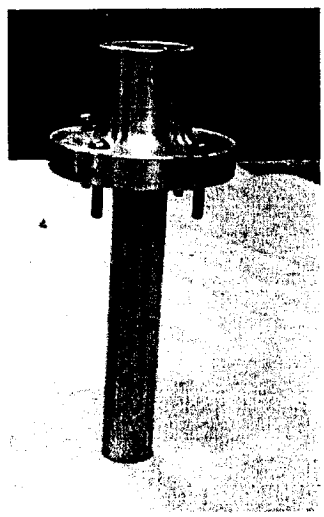

Figure 43: Vortex finder.

3.2.3.5 Hydrocyclone's Length

The hydrocyclone's length was not a significant parameter for separation efficiency, but excessive length (L/D > 8) may have an adverse effect on separation performance and increases the pressure drop. "L" is hydrocyclone length and "D" is the diameter.

3.2.3.6 Pedestal

A cylindrically shaped pedestal was mounted in the bottom of the hydrocyclone to prevent or reduce the air-phase leakage to the under-flow. The dimensions of the pedestal were 1.50 cm long and 1.27 cm diameter **(Figure 44).**

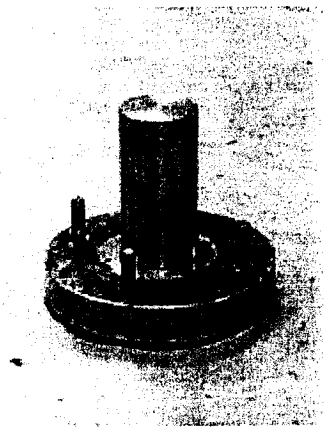

Figure 44: Pedestal.

3.2.4 Malvern 2600-C Particle Size Analyzer

Gas bubble sizes were measured, in-line, using a Malvern 2600C particle size analyzer. This equipment is shown in **Figure 45**.

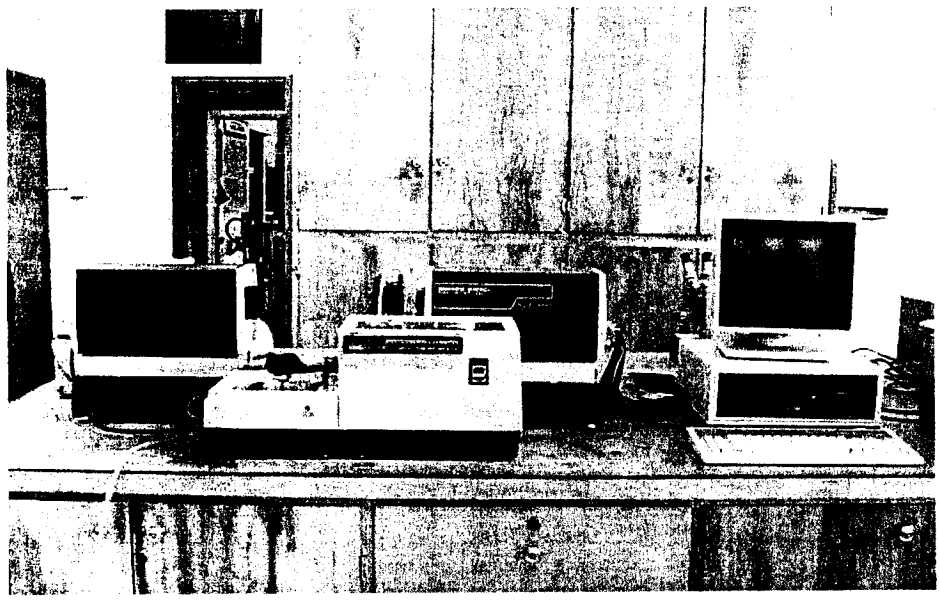

Figure 45: Malvern 2600 C particle size analyzer.

4 PROCEDURE

4.1 Introduction

The experimental test program provided the data required for modeling. A series of experiments was carried out in order to evaluate hydrocyclone separation efficiency, pressure drop and bubble size distributions. The results are presented and analyzed on the basis of bubble size distribution (BSD) and bubble volume distribution (BVD). Samples were taken from the over-flow stream (OF), under-flow stream (UF) and the turbulent unit streams at steady state. Flow-rates, superficial velocity and pressure drops were recorded. Bubble size distributions in selected streams were measured and analyzed.

4.2 System to be investigated

1. System dispersion characteristics when using a positive displacement pump.
2. Bubble breakage as a function of pressure drop and turbulent intensity.
3. Interfacial characteristics of the dispersion modified using surfactants (Triton x100) with a concentration between 0.01-1% mole/m^3.

4.3 Feed Material

The feed material in this research was tap water (**Appendix A**), air (**Table 5**) and the non-ionic surfactant Triton ×100 – an octyphenol ethylene oxide shown in **Figure 46**. Tests using Triton X100 were at concentrations ranging from 1 – 50 ppm.

Table 5: Dry air properties.

Property	Value (Metric)
Density ρ	1.22 kg/m^3
Specific Volume(v)	0.814 m^3/Kg
Pressure (P)	101.3 Kpa
Temp (t)	15°C

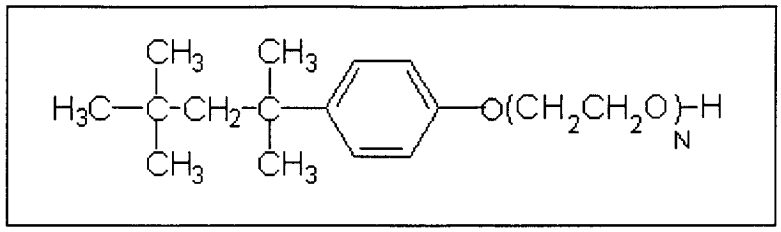

Figure 46: Triton X100 chemical structure.

In this work, a known amount of air was mixed with tap water. The gas-phase hold-up measured using mass balance method and varied between 0.5 to 1%. The dispersion was created using both a positive displacement pump and a turbulent unit.

4.4 Gas- Liquid Contact

A summary of the turbulent unit test conditions is shown in **Table 6.**

Table 6: Summary of Collision promoter's tests conditions.

No	β	Flow Rate l/m	Superficial Feed Velocity	Feed Pressure psi	Pressure Drop (Δ)	Air Flow Rate l/m	Replica tions
1	0.1	50	10	40	25	3	3
2	0.2	60	7	60	20	5	3
3	0.4	70	5	80	15	8	3
4	0.6	80	3	90	8	10	3

4.5 Baseline Tests for Gas-Liquid Cyclonic Separation

The baseline tests for the hydrocyclone are summarized as follows.

- Tests without injection of surfactant or entrained air; but including dissolved air, to determine the separation efficiency.
- Air injection tests to determine possible increases in separation efficiency.
- Tests with surfactant and air injection to determine pressure drop across the hydrocyclone.

Pressure drops across the turbulent unit, at various superficial velocities of two-phase flow baseline tests, were measured to determine the separation performance of the hydrocyclone.

4.5.1 Pressure Drop across the Orifice Plate

The bubble size distribution created by the orifice unit is affected by the flows of the different phases. These flows also affect the pressure drop across the unit. Thus, pressure drop for a particular orifice can be used to give an indication of bubble size distribution. In order to determine the differential pressure across the plate, pressures were measured using two pressure gauges mounted before and after the orifice flange.

4.5.2 Pressure Drop in the Hydrocyclone

The following variables that influence pressure drop were investigated.

1. Operating Water Pressure (P_w)
2. Operating Air Pressure (P_A)
3. Pressure Drop Inlet to Underflow (Δp_1)
4. Pressure Drop Inlet to Reject flow (Δp_2)
5. Underflow stream Pressure (P_u)
6. Overflow Stream Pressure (P_o)
7. Inlet Stream Pressure (P_i)

The operating pressure of the hydrocyclone was approximately 276 kPa and the reject flow and underflow pressures were close to atmospheric.

4.5.3 Flow Rate

Water flow rate in the system was varied between 50-70 litres per minute. The gas-phase flow-rate varied between 0.1-1% by volume, of the continuous-phase depending on the test.

4.5.4 Gas Hold-up in the Two-Phase Stream.

The purpose of the air-water cyclone was to remove the air through the reject flow. Gas hold-up in the under-flow was measured using the Malvern. Data and mass balance calculations were conducted based on the volume, density and phase holdups.

4.6 Source and Estimate of Error

4.6.1 Introduction

No measurement is perfectly accurate or exact. Many instrumental, physical and human limitations cause measurements to deviate from "true" values. In this section, instrumental and material errors are discussed.

4.6.2 General Instrument and Equipment Measurement Errors

Analytical balances and graduate glassware such as beakers, cylinders, pipettes and filtration have errors on the order of ± 0.1-0.2%.

4.6.3 Malvern 2600 C (Bubble Size Measurement) Errors

Instrumental error is a part of the systematic error. This type of error includes particle size analyzer errors such as laser beam alignment, incorrect lens, insufficient signal accumulation and inappropriate background measurement. Other errors include those arising from the sample and the experiment.

Error arising from the sample

1. Sample distribution that is not appropriate to the model.
2. Sample bubbles that do not exhibit normal diffraction properties.
3. Sample contaminated with particles (bubbles) out of range of the measurement.

Error arising from experiment

1. Incorrectly aligned optics (laser beam).
2. Background measurement that is not appropriate to the sample measurement.
3. Dirt on optics.

The gas-phase flow rate was about 2.5 lit/min. This low flow rate helped to minimize the bubble size experimental error. Total instrumental and human error in this method was approximately ±0.5%.

4.6.4 Flow Measurement Errors

For measurement of the continuous-phase, an appropriate Dwyer model flow meter was used (accuracy ±3%). For measurement of the air-phase, a Dwyer flow meter was also used (accuracy ±1%).

4.6.5 Number of Replications for Reduction of Error

Duplicate tests were carried out to reduce the experimental and human error. Measurement of bubble size was a challenge, thus many replications were carried out to minimize this error.

5 RESULTS

5.1 Introduction

This chapter presents the results, data treatment and bubble size distributions. A total of 120 experimental runs were conducted. The effect of feed pressure, volumetric feed rate, pressure drops, under-flow stream pressure, bubble size and bubble volume distribution in feed stream and under-flow stream were examined. The fixed experiment variables used in this study is shown in **Table 7.**

Table 7: Dimensional independent variables.

Variable	Description
d_i	Equivalent inlet diameter
d_o	Inside diameter of overflow.
D_c	Cyclone diameter
L	Length of hydrocyclone.
d_u	Inside Diameter of Underflow.
d_v	Vortex Finder Diameter

5.2 Pressure Drop Data

Pressure drop measurement across the turbulent unit and the hydrocyclone (inlet "Δp_{in}", body "Δp_{body}" and vortex finder "Δp_x") are important variables in terms of turbulence and phase disengagement.

5.2.1 Turbulent Unit Pressure Drop

Pressure drop across the turbulent unit indicates turbulence and bubble formation and sizing. Pressure drop is affected by flow rate, orifice diameter and operating pressure. Experimental and Bernoulli's model predicted pressure drops are shown in **Figure 47** and **Figure 48**. It was found that pressure drop increases when flow rate increases.

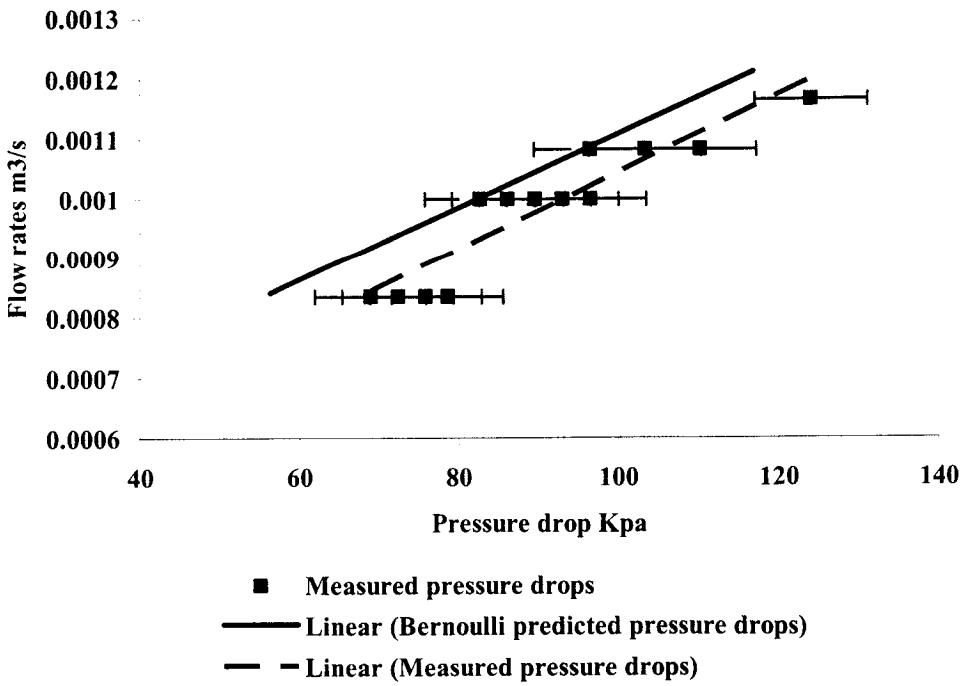

Figure 47: Comparison of pressure drop vs. flow rate in turbulent unit ($\beta = 0.5$).

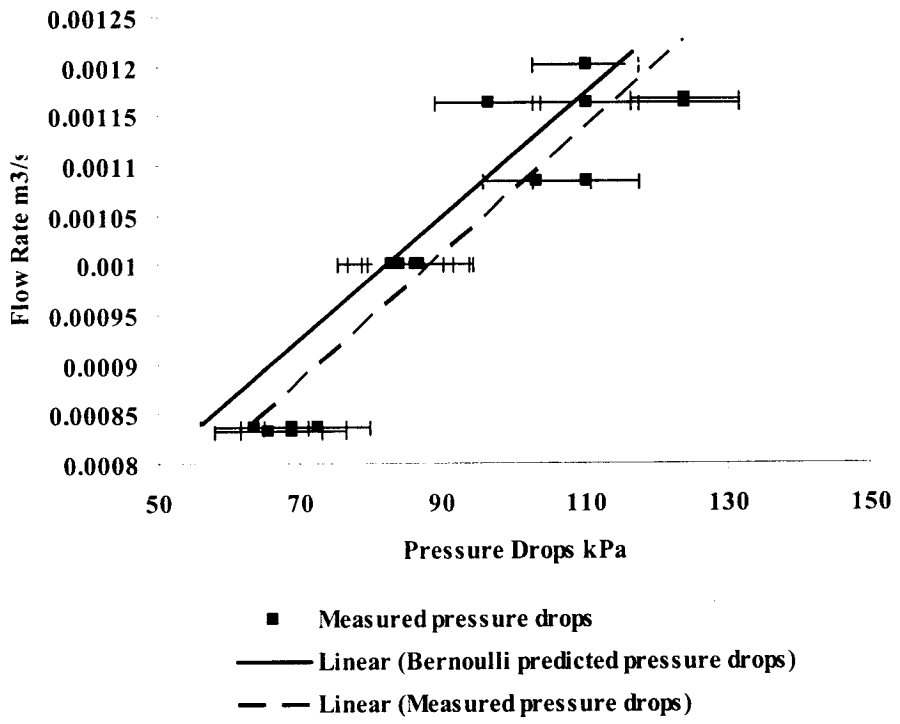

Figure 48: Comparison of pressure drop vs. flow rate in turbulent unit ($\beta = 0.4$).

The measured and model predicted pressure drops across the orifice plate and the superficial flow velocity in the pipe and orifice plate are detailed in **Appendix B** and **Appendix D.** The measured pressure drop varied between 75-125 kPa while the model pressure drop predictions were between 56-125 kPa. The calculated superficial velocity of the two-phase flow across the turbulent unit was between 10 and 16 m/s (**Appendix D**).

Pressure drop across the orifice plates is proportional to the superficial flow velocity through the orifice plate. This relationship is shown in **Figure 49**.

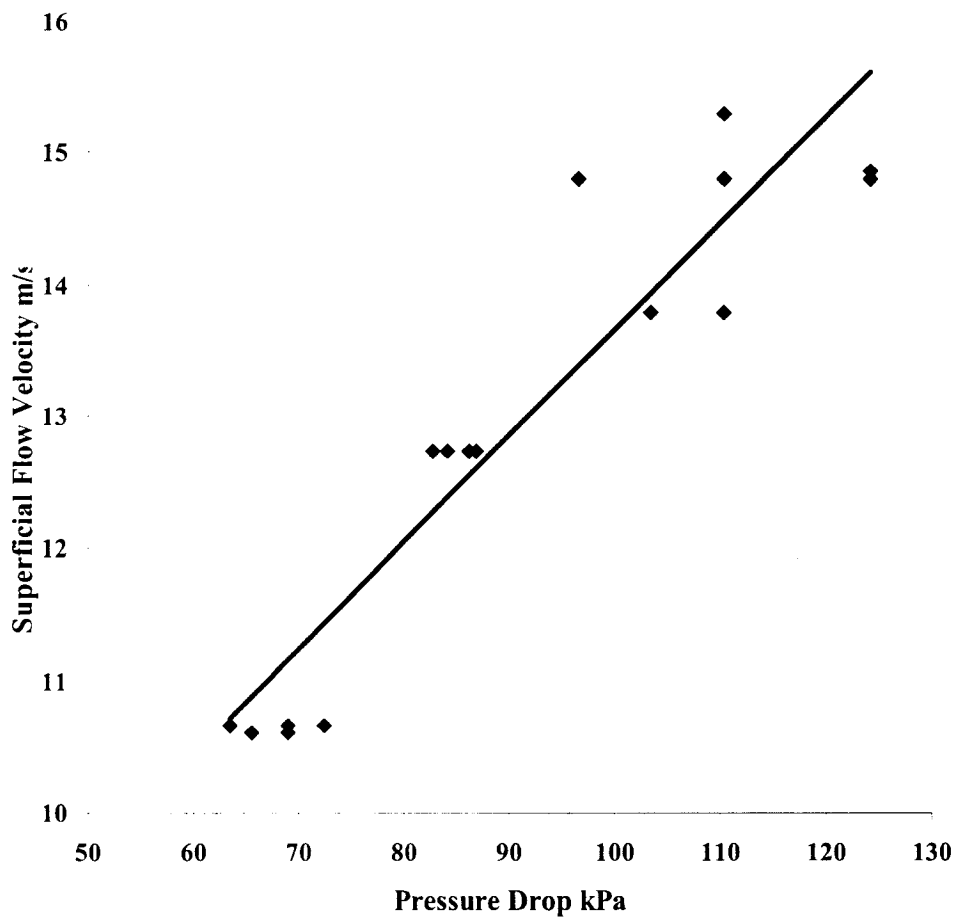

Figure 49: Relationship between pressure drop and superficial velocity across the turbulent unit.

5.2.2 Hydrocyclone Pressure Drop

Measured pressure drop across the hydrocyclone varied between 25-100 kPa. These results are detailed in **Appendix F**.

Several empirical models including the Bart and Muschelknautz models were used to predict hydrocyclone pressure drop -- these results are detailed in **Appendix R** and **Appendix S**.

5.3 Bubble Size Distribution Measurement

When measuring the bubble size distribution of a two-phase flow, it is necessary to get a representative sample. In a two-phase air-water system bubble break-up and coalescence occurs in the turbulent unit and the hydrocyclone. Bubble size distributions were obtained from the inlet flow, reject flow and under-flow of the cyclone. Sampling was accomplished, inline, using a 6 mm inside diameter P.V.C hose connected to the Malvern system. Detailed results of bubble size distribution are shown in **Appendix G**.

Bubble size distribution has measured in micrometers (μm). Some important relationships used when determining the bubble size distribution using a laser scattering method are as follows:

Obscuration:

$$\text{Obscuration} = 1 - \frac{\text{Light Intensity with Sample}}{\text{Light Intensity Without Sample}} \qquad \text{Equation 133}$$

Experimental error increases with obscuration (**Equation 133**).

Sauter Mean Diameter:

$D_{(3,2)}$ is a measure of the ratio of the total volume of particles [cm^3] to the total surface area [cm^2]. In droplet and bubble size distribution studies, this diameter is a good indicator of size and surface area.

Distribution Span

Span is an indicator of the bubble size distribution. The span of the distribution measures the spread between the 10% and 90% points of the cumulative undersize distribution, normalized in terms of the 50% point. This span is defined by **Equation 134.**

$$Span = \frac{D(90) - D(10)}{D(50)} \qquad \text{Equation 134}$$

Display Fit

Display fit gives the measured and calculated light energy distributions and residuals in Malvern calculation software. The log difference indicates the goodness of the least squares fitting process. This relationship is shown in **Equation 135.**

$$\text{Log difference} = \log \sum_{j=1}^{n} [\text{light calculated} - \text{light measured}]^2 \qquad \text{Equation 135}$$

The value of this parameter is an indication of the adequacy of the model. A qualitative interpretation of this parameter is shown in **Table 8**.

Table 8: Description of the log-difference in laser scattering technique.

No	Log Difference	Description
1	<6	Model not appropriate or experiment incorrectly performed.
2	5.5 < Log. diff. < 6	Poor Fit. May be adequate for trend analysis only.
3	5 < Log. diff. < 5.5	Adequate fit but look for evidence of systematic misfitting.
4	4< Log. diff. <5	Good Fit. Well- Presented sample.
5	Log. diff. <4	Very unlikely with measured data but normal with analytic data.

5.3.1 Bubble Size Distribution after the Turbulent Unit

The bubble size distribution data after the turbulent unit is detailed in **Appendix G**. A summary of the bubble size distribution measurements after the turbulent unit, obtained by the Malvern 2800-C, is shown in **Figure 50:**

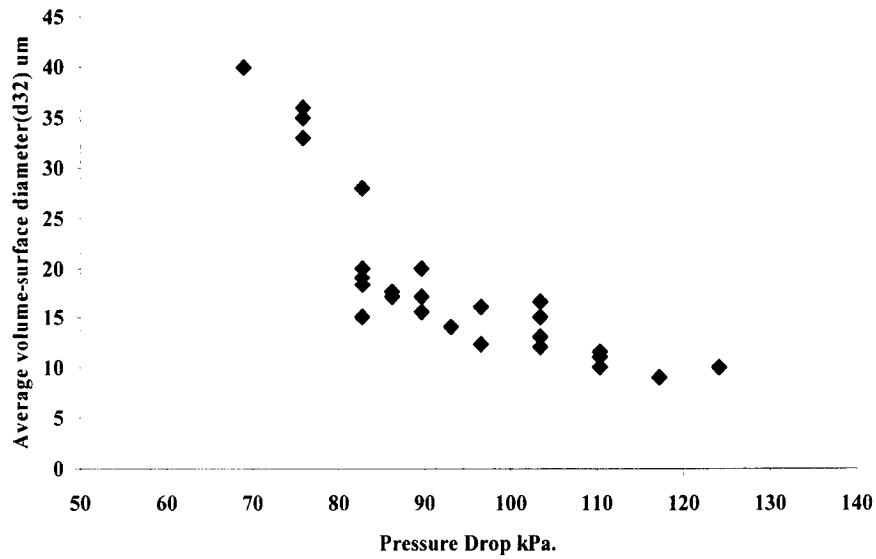

Figure 50: Average volume-surface diameter of the bubbles; "$d_{(3,2)}$" as function of Pressure drop across turbulent unit.

The Sauter mean diameter $d_{(3,2)}$ was found to be between 17.5 - 41 μm depending on test conditions. Experiments with a log.diff > 6 have been removed from this analysis.

5.3.2 Underflow Stream

A summary of the bubble size distribution measurements in the under-flow stream are detailed in **Appendix I**. The mean sauter diameter; $d_{(3,2)}$,was found to be between 8.4 - 25 μm.

5.3.3 Over-flow Stream

The bubble size distribution measurements in overflow stream are detailed in **Appendix K**. The mean sauter diameter; $d_{(3,2)}$ was found to be between 18.4 - 229 μm. The sauter mean diameter is an indication of the bubble surface area, which is important when there is contact or interaction between phases.

5.3.3.1 Bubble Size Distribution Data Treatment

The bubble size distribution and different cut-sizes including d_{10}, d_{32}, d_{50} and d_{90} were measured. Bubble sizes are important in the evaluation of cyclone separation

performance. A separation of the fine bubbles from the water is more difficult than the larger bubbles. Bubble size data from the in-flow, over-flow, under-flow and turbulent unit streams were examined using both linear and non-linear regression after transforming the data using the Rosin-Rammler (Weibull function) model applied to bubble size (**Equation 136**). This distribution can model particles, sprays and bubbles.

$$\bar{y}_i = 1 - e^{-\left(\frac{x_i}{\bar{x}_i}\right)^{\beta}} \qquad \text{Equation 136}$$

In **Equation 136**, "$\bar{x}_i$" is a measure of the average bubble size (size modulus) and β is a measure of the spread of sizes (distribution modulus). The Rosin-Rammler distribution is practical because it has only two parameters, is simple and can easily be manipulated.

5.3.3.2 Rosin- Rammler Linear Method

By linearizing the Weibull function, using natural logs (ln), Equation 136 can be presented as **Equation 137** which is in the form of **Equation 138**.

$$\ln\left(-\ln\left[1-\bar{y}_i\right]\right) = \beta \ln x_i - \beta \ln \bar{x}_i \qquad \text{Equation 137}$$

$$y = ax + b \qquad \text{Equation 138}$$

The slope and intercept of the linear function can be calculated using **Equation 139** and **Equation 140.**

$$\alpha = \beta = \frac{n\sum_{i=1}^{n} x_i y_i - \sum_{i=1}^{n} x_i \sum_{i=1}^{n} y_i}{n\sum_{i=1}^{n} x_i^2 - \left(\sum_{i=1}^{n} x_i\right)^2} \qquad \text{Equation 139}$$

$$b = -\beta \ln \eta = \frac{\sum_{i=1}^{n} y_i - \alpha \sum_{i=1}^{n} x_i}{n}$$

Equation 140

The correlation coefficient of this fit is calculated using **Equation 141**.

$$r = \frac{n\sum_{i=1}^{n} x_i y_i - \sum_{i=1}^{n} x_i \sum_{i=1}^{n} y_i}{\sqrt{[n\sum_{i=1}^{n} x_i^2 - (\sum_{i=1}^{n} x_i)^2][n\sum_{i=1}^{n} y_i^2 - (\sum_{i=1}^{n} yi)^2]}}$$

Equation 141

5.3.3.3 Rosin- Rammler Non-Linear Method

The information obtained from the Malvern included bubble size *(x_i)*, volume within band, and cumulative measured *(y_i)*. This data was used to calculate the Rosin-Rammler cumulative predicted"$\hat{y}_i$", un-weighted residuals$(y_i - \hat{y}_i)$, weighted residuals "$\hat{y}_i(y_i - \hat{y}_i)$" and a non-linear regression curve of the bubble volume distribution (BVD).

The non-linear correlation coefficient; "η^2" can be determined using the **Equation 142**. When "η^2" and "r^2" are equal the relationship is linear but if "η^2" (relation-coefficient) > "r^2" then the relationship is not linear.

$$\eta^2 = 1 - \frac{\Sigma(y_i - \hat{y}_i)^2}{\Sigma(y_i - \bar{y}_i)^2}$$

Equation 142

5.3.4 Bubble Size Distribution Fitting.

Bubble size distribution data obtained from the Malvern Bubble size analyzer was fitted into the Rosin-Rammler distribution with a correlation coefficient (η^2) to 0.99-1. Details of this curve fitting (non-linear cumulative curve) is shown in **Appendix-O**.

5.3.4.1 Rosin-Rammler Non-Linear Regression Method

In-flow, over-flow, under-flow and turbulent unit streams were tested. This information is presented in **Appendix-O** as a bubble size, "x_i" (μm) and fractional bubble volume that lie within the band bounded by that bubble size and the size smaller. A sample of non-linear regression results is shown in (**Figure 51**).

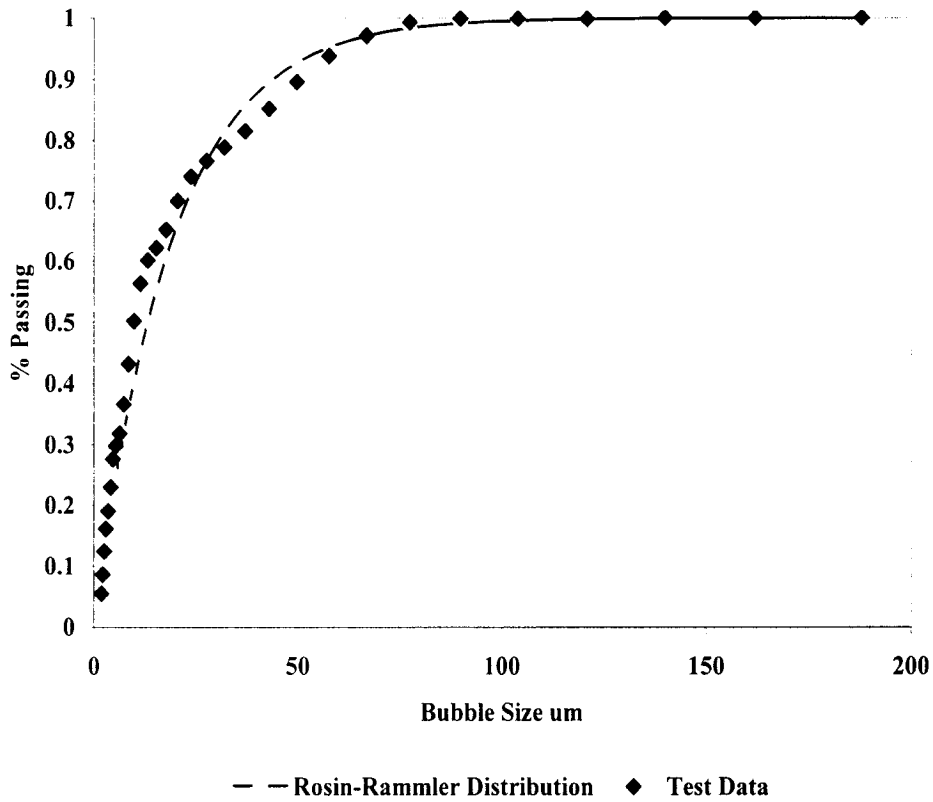

Figure 51: Underflow stream size class data and Rosin-Rammler distribution predicted size distribution.

The difference between the measured values and those predicted by the Rosin-Rammler distribution model; ($y_i - \hat{y}$) are the un-weighted residuals shown here in **Figure 52.**

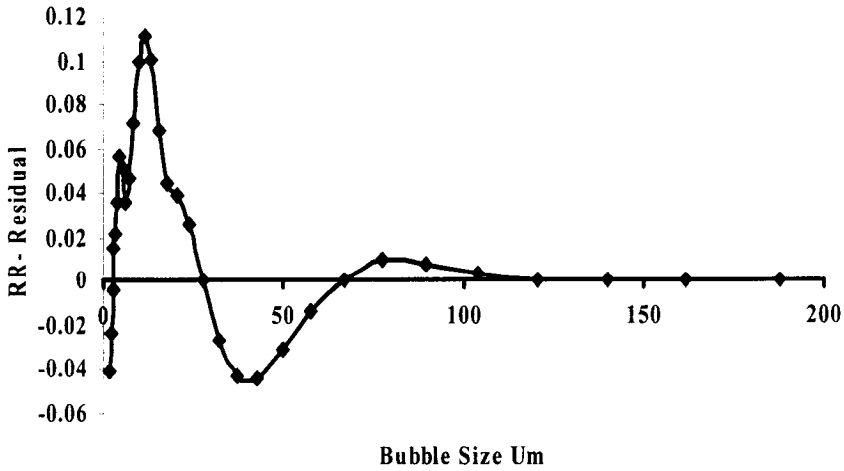

Figure 52: Hydrocyclone underflow stream size class data Rosin-Rammler distribution un-weighted residuals.

The residual data is presented as weighted residuals in **Figure 53**.

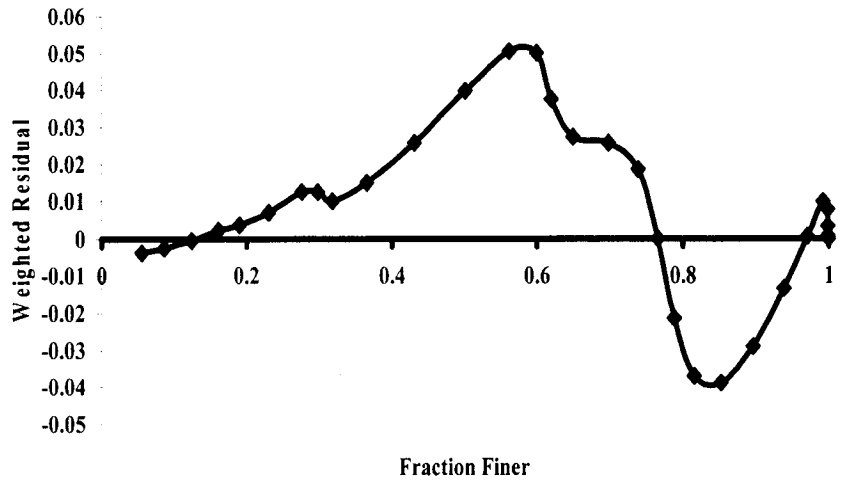

Figure 53: Hydrocyclone underflow stream size class data Rosin-Rammler distribution weighted residuals.

Weibull continuous frequency distribution transforms the variables from nonlinear to linear. Weighted residuals are used as a diagnosis tool that visually indicates the goodness of the fit. In **Figure 53** the goodness of the fitness is ± 0.05%.

5.3.4.2 Linearalization of Bubble Size Distribution (Rosin-Rammler Method)

The Rosin-Rammler regression can be determined by linearizing the nonlinear function by using natural logs (ln). The relevant equation and descriptions explained in the

Equation 137 and **Equation 138**. The results of this regression are detailed in **Appendix P**. When plotted this data produces a straight line as shown in **Figure 54**.

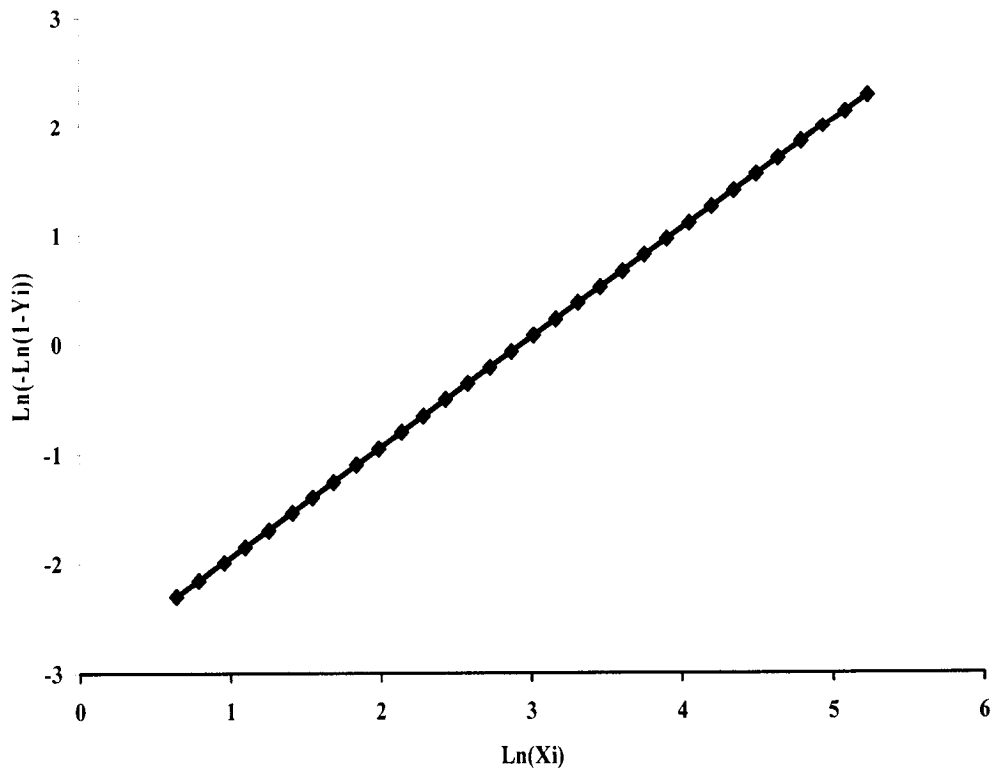

Figure 54: Lineralized plot of under-flow stream data.

5.4 Bubble Volume Distribution.

Bubble volume distribution may change rapidly as a two-phase flow passes through the hydrocyclone and sampling tubes because of breakage and coalescence. A single model or formula could probably not describe the broad variety of the bubble volume distributions observed in this flow. However, it is more useful to use simple bubble volume distributions than to assume that all the bubbles in the stream have the same diameter. In order to improve a better understanding of air-water contact system in an orifice plate type contactor it is useful to measure bubble size distribution and calculate the bubble volume distribution base on the bubble diameters. Bubble volume distribution is a useful tool to study the interfacial volume and surface between the two phases.

5.4.1 Bubble Volume Distribution Calculation

Laser scattering and other particle or bubble size measuring devices produce results based on diameter. Particle or bubble volume distribution is practical when using balances or system gas hold-ups. "d_{50V}" is the diameter for which 50% of the total volume of the sample is composed of larger bubbles and fifty percent is in smaller bubbles.

The conversion of bubble size distribution (BSD) to bubble volume distribution (BVD) assumes that the bubbles have a spherical shape. One method of conversion is that of Nelson, R.D. (2001) who used **Equation 143** through **Equation 145**. The author converted a set of bubble size distribution data – expressed as a series of coordinates (d_i, N_i) -- to bubble volume distribution by computing of the volume of bubbles in each channel (m^3).

$$V_i = f_{(vshape,i)} N_{(i)} \bar{d}_{(i)}^{\,3} \qquad \text{Equation 143}$$

The net volume of the all bubbles counted by the Malvern and the cumulative percent of volume of bubbles smaller than the upper bound of the m^{th} channel can be determined using **Equation 144** and **Equation 145**.

$$V_{p,net} = \sum_{i=1}^{n} N_i V_i \qquad \text{Equation 144}$$

$$P_{cumV,m} = \frac{100\%}{V_{p,net}} \sum_{i=1}^{m} N_i V_i \qquad \text{Equation 145}$$

The experimental data output of the Malvern does not list the diameter of the individual bubbles, but reports the number of bubbles; "N_i", counted in a series of "n" channels with lower diameters; "$d_{low,I}$" and upper diameters; "$d_{up,I}$". In **Equation 143**, "V_i" is a bubble volume in each channel, "$f_{(vshape,i)}$" is a volume shape factor relating particle diameter cubed to particle volume -- "$f_{(vshape,i)}$" is $\pi/6$ for a sphere shaped bubbles and d_i mid,i, is channels mid diameter.

5.4.2 Bubble Volume Distribution Calculation

In order to show a precise relation to either diameter or volume a cumulative bubble volume distribution was calculated, some of the representative results are summarized in **Appendix L**. It has been assumed in these calculations that all bubbles are spherical.

Bubble volume distribution (d_{10V}, d_{50V}, d_{90V}), used for volume balance calculations and bubble size distributions where calculated using the Rosin-Rammler method which is necessary to explain the separation performance of the hydrocyclone. "D_{50V}" is the diameter for which 50% of the total volume sample is in larger bubbles and 50% is in smaller bubbles. Three representative samples of bubble volume distribution are shown in **Figure 55** ; **Figure 56 and Figure 57.**

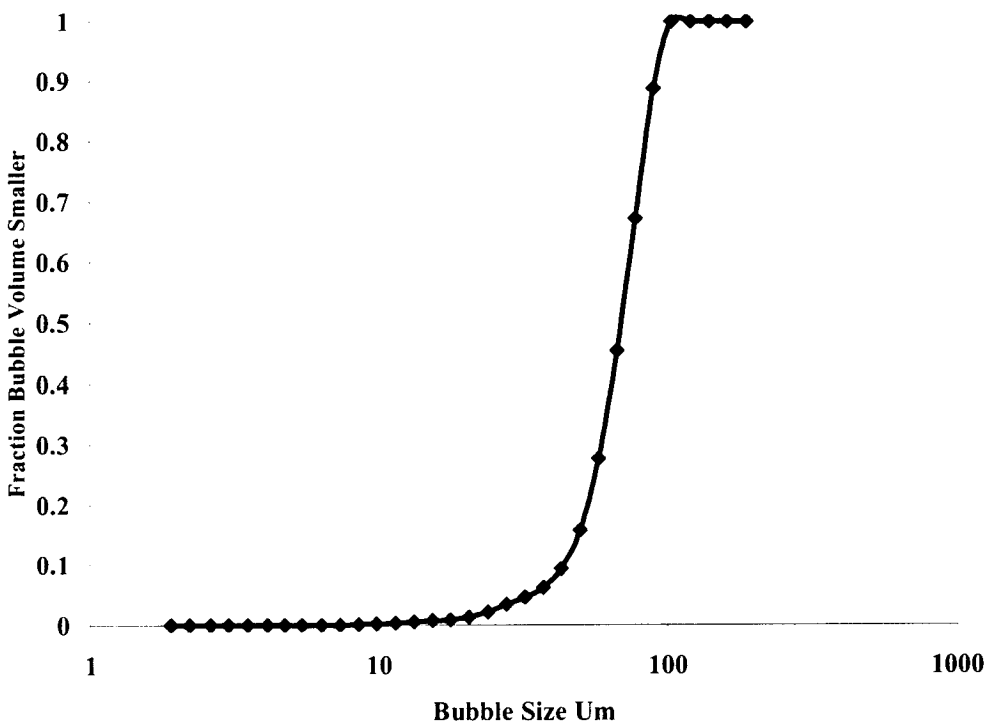

Figure 55: Bubble volume distribution (BVD-23) in underflow stream.

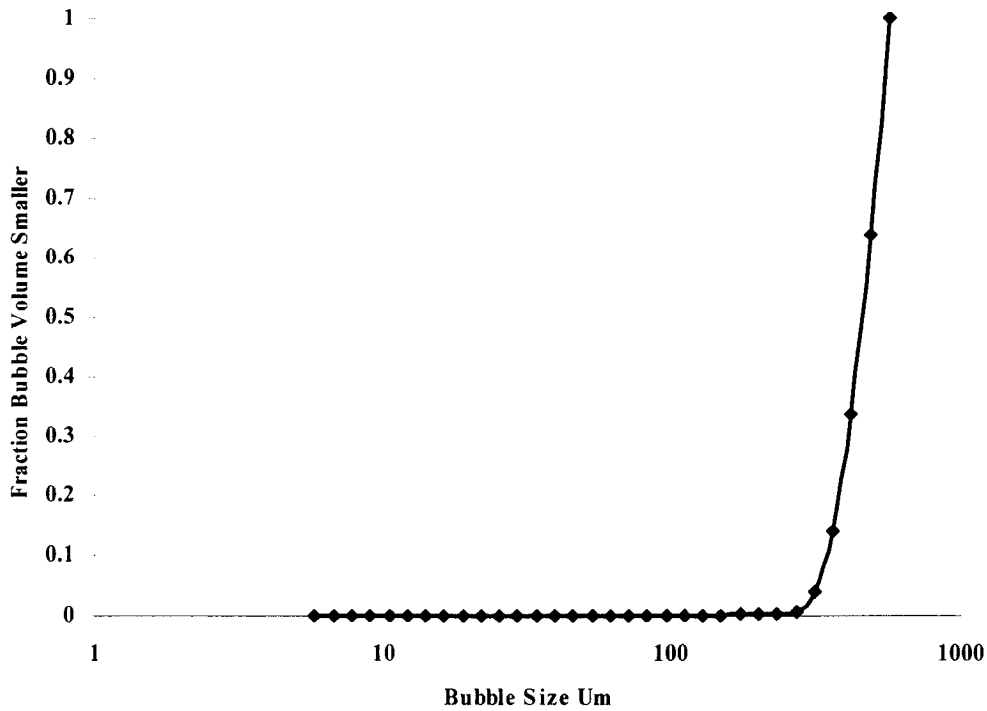

Figure 56: Bubble volume distribution (BVD-37) in overflow stream.

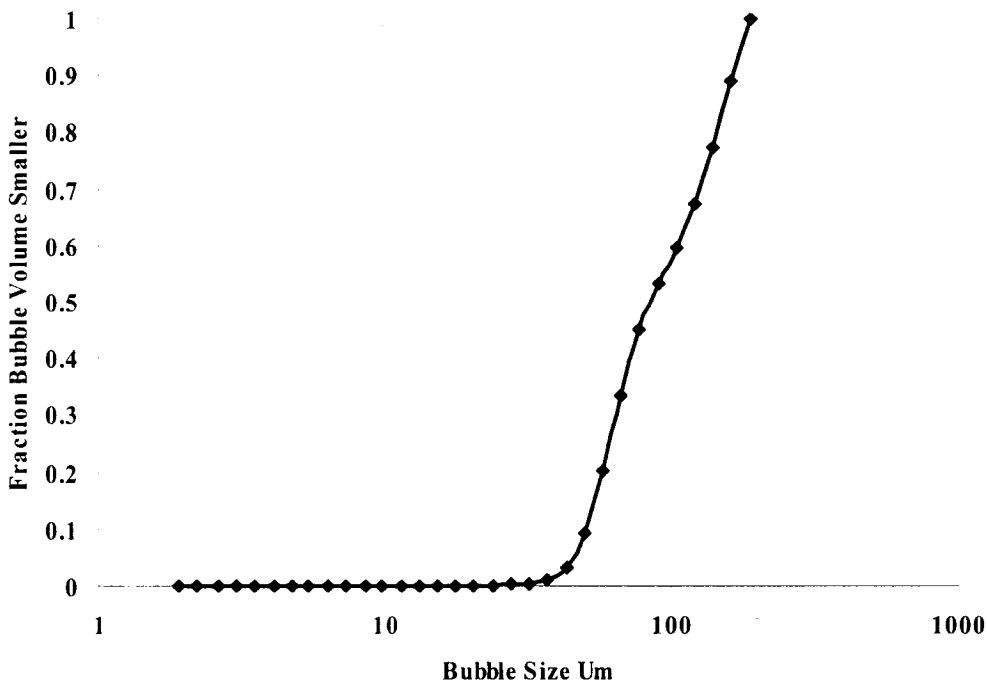

Figure 57: Bubble volume distribution (BVD-48) in turbulent unit stream (cyclone feed).

5.5 Mass Balance Calculations

To get an idea of the separation efficiency across the hydrocyclone, volume balance calculations were conducted. These calculations estimate how much gas can be separated in single stage. In each test the volume of the inlet feed flow as well as the gas volume contents were determined and the gas volume in the overflow stream was calculated by mean of volumetric mass balances. The gas volume in the overflow stream ranged between 0.73-0.99. The relationship between inlet gas volumes to overflow gas volume is shown in **Figure 58**. The operational condition details and volume input is detailed in **Appendix M**.

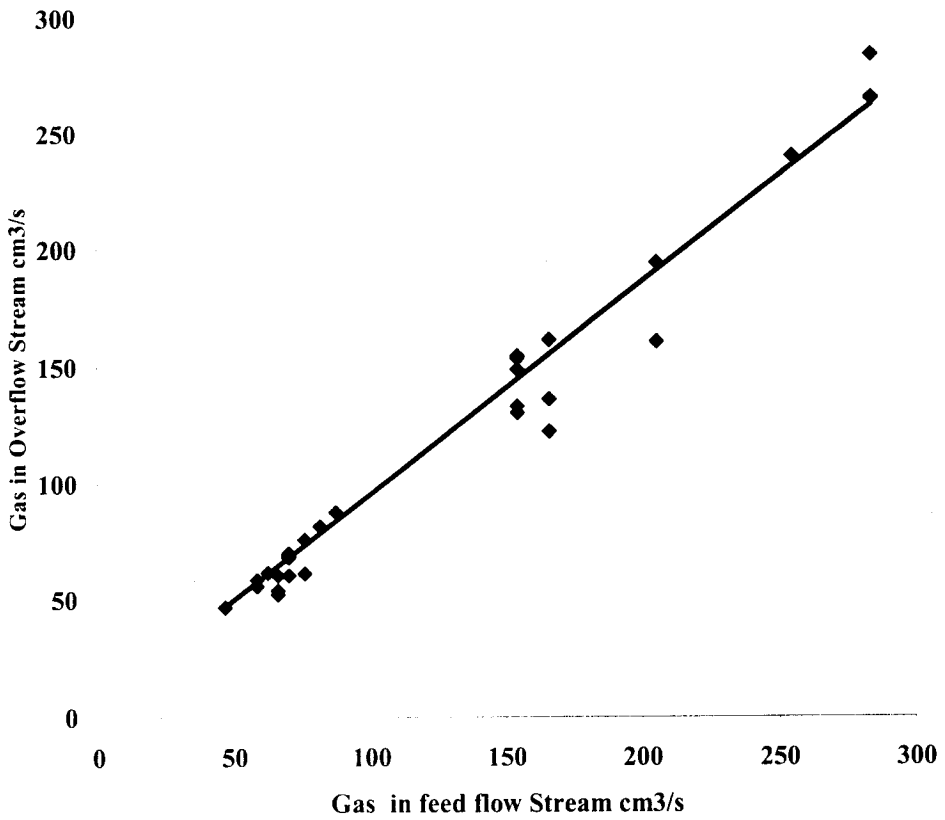

Figure 58: Relationship between feed inlet volumetric gas and gas in overflow stream.

5.6 Separation Efficiency

The models used for prediction of the separation efficiency in the hydrocyclone are shown in **Equation 119** and **Equation 120**. The relationship between separation efficiency and some other variables, including bubble cut-size, are shown in **appendix Q**.

6. DISCUSSION

6.1 Introduction

The purpose of the designed hydrocyclone was to remove low hold-up air from water. In this section, the performance of the air-water hydrocyclone separator is discussed. The effect of pressure drop, bubble size distribution and flow rate on separation performance was investigated. Air separates from water in swirl flow due to centrifugal forces. Centrifugal acceleration depends on the tangential velocity in the hydrocyclone, which in turn depends on the feed inlet flow rate.

Pilot-scale experiments where used to determine the performance of the orifice plate contactor and hydrocyclone in a recycled batch flow system. This data was used to develop an empirical model to predict equipment separation performance.

This thesis defines an empirical model that characterizes hydrocyclone separation efficiency, pressure drop and mean bubble size in the product streams. The parameters generated by these models may be used for geometric design, minimization of energy consumption and to optimize operational parameters.

In this section, modeling of the separation process in a 2.54 cm diameter cylindrical hydrocyclone is discussed. The resulting model and parameters are valid only within the conditions tested. The models are empirical in nature and are an adaptation of current gas-liquid hydrocyclone models. For optimum phase, separation the balance of the two-phase flow to the underflow (K_2) and overflow (K_1) is required $K_2/K_1 \cong 0.9$. Models are presents for the prediction of the test hydrocyclone's cut-size diameter (d_{50}), pressure drop (Δp_x) and separation efficiency (η). This relationship is useful to optimize the operational conditions.

These models used as a starting point in this study are suitable for conventional (cylinder to cone) gas hydrocyclones. The following assumptions are made concerning the hydrocyclone modeling process.

1. The temperature of the two-phase flow is constant (the positive displacement pump increases the temperature of the fluid after a period of time but this effect is neglected).

2. There are no chemical reactions occurs between surfactants and the water phase.

3. Geometrical variables are constant.

6.2 Model Introduction

Empirical bubble cut-size (d_{50}), efficiency (η), overall efficiency and pressure drop models are discussed. In addition, some important cyclone parameters including size distribution and dimensionless numbers are also analyzed. The models developed in this thesis are based on those of W. Barth and E. Muschelknautz. Hydrocyclone behaviour is complex, thus, experimental studies are necessary to understand the separation efficiency in relation to geometry and operational conditions.

6.3 Variables

Hydrocyclone variables can be categorized in three major groups.

1. Dimensional variables
    a. Cyclone diameter (D).
    b. Inlet, outlet and underflow diameters (d_{in}, d_{of}, d_{uf}).
    c. Vortex finder and pedestal diameters (D_x, D_{ped}).

2. Operational Variables
    a. Pressure drop between inlet and underflow stream.
    b. Pressure drop between inlet and overflow stream.
    c. Inlet, reject and underflow stream flow-rates.

3. Feed Stream Variables

a. Feed viscosity (μ).
b. Gas hold-up (ϕ)
c. Bubble size distribution (BSD)
d. Density differences between the phases ($\Delta\rho$).

In this research cyclone dimensions and feed stream variables are assumed to be constant.

Pressure drop is an important variable for evaluation of hydrocyclone separation performance. In air-water and immiscible liquid hydrocyclones, a low-pressure drop is desired as this minimizes power consumption and bubble breakage. The main cause of pressure drop is hydrocyclone wall effects and air-water phase frictions. Pressure drop is related to the tangential velocity.

Separation efficiency, bubble cut-size and pressure drop were experimentally investigated in order to validate the developed models.

6.4 Separation Efficiency Models (η)

Hydrocyclone performance can be analyzed using a efficiency curve (EC). The operational principles of a cylindrical hydrocyclone are different from that of conventional conical hydrocyclones. Thus, a new EC curve is generated for test hydrocyclone.

No phase separation theory of cylindrical hydrocyclones in the literature is capable of a complete or reliable description of hydrocyclone performance. In this research, the least square method is used to determine parameters of a model that predict pressure drop cut-size and separation efficiency.

Overall efficiency is not a good measure of air-water separation since the separation depends on bubble size. The separation efficiency can be described by an efficiency using a efficiency curve (EC) for a certain bubble or droplet cut-size.

6.4.1 Model Description (η)

Hydrocyclone efficiency is modeled by fitting the bubble size distribution and different bubble cut-sizes, including d_{10}, d_{32}, d_{50} and d_{90}, into the model based on those of Muschelknautz and Dirgo-Leith (**Figure 59**).

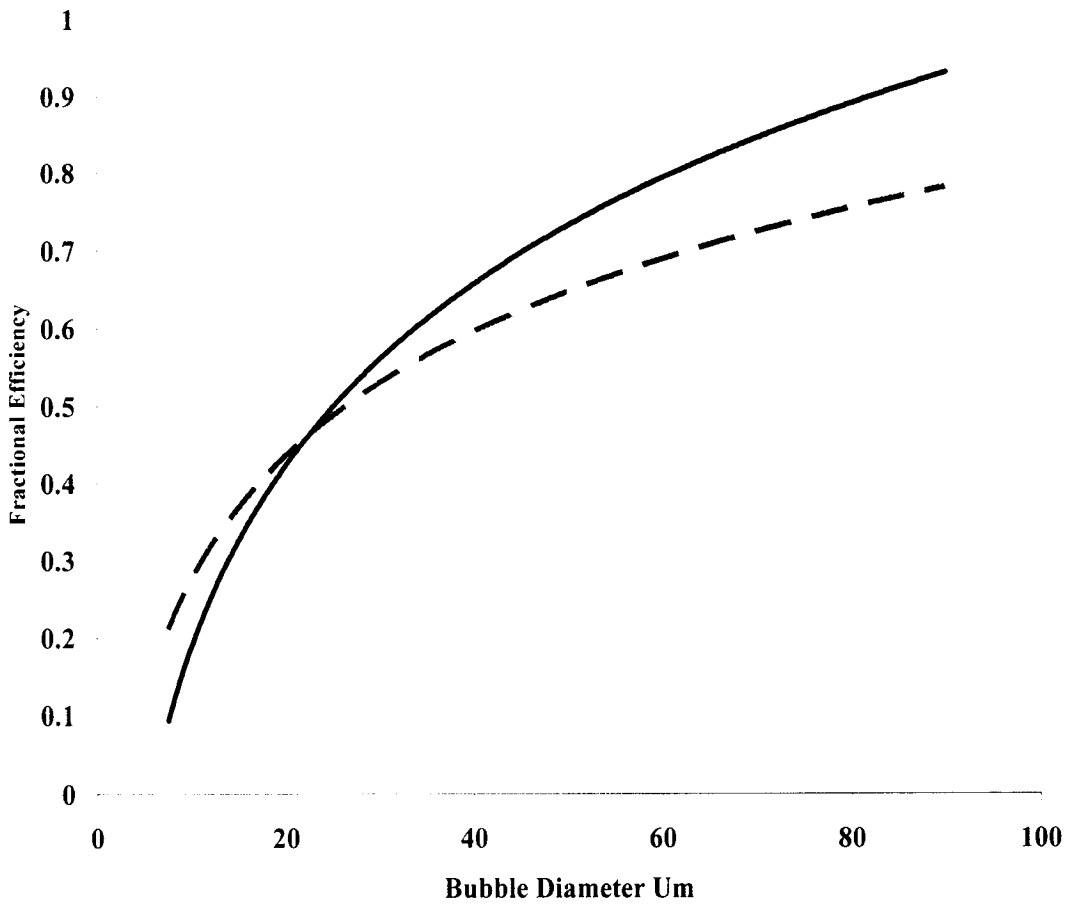

_ _ _ Dirgo et al. efficiency model. ___ Developed efficiency model.

Figure 59: Models predicted average efficiency Curve (EC) for different cut-sizes.

6.4.2 Application of the Model (η)

Separation efficiency of a hydrocyclone can be described by means of the cut-size; "d_{50}". The bubble cut-size, provided by the Malvern is the only parameter can be used to analyze the separation efficiency and separation capability of the hydrocyclone.

The efficiency curve (**Figure 59**) for the hydrocyclone is derived from bubble size analysis. This curve is ideally an S shaped cumulative curve, for solid-water separation, but for air-water or immiscible liquid separation it is different. In this plot, the d_{50} cut-sizes represent a 50% probability of bubbles being separated. This means that bubbles above the cut-size are generally discharged in the underflow stream.

6.4.3 Effect of Feed Bubble Size Distribution on Separation Efficiency.

6.4.3.1 Introduction

The hydrocyclone separation performance is sensitive to the feed bubble size distribution (B.S.D.), thus, a good characterization of this distribution is required. Generally, this distribution is described by different cut-sizes, including d_{10}, d_{32}, d_{50} and d_{90}. Experimentally determined cut-sizes are summarized in **Appendix I** and **Appendix K**.

The experimental data was compared with predicted data. Bubble cut-sizes in the over-flow stream were higher than predicted by the Barth models **(Equation 112)** and **(Figure 61)**. This may be caused by coalescence of the air bubbles in the low-pressure inner core or by the geometry difference with cylinder to cone hydrocyclone (**Figure 60**). The relationship between measured and Barth model predicted d_{50} in underflow streams is shown in **Figure 61**.

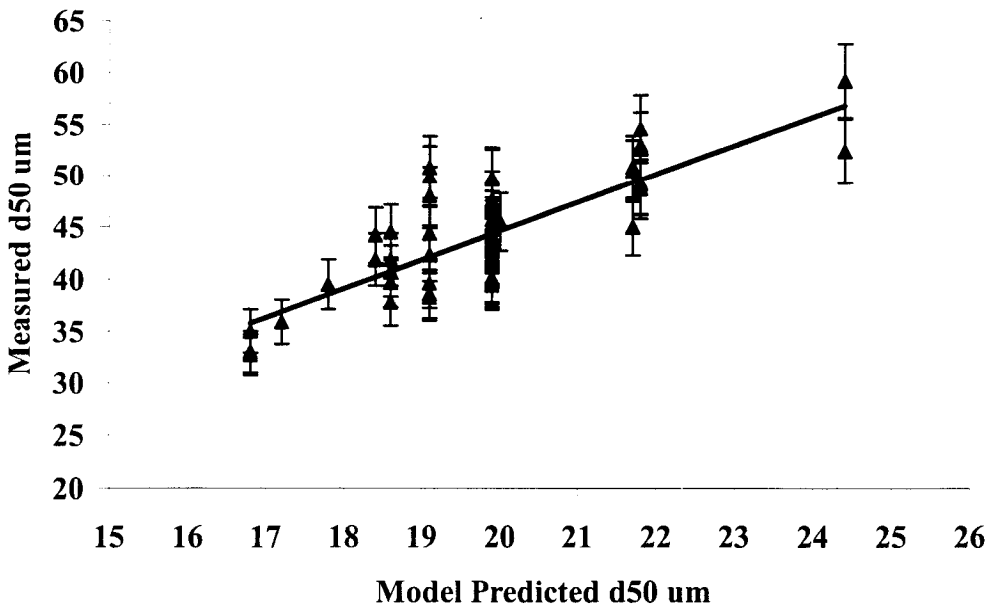

Figure 60: Comparison of the measured and Muschelknautz model predicted d_{50} in underflow stream. Experimental error in measurements is ± 6 %.

The measured mean bubble cut-size (d_{50}) is almost twice the Muschelknautz model predicted mean cut-size. There are probably two reasons for this overestimation:

First, the bubbles have more tendency to break and coalescence than droplets, or flocs. Second, the separation performance may be different due to the geometry difference between the prototype and conventional conical hydrocyclones. In the cylindrical hydrocyclone, bubbles are subjected to more coalescence because of the decay in tangential velocity and swirl flow with cyclone length (L_n).

A similar result is found when using the Barth model **(Equation 112)**. The relationship between measured and Barth model predicted cut-size d_{50} in the underflow streams shown in **Figure 61**.

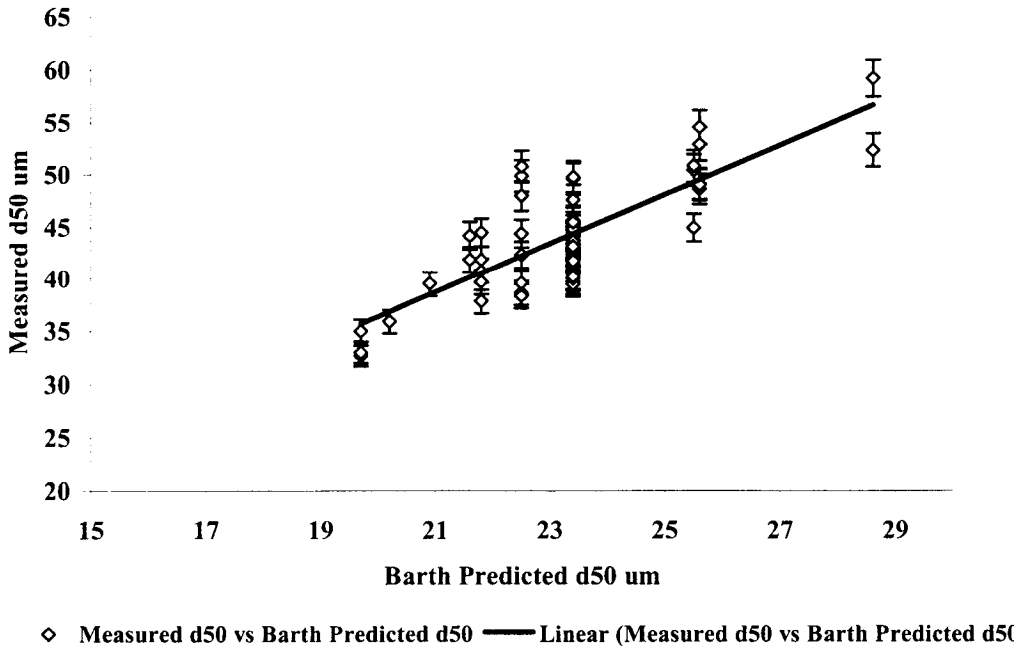

Figure 61: Comparison of a measured and Barth model predicted d_{50}.

Comparison of measured mean bubble cut-size with the Barth model predicted mean cut-size shows that the measured bubble cut-size is almost twice that of the model predicted values.

Bubble coalescence and breakage in a turbulent regime occurs within milliseconds after birth or death of each bubble (Luo, J. J, 2002). Larger bubbles are susceptible to breakage in high shear and high Reynolds number. However, bubble coalescence occurs in the low Reynolds number conditions found in the underflow and overflow streams.

The Muschelknautz and Barth models are more accurate in the prediction of bubble size in under-flow stream than the overflow. This is probably due to the fact that these models were designed for conventional conical hydrocyclones and the flow spin in the lower conical section is higher than cylindrical hydrocyclones. Coalescence in the low-pressure inner core is significant; however fine bubbles in the lower part of the hydrocyclone may not get a chance to reach to the central inner core.

6.4.3.2 Bubble Size Effect

The hydrocyclone collection efficiency, "η", is defined as the fraction of bubbles of a given size that are removed by the hydrocyclone from the under-flow stream. The current separation efficiency theories have been developed based on the operating parameters of the separation system including particle, droplet and bubble diameters, density and velocity.

Efficiency models were developed based on Muschelknautz and Dirgo-Leith approaches, (**Equation 119** and **Equation 120).** Measured bubble size distribution data was used to develop these models (**Appendix W**). The separation efficiency curves (SEC) for d_{10}, d_{32} and d_{90} sizes, are plotted in (**Figure 59**). Figure 59 show that efficiency increases with increasing the bubble size.

6.4.4 Efficiency parameters of the hydrocyclone.

6.4.4.1 Introduction

Dimensionless numbers are used to characterize conditions within the cyclone. These numbers may be used to give indications of performance. Stokes number gives an indication of actions within the hydrocyclone. Euler number is a dimensionless that indicates pressure drop and hydrocyclone performance. Selection of a hydrocyclone is dependent on the pressure drop. Even if the hydrocyclone has a high efficiency it may not be chosen if the pressure drop and power consumption are too high.

6.4.4.2 Correlation between Stokes' and Reynolds number

The correlation between Stokes' and Reynolds' numbers should be analyzed in order to examine the role of feed flow rate in hydrocyclone efficiency, to explain the influence of the cyclone body on bubble movement and to study the interaction between bubbles and liquids. Reynolds number indicates the turbulent decay and stokes number may be used as hydrocyclone scale-up criterion. Reynolds' and Stokes' numbers are measured using **Equation 21** and **Equation 22**. The adapted Barth and Muschelknautz models predictions of Stokes' number and Reynolds' number are plotted in **Figure 62, Figure 63**

and **Figure 64**. A linear regression was performed and the results show a good agreement with the modified Barth and Muschelknautz models. This correlation shows the relationship between the Stokes' and Reynolds numbers -- Stokes' number increases with increasing Reynolds number. $Stks_{50}$ is calculated using **Equation 131**.

In this study, correlation between Reynolds number and Stokes' number is based on the experimental data. This data agrees well with the model predictions. However, predicted Stokes' number is lower than the measured values. Experimental Stokes' number ranged from 0.0 to 0.9.

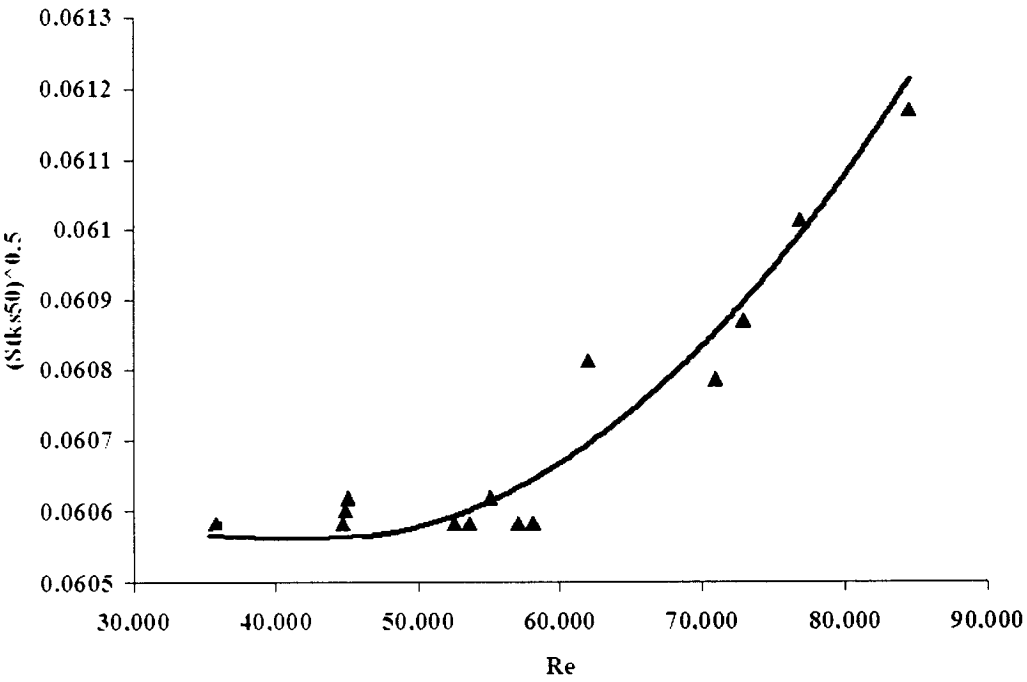

Figure 62: Correlation between Reynolds and Stokes' number based on Barth model.

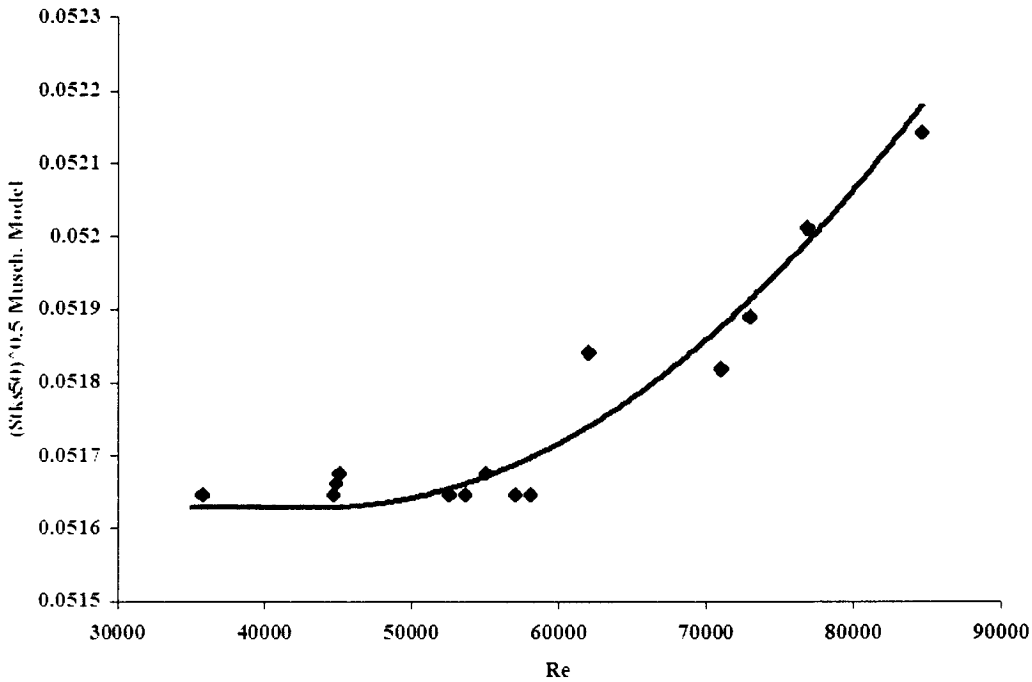

Figure 63: Correlation between Reynolds and Stokes' number based on the Muschelknautz model.

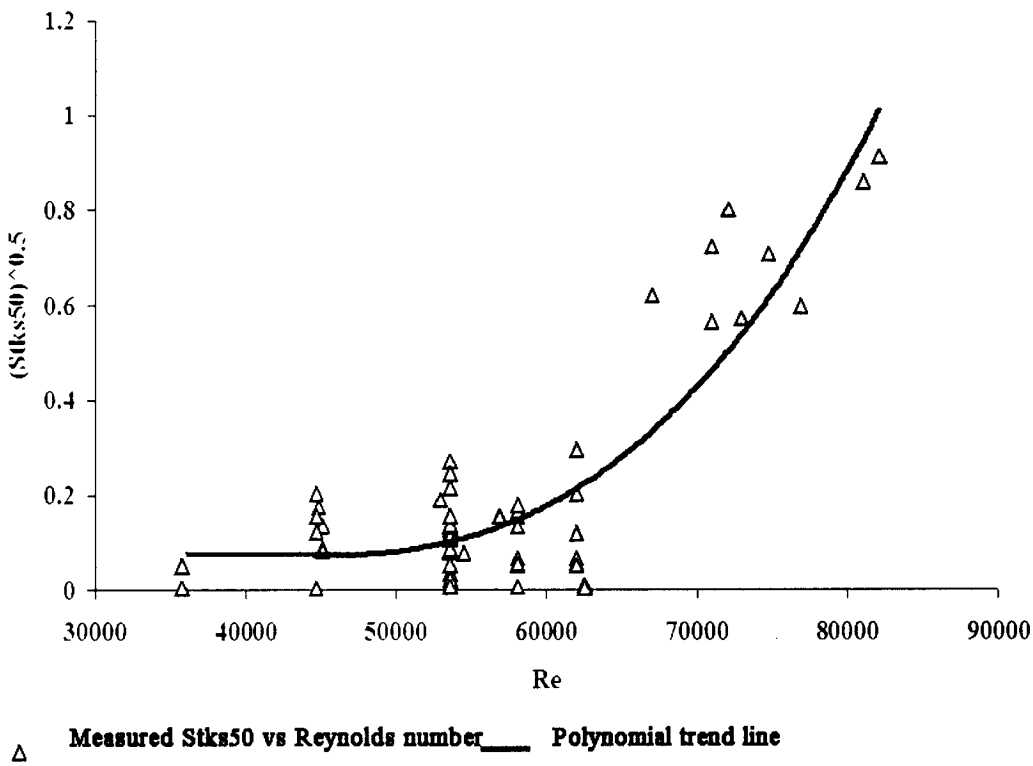

Figure 64: Correlation between Reynolds and Stokes' number based on experimental data.

Comparison of the $Stks_{50}$ and Reynolds number calculated based on experimental data shows that $Stks_{50}$ is correlated with Reynolds number in a gas-liquid cylindrical separator when this Reynolds number is larger than 60,000. There was no dependency between $Stks_{50}$ and Reynolds number (**Figure 63** and **Figure 64**).

6.4.4.3 Correlation between Euler and Reynolds Numbers

The dimensionless Euler number and Reynolds number, which are factors for pressure drop and flow regime, were correlated (**Figure 65**) using two adapted Euler number models using conditions in the vortex finder. It was predicted that highly turbulent flow, Re > 50,000, increases the pressure drop across the hydrocyclone and in that low turbulent flow, Euler number is weakly correlated with Reynolds number.

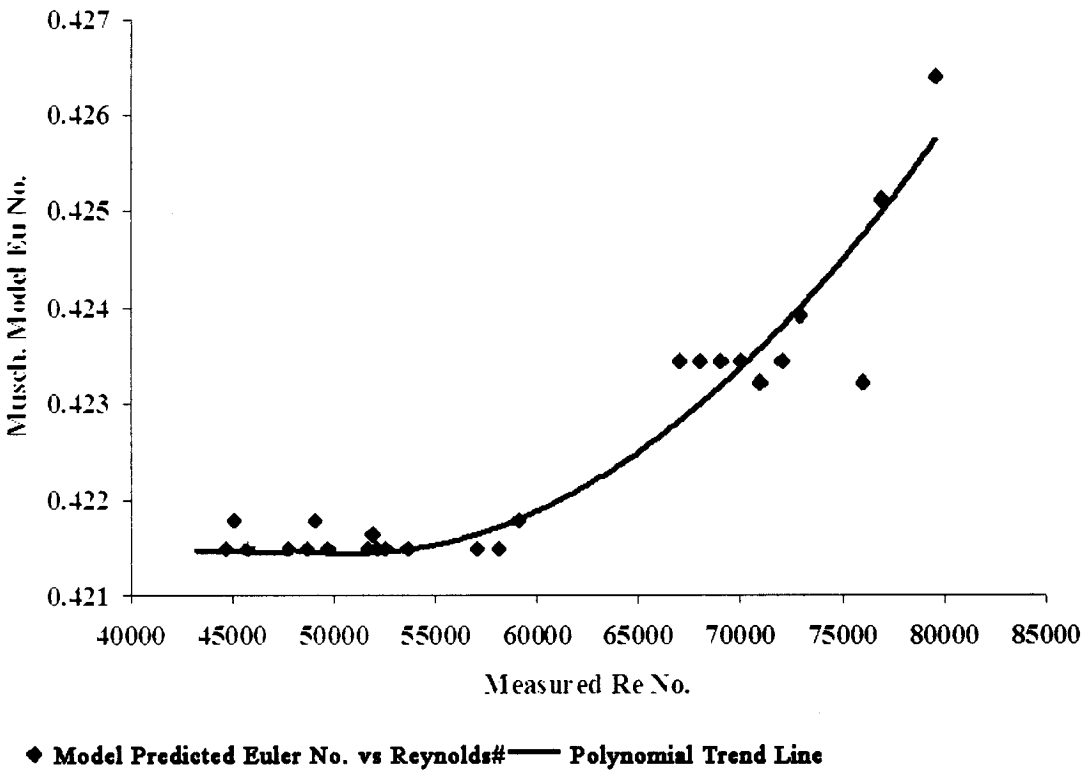

Figure 65: Relationship between Reynolds and Euler numbers.

6.5 Pressure Drop Models (Δpx)

6.5.1 Introduction

Pressure drop occurs in three zones; within the inlet, the body and vortex finder. The swirling flow inside the hydrocyclone body is too complicated to completely describe mathematically. The developed model estimates the total pressure loss in the vortex finder. The loss in the inlet zone is small and Euler number in inlet area is less than 1.3 (**Appendix EE**).

A large pressure drop was found to occur in the vortex finder. The pressure drop across the vortex finder (Δp_x) was found to be about 70% of total pressure drop. This is caused by the friction between the two phases and the surface of the vortex finder. When the air phase moves toward the inner core, from the wall, it is accelerated and its pressure decreases while the pressure increases in the vortex finder. Pressure is highest at the wall of the separation device.

The pressure drop across the vortex finder is proportional to hydrocyclone inlet flow rate.

Pressure measurements in the inlet and wall area are more accurate because there is less swirl motion. However, in inner vortex zone swirl motion is dominant, thus, pressure in the overflow stream is more dynamic and measurements using surface pressure gauges may be inaccurate. In other words, pressure drop measurement in the upper flow stream is complicated by the high swirl motion.

The Euler number is a good indication of pressure drop. Calculation of Euler number in different areas of the hydrocyclone is shown in **Appendix EE**.

The inlet flow velocities of the tested hydrocyclone were between 8-12 m/s, which resulted in tangential velocities in the vortex finder between 4.5 and 8 m/s, (**Appendix T**). Under these conditions, pressure can be expected to be approximately $0.5\rho v_\theta^2$ Pa.

The model developed estimates the pressure drop across the vortex finder. K is an empirical value that for air-water separation within a hydrocyclone. In **Equation 146**, it is shown as the value four. Barth, W (1956) found this value, empirically, to be between 3.41-4.4 for vortex finders with rounded and sharp edges.

$$\Delta p_x = \frac{1}{2}\rho v_x^2 \left(\left(\frac{v_{\theta CS}}{v_x} \right)^{2.35} + 4 \left(\frac{v_{\theta CS}}{v_x} \right)^{\frac{4}{3}} \right) \qquad \text{Equation 146}$$

The Muschelknautz (1980) model, for estimation of pressure drop over a hydrocyclone inner core with a tangential inlet flow, is shown in **Equation 147**.

$$\Delta p_x = \frac{1}{2}\rho v_x^2 \left(2 + \left(\frac{v_{\theta CS}}{v_x} \right)^{2} + 3 \left(\frac{v_{\theta CS}}{v_x} \right)^{\frac{4}{3}} \right) \qquad \text{Equation 147}$$

The model developed in this study for the air-water cylindrical hydrocyclone is shown in **Equation 148**.

$$\Delta p_x = \frac{1}{2}\rho v_x^2 \left(5 + \left(\frac{v_{\theta CS}}{v_x} \right)^{2.42} + 3 \left(\frac{v_{\theta CS}}{v_x} \right)^{\frac{4}{3}} \right) \qquad \text{Equation 148}$$

A comparison of the inner core pressure drop with body pressure drop shows that about 70% of the overall pressure loss is occurs across the inner core.

6.5.2 Model Structure (Δpx)

Pressure drop is a function of the dynamic pressure ($0.5\rho v_x^2$), inner core tangential velocity ($v_{\theta CS}$) and velocity of the fluid in vortex finder (v_{ex}).

6.5.3 Application of the Model (ΔP_x)

Pressure drop across the vortex finder model is determined by minimizing the difference between the model response and the experimental data using least squares. This model uses the dynamic pressure and inner core tangential velocity along with the response predicted by **Equation 146** and **Equation 148**.

6.5.4 Model validation (Δp_x)

Previous work indicates that the pressure drop across the hydrocyclone increases with increasing flow rate **(Jiang, M, 1998)**. The measured pressure drop data and model predicted pressure drops across the hydrocyclone inlet, body and vortex finder are summarized in the **Figure 66**. The Barth model predicted pressure drop data is about two times larger then Muschelknautz model predicted data (**Figure 66**).

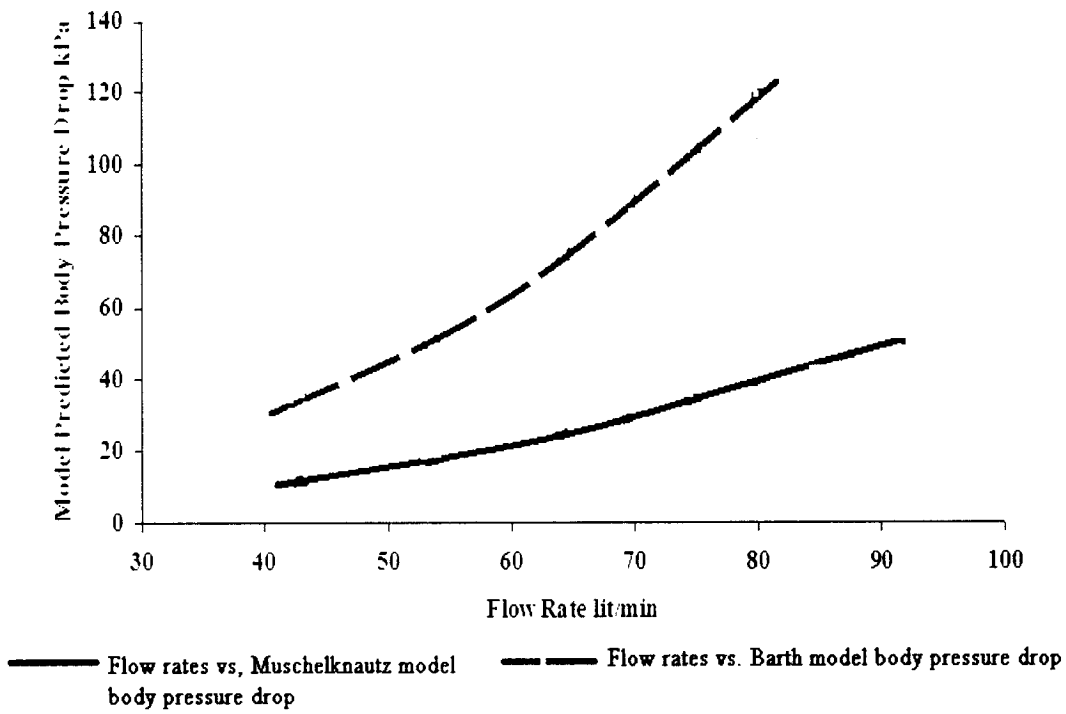

Figure 66: Inlet flow rates vs. model predicted body pressure drop.

The predicted values of the Muschelknautz model **(Figure 67)** are similar to the experimental data (**Figure 67**). According to the measured and predicted pressure drop values, pressure drop across the inlet is small and across the body of the hydrocyclone is

moderate. However, pressure drop in the inner core (vortex finder) is larger than inlet and hydrocyclone body pressure drop. Barth model can be used to predict pressure drop in the hydrocyclone but the values are higher than measured values.

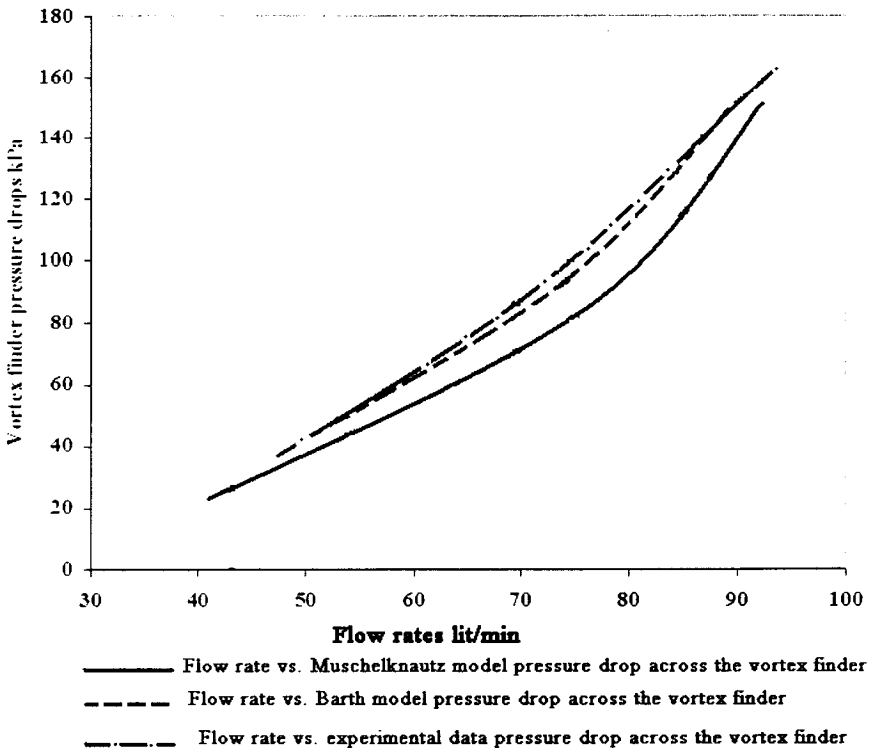

Figure 67: Comparison between measured and models predicted pressure drop across the vortex finder.

6.5.5 Pressure Drop Ratio (PDR = C)

Jiang, M., et al. (1998) state that pressure drop ratio (PDR) is an important performance parameter in air-water and immiscible liquid hydrocyclone separations. It is defined as the ratio between feed to overflow pressure drops and the feed to underflow pressure drop **(Equation 149).**

$$PDR = \frac{\Delta P_o}{\Delta P_u} = \frac{P_{inlet} - P_{overflow}}{P_{inlet} - P_{underflow}} \qquad \text{Equation 149}$$

The effect of the operating condition changes on the cyclone are monitored by tracking "C". The pressure difference between the inlet and underflow streams is used as an indicator of power consumption during operation.

The linear relationship between inlet flow rate and pressure drop ratio; "C", is shown in **Figure 68.** The linear regression for the data is shown in **Equation 150.** The regression slope of 0.0035 indicates that the pressure drop ratio should remain approximately constant with variation in volumetric feed flow. This regression is valid with the flow rate range of 700-1600 ml/s for the cyclone tested.

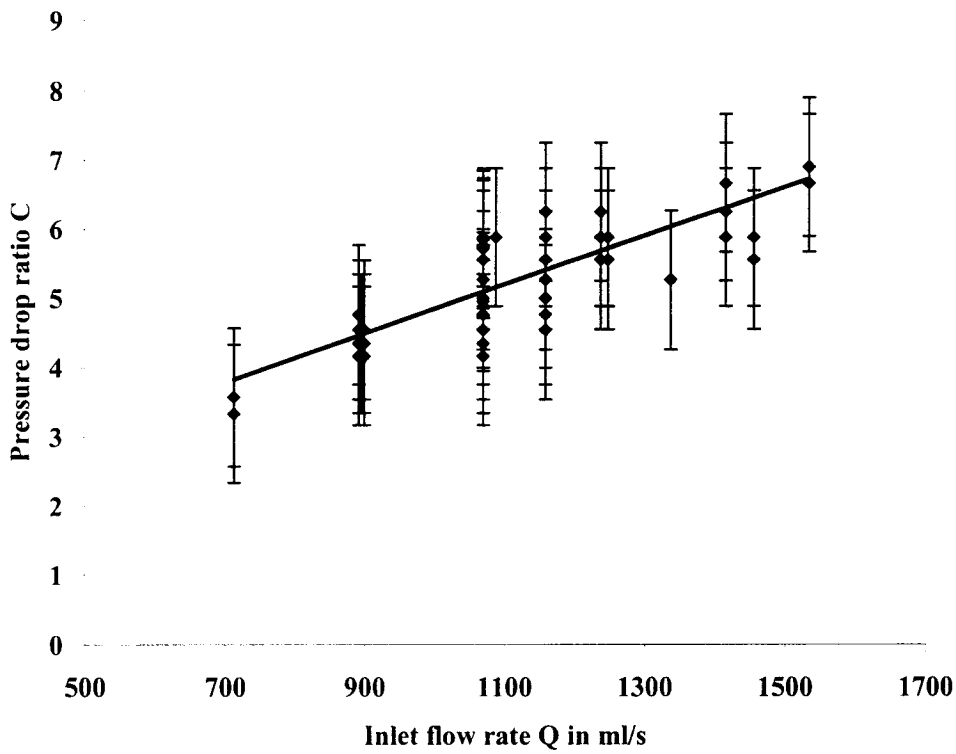

Figure 68: Relationship between inlet flow rate Q_{in} and pressure drop ratio C.

$$C = 0.0035Q_{in} + 1.317 \qquad \text{Equation 150}$$

Standard error in this correlation is about ± 10% (**Equation 150**). This model can be used for optimize operational conditions of the test hydrocyclone.

6.5.6 Relationship between pressure ratio and split ratio

Split ratio is defined as the ratio of over-flow to inlet volumetric flow rate **(Equation 7).** The relationship between pressure drop and split ratio is important for hydrocyclone operation. The correlation between the split-ratio and pressure drop ratio is shown in **Figure 69** and **Equation 151**. In these experiments the overflow stream flow was kept constant ($Q_{overflow}$ = 0.1 Q_{feed}). The trend-line shows that pressure drop ratio increases with an increase in split ratio. Therefore, the pressure of the overflows stream drops. This plays an adverse effect on phase disengagement. The supportive data is shown in **Table 9**.

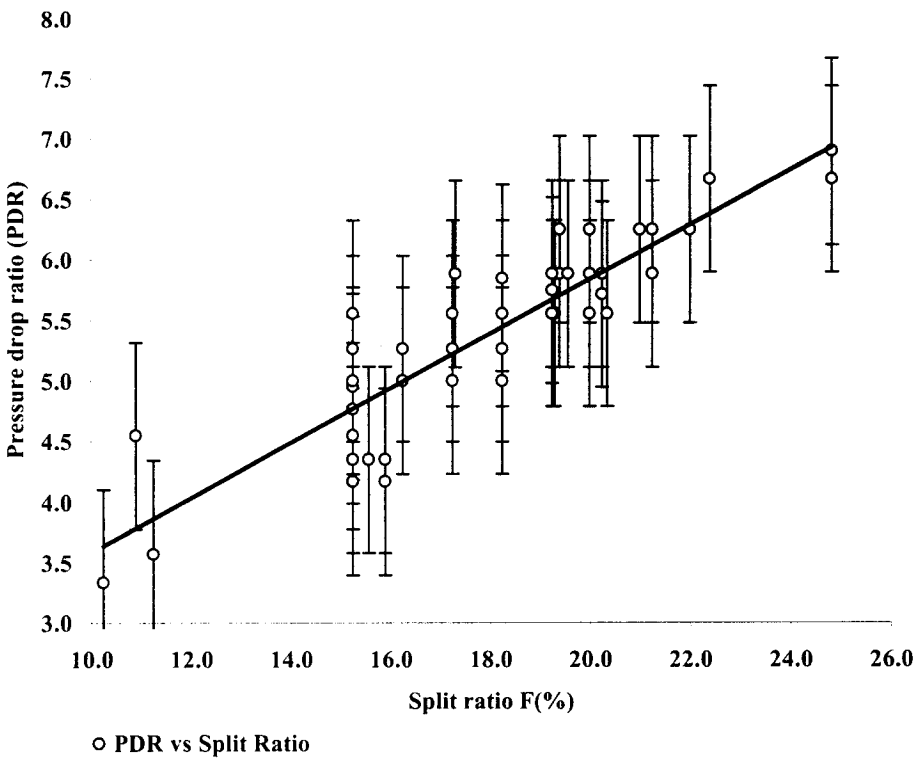

Figure 69: Linear relationship between split ratio and pressure drop ratio.

$$C = 0.2257F + 1.3266 \qquad \text{Equation 151}$$

Table 9: Split Ratio and Pressure Drop Data.

Split Ratio (F)	Measured Δp Ratio (PDR)	Split Ratio (F)	Measured Δp Ratio (PDR)
20.34	5.56	19.99	6.25
15.23	5.26	15.89	4.35
15.23	5.00	15.89	4.17
15.23	4.76	15.23	4.55
15.23	4.55	15.23	4.76
15.23	4.35	15.56	4.35
15.23	4.17	22.39	6.67
15.23	4.35	19.39	6.25
15.23	4.17	19.39	5.88
15.23	5.56	24.82	6.67
15.23	4.76	24.82	6.67
17.23	5.56	24.82	6.90
15.23	4.76	15.23	4.17
15.23	4.55	17.30	5.88
16.23	5.26	19.30	5.56
20.23	5.88	17.23	5.26
15.23	5.26	15.23	4.76
16.23	5.00	15.23	5.00
15.23	4.95	15.23	4.55
17.23	5.00	15.23	5.26
18.23	5.00	18.23	5.56
18.23	5.26	19.23	5.88
15.23	5.26	19.23	5.56
15.23	5.00	15.23	4.35
15.23	4.76	21.23	5.88
20.23	5.88	20.23	5.71
19.23	5.88	19.23	5.75
21.23	6.25	18.23	5.85
19.99	5.88	15.23	5.26
20.99	6.25	15.23	4.76
21.99	6.25	15.23	4.55
21.99	6.25	11.23	3.57
19.99	5.88	10.23	3.33
19.99	5.88	19.56	5.88
19.99	5.88	10.89	4.55
19.99	5.56		

6.5.7 Pressure drop across the vortex finder

Pressure drop across the hydrocyclone occurs in the three different areas, at the inlet, the cyclone body and the vortex finder. The pressure drop across the body of the hydrocyclone is caused by the reduction of dynamic pressure due to the friction (Hoffman, 2002). In air-water dispersions, the body pressure drop is less than that found in solid-water dispersion applications. The main pressure loss usually occurs in the vortex finder (Hoffman, 2002).

6.5.7.1 Muschelknautz and Barth models

Pressure drop in the vortex finder region is significant (Hoffman, 2002). Both the Muschelknautz and Barth models **(Equation 124** and **Equation 125)** predict pressure drop across the hydrocyclone "Δp_x". These predicted pressure drops, compared to inlet flow rate, are shown in **Figure 70**.

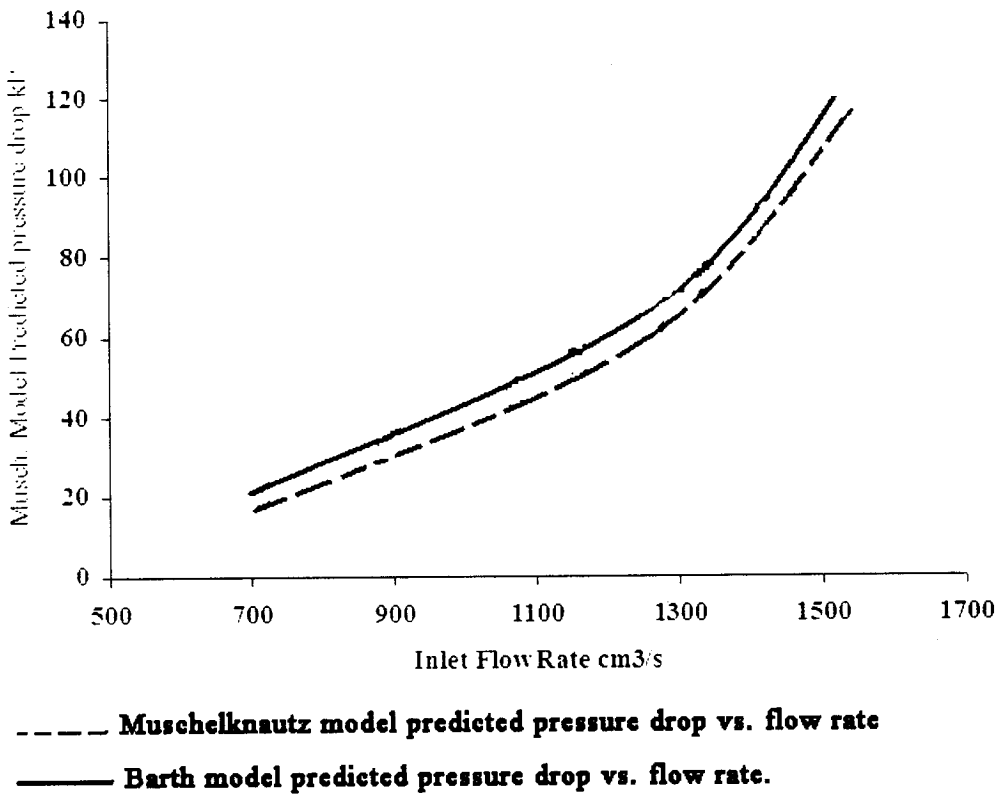

Figure 70: Correlation of vortex finder pressure drop vs. inlet flow rate (Muschelknautz, 1980 and Barth models, 1956).

Barth model predicts the pressure drop a little bit higher than Muschelknautz model predicted pressure drop (**Figure 70**).

6.5.7.2 Relationship between calculated Euler number and measured pressure drop across the vortex finder

Water pressure and its physical and chemical properties are assumed constant during the separation operation; thus, the turbulent condition and Reynolds number can be considered a function of the feed flow rate. The dimensionless Euler number (Equation 23) was investigated to see if it could be used to characterize the effect of pressure drop on hydrocyclone separation performance. This relationship is plotted as **Figure 71** and the linear trend line is shown as **Equation 152**.

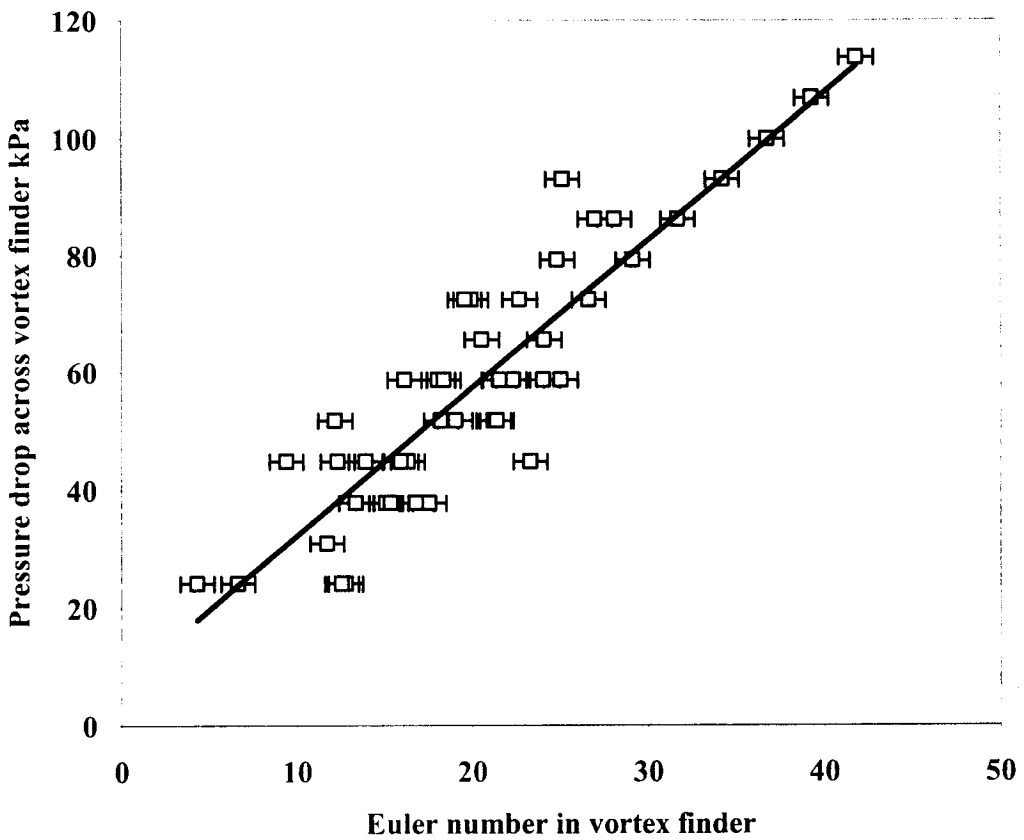

Figure 71: Relationship between calculated Euler number and measured pressure drop.

$$\Delta p_x = 2.516 Eu_x + 7.0867 \qquad \text{Equation 152}$$

6.5.7.3 Inlet pressure Drop

The relationship between the Muschelknautz model predicted inlet pressure drop and body pressure drop is plotted in **Figure 72.** This relationship shows that the pressure drop in the body of hydrocyclone is more important than the inlet area. The relationship between the inlet and body Euler numbers is shown in **Equation 153**.

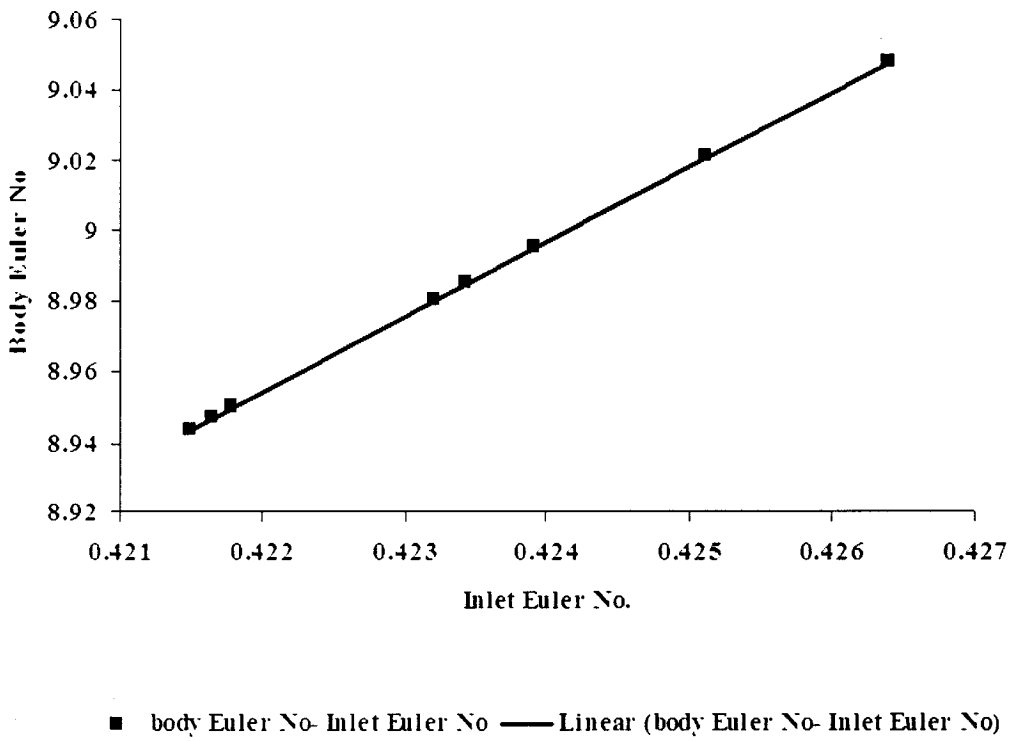

Figure 72: Comparison between Musch Predicted inlet Euler No. vs. Body Euler No.

$$Eu_{body} = 21.219 Eu_{in} + 3\times10^{-5} \qquad \text{Equation 153}$$

The implication of **Equation 153** is that the Euler number in cyclone body is about 21 times larger than cyclone body Euler number. Thus, the pressure drop in inlet area is low and can be minimized with a good design and a very low friction lining.

6.6 Flow Velocity in Hydrocyclone

Both the pressure drop and cut-size models used flow as a variable. Thus, characterization of flows in the cyclone are important.

6.6.1 Inlet Velocity (v_{in})

High inlet flow velocity creates sufficient centrifugal action to generate separation. The feed inlet velocity is calculated using the volumetric flow rate and cross section of the tangential inlet as shown in **Equation 154**. Inlet velocities (v_{in}) ranging from 6.5 to 13 m/s were tested in this hydrocyclone

$$v_{in} = \frac{Q}{A_{in}} = \frac{Q}{ab} \qquad \text{Equation 154}$$

In **Equation 154** Q is inlet velocity and A_{in} is inlet area of the hydrocyclone.

6.6.2 Characteristic Velocity (v)

The characteristic flow velocity across the hydrocyclone is calculated using $v = 4Q/\pi D_c^2$. Tested values ranged from 1.4 - 3 m/s.

6.6.3 Radial Velocity (v_{rCS})

The radial velocities can be predicted using the Muschelknautz, (1980) model (**Equation 113**). Using this method, the wall axial velocity ranged from 0.19 to 0.32 m/s.

6.6.4 Axial Velocity (v_z)

Streams in the body of the hydrocyclone have a low axial velocity outside the inner core **(Equation 122)**.

6.6.5 Wall Axial Velocity (v_{zw})

Wall axial velocities in this hydrocyclone can be predicted using **Equation 107**. Predicted wall axial velocities ranged from 3.6 to 5.2 m/s.

6.6.6 Wall Tangential Velocity ($v_{\theta w}$)

Wall velocities can be predicted using **Equation 109.** Predicted wall velocities ranged from 3.5 to 7 m/s.

6.6.7 Flow Velocity in Vortex Finder (v_x)

Flow velocity in the vortex finder is calculated using overflow rate and overflow orifice diameters and ranged from 1-3.4 m/s.

7 PROPOSED MODELS

The proposed model has been developed in order to improve predict the performance of a small diameter cylindrical hydrocyclone performing air-water separation. These relationships predict cut-size, pressure drop and efficiency. A supporting Java software program was developed to run these models (**Appendix V**).

7.1 Cut-size (d_{50}) prediction models

7.1.1 Introduction

The purpose of these models is to predict bubble cut-size for both the underflow and overflow streams of the prototype cylindrical hydrocyclone. Mean cut-size is an important parameter determining the hydrocyclone efficiency curve (Hoffman, A. C., and Stein, E. L, 2002). The cut-size models are based on Stokes' law and settling velocity.

7.1.2 Developed d_{50} Models

This model uses tangential velocity at the surface CS ($v_{\theta CS}$) (**Figure 35**), radial gas velocity at the surface CS, viscosity; "μ" and flow rate; "Q". The Muscshelknautz (1980) model makes the following assumptions that make it unsuitable for modelling of cylindrical hydrocyclones:

1. Assumes that no separation occurs within the cylindrical section. This can be seen by the H-S term in the denominator of this model.
2. Assumes that "k" has a value of 0.9. This number represents the fraction of feed volume that passes into the vortex finder. This value may vary from this value.
3. Groups the entrance radius, instantaneous and exit radius into a proportionality constant that is empirically determined.
4. Assumes a dilute suspension and that no hindered settling occurs. Larger concentrations will cause hindered settling that can be accounted for by the empirical constant but this restricts the usefulness of the model.

This model is based on the residence time model of Muschelknautz (Muschelknautz, E, 1980) where bubbles are assumed to start at some point near the cyclone outside radius and move inward to an imaginary boundary. Thus, those bubbles that pass that boundary flow through the vortex finder. A further assumption is made that Stokes equations of settling are valid. With this assumption, **Equation 155** can be used to predict bubble velocity.

$$u_b = \frac{g d_b^2 \Delta\rho \varepsilon_l^{2.7}}{18\mu} \qquad \text{Equation 155}$$

Bubbles occur at radius r_i (cyclone) where $r_{i,0}$ is their initial radius and $r_{i,1}$ is their final radius all at t_i. These radii are unknown. All bubbles that progress past the imaginary boundary at r_o report through the vortex finder. All those at r_o report half to the vortex finder and half to the apex. Thus, those bubbles that exactly traverse r_c to r_o in time t form the d_{50} cut-size. In the real system, bubbles have a range of $r_{i,o}$ values.

The residence time of a bubble; "t_i", is determined by the volumetric flow passing through a cross-sectional area. This is not an exact time since some of the water, and bubbles, pass more quickly into the vortex finder than others. Also, bubbles pass into the core at varying heights. Thus, a proportionality constant must be included in the relationship as shown in **Equation 156**.

$$t_i = k_1 \frac{\pi r_c^2 h}{Q} \qquad \text{Equation 156}$$

The distance travelled by a bubble is "$u_b t_i$". Thus, the position in the cyclone of a bubble can be estimated by **Equation 157**.

$$r_{i,o} - r_{i,1} = \frac{v_i^2}{r_i} \frac{d_b^2 \Delta\rho \varepsilon_l^{2.7}}{18\mu} \frac{\pi r_c^2 h}{Q} \qquad \text{Equation 157}$$

In **Equation 157** u_b has been replaced using Equation 155 and t_i by using **Equation 156**. The "g" term in Equation 155 has been replaced with centrifugal acceleration. A further assumption is made that v_i is proportional to v_c and can be represented by v_c and a proportionality constant. Finally, r_i and r_c, which are unknown, are grouped with $r_{i,o}$ and $r_{i,1}$, both also unknown, and all other proportionality constants to form an empirically determined constant. With these assumptions, **Equation 157** reduces to **Equation 158**.

$$k = \frac{v_c^2 d_b^2 \Delta\rho \varepsilon_l^{2.7}}{18\mu} \frac{\pi r_c^2 h}{Q} \qquad \text{Equation 158}$$

Isolating for d_b in **Equation 157**, incorporating all constants into k, and assuming a dilute concentration of bubbles gives **Equation 159**.

$$d_b = k\sqrt{\frac{\mu Q}{\Delta\rho v_c^2 h}} \qquad \text{Equation 159}$$

Equation 159 is similar to the Barth relationship **(Equation 112)** without the restrictions. The value of "k" is still empirical in nature. The Q value in **Equation 159** is that reporting to the underflow only.

The "k" value of this model was determined to be 1.755 for the cylindrical hydrocyclone separating bubbles from water and predicting the underflow d_{50} **(Equation 160)**.

In **Equation 160,** μ is viscosity, Q is flowrate, Δp is density differences, $v_{\theta CS}$ is inner core tangential velocity and h is hydrocyclone height. The measured and model predicted mean cut-size (d_{50}) is shown in **Figure 73**.

$$d_{50underflow} = 1.755\sqrt{\frac{\mu Q}{\Delta\rho v_{\theta CS}^2 h}} \qquad \text{Equation 160}$$

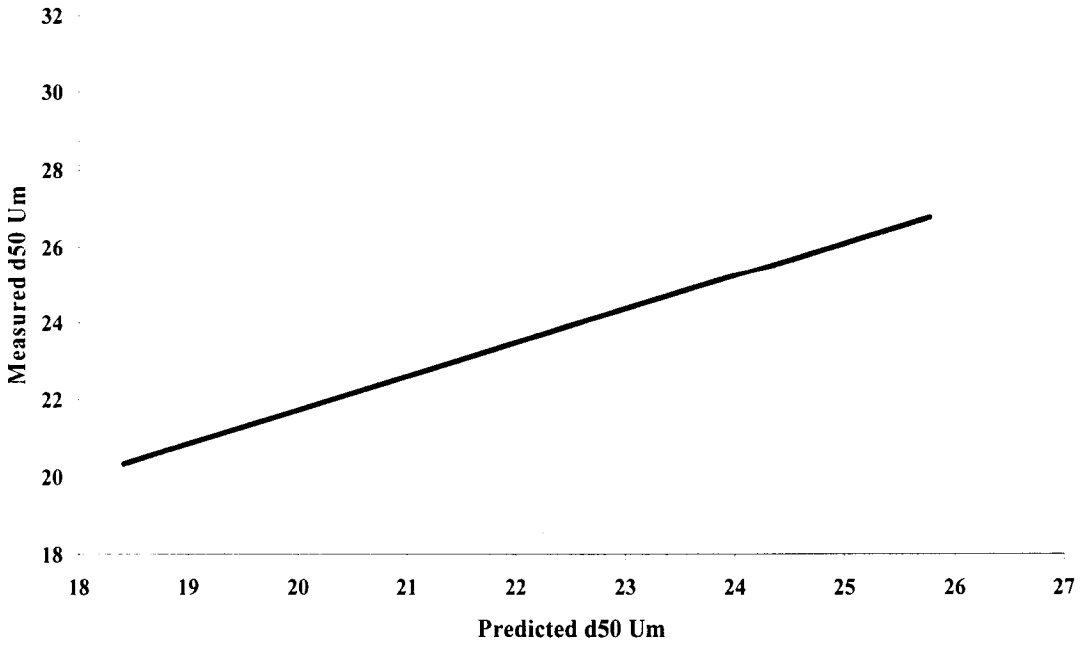

Figure 73: Measured and model predicted mean bubble cut-size in underflow stream.

The relationship between the measured and developed model mean cut-size (d_{50}) is statistically examined and is shown as the residual plot **Figure 74.**

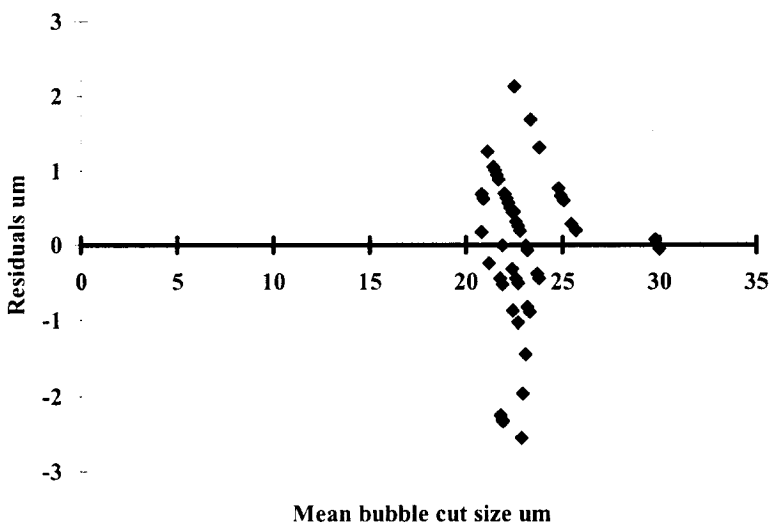

Figure 74: Residual plot for the measured and Muschelknautz (1980) predicted mean cut-size.

This model was developed to predict overflow cut-size using measured data. However, the measured data was found to be larger than the model predictions; the main reason of

this phenomenon is bubble coalescence across the low-pressure inner core. The developed model for prediction of bubble cut-size (d_{50}) in the overflow of a small diameter air-water cylindrical hydrocyclone is shown in **Equation 161.**

$$d_{50overflow} = 2.5\sqrt{\frac{\mu Q}{\Delta\rho v_{\theta CS}^{2} h}} \qquad \text{Equation 161}$$

In the separation of solid from water d_{50} is the size of the particles that reports half to the overflow and to the underflow. In the case of air-water and immiscible liquid separation, bubbles and droplets are subjected to breakage and coalescence. In this case, bubble coalescence occured in the low-pressure inner core and the measured bubble size will be larger than those in the underflow. The ratio of ($d_{50\ Overflow}$/ $d_{50\ Underflow}$) in this study was 1.43.

The experimental data was ranged from 25-35 μm. The predicted data where compared with the experimental data, which ranged from 33-35 μm (**Figure 75**).

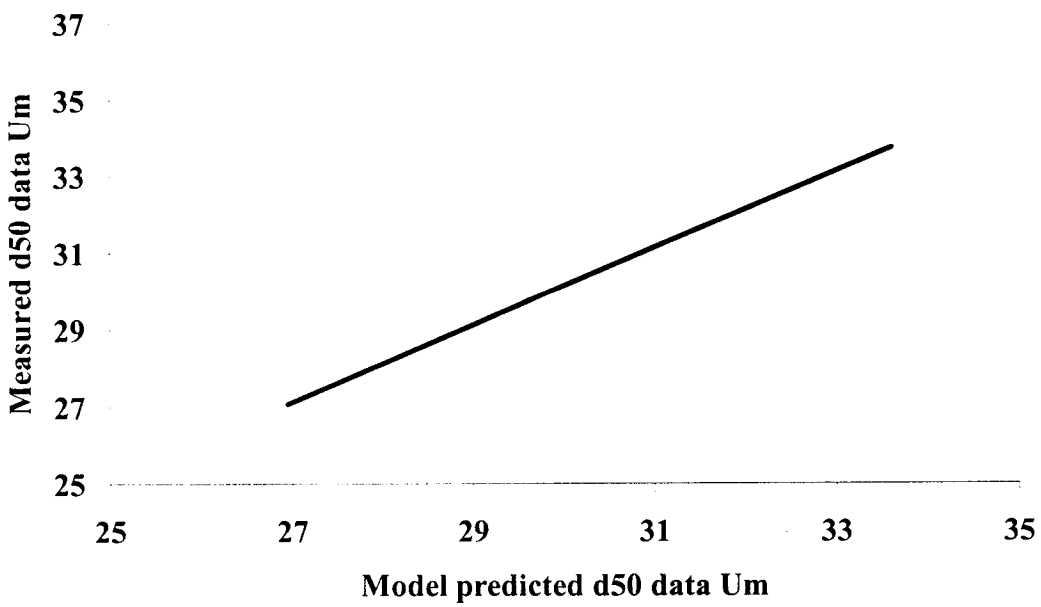

Figure 75: Measured and model predicted mean bubble cut-size in overflow stream.

The relationship between measured and model mean cut-size d_{50} in the overflow stream was statistically examined as is shown here as the residual plot in **Figure 76**.

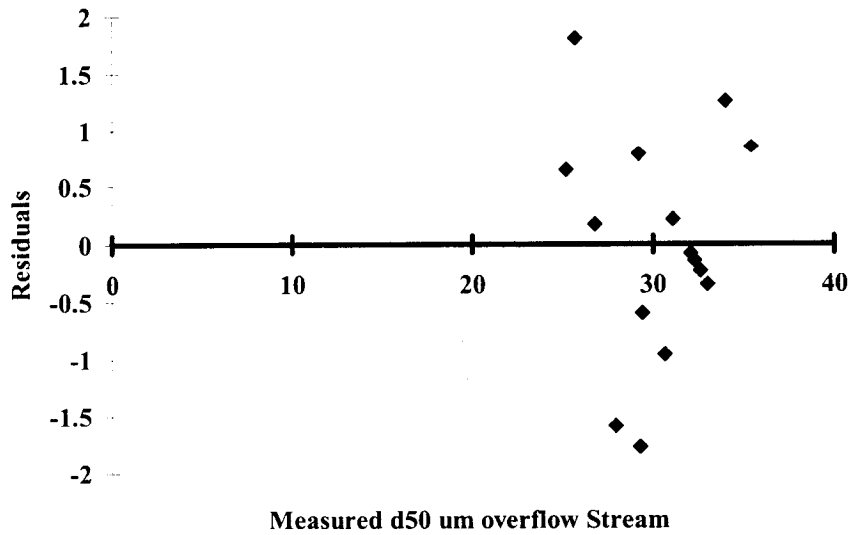

Figure 76: Residual plot for the measured and Muschelknautz predicted mean cut-size (Overflow streams).

The mean bubble cut-size in the underflow and overflow streams were compared. The size of the bubbles in overflow streams where 1.60 times larger than the bubbles in the underflow streams. The main reason for this difference is the coalescence of small bubbles in the low-pressure inner core.

The mean cut-size model was developed based on the Barth cut-size model. The Barth model is not valid for a cylindrical gas-liquid hydrocyclone because no conical part exists. Measured and model predicted mean cut-size (d_{50}) in underflow streams is shown in **Figure 77**. Error analysis was performed and residuals were between ± 3 μm. (**Figure 78**). The main independent variables in Barth models are radial gas velocity (v_{rcs}) and inner core velocity ($v_{\theta cs}$). The inner core velocity plays an inverse role in bubble cut-size. The developed model is capable of predicting bubble cut-size (d_{50}) in both underflow and overflow streams of a small diameter gas liquid cylindrical hydrocyclone and is shown in **Equation 162**.

$$d_{50\ underflow} = 0.98\sqrt{\frac{9\nu_{rcs}\mu D_x}{\rho_l \nu_{\theta CS}^2}}$$ Equation 162

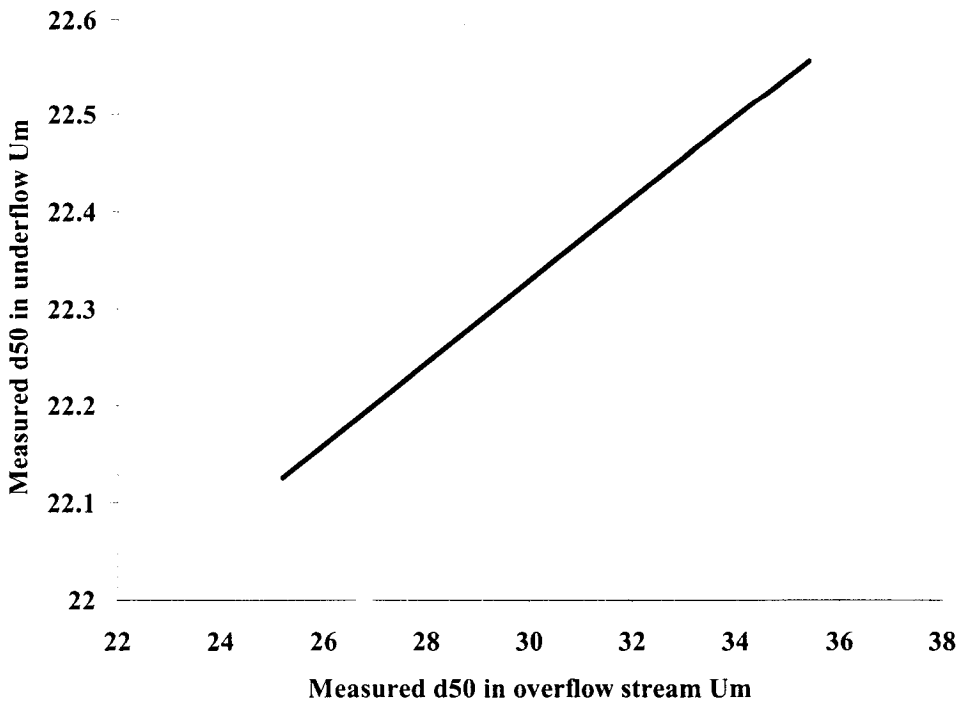

Figure 77: Measured, model and modified model predicted mean bubble cut-size in underflow stream.

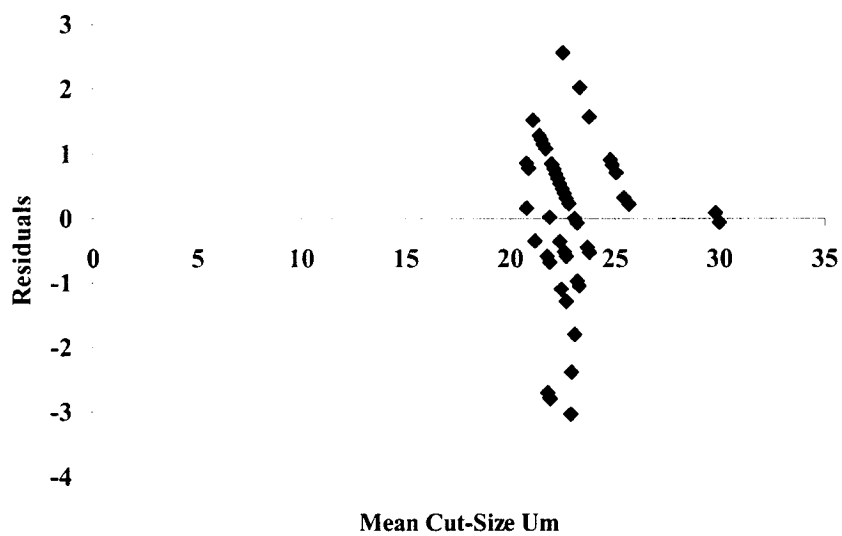

Figure 78: Residual plot of the developed mean bubble cut-size (underflow streams).

The relationship between Barth d_{50} model and the developed d_{50} model is shown in **Figure 79**. Residuals for the developed model were ± 0.06 μm (**Figure 80**).

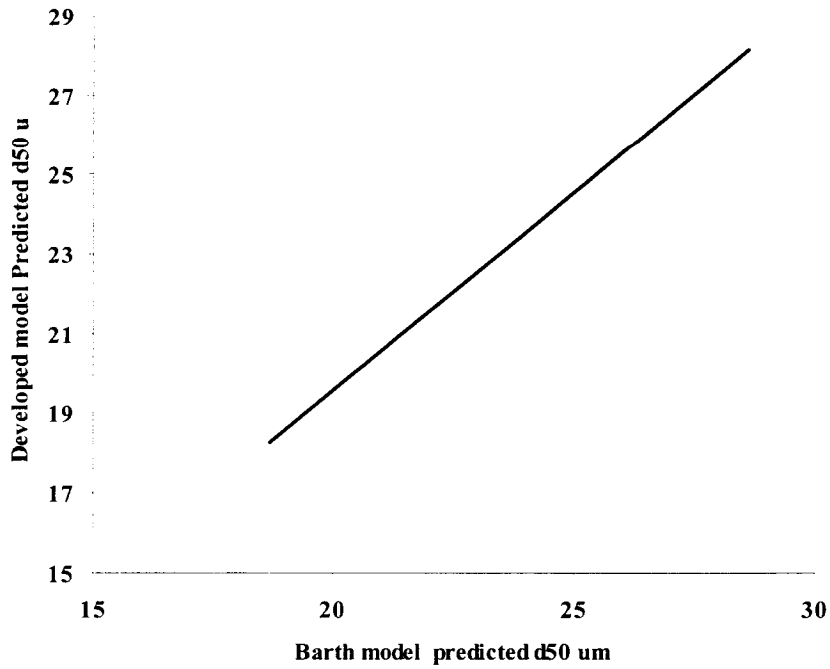

Figure 79: Correlation between measured and modified Barth model predicted mean cut-size (d_{50}) data in underflow streams.

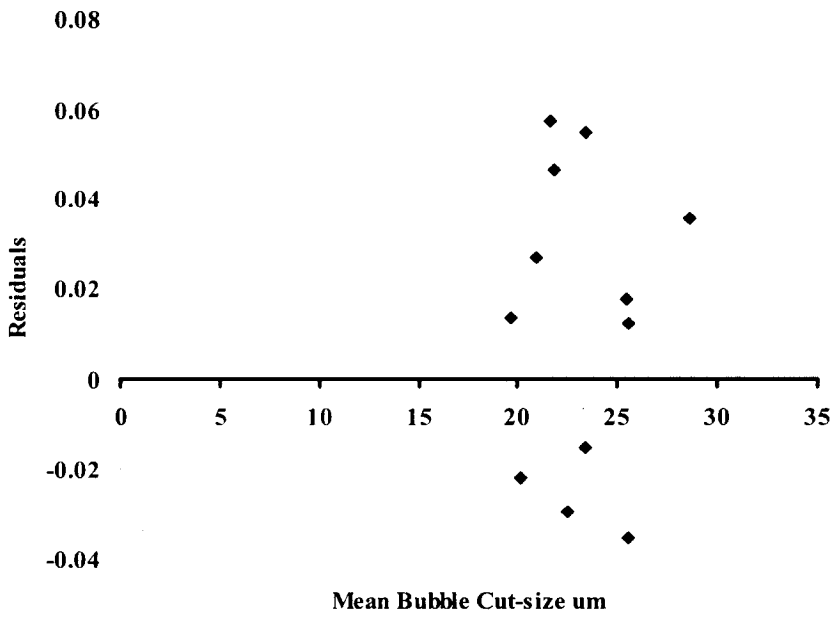

Figure 80: Residual plot for the measured and modified Barth predicted mean cut-size (underflow streams).

This data clearly indicates that the form of the Barth model and the value of the empirical constant provide a good description of the cylindrical hydrocyclone underflow performance and that only minor modifications of this empirical constant are necessary.

The Barth cut-point model was also modified to predict cut-size in overflow stream (**Equation 163**). The experimental bubble size was found to be larger than model predicted values. The main reason of this is the bubble coalescence in low-pressure inner core. The model was fitted to the experimental data using least square data fitting method.

$$d_{50\ overflow} = 3.66\sqrt{\frac{(v_{rcs})\mu D_x}{\rho_l v_{\theta CS}^2}} \qquad \text{Equation 163}$$

The comparison between measured and developed model predicted mean bubble cut-size "d_{50} is shown in **Figure 81**.

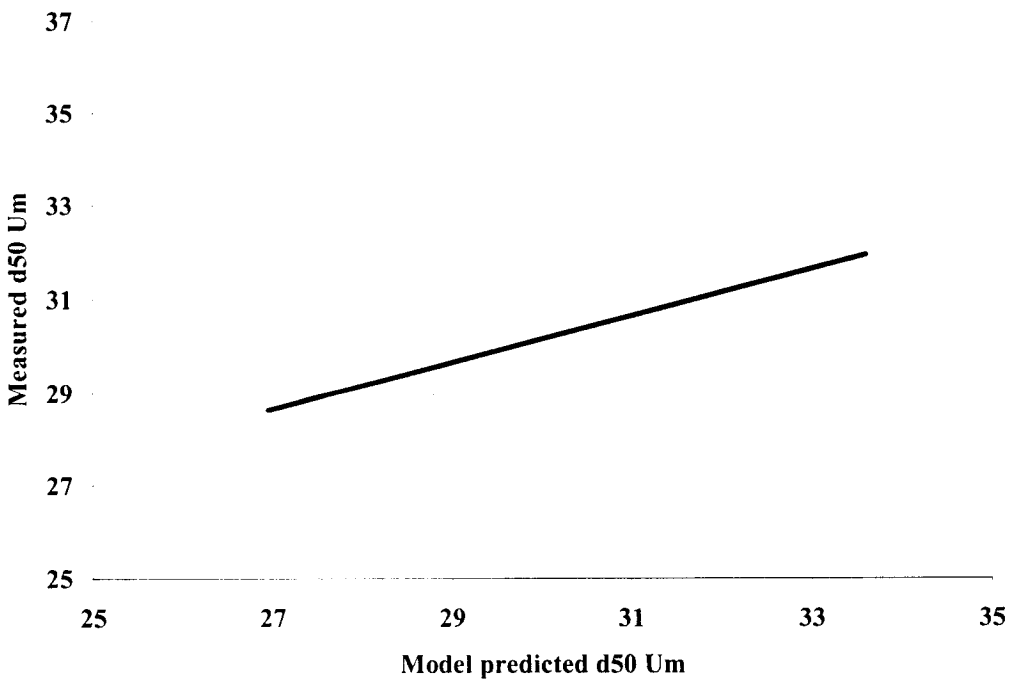

Figure 81: Measured, model and modified model predicted mean bubble cut-size in overflow stream.

The relationship between measured and developed model predicted d_{50} in overflow stream is statistically examined. Residual plot is shown in **Figure 82.**

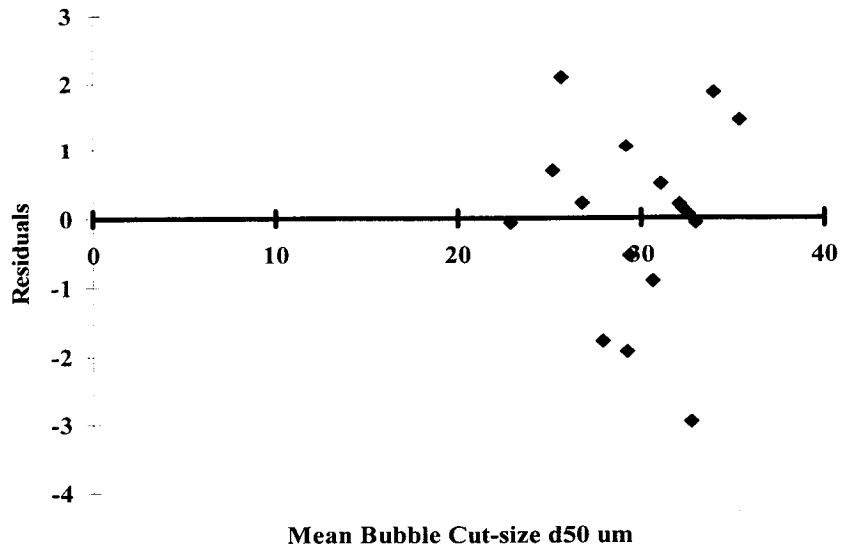

Figure 82: Residual plot for the measured and modified Barth predicted mean cut-size (Overflow Streams).

The data predicted by modified Bart model for underflow and overflow are compared. The size of the bubbles in overflow stream is about 1.3 times larger than the underflow stream. Bubble coalescence is the main reason for these differences (**Figure 83**).

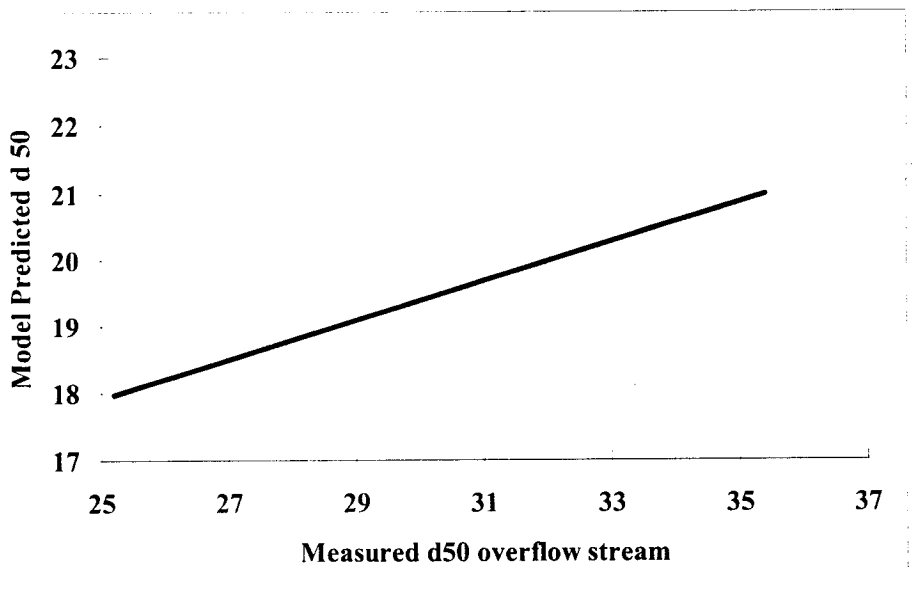

Figure 83: Comparison between modified Barth cut-size (d_{50}) model for underflow and overflow streams.

These two models (Barth and Muschelknautz) almost are the same and the outcome of those is very close to each other.

7.1.3 Purpose

The purpose of this model is to predict bubble cut-size for both the underflow and overflow streams in the prototype cylindrical hydrocyclone.

7.1.4 Model Structure (d_{50})

Bubble cut-size models are determined by minimizing the difference between the model response and the experimental data using a least square approach. This model uses tangential velocity at the surface CS ($v_{\theta CS}$), radial gas velocity at the surface CS, viscosity and volumetric flow rate.

7.1.5 Application of the Model (d_{50})

This bubble cut-size model was developed for the 2.54 cm air-water cylindrical hydrocyclone for the prediction of bubble cut-size in underflow and overflow streams.

7.2 Pressure Drop Prediction Models

Different authors have developed models of pressure drop across the vortex finder. The Barth and Muschelknautz predicted pressure drop (**Equation 123** and **Equation 124**) model response, is presented in **Appendix AA.** There is a perfect correlation between these two models (**Figure 84).**

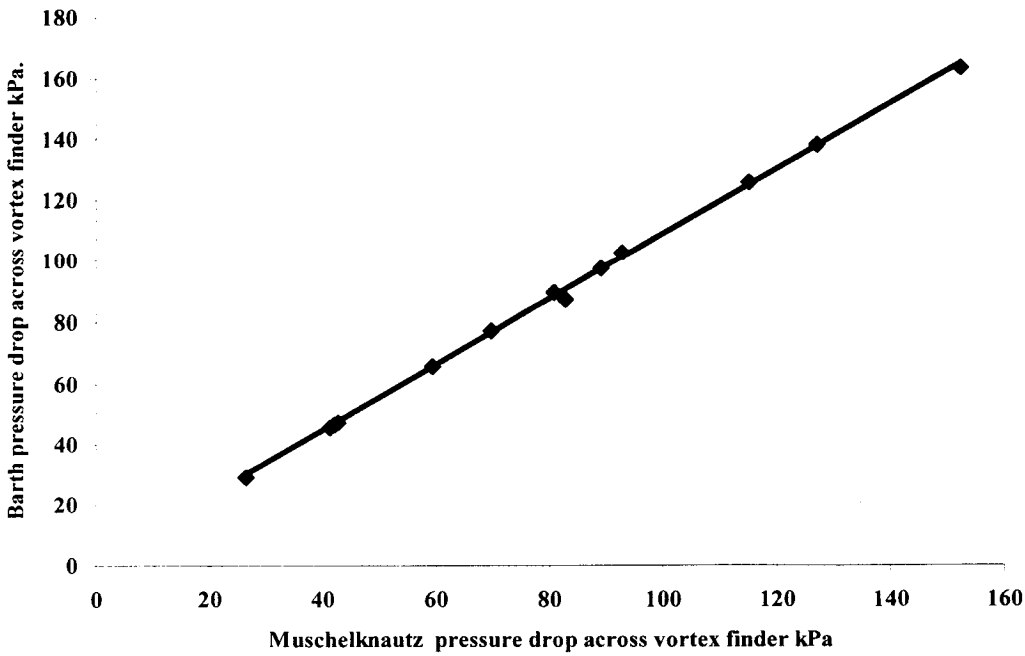

Figure 84: Relationship between Barth and Muschelknautz, models predicted pressure drop across the vortex finder.

Both models use the ratio of inner core velocity to flow velocity across the vortex finder ($v_{\theta cs}/v_x$). Fluid velocity affects the pressure drop and phase disengagement across the inner core. Tangential velocity ($v_{\theta cs}$), mean gas velocity (v_x), and ratio of these provides a dimensionless value that is used in modeling process. The proposed model for prediction of the pressure drop across the vortex finder is shown in **Equation 164**. This model estimates the pressure drop across the vortex finder. In equation 164, K= 3 is an empirical value that for air-water separation within a hydrocyclone with a cylindrical bodied vortex tube is four, **Equation 164**.

$$\Delta p_x = \frac{1}{2}\rho v_x^2\left(5+\left(\frac{v_{\theta CS}}{v_x}\right)^{2.42}+3\left(\frac{v_{\theta CS}}{v_x}\right)^{\frac{4}{3}}\right) \qquad \text{Equation 164}$$

$$\Delta p_x = \frac{1}{2}\rho v_x^2\left(\left(\frac{v_{\theta CS}}{v_x}\right)^{2.35}+K\left(\frac{v_{\theta CS}}{v_x}\right)^{\frac{4}{3}}\right) \qquad \text{Equation 165}$$

The model was fitted to the experimental data using the least square method by minimizing sum of the square errors (SSE). The model-fitting curve is shown in **Figure 85.**

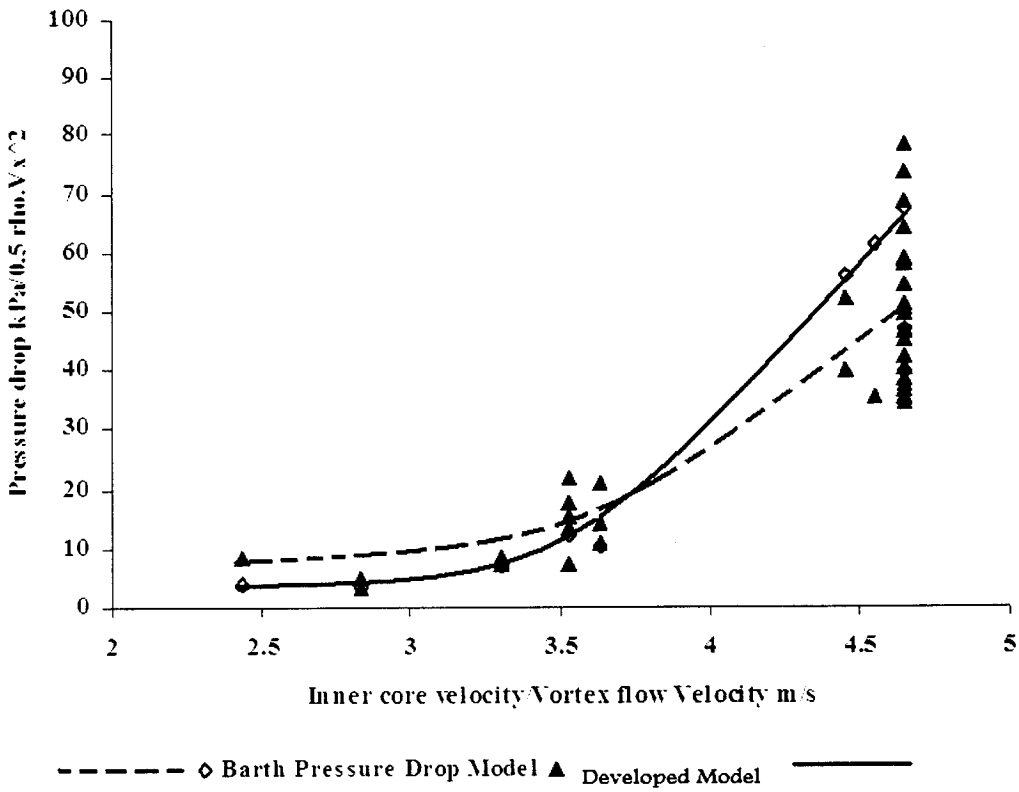

Figure 85: Developed Pressure Drop Model (Vortex Finder).

Pressure drop in the vortex finder is a function of dynamic pressure in the inner core zone ($0.5\ \rho v_x^2$). Both the Barth and Muschelknautz models assume a polynomial function in the form of **Equation 166**.

$$\Delta p_x = \frac{1}{2}\rho v_x^2\left[ab + cx^d + ex^f\right] \qquad \text{Equation 166}$$

In **Equation 166,** x is the ratio of $v_{\theta CS}$ to v_x and parameters "a" through "e" are determined by regression. The value of these parameters depend on geometry and operational conditions and are only valid with specific range or condition. The structure of the developed models are shown in **Equation 166, Table 10** and **Table 11** .

Table 10: Parameters determined by Barth, and this work.

Parameters	This Work	Barth Model
a	0	0
b	0	0
c	1	1
d	2.35	2
e	4	3.41-4.4
f	4/3	4/3

Table 11: Parameters determined by Muschelknautz and this work.

Parameters	This Work	Muschelknautz Model
a	5	2
b	1	1
c	1	1
d	2.42	2
e	3	3
f	4/3	4/3

This model has been validated to a $\frac{v_{\theta CS}}{v_x}$ ratio of 4.7. Beyond this ratio, the modified model may not be accurate. The relationship between the Muschelknautz model predicted pressure drop and developed pressure drop model is shown in **Figure 86**.

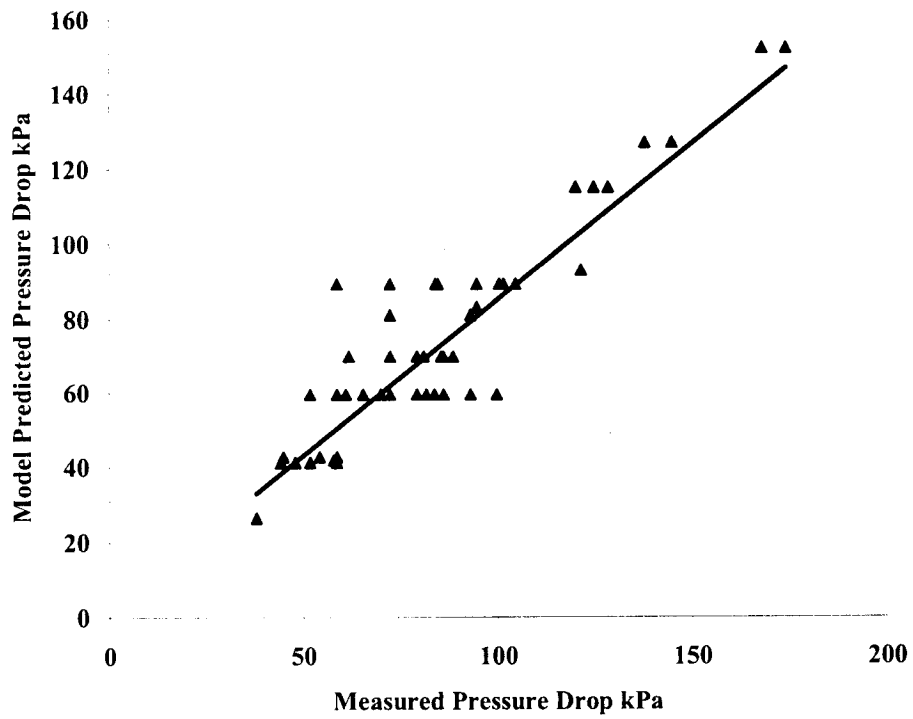

Figure 86: Comparison of experimental and Muschelknautz model predicted pressure drop.

The Muschelknautz pressure drop model was modified based on the experimental data. This modified Muschelknautz pressure drop model is shown in **Figure 87**.

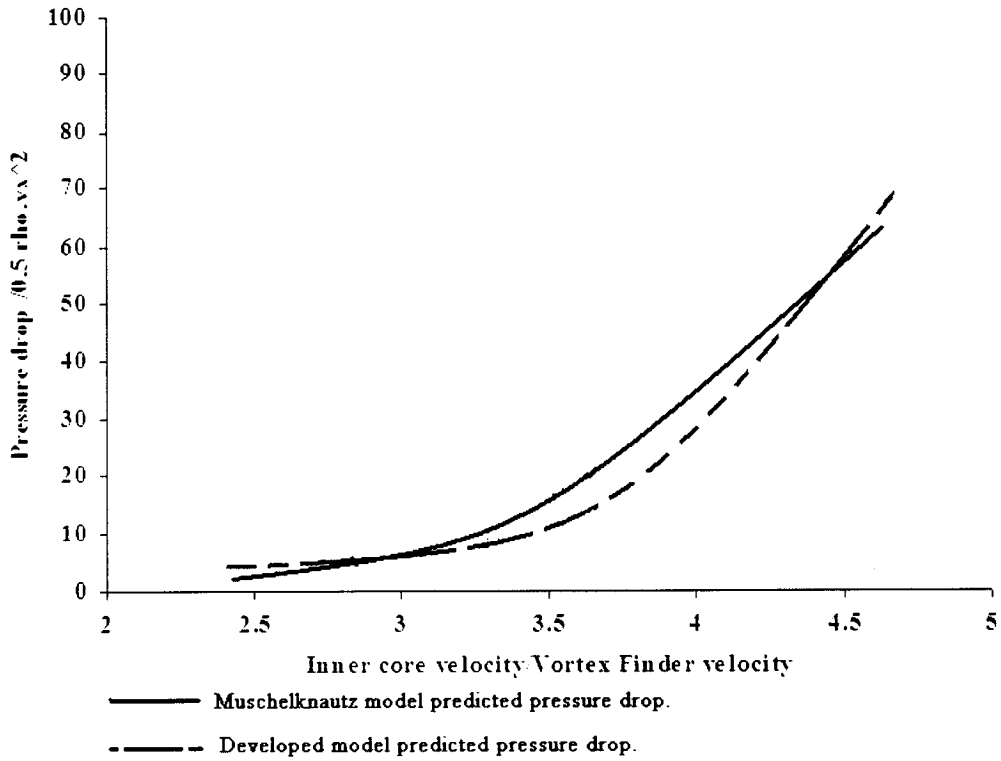

Figure 87: Modified Muschelknautz Pressure Drop (Δp_x) model.

The developed model, in the form of equation 167, may be used to predict the pressure drop across the small diameter air-water cylindrical hydrocyclone body shown in **Equation 167.**

$$\Delta p_x = \frac{1}{2}\rho v_x^2 \left(5 + \left(\frac{v_{\theta CS}}{v_x} \right)^{2.42} + 3 \left(\frac{v_{\theta CS}}{v_x} \right)^{\frac{4}{3}} \right) \qquad \text{Equation 167}$$

The comparison between the modified Barth and Muschelknautz form of the pressure drop model is shown in **Figure 88**.

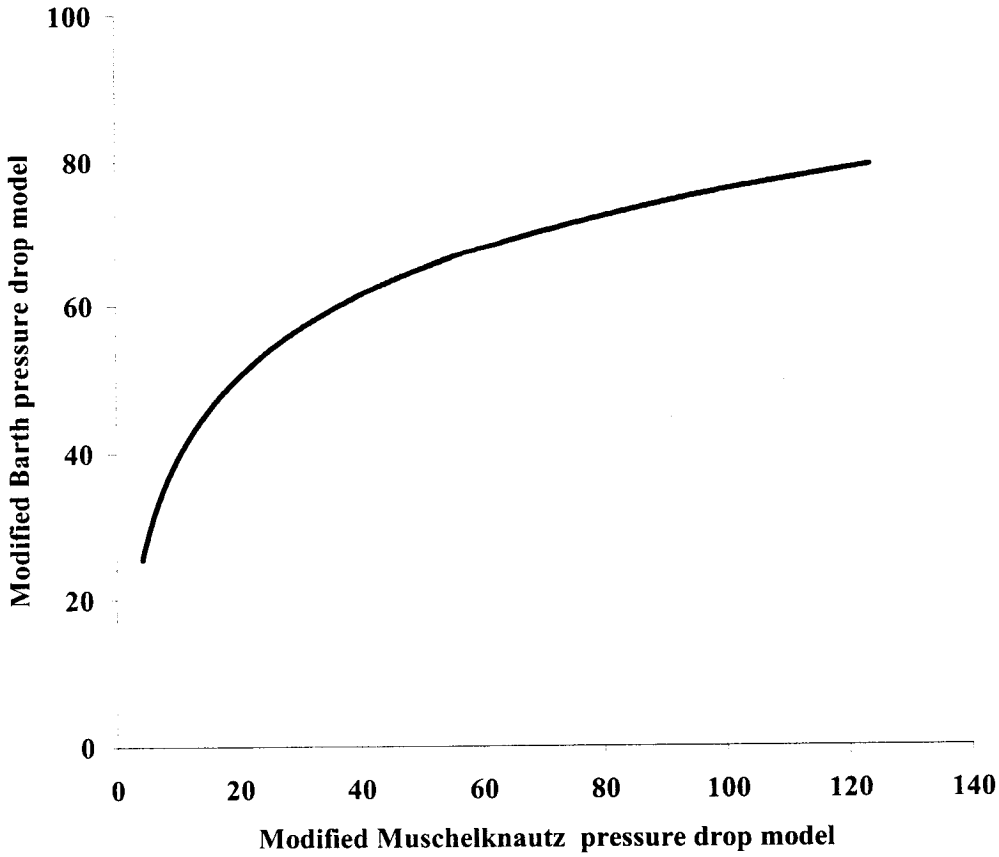

Figure 88: Comparison between the modified Barth and Muschelknautz pressure drop model.

The modified Muschelknautz model predicts a pressure drop higher than the modified Barth predicted model.

7.3 Efficiency Model

7.3.1 Introduction

Separation performance of the air-water cylindrical hydrocyclone depends on the feed inlet bubble size distribution. Efficiency curves can be generated using experimental bubble size data. In this model, three cut-sizes and efficiency curves were calculated based on more than 50 experiments (**Appendix W**). The 50% efficiency point is generally used for separation.

7.3.2 Model Description (η)

Efficiency model was determined by adjusting the parameters of the Dirgo-Leith relationship to fit the experimental data. The slope of the linearalized curve describes the prototype air-water cylindrical hydrocyclone.

7.3.3 Application of the Model (η)

The efficiency model for air-water separation is used to estimate how the well dispersed phase (bubbles) is separated based on the size. In this case, this is used to evaluate the air-water cylindrical hydrocyclone. It could also be used for hydrocyclone with similar geometries.

7.3.4 Model validation (η)

Different aspects of the efficiency model have been validated using the data from operating hydrocyclone.

7.3.5 Developed Efficiency Models

The efficiency model, based on the Dirgo form is shown in **Equation 168.** The slope of the efficiency curve is 3.4, which is half of the value of the original Dirgo model. In Equation 168 d_{50} is mean bubble cut-size and d_i is the given bubble cut-size.

$$\eta = \frac{1}{1+\left(\frac{d_{50}}{d_i}\right)^{3.4}} \qquad \text{Equation 168}$$

Figure 89 shows that the efficiency in the air-water cylindrical hydrocyclone is higher than in a conventional hydrocyclone based on comparison of it with the Dirgo et al. model.

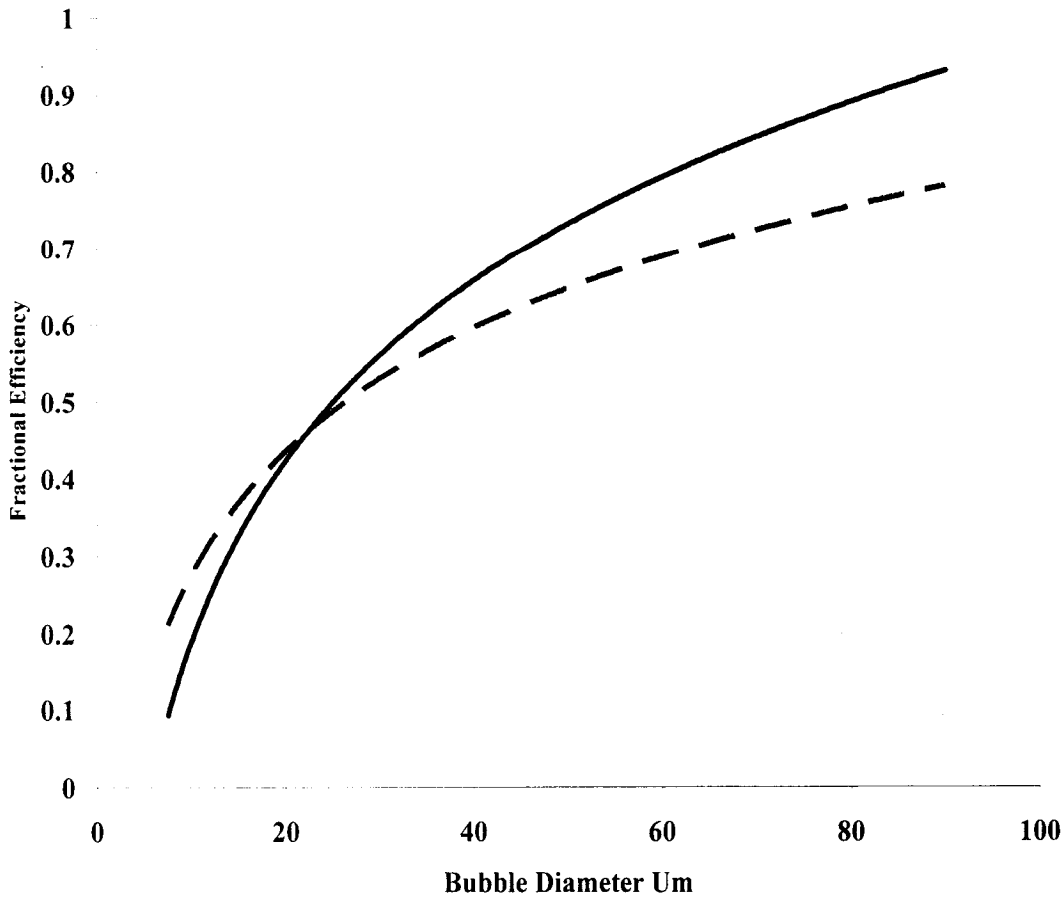

_ _ _ Dirgo et al. efficiency model. ___ Developed efficiency model.

Figure 89: Comparison of the develop efficiency model with Dirgo et al. model.

8. CONCLUSIONS

This study was based on experimental research and provided equations and their parameters for pressure drop, bubble cut-size and efficiency for a small diameter air-water cylindrical hydrocyclone. Empirical models were developed based on existing models. The original models, both for cut-size (d_{50}) and pressure drop across the vortex finder (Δp_x), provided poor estimations of the experimental data. The suspected reasons for this are geometry differences and the behavior of bubbles when compared to that of droplets and particles. The models developed for this thesis are capable of estimating vortex finder pressure drop, efficiency and cut-size in the under-flow and over-flow streams. The empirical parameters of the models were adjusted to fit the experimental data. Thus adjusted, the model predictions showed good agreement with experimental data (variance of approximately ± 10%). Furthermore, it has been shown that bubble size has a significant impact on air-water separation of the hydrocyclone as shown in **Figure 90**.

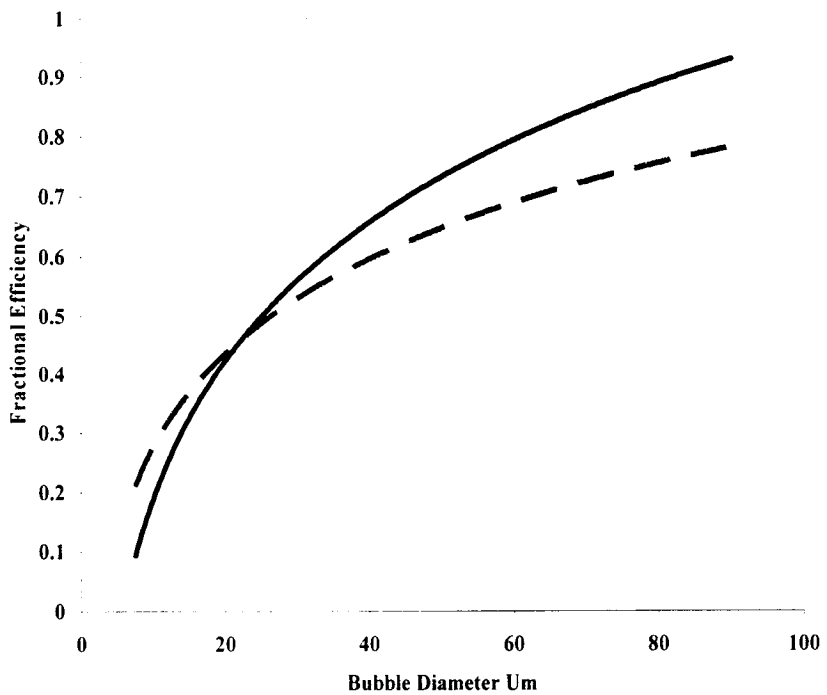

_ _ _ Dirgo et al. efficiency model. ___ Developed efficiency model.

Figure 90: Developed efficiency model (Figure 59).

- **Pressure Drop Model in Vortex Finder**

Both the form of the Muschelknautz (**Equation 169**) and Barth **(Equation 170)** pressure drop models were used to estimate the performance of the cylindrical hydrocyclone in recycled batch mode. Both models require a calculation of fluid velocity in the vortex finder and inner core tangential velocity. These variables were calculated using a series of equations, which are located in this section.

$$\Delta p_x = \frac{1}{2}\rho v_x^2 \left[2 + \left(\frac{v_{\theta CS}}{v_x} \right)^2 + 3 \left(\frac{v_{\theta CS}}{v_x} \right)^{\frac{4}{3}} \right] \qquad \text{Equation 169}$$

$$\Delta p_x = \frac{1}{2}\rho v_x^2 \left(\frac{v_{\theta CS}}{v_x} \right)^2 + K \left(\frac{v_{\theta CS}}{v_x} \right)^{\frac{4}{3}} \qquad \text{Equation 170}$$

These models use density, inner core tangential velocity, and flow velocity in the vortex finder. The form of the developed pressure models are polynomials that are fitted to the data with (± 10%) variance **(Equation 171 & Equation 172)**.

$$\Delta p_x = \frac{1}{2}\rho v_x^2 \left(5 + \left(\frac{v_{\theta CS}}{v_x} \right)^{2.42} + 3 \left(\frac{v_{\theta CS}}{v_x} \right)^{\frac{4}{3}} \right) \qquad \text{Equation 171}$$

$$\Delta p_x = \frac{1}{2}\rho v_x^2 \left(\left(\frac{v_{\theta CS}}{v_x} \right)^{2.35} + 4 \left(\frac{v_{\theta CS}}{v_x} \right)^{\frac{4}{3}} \right) \qquad \text{Equation 172}$$

The parameters of these equations were determined by the least square method using experimental data.

- **Bubble Cut-Size Models**

A mechanistic based model with an empirical constant to compensate for geometric and operating condition was developed. The "k" value of this model was determined to be

1.755 for the cylindrical hydrocyclone separating bubbles from water when predicting the underflow d_{50} **(Equation 173).**

$$d_{50underflow} = 1.755\sqrt{\frac{\mu Q}{\Delta\rho v_{\theta CS}^2 h}} \qquad \text{Equation 173}$$

The developed model for the prediction of bubble cut-size (d_{50}) in the overflow of a small diameter gas-liquid cylindrical hydrocyclone is shown in **Equation 174**.

$$d_{50overflow} = 2.5\sqrt{\frac{\mu Q}{\Delta\rho v_{\theta CS}^2 h}} \qquad \text{Equation 174}$$

In **Equation 174,** μ is viscosity, Q is flowrate, Δp is density differences, $v_{\theta CS}$ is inner core tangential velocity and h is hydrocyclone height. In this case bubble coalescence occured in the low-pressure inner core area and the measured bubble size is larger than the underflow resulting is a $d_{50\ Overflow}/\ d_{50\ Underflow}$ ratio of 1.43.

The mean bubble cut-size model was developed for the tested hydrocyclone using the Barth from of the model **(Equation 175)**.

$$d_{50\ underflow} = 0.98\sqrt{\frac{9v_{rcs}\mu D_x}{\rho_l v_{\theta CS}^2}} \qquad \text{Equation 175}$$

The data indicates that the Barth form, with the appropriate empirical constant, provides a good description of the cylindrical hydrocyclone underflow performance. Only minor modifications of this empirical constant were necessary.

The Barth cut-size model was also modified to fit the overflow stream **(Equation 176)**.

$$d_{50\ overflow} = 3.66\sqrt{\frac{(v_{rcs})\mu D_x}{\rho_l v_{\theta CS}^2}}$$ Equation 176

The experimental data was found to be larger than predicted. This is attributed to bubble coalescence in the low-pressure inner core.

- **Efficiency Model**

The developed efficiency model for the test hydrocyclone is shown in **Equation 177.** The slope of the efficiency curve was found to be 3.4, which is approximately half of the value predicted, by the Dirgo et al. model.

$$\eta = \frac{1}{1+\left(\frac{d_{50}}{d_i}\right)^{3.4}}$$ Equation 177

In **Equation 177,** d_{50} is mean bubble cut-size, d_i is given cut-size. Predicted results show that the efficiency in the air-water cylindrical hydrocyclone is higher than conventional hydrocyclone.

Other conclusions of this research are as follows:

- The measured bubble size distribution in the test cylindrical hydrocyclone was approximately two times that of those predicted by established models. This has been corrected.
- The pressure drop ratio increases when the split ratio or inlet feed flow rate increases.
- The inlet Euler number is much smaller than Euler number in the inner core, which means pressure drops in the vortex finder area, is significantly higher than in the inlet area.
- Separation efficiency increases when the bubble size increases.
- Reynolds number increases when the inlet feed pressure drop increases.

The technical contributions of this thesis are:

- The development a 2.54 cm diameter gas-liquid cylindrical hydrocyclone capable of separating gas from liquid.
- The design of an orifice type phase contactor capable of providing controlled bubble sizing and phase contacting.
- The generation of fine bubbles without using conventional bubble generators such as static and dynamic spargers.
- Proof that significant bubble coalescence takes place in hydrocyclone particularly in the low-pressure inner core.
- The experimental results on bubble size distribution show that in a cylindrical hydrocyclone without a conic section bubble coalescence increases across the hydrocyclone -- this is desirable for the over-flow stream but not for the under-flow stream (**Appendix I**).

The main objective of this work was to design, construction and model a small diameter gas-liquid cylindrical hydrocyclone. The results presented in this thesis show that a cylindrical hydrocyclone prototype designed and constructed for air, and possibly small amounts of organic phase, removal is capable of meeting the research objectives. The hydrocyclone separation efficiency depends on the feed inlet bubble size distribution, feed flow rate and pressure drop across the hydrocyclone. The best hydrocyclone separation performance, with the designed geometry, was obtained with a high swirl and low Reynolds number flow. These conditions prevent bubble and/or droplet size breakage. Under these conditions, the bubble size distribution in the underflow ranged from 30-60 μm.

9. RECOMMENDATIONS for FURTHER WORKS

The following further works are recommended as a follow-up to this research.

1. Further work on the effect of geometry would contribute to expanded application of small diameter cylindrical hydrocyclone for air-water separation.

2. Testing the prototype using low hold-up oil in water (O/W) emulsion and measurement of oil content in over-flow stream using GC-Mass or Fourier Transform Infrared Spectroscopy (FT-IR).

3. Fabricating and testing of a turbulent unit with more accurate measuring and control devices such as multi-phase flow meters and magnehelic pressure gauges.

4. Study and measurement of radial, tangential and axial flow inside the hydrocyclone using laser Doppler anemometer (L.D.A) and investigate the swirl flow and air core stability.

5. Study of bubble size distribution across the hydrocyclone using in-line bubble size analyzer on all streams to reduce the errors originated of bubble coalescence and breakage effects inside the hydrocyclone and connection pipes and use of information to model the coalescence and breakage of bubbles in the hydrocyclone. This will refine the prediction of bubble distributions in the hydrocyclone product streams.

6. Three-phase separations, such as flotation systems, should be investigated where the cyclone is used as a loaded bubble separator. This type of system could be promising, and possibly cost effective, for the removal of selected solids or of two immiscible fluids.

7. Simulation and mathematical modeling, by the incorporation of mechanistic models for pressure drop and efficiency, of the cylindrical hydrocyclones for extending the accuracy and application.

8. Investigation the effect of different materials, used as liners, to reduce wall friction, erosion and corrosion.

10. ADDITIONAL POSSIBLE APPLICATIONS

- Most oil fields produce water and gas mixtures that are dispersed and dissolved. This hydrocyclone may capable of removing gas and small amounts of organics from water. It has the potential to be standard for oil field production separations, refineries and mine water treatment, especially for coal mines for the removal of methane from water.
- Conventional separation systems require chemicals to operate. Most of these chemicals are not biodegradable, so cyclonic separation systems that minimize chemical usage would be of benefit.
- This device may also be used for in situ offshore oil spill clean-up operations with minimum capital and chemical cost.

11. ECONOMICS

Construction of the each hydrocyclone unit is cost approximately 500 CD$. The rest of the separation system including pumps, compressors, valves, gauges piping should be calculated separately. The capital cost is less than centrifugal air-water separation systems and gravity based separators. This hydrocyclone can be installed in downstream and upstream oil and gas production facilities to evaluate the real economic benefits of this system. This system may used in oil tank farms, water transfer facilities, production platforms and produced water treatment systems. Because of minimal leakage potential, this cyclone may be tested for the removal of volatile hydrocarbons from oil slicks. Air-water hydrocyclones may be installed down-hole for separation of produced water and gases.

12. SAFETY

This hydrocyclone is inherently safe to operation compare to other gas liquid separators. This system requires a very small area where space is limited; for example as drilling rigs, offshore production platforms, and underground mines. This device is present minimal gas leakage potential.

13. REFERENCES

Alexander, R., "Fundamental of Cyclone Design and Operation", procedures of the Australian Inst. Min. Metall. No. 152, pp 203-208 (1949).

Arpandi, A., Joshi, R., Shoham, O. and Shirazi, S., "Hydrodynamics of Two-Phase Flow in Gas-Liquid Cylindrical Cyclone Separators", SPE. 30683 (1995).

Barth, W., "Design and Layout of the cyclone separator on the Basis of New Investigations", Brennst, Waerme, Kraft, 8:1 (1956).

Belaidi, A., Thew, M. and Munaweera, S., "Drop Size Effects on a De-Watering Hydrocyclone", Vortex. Separation. 5th Int. Conf. Cyclone. Tech. 119-129, Pub. BHR, Cranfield, May- June (2000).

Bradley, D., The Hydrocyclone, Pergamon Press, Oxford (1965).

Bradley, D. and Pulling, D. J., "Flow Patterns in the Hydraulic Cyclones and Their Interpretation in Terms of Performance", Trans. Instn. Chem. Engrs. 37, no 34(1959).

Coelho, M. A. Z and Medronho, R. A., "A model for Performance Prediction of Hydrocyclones", Chem. Eng. J. **84**, p 7-14 (2001).

Colman, D. A. and Thew. M. T., "The Concept of Hydrocyclones for Separating Light Dispersions and a Comparison of Field Data with Laboratory Work", 2nd Int. Conf. Hydrocyclones. 217-232, Bath. England. 19-21, Sep. (1984).

Colman, D. A., Thew, M. T and Corney, D. R., "Hydrocyclone for Oil- Water Separation", Papers, 1st Int. Conf. On Hydrocyclones. Cambridge (1980).

Dirgo, J. and Leith D, "Performance of Theoretically Optimized Cyclones", Filtration and Separation, March-April issue, pp 119-125 (1985).

Driessen, M. G., "Cleaning of Coal by Heavy Liquids, with Special References to the Staatsmijnen Process", J. Inst. Fuel. **12**, no 6, p 327 (1939).

Dyakowski, T. and Williams, R. A., "Hydrocyclone Flow Modeling – a Continuous Research Challenge", Innovation in Physical Separation Technologies Richard Mozley Memorial Symposium, Falmouth, I.M.M., London, UK (1997).

Davidson, M. R, "An Adaptive Method of Predicting the Air Core Diameter for Numerical Models of Hydrocyclone Flow", Int. J. Miner. Process. **43**, pp 167-177 (1995).

Einstien, A., Ann. Phys. **19**, p 289, (1906).

Erdal, M. F., "Local Velocity Measurements and CFD Simulations in GLCC Separators", Ph.D. Dissertation. The University of Tulsa, USA (2001).

Erdal, M. F., Mantilla, I., Shirazi, A. S. and Shoham, O., "Simulation of Free Interface Shape and Complex Two-Phase Flow Behavior in a Gas-Liquid Cylindrical Cyclone Separator", Proceed. ASME, Fluid Eng. Division. Summer. (1998a).

Erdal, M. F., Shirazi, S. A., Mantilla, I. And Shoham, O., "CFD Study of Bubble Carry-Under in Gas-Liquid Cylindrical Cyclone Separators", SPE, 49309 (1998b).

Farchi, D., "A Study of Mixer and Aeparators for Two-Phase Flow in M. H. D. Energy Conversion System", M.S. Thesis (in Hebrew), Ben-Gurion University, Israel (1990).

Flanigan, D. A., Stolhand, J. E., Shimoda, E. and Skilbeck, F., "Use of Low-Shear Pumps and Hydrocyclones for Improved Performance in the Clean-up of Low-Pressure Water", SPE report 19743. SPE. Production Eng. 295-422, August (1992).

Fahlstrom, P. H., "Studies of the Hydrocyclone as a Classifier", Mineral Processing Proceeding. 6^{th} Int. Congress. Cannes (1963).

Farrell, C. W., "Oilfield Process Stream Treatment by Means of Alternating Current Electrocoagulation", Advance. Filtration. Separation. Tech. Gulf. Pub. Co. V **3,** Oct. 29-30 (1991).

Gel' Perin, N. I., "The Use of Hydrocyclones in Extraction Setups", Zh. VkhO im. Mendeleeva, **20,** no. 6, p. 716 (1975).

Gomez, C., Caldentey, J., Wang, S., Gomez, L., Mohan, R and Shoham, O., "Oil-Water Separation in Liquid-Liquid Hydrocyclones (LLHC) – Experiment and Modeling", SPE Report. No. 71538 (2001).

Gomez, L. E., Mohan, S. R., Shoham, O., Marrelli, J. D. and Kouba, E. G., "State of the Art Simulator for Field Applications of Gas-Liquid Cylindrical Cyclone Separators", SPE, 56581, (1999).

Hoffman , A. C., "The Effect of the Length in Hydrocyclone Performance", AIchE. J, **47**, no 11 (2001).

Hoffmann, A. C and Stein, L. E, "Gas Cyclones and Swirl Tubes", Springer Verlag Berlin, Heidelberg, New York, ISBN 3-540-433326-0 (2002).

Holland-Batt, A. B., "A Bulk Model for Separation in Hydrocyclones", Trans. Inst. Min. Metall. (Sect. C: Min. Process Extr. Metall.), **91**, (1982).

Jayalakshmi, Y. and Beysens, D., "Rayleigh-Taylor Instability in a Phase Separating Mixture Under a Concentration Gradient", J. Phys.11, France. **5**, p. 1067-1076, July (1995).

Jiang, M., Zhao, L and He, J., "Pressure Drop Ratio-An Important Performance Parameter in Liquid-Liquid Hydrocyclone Separation", Proceed. 8th Int. Offshore and Polar Eng. Conf. Montreal, Canada. May, 24-29 (1998).

Kelsall, D. F., "A study of the Motion of Solid Particles in a Hydraulic Cyclone", Trans. Inst. Chem. Eng. 30, p 87, (1952).

Kimber, G. R and Thew, M. T., "Experiments on Oil-Water Separation with Hydrocyclones", Proc. 1st European Conf. On Mixing and Centrifugal Separation. N. G. Coles, ed. Cambridge, 1974, B. H.R.A., Cranfield, E1-E28 (1974).

Kireev, V. A., "Kurs Fizicheskoi Khimi (Course on Physical Chemistry), Moscow: Khimiya (1975).

Kondrat'ev, S. A., "Investigation of the Fragmentation of Gas Bubbles in a Turbulent Liquid Flow, Fiziko Khimicheskie problemy Razrabotki Poleznykh Iskopaemykh, 5, p. 97 (1987).

Kouba, G. E., "Analysis of Gas Carry-Under in Gas-Liquid Cylindrical Cyclones), Presented at the Hydrocyclones, International Meeting, St. Johns College, Cambridge, England, April 2-4 (1995).

Krasny, R., "Desingularization of Periodic Vortex Sheet Roll-up", J. Com. Phys. **65**, p. 292-313 (1986).

Lagutkin, M. G and Klimov, A. P., "The Behavior of Gas Bubbles in a Hydrocyclone", Theo. Found. Chem. Eng. 27, no. 5, 426-430 (1993).

Levich, V. G., "Fiziko-Khimicheskaya Gidrodinamika (Physicochemical Hydrodynamics), Moscow: Fizmatgiz (1959).

Luo, J. J, "Bubble Dispersion and Coalescence in Turbulent Pipe Flow", Ph.D. Thesis, Dalhousie Univ. Halifax, NS, Canada (2002).

Millington, B. C and Thew, M. T., "LDA Study of Component Velocities in Air-Water Models of Steam-Water Cyclone Separators", Proceed. 3rd Int. Conf. Multiphase. Flow, Hague. Netherlands. P. 115-125, May 18 (1987).

Meldrum, N., "Hydrocyclones: A Solution to Produced-Water Treatment", SPE. Production. Eng. SPE. 16642. 669-676 (1988).

Motta, B., Erdal, F. M., Shirazi, S. A and Shoham, O., "Simulation of Single-Phase and Two Phase Flow in Gas-Liquid Cylindrical Hydrocyclones", presented at the 1997 ASME Fluids Engineering Division Summer Meeting, Vancouver, BC, Canada, June 22-26 (1997).

Muschelknautz, E and Trefz, M., "Design and Calculation of Higher and Highest Loaded Gas Cyclones", Proceeding of Second World Congress on Particle Technology, Kyoto, Japan, p. 52-71 (1990).

Muschelknautz, E., "Theorie der Fliehkraftabscheider mit besondered Berucksichtigung holer Temperaturen un Drucke", VDI-Berichte. 363: p. 49-60 (1980).

Nelson, R. D., "Dispersing Powders in Liquids, Part 1, Particle Volume Distribution", www.erpt.org (2001).

Nezhati, K and Smyth, I. C., "A System Approach to Oil/Water Separation-Further Hydrocyclone Treatment of a De-Watering Hydrocyclone Reject Flow" unpublished report. Univ. Southampton (1989).

Okada, K., Akagi, Y. and Yoshioka, N., "Effect of Zeta Potentials of Oil Droplets and Bubbles on Flotation of Oil-in-Water Mixtures", Can. J. Chem. Eng., 66, 276-281 (1988).

Plitt, L. R., "A Mathematical Model of the Hydrocyclone Classifier", CIM. Bull. 114-123, Dec. (1976).

Regehr, H. U., "The Use of the Hydrocyclone for Separation", (In German), Forsch. Ing. Wes. 28, 11-27 (1962). English Translation, Mech. Eng. Dept. Univ. Southampton, UK (1968).

Rietema, K., " Performance and Design of Hydrocyclones", Chem. Eng. Sci. 15, 298-302 (1961).

Rios, G., Pazos, C and Coca, J., "Zeta Potentials of Cutting-Oil Water Emulsions: Influence of Inorganic Salts", J. Dispersion. Sci. Tech. **19**, no 5, p. 661-678 (1998).

Schubert, H. and Neese, T., "On the Hydrodynamics and the Scale-up of Flotation Processes", DDR, 636-649 (1980a).

Schubert, H. and Neese, T., "A Hydrocyclone Separation Model in Consideration of the Turbulent Multi-Phase Flow", Proc. Int. Conf. On Hydrocyclones (Cambridge, 1980). Paper 3, pp.23-36, BHRA Fluid Engineering, Cranfield (1980b).

Shaw, D. J., Introduction to Colloid and Surface Chemistry, Butterworth. Pub. London. Uk. 3th. Edition. (1980).

Shepherd CB and Lapple CE., " Flow Pattern and Pressure Drop in Cyclone Dust Collectors)", Ind. & Eng. Chem. 32: 1246-1248 (1940).

Simms, K. M., Zaidi, S. A., Hashemi, K. A., Thew, M. T. and Smyth, I. C., " Testing of the Vortoil Deoiling Hydrocyclone using Canadian Offshore Crude Oil", Kulwer Academic Publishers, Dordrecht, the Netherlands, 295-308 (1992).

Sinker, A. B and Thew, M. T., "Drop Size Distributions in De-Watering Type Hydrocyclones", Hydrocyclones, 96 Eds. D. Claxton, Svarovsky, L. and Thew, M. T. Pub. MEP, London (1996a).

Smyth, I. C., Thew, M. T., "Small Scale Experiments in Hydrocyclones for De-Watering Light Oils", IBID. (1980).

Svarovsky, L., Hydrocyclones, Holt, Rinehart, and Winston, London (1984).

Sylvester, N. D., and Byeseda, J. J, "Oil/ Water Separation by Induced-Air Flotation", SPE. Dec. 579-590 (1980).

Trawinski, H. F., "The Application of Hydrocyclones as Versatile Separators in Chemical and Mineral Industries", Int. Conf. Hydrocyclones, BHRA, Cambridge, p 179-80 (1980)

Vennard, J. K and Street, R. L., *Elementary Fluid Mechanics*, 6th ed. Page 283, John Wiley and Sons, 1982.

Voinov, O. V. and Petrov, A. G, "The Motion of Bubbles in Liquid, Mekhanika Zhidkosti I Gaza (The Mechanics of Liquids and Gases), Moscow: VINITI, 10, p86 (1976).

Welker, J. R., Sheng, H. P. and Sliepcevich, C.M., "Liquid-Liquid Separations in a Conventional Hydrocyclone", Canadian J. Chem. Eng., 52, No.8, p. 487 (1974).

White, D. A., "Efficiency Curve Model for Hydrocyclones Based on Crowding Theory", Inst. Min. Metall, 100, Sept.- Dec. (1991).

Wolbert, D., Ma, B. F. and Aurelle, Y., "Efficiency Estimation of Liquid-Liquid Hydrocyclones Using Trajectory Analysis", AIChE. J. 41, No. 6 pp 1395-1402 (1995).

Yoshioka, N and Hotta, Y, "Liquid Cyclone as a Hydraulic Classifier", Chem. Eng. Japan. 19, no 12, p 632 (1955).

Young, G. A., Wakley, W. D. Taggart, D. L., Andrews, S. L. and Worrell, J. R, " Oil-Water Separation Using Hydrocyclnes, an Experimental Search for Optimum Dimensions", Amoco. Product. Co. 102-122 (1996).

14. APPENDICES

Appendix A: Typical Analysis of Pockwock / Lake Major Water (1999-2000).

Parameters	Pockwock Raw	Pockwock Treated	Major Lake Raw	Major Lake Treated
Alkalinity ($CaCO_3$)	<1.0	33.0	<1.0	19
Ca^{++}	1.0	17	0.95	92
Cl^-	6.3	8.0	6.5	7.0
EC(μmhos/cm)	35.0	110.0	34.10	90
Hardness ($CaCO_3$)	4.4	40.4	4.2	24
Langelier Index @ 5°C	-6.1	-0.1	-6.5	-1.4
Mg^{++}	0.48	0.52	0.40	0.40
pH	5.6	8.7	5.2	7.6
K^+	0.5	0.5	0.3	0.4
Na^+	3.7	3.6	3.5	9.0
TSS	27.0	85.0	24.0	75
TS	27.0	85.0	24.0	75
SO_4	4.8	8.2	5.0	20.4
TOC	2.4	1.4	4.0	2.5

Source: Division of Clinical Chemistry, Province of Nova Scotia, Halifax Tap Water

Units: mg/L

Appendix B: Turbulent Unit's Experimental Conditions.

No.	Q_W lit/min	Q_W m3/s	Q_A SCFH	Q_A lit/m	Q_A m3/s	Q_{2phse} lit/min	Q_{2phse} m3/s
Exp. 12	60.0000	0.0010			0.0000	60.0000	0.0010
Exp. 19	60.0000	0.0010			0.0000	60.0000	0.0010
Exp. 22	60.0000	0.0010			0.0000	60.0000	0.0010
Exp. 22-R	60.0000	0.0010			0.0000	60.0000	0.0010
Exp. 24	65.0000	0.0011			0.0000	65.0000	0.0011
Exp. 24-R	65.0000	0.0011			0.0000	65.0000	0.0011
Exp. 29	65.0000	0.0011	10.00	4.7192	0.0001	75.0000	0.0012
Exp. 29-R	65.0000	0.0011	10.0000	4.7192	0.0001	75.0000	0.0012
Exp. 30	65.0000	0.0011	15.0000	7.0788	0.0001	80.0000	0.0012
Exp. 30-R	65.0000	0.0011	10.0000	4.7192	0.0001	75.0000	0.0012
Exp. 36	50.0000	0.0008	0.5000	0.2360	0.0000	50.5000	0.0008
Exp. 36-R	50.0000	0.0008	0.5000	0.2360	0.0000	50.5000	0.0008
Exp. 39	55.0000	0.0009			0.0000	55.0000	0.0009
Exp. 39-R-1	55.0000	0.0009			0.0000	55.0000	0.0009
Exp. 39-R-2	60.0000	0.0010			0.0000	60.0000	0.0010
Exp. 41	70.0000	0.0012			0.0000	70.0000	0.0012
Exp. 41-R-1	65.0000	0.0011			0.0000	65.0000	0.0011
Exp. 41-R-2	75.0000	0.0013			0.0000	75.0000	0.0013
Exp. 42-R-1	65.0000	0.0011			0.0000	65.0000	0.0011
Exp. 42-R-2	70.0000	0.0012			0.0000	70.0000	0.0012
Exp. 44	60.0000	0.0010			0.0000	60.0000	0.0010

Appendix C: Turbulent Unit's Experimental Conditions (Cont.).

No.	Q_W lit/min	Q_W m3/s	Q_A SCFH	Q_A lit/m	Q_A m3/s	Q_{2phse} lit/min	Q_{2phse} m3/s
Exp. 44-R-1	60.0000	0.0010			0.0000	60.0000	0.0010
Exp. 46	50.0000	0.0008			0.0000	50.0000	0.0008
Exp. 46-R-1	70.0000	0.0012			0.0000	70.0000	0.0012
Exp. 48	50.0000	0.0008			0.0000	50.0000	0.0008
Exp. 51	60.0000	0.0010			0.0000	60.0000	0.0010
Exp. 51-R-1	60.0000	0.0010			0.0000	60.0000	0.0010
Exp. 52	50.0000	0.0008			0.0000	50.0000	0.0008
Exp. 59	50.0000	0.0008	0.5000	0.2360	0.0000	50.5000	0.0008

Appendix D: Turbulent Unit's Model, Measured Pressure Drops and superficial liquid and gas velocity.

No.	P_{in} Kpa	P_{out} kpa	Δp Psi	Δp Kpa Measured	β	Model P Kpa	ΔP Model Kpa	SV in Pipe m/s	SV in Orifice m/s
Exp. 12	310.264	224.0796	12.5	86.18446621	0.3937	229.207326	81.0567522	0.019735252	12.73239545
Exp. 19	310.264	220.6322	13	89.63184486	0.3937	229.207326	81.0567522	0.019735252	12.73239545
Exp. 22	310.264	227.527	12	82.73708756	0.3937	229.207326	81.0567522	0.019735252	12.73239545
Exp. 22-R	310.264	217.1849	13.5	93.0792235	0.3937	229.207326	81.0567522	0.019735252	12.73239545
Exp. 24	413.685	310.2641	15	103.4213595	0.3937	318.5563326	95.129105	0.021379857	13.7934284
Exp. 24-R	413.685	303.3693	16	110.3161168	0.3937	318.5563326	95.129105	0.021379857	13.7934284
Exp. 29	310.264	206.8427	15	103.4213594	0.3937	215.1349732	95.129105	0.021379857	13.7934284
Exp. 29-R	310.264	199.948	16	110.3161167	0.3937	215.1349732	95.129105	0.021379857	13.7934284
Exp. 30	344.738	234.4217	16	110.3161168	0.3937	249.6087597	95.129105	0.021379857	13.7934284
Exp. 30-R	310.264	213.7375	14	96.52660215	0.3937	215.1349732	95.129105	0.021379857	13.7934284
Exp. 36	344.738	268.8955	11	75.84233031	0.3937	288.4484535	56.2894112	0.016446044	10.61032954
Exp. 36-R	344.738	262.0008	12	82.7370876	0.3937	288.4484535	56.2894112	0.016446044	10.61032954
Exp. 39	358.527	282.685	11	75.84233023	0.4961	290.4171916	68.1101876	0.018090648	11.67136249
Exp. 39-R-1	344.738	268.8955	11	75.84233031	0.4961	276.6276771	68.1101876	0.018090648	11.67136249
Exp. 39-R-2	379.212	289.5798	13	89.63184484	0.4961	298.1548989	81.0567522	0.019735252	12.73239545
Exp. 41	344.738	241.3165	15	103.4213595	0.4961	234.4106186	110.3272461	0.023024461	14.85446136
Exp. 41-R-1	413.685	310.2641	15	103.4213595	0.4961	318.5563326	95.129105	0.021379857	13.7934284
Exp. 41-R-2	330.948	220.6322	16	110.3161168	0.4961	204.2971748	126.6511753	0.024669066	15.91549431
Exp. 42-R-1	344.738	241.3165	15	103.4213595	0.4961	249.6087597	95.129105	0.021379857	13.7934284
Exp. 42-R-2	379.212	262.0008	17	117.210874	0.4961	268.884405	110.3272461	0.023024461	14.85446136
Exp. 44	310.264	227.527	12	82.73708756	0.3937	229.207326	81.0567522	0.019735252	12.73239545
Exp. 44-R-1	310.264	224.0796	12.5	86.18446621	0.3937	229.207326	81.0567522	0.019735252	12.73239545

Appendix E: Turbulent Unit's Model, Measured Pressure Drops and superficial liquid and gas velocity.

No.	P_{in} Kpa	P_{out} kpa	Δp Psi	Δp Kpa Measured	β	Model P Kpa	ΔP Model Kpa	SV in Pipe m/s	SV in Orifice m/s
Exp. 46	344.738	262.0008	12	82.7370876	0.3937	288.4484535	56.2894112	0.016446044	10.61032954
Exp. 46-R-1	344.738	220.6322	18	124.1056314	0.3937	234.4106186	110.3272461	0.023024461	14.85446136
Exp. 48	344.738	255.106	13	89.6318449	0.3937	288.4484535	56.2894112	0.016446044	10.61032954
Exp. 51	344.738	248.2113	14	96.52660219	0.3937	263.6811125	81.0567522	0.019735252	12.73239545
Exp. 51-R-1	344.738	262.0008	12	82.7370876	0.3937	263.6811125	81.0567522	0.019735252	12.73239545
Exp. 52	344.738	268.8955	11	75.84233031	0.3937	288.4484535	56.2894112	0.016446044	10.61032954
Exp. 59	344.738	275.7903	10	68.94757302	0.3937	288.4484535	56.2894112	0.016446044	10.61032954

Appendix F: Measured pressure drop across the hydrocyclone.

Exp. # No.	P_{in} kPa	ΔP kPa	Exp. # No.	P_{in} kPa	ΔP kPa
Exp. 1	127.55	58.61	Exp. 32-R	189.61	101.71
Exp. 1-R	134.45	79.29	Exp. 33	141.34	44.82
Exp. 2	162.03	79.29	Exp. 33-R	148.24	58.61
Exp. 3	162.03	93.08	Exp. 34	162.03	47.92
Exp. 4	175.82	79.29	Exp. 34-R	162.03	51.71
Exp. 5	196.5	93.08	Exp. 35	148.24	57.92
Exp. 6	196.5	99.97	Exp. 37	189.61	128.61
Exp. 7	175.82	93.08	Exp. 37-R-1	210.29	120.18
Exp. 8	196.5	72.39	Exp. 37-R-2	162.03	124.82
Exp. 9	196.5	86.18	Exp. 38	162.03	167.92
Exp. 10	175.82	72.39	Exp. 38-R-1	162.03	174.13
Exp. 11	196.5	79.29	Exp. 38-R-2	175.82	167.92
Exp. 13	175.82	72.39	Exp. 40	196.5	58.61
Exp. 14	175.82	79.29	Exp. 40-R-1	182.71	144.82
Exp. 15	196.5	86.18	Exp. 40-R-2	162.03	137.92
Exp. 16	217.18	60.87	Exp. 40-R-3	175.82	121.71
Exp. 17	203.4	86.18	Exp. 41-R-3	162.03	81.03
Exp. 18	148.24	81.71	Exp. 42	265.45	72.39
Exp. 20	203.4	93.08	Exp. 42-R-3	265.45	88.61
Exp. 20-R-1	217.18	83.76	Exp. 43	196.5	72.39
Exp. 20-R-2	196.5	69.97	Exp. 43-R-1	230.97	85.5
Exp. 20-R-3	217.18	99.97	Exp. 45	368.87	93.08
Exp. 21	203.4	72.39	Exp. 45-R-1	368.87	72.39
Exp. 23	189.61	58.61	Exp. 47	189.61	58.61
Exp. 23-R	148.24	51.71	Exp. 49	230.97	58.61
Exp. 25	162.03	61.71	Exp. 49-R-1	230.97	65.5
Exp. 25-R-1	175.82	79.29	Exp. 49-R-2	265.45	93.08
Exp. 25-R-2	196.5	86.18	Exp. 50	217.18	51.71
Exp. 26	162.03	94.82	Exp. 50-R	196.5	72.39
Exp. 27	175.82	100.61	Exp. 53	203.4	58.61
Exp. 27-R	175.82	72.39	Exp. 54	162.03	44.13
Exp. 28	162.03	104.82	Exp. 55	134.45	37.92
Exp. 28-R	182.71	58.61	Exp. 56	162.03	37.92
Exp. 31	189.61	72.39	Exp. 57	162.03	94.82
Exp. 31-R	162.03	84.13	Exp. 58	148.24	54.13
Exp. 32	196.5	84.82	Exp. 58	148.24	101.71

Appendix G: Bubble Size Distribution in Turbulent Unit Stream. (Malvern Data).

Sample	Focal L	Beam L	Obscuration	Volume	Log. Diff.	D (v,o.5)	D (v,0.9)	D(v, 0.1)	D(4,3)	D(3,2)	Span	Spec. Surf.
No	mm	mm		Conc. %		µm	µm	µm	µm	µm		m2/s
Exp.12	300	2	0.4826	0.94	4.03	38	65	7	50	17	3.1	0.02
Exp.19	100	2	0.1216	0.12	5.38	35	61	8.2	47	15.5	1.3	0.06
Exp.22	100	2	0.0002	0	5.86	41	70	8.1	64	20	1.1	0.19
Exp.22-R	100	2	0	0	6.68	30	58.5	9	50	14	0.6	0.25
Exp.24	100	2	0.0024	0.0019	6.13	26	55	5	41	12	0.4	0.11
Exp.24-R	100	2	0.0081	0.0004	5.6	39.8	68.8	5.5	57	10	1.2	0.13
Exp.29	100	2	0.6703	1.5041	2.98	44.5	76	6	53	13	1	0.05
Exp.29-R	100	2	0.0299	0.0527	5.3	41	80	5.3	65	11	0.5	0.05
Exp.30	300	2	0.6809	2.4137	4.06	45	85	5.5	70	11.5	1.4	0
Exp.30-R	300	2	0.8235	4.6748	4.79	50	88	6	66	16	1.4	0.02
Exp.36	100	2	0.9069	2.581	4.18	57	95	22.5	67	33	1.3	0.05
Exp.36-R	100	2	0.9024	2.557	4.26	45.3	86	23	75	28	1.2	0.05
Exp.39	300	2	-0.0023	0	6.44	60	95	24	78	35	0.6	0.04
Exp.39-R-1	300	2	0.8138	3.9826	4.24	73	112	25	90	36	1.2	0.02
Exp.39-R-2	300	2	0.4363	1.1943	4.59	44	87	18	75	20	1.1	0.03
Exp.41	300	2	0.0024	0.0011	6.82	45	85	6.1	74	13	1.4	0.03
Exp.41-R-1	300	2	0.0144	0.0738	5.02	48	90	5.6	61	15	0.6	0.02
Exp.41-R2	300	2	0.0144	0.0006	6.98	39.5	78	6	56	11	1.6	0.02
Exp.41-R3	300	2	0.7677	1.4143	4.7	42	75	6.5	55	16.5	0.7	0.04

Appendix H: Bubble Size Distribution in Turbulent Unit Stream. (Malvern Data) cont.

Sample	Focal L	Beam L	Obscuration	Volume	Log. Diff.	D (v,o.5)	D (v,0.9)	D(v, 0.1)	D(4,3)	D(3,2)	Span	Spec. Surf.
No	mm	mm		Conc. %		µm	µm	µm	µm	µm		m2/s
Exp.42-R-2	300	2	1.1943	0.4363	4.59	28	54	5	42	9	1.1	0.03
Exp.44	100	2	0.0204	0.0063	5.81	56	90	10	70	18.2	1.5	0.05
Exp.44-R-1	100	2	-0.0723	0	5.15	55	95	13	74	17.5	1.3	0.05
Exp.46	63	2	0.04241	0.0009	5.15	39.5	77	9	53	19	1.6	2.15
Exp.46-R-1	63	2	-0.0043	0	6.11	79.4	101.3	16	79	10	0.5	0.07
Exp.48	100	2	0.9303	1.7505	4.21	44.3	68.3	8.1	48	17	0.9	0.08
Exp.51	100	2	0.0204	0.0063	5.81	52	95.5	7.5	80	12.3	1.5	0.05
Exp.51-R-1	100	2	-0.0723	0	5.15	58.4	101.4	9	85.5	15	1.3	0.05
Exp.52	100	2	0.9088	1.8558	3.89	71.4	103.5	18	87	33	1.1	0.07
Exp.59	100	2	0.9069	2.581	4.18	79.6	112	25	90	40	1.3	0.05

Appendix I: Bubble Size Distribution Results in Underflow Stream.

Sample	Focal L	Beam L	Obscuration	Volume	Log. Diff.	D (v,o.5)	D (v,0.9)	D(v, 0.1)	D(4,3)	D(3,2)	Span	Spec. Surf.
No	mm	mm		Conc. %		µm	µm	µm	µm	µm		m2/s
Exp.1	100	2	0.0078	0.0081	4.54	22	149.7	40.3	55.1	14.2	1.1	0.05
Exp.1-R	100	2	0.2306	0	4.54	21.7	50.9	3.6	23	8.4	3	0
Exp.2	100	2	0.2306	0	0	22.7	50.9	3.6	23	8.4	3	0
Exp.3	100	2	0.0367	0.0372	5.17	22.4	119.5	36.7	70.8	17.5	1.3	0.06
Exp.4	100	2	0.0163	0.0096	4.12	22.1	61.4	25.7	41.9	14.2	0.9	0.09
Exp.5	100	2	-0.0143	0	4.45	21.6	78.2	24.9	45.4	18.5	1.4	0.07
Exp.6	100	2	0.0772	0.075	4.92	23.1	106.4	37.7	64.2	19.2	1.2	0.06
Exp.10	100	2	0.1403	0.1252	4.92	21.1	82.4	34.9	42.6	20.7	1	0.07
Exp.11	300	2	0.4545	0.9961	5.11	22	110.2	90.1	54.7	21.2	0.2	0.06
Exp.14	100	2	0.0974	0.1116	5.63	21.4	156.4	42.9	98	20.1	1	0.05
Exp.15	100	2	-0.0233	0	5.16	23.7	83.8	37.7	104.2	33.1	0.9	0.07
Exp.16	100	2	0.1905	0.2136	5.08	23.1	83.7	45.2	52.9	21.7	0.6	0.08
Exp.17	100	2	0.0913	0.1008	5.18	23.2	87.5	45.5	61.4	20.4	0.7	0.07
Exp.18	100	2	0.153	0.1763	5.07	22.4	111.6	42	61.2	20.6	1.1	0.06
Exp.21	100	2	0.0054	0.0054	5.93	23.2	135	33.2	70.7	18.9	1.4	0.05
Exp.23	100	2	-0.0088	0	5.99	23.8	50.3	2.4	78.3	16.4	4.9	0.11
Exp.23-R	100	2	-0.0259	0	6.45	22.2	125.6	10.8	18.4	16.1	1.6	0.05
Exp.25	100	2	-0.0049	0	6.25	22.6	79.9	58.8	69.7	18.7	0.3	0.09
Exp.25-R	100	2	-0.0049	0	6.75	22.7	44.8	7	69	18.2	1.3	0.13
Exp.25-R-2	100	2	-0.0021	0.0002	6.06	23.3	26.4	2.7	27.7	18.2	1	0.25

Appendix J: Bubble Size Distribution Results in Underflow Stream. Cont.

Sample	Focal L	Beam L	Obscuration	Volume	Log. Diff.	D (v,o.5)	D (v,0.9)	D(v, 0.1)	D(4,3)	D(3,2)	Span	Spec. Surf.
No	mm	mm		Conc. %		µm	µm	µm	µm	µm		m2/s
Exp.28	100	2	0.0355	0.0822	5.81	21.8	161.6	101.1	16.4	26.1	0.5	0.05
Exp.28-R	100	2	0.0615	0.0929	5.32	22.7	134.9	62.8	69.8	26	0.8	0.05
Exp.31	300	2	0.9415	2.1729	3.93	21.9	112.8	30.5	92.9	18.7	1.6	0.02
Exp.31-R	300	2	0.9135	1.915	4.17	20.8	113.7	31.6	72.3	1.9	1.6	0.02
Exp.33	100	2	0.483	0.7299	4.98	23.8	54.6	54.2	70.9	23.5	0.4	0.08
Exp.33-R	100	2	0.9364	1.7292	3.89	22.5	54.6	29.3	41.8	19.6	1	0.08
Exp.34	100	2	0.027	0.001	6.26	23.3	153.1	0.8	62.8	19.9	1.5	0.05
Exp.34-R	100	2	0.0033	0.001	5.33	25.7	5.5	0.7	46.5	23.5	4.2	1.18
Exp.35	100	2	0.0627	0.0929	4.95	24.9	141	52.8	73.9	22.2	1	0.05
Exp.38	300	2	0.0352	0.0402	4.94	21.9	423.3	33.9	32.1	21.2	1.7	0.02
Exp.38-R-1	300	2	0.7481	1.3647	4.63	21.8	149.7	4.3	66.4	46	0.6	0.04
Exp.38-R-2	300	2	0.7677	1.4143	4.7	21.9	70.9	3.6	69.1	18.8	0.7	0.04
Exp.40	300	2	0.0593	0.3295	6.76	25.1	80.9	3.6	54	20.9	0.6	0.02
Exp.40-R-1	300	2	0.7789	3.4346	5.88	22.9	119.5	6.7	71.1	14.2	1.7	0.02
Exp.40-R-2	300	2	0.4934	0.8521	5.28	23	61.4	5.7	62.8	18.3	0.2	0.08
Exp.40-R-3	300	2	-0.00308	0	6.45	21.9	78.2	4.9	69.1	20.2	1.2	0.02
Exp.42	300	2	-0.0056	0	7.02	20.9	106.4	7.7	74.1	23.8	0.2	0.08
Exp.42-R-3	300	2	-0.0056	0	7.02	28.4	60.6	5.6	40.1	23.8	0.2	0.08
Exp.43	100	2	-0.057	0	6.26	23.2	82.4	4.9	39.6	13.4	12.9	0.14
Exp.43-R-1	100	2	0.0711	0.0074	5.09	20.8	110.2	9.1	46.1	15.9	1.2	0.21

Appendix F: Bubble Size Distribution Results in Underflow Stream (Cont).

Sample	Focal L	Beam L	Obscuration	Volume	Log. Diff.	D (v,o.5)	D (v,0.9)	D(v, 0.1)	D(4,3)	D(3,2)	Span	Spec. Surf.
No	mm	mm		Conc. %		µm	µm	µm	µm	µm		m2/s
Exp.45	63	2	0.0266	0.001	4.93	21.2	156.4	4.9	1.8	2.6	2.3	0.61
Exp.45-R-1	63	2	0.0342	0.0008	4.7	23.1	83.8	7.7	72.6	21.5	0.9	2.7
Exp.47	63	2	0.0009	0.0002	6.52	24.8	83.7	5.2	62.3	10.1	1.6	0.05
Exp.49	100	2	0.0112	0.0014	5.85	22.3	87.5	5.5	3.9	6.3	1.4	0.05
Exp.49-R-1	100	2	0.0437	0.0028	7.03	21.5	111.6	4.2	17.6	13.7	0.6	1.43
Exp.49-R-2	100	2	0.0349	0.003	5.15	22.1	135	3.2	10.1	15.2	8.5	0.14
Exp.50	100	2	-0.057	0	6.26	23.2	50.3	2.4	19.6	13.4	12.9	0.14
Exp.50-R-1	100	2	-0.0711	0.0074	5.09	22.8	125.6	10.8	42.5	15.9	1.2	0.21
Exp.55	100	2	0.0189	0.0007	4.94	30	79.9	5.8	29.8	12	30.2	0.09
Exp.56	100	2	0.013	0.0008	4.69	29.8	44.8	7	37.8	13.5	2.5	0.09
Exp.57	100	2	0.974	1.5261	3.73	22.5	46.4	2.7	44.5	25	1.2	0.09
Exp.58	100	2	0.9387	1.5347	3.66	25.5	161.6	11.1	66.4	20.7	1.1	0.08

Appendix K: Bubble Size Distribution Results in Overflow Stream.

Sample	Focal L	Beam L	Obscuration	Volume	Log. Diff.	D (v,o.5)	D (v,0.9)	D(v, 0.1)	D(4,3)	D(3,2)	Span	Spec. Surf.
No	mm	mm		Conc. %		µm	µm	µm	µm	µm		m2/s
Exp.7	100	2	-0.0089	0	4.65	29.2	127.9	9.2	70.6	22.3	1.6	0.06
Exp.8	100	2	0.2306	0	0	25.7	50.9	4.8	23	18.4	3	0
Exp.9	100	2	0.0053	0.0033	5.54	39.6	60.6	3.7	42.6	36.7	0.9	0.09
Exp.13	300	2	0.0164	0.0129	6.32	32.6	88.2	8.8	67	30	0.7	0.08
Exp.20-R-1	100	2	-0.0071	0	6.2	31.1	132.6	13.8	36.7	25.8	16.1	0.05
Exp.20-R-2	100	2	0.0016	0.0013	5.78	33.3	160.6	48	123.5	30.9	0.5	0.05
Exp.20-R-3	100	2	0.0016	0.0013	5.78	32.3	160.6	68	123.5	30.9	0.5	0.05
Exp.26	100	2	-0.0001	0	6.54	25.2	75.2	2.3	35.9	21.8	2.8	0.09
Exp.27	100	2	-0.0082	0	5.43	29.4	34.8	6.8	19.1	25.5	1.1	0.19
Exp.27-R	100	2	0.0287	0.105	6.6	26.8	26.2	3.9	22.3	23.6	0.4	0.4
Exp.32	300	2	0.2051	1.9143	4.33	30.6	167.1	2.9	337.2	27	0.7	0.02
Exp.32-R	300	2	0.0905	0.5091	5.69	39.5	168.4	5.5	341.8	32.6	0.6	0.02
Exp.37	300	2	0.0684	0.3692	5.61	347.5	467.8	3.3	336.4	229.2	0.7	0.02
Exp.37-R-1	300	2	0.7789	3.4346	5.88	229.1	389.3	3.2	232.2	144.2	1.4	0.02
Exp.37-R-2	300	2	0.7789	3.4346	5.88	29.1	189.3	3.1	280.6	18.4	1.2	0.02
Exp.53	100	2	0.0472	0.0019	5.63	35.4	141.4	2.3	43.2	21.9	57.7	0.05
Exp.54	100	2	0.0316	0.0058	5.77	34	89.9	3.8	55.7	20.9	1.4	0.07

Appendix L: Bubble Volume Distribution (BVD)

Results Sample: BVD-1-Underflow

Channel #	$d_{up,i}$	*Ni*	$\overline{d}$	*Vi*	*Ni.Vi*	*P*	$P_{cum}.V$
1	188	4.6	188				1
2	162	11.2	174.51647	2782966.1	31169220.5	0.3400788	0.6599212
3	140	14.8	150.5988	1788394	26468230.8	0.2887876	0.3711336
4	121	15.7	130.15376	1154433	18124598	0.1977525	0.1733811
5	104	12.3	112.17843	739139.97	9091421.6	0.099194	0.074187
6	89.9	7.1	96.69333	473356.31	3360829.79	0.0366691	0.037518
7	77.5	3.1	83.470055	304502.4	943957.426	0.0102993	0.0272187
8	66.9	2.9	72.005208	195474.61	566876.366	0.006185	0.0210337
9	57.7	6	62.129944	125574.52	753447.106	0.0082207	0.012813
10	49.8	8.8	53.604664	80650.369	709723.243	0.0077436	0.0050694
11	42.9	6.8	46.221424	51704.528	351590.788	0.0038361	0.0012333
12	37.1	2.3	39.894736	33246.461	76466.8607	0.0008343	0.000399
13	32	0.5	34.455769	21418.273	10709.1366	0.0001168	0.0002821
14	27.6	0.9	29.718681	13743.179	12368.8614	0.000135	0.0001472
15	23.8	0.9	25.62967	8815.1089	7933.59799	8.656E-05	6.063E-05
16	20.5	0.7	22.088459	5642.8025	3949.96174	4.31E-05	1.753E-05
17	17.7	0.4	19.048622	3619.0061	1447.60243	1.579E-05	1.738E-06
18	15.3	0	16.456306	2333.4348	0	0	1.738E-06
19	13.2	0	14.211263	1502.7844	0	0	1.738E-06
20	11.4	0.1	12.267029	966.53324	96.6533244	1.055E-06	6.835E-07
21	9.8	0	10.569768	618.29397	0	0	6.835E-07
22	8.5	0	9.1268834	398.07612	0	0	6.835E-07
23	7.3	0.1	7.8771822	255.92417	25.5924169	2.792E-07	4.043E-07
24	6.3	0	6.7815927	163.30284	0	0	4.043E-07
25	5.4	0.2	5.8326666	103.8963	20.7792602	2.267E-07	1.776E-07
26	4.7	0.1	5.0378567	66.94776	6.69477598	7.304E-08	1.045E-07
27	4.1	0.1	4.3897608	44.291582	4.42915822	4.833E-08	5.62E-08
28	3.5	0.1	3.7881394	28.462725	2.84627248	3.105E-08	2.514E-08
29	3	0	3.2403703	17.814866	0	0	2.514E-08
30	2.6	0.1	2.792848	11.406188	1.1406188	1.244E-08	1.27E-08
31	2.2	0.1	2.3916521	7.1629623	0.71629623	7.815E-09	4.882E-09
32	1.9	0.1	2.0445048	4.4746909	0.44746909	4.882E-09	0
BVD-1				**Σ NiVi =**	**91652931**		

Appendix H: Bubble Volume Distribution (BVD)

Sample: BVD-1

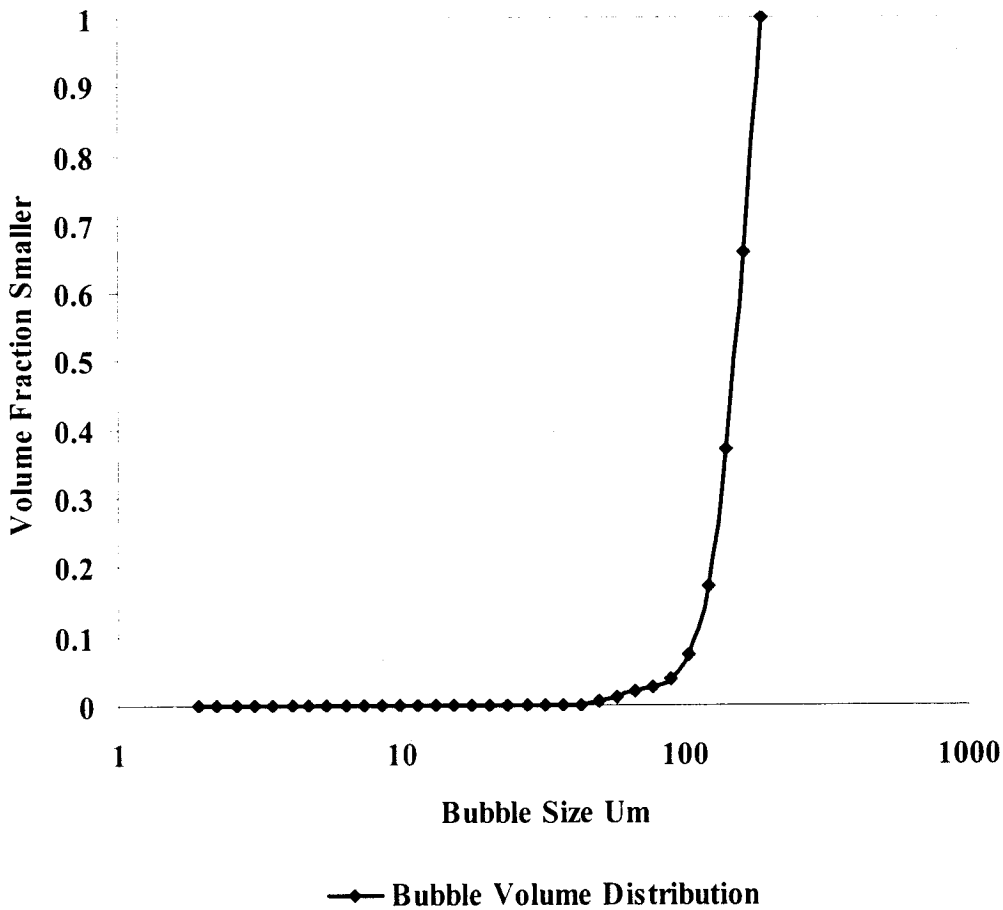

Appendix H:

Bubble Volume Distribution (BVD)

Sample: BVD-50-R.

Channel #	$d_{up,i}$	*Ni*	$\overline{d}$	*Vi*	*Ni.Vi*	*P*	$P_{cum}.V$
1	188	0	188				1
2	162	0	174.51647	2782966.1	0	0	1
3	140	0	150.5988	1788394	0	0	1
4	121	0	130.15376	1154433	0	0	1
5	104	0	112.17843	739139.97	0	0	1
6	89.9	0	96.69333	473356.31	0	0	1
7	77.5	0	83.470055	304502.4	0	0	1
8	66.9	0	72.005208	195474.61	0	0	1
9	57.7	0.1	62.129944	125574.52	12557.452	0.0101326	0.9898674
10	49.8	0.1	53.604664	80650.369	8065.0369	0.0065077	0.9833597
11	42.9	0	46.221424	51704.528	0	0	0.9833597
12	37.1	11.9	39.894736	33246.461	395632.89	0.3192365	0.6641231
13	32	22.2	34.455769	21418.273	475485.67	0.3836698	0.2804533
14	27.6	20.5	29.718681	13743.179	281735.18	0.2273324	0.0531209
15	23.8	5.4	25.62967	8815.1089	47601.588	0.0384098	0.0147112
16	20.5	0	22.088459	5642.8025	0	0	0.0147112
17	17.7	0.4	19.048622	3619.0061	1447.6024	0.0011681	0.0135431
18	15.3	1	16.456306	2333.4348	2333.4348	0.0018829	0.0116602
19	13.2	3.5	14.211263	1502.7844	5259.7452	0.0042441	0.0074162
20	11.4	5.4	12.267029	966.53324	5219.2795	0.0042114	0.0032047
21	9.8	2.7	10.569768	618.29397	1669.3937	0.001347	0.0018577
22	8.5	2.4	9.1268834	398.07612	955.38269	0.0007709	0.0010868
23	7.3	2.9	7.8771822	255.92417	742.18009	0.0005989	0.0004879
24	6.3	2.1	6.7815927	163.30284	342.93596	0.0002767	0.0002112
25	5.4	1	5.8326666	103.8963	103.8963	8.383E-05	0.0001274
26	4.7	0.6	5.0378567	66.94776	40.168656	3.241E-05	9.495E-05
27	4.1	0.6	4.3897608	44.291582	26.574949	2.144E-05	7.351E-05
28	3.5	0.8	3.7881394	28.462725	22.77018	1.837E-05	5.513E-05
29	3	1.1	3.2403703	17.814866	19.596353	1.581E-05	3.932E-05
30	2.6	1.4	2.792848	11.406188	15.968663	1.289E-05	2.644E-05
31	2.2	2.7	2.3916521	7.1629623	19.339998	1.561E-05	1.083E-05
32	1.9	3	2.0445048	4.4746909	13.424073	1.083E-05	0
BVD-50-R				**Σ NiVi =**	**1239309**		

Appendix H:

Bubble Volume Distribution (BVD)

Sample: BVD-50-R.

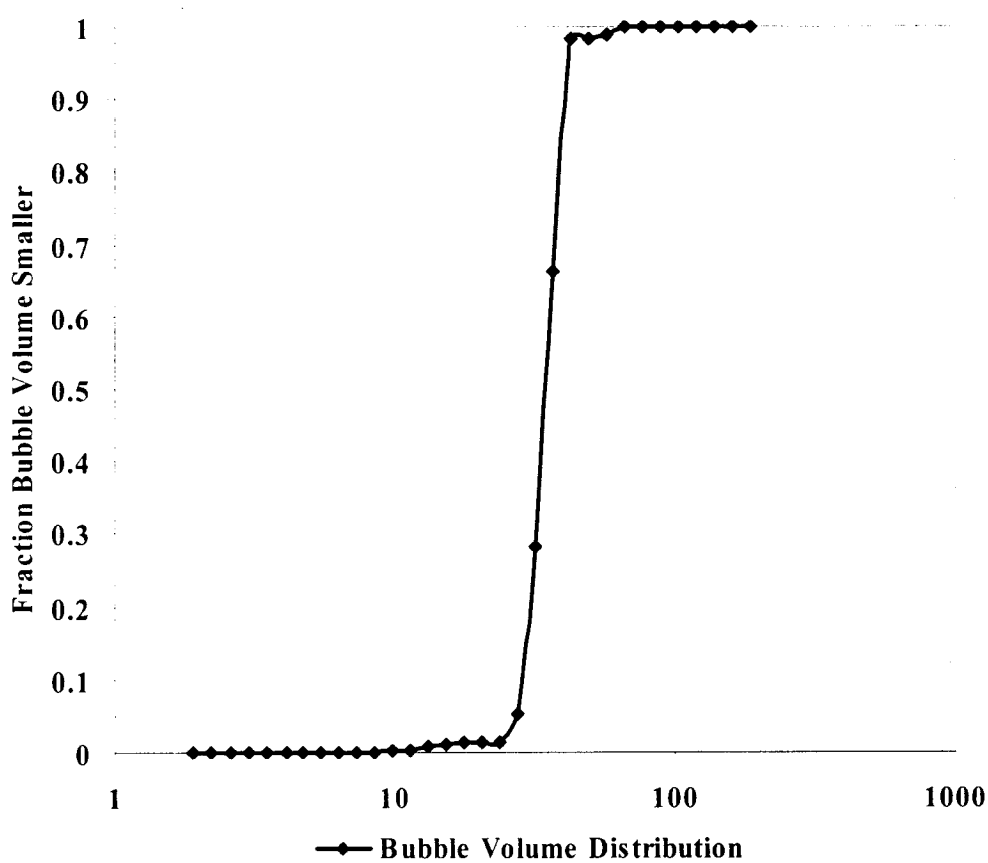

Appendix M: Mass balance calculations across the gas liquid cylindrical hydrocyclone.

Exp. #	Sampling Point	Dissolved Air	Introduced Air	Total Inlet Flow	Inlet Water Flow	Inlet Water Flow	Inlet Air Flow
No.	OF	cm3/Qw	cm3/s	Σqin cm3/s	Qin.w lit/min	Qin.w cm3/s	Qin.A cm3/s
Exp. 24	OF	75.83	0	1159.167	65	1083.33	75.83
Exp. 24-R	OF	75.83	0	1159.167	65	1083.33	75.83
Exp. 25	OF	75.83	0	1159.167	65	1083.33	75.83
Exp. 25-R-1	OF	75.83	0	1159.167	65	1083.33	75.83
Exp. 25-R-2	OF	75.83	0	1159.167	65	1083.33	75.83
Exp. 26	OF	75.83	78.67	1237.83	65	1083.33	154.50
Exp. 27	OF	75.83	78.67	1237.83	65	1083.33	154.50
Exp. 27-R	OF	75.83	78.67	1237.83	65	1083.33	154.50
Exp. 28	OF	75.83	78.67	1237.83	65	1083.33	154.50
Exp. 28-R	OF	75.83	78.67	1237.83	65	1083.33	154.50
Exp. 29	OF	75.83	78.67	1237.83	65	1083.33	154.50
Exp. 29-R	OF	75.83	78.67	1237.83	65	1083.33	154.50
Exp. 30	OF	75.83	78.67	1237.83	65	1083.33	154.50
Exp. 30-R	OF	75.83	78.67	1237.83	65	1083.33	154.50
Exp. 31	OF	75.83	78.67	1237.83	65	1083.33	154.50
Exp. 31-R	OF	75.83	78.67	1237.83	65	1083.33	154.50
Exp. 32	OF	75.83	78.67	1237.83	65	1083.33	154.50
Exp. 32-R	UF	75.83	78.67	1237.83	65	1083.33	154.50
Exp. 33	UF	58.33	7.867	899.53	50	833.33	66.20

Appendix N: Mass balance calculations across the gas liquid cylindrical hydrocyclone.

Exp. #	Sampling Point	Dissolved Air	Introduced Air	Total Inlet Flow	Inlet Water Flow	Inlet Water Flow	Inlet Air Flow
No.	UF	cm3/Qw	cm3/s	Σqin cm3/s	Qin.w lit/min	Qin.w cm3/s	Qin.A cm3/s
Exp. 33-R	UF	58.33	7.86	899.53	50	833.33	66.20
Exp. 34	UF	58.33	0	891.67	50	833.33	58.33
Exp. 34-R	UF	58.33	0	891.67	50	833.33	58.33
Exp. 35	UF	58.33	3.93	895.60	50	833.33	62.26
Exp. 36	UF	58.33	3.93	895.60	50	833.33	62.26
Exp. 36-R	UF	58.33	3.93	895.60	50	833.33	62.27
Exp. 37	UF	87.5	78.67	1416.17	75	1250	166.17
Exp. 37-R-1	UF	87.5	78.67	1416.17	75	1250	166.17
Exp. 37-R-2	UF	87.5	78.67	1416.17	75	1250	166.17
Exp. 38	UF	87.5	196.67	1534.17	75	1250	284.17
Exp. 38-R-1	UF	87.5	196.67	1534.17	75	1250	284.17

Appendix I: Mass balance calculations across the gas liquid cylindrical hydrocyclone cont'd.

Exp. #	Sampling Point	Dissolved Air	Introduced Air	Total Inlet Flow	Inlet Water Flow	Inlet Water Flow	Inlet Air Flow
No.	Under-flow	cm3/Qw	cm3/s	Σqin cm3/s	Qin.w lit/min	Qin.w cm3/s	Qin.A cm3/s
Exp. 38-R-2	UF	87.5	196.6667	1534.16	75	1250	284.17
Exp. 39	UF	70	0	1070	60	1000	70
Exp. 39-R-1	UF	70	0	1070	60	1000	70
Exp. 39-R-2	UF	70	0	1070	60	1000	70
Exp. 40	UF	58.33	0	891.67	50	833.33	58.33
Exp. 40-R-1	UF	87.5	118	1455.5	75	1250	205.5
Exp. 40-R-2	UF	87.5	118	1455.5	75	1250	205.5
Exp. 40-R-3	UF	87.5	0	1337.5	75	1250	87.5
Exp. 41	UF	75.83	0	1159.17	65	1083.33	75.83
Exp. 41-R-1	UF	87.5	0	1337.5	75	1250	87.5
Exp. 41-R-2	UF	87.5	0	1337.5	75	1250	87.5
Exp. 41-R-3	UF	75.83	0	1159.17	65	1083.33	75.83
Exp. 42	UF	75.83	0	1159.17	65	1083.33	75.83
Exp. 42-R-1	UF	75.83	0	1159.17	65	1083.33	75.83
Exp. 42-R-2	UF	75.83	0	1159.17	65	1083.33	75.83
Exp. 42-R-3	UF	75.83	0	1159.17	65	1083.33	75.83
Exp. 43	UF	75.83	0	1159.17	65	1083.33	75.83
Exp. 43-R-1	UF	75.83	0	1159.17	65	1083.33	75.83
Exp. 44	UF	70	0	1070	60	1000	70
Exp. 44-R-1	UF	70	0	1070	60	1000	70

Appendix I: Mass balance calculations across the gas liquid cylindrical hydrocyclone cont'd.

Exp. #	Sampling Point	Dissolved Air	Introduced Air	Total Inlet Flow	Inlet Water Flow	Inlet Water Flow	Inlet Air Flow
No.	Under-flow	cm3/Qw	cm3/s	Σqin cm3/s	Qin.w lit/min	Qin.w cm3/s	Qin.A cm3/s
Exp. 45	UF	81.66666667	0	1248.333333	70	1166.666667	81.66666667
Exp. 45-R-1	UF	81.66666667	0	1248.333333	70	1166.666667	81.66666667
Exp. 46	UF	58.33333333	0	891.6666667	50	833.3333333	58.33333333
Exp. 46-R-1	UF	58.33333333	0	891.6666667	50	833.3333333	58.33333333
Exp. 47	UF	58.33333333	0	891.6666667	50	833.3333333	58.33333333
Exp. 48	UF	58.33333333	0	891.6666667	50	833.3333333	58.33333333
Exp. 49	UF	70	0	1070	60	1000	70
Exp. 49-R-1	UF	70	0	1070	60	1000	70
Exp. 49-R-2	UF	70	0	1070	60	1000	70
Exp. 50	UF	70	0	1070	60	1000	70

Appendix I: Mass balance calculations across the gas liquid cylindrical hydrocyclone cont'd.

Exp. #	Sampling Point	Dissolved Air	Introduced Air	Total Inlet Flow	Inlet Water Flow	Inlet Water Flow	Inlet Air Flow
No.	Underflow	cm3 Qw	cm3/s	Σqin cm3/s	Qin.w lit/min	Qin.w cm3/s	Qin.A cm3/s
Exp. 50-R	UF	70	0	1070	60	1000	70
Exp. 51	UF	70	0	1070	60	1000	70
Exp. 51-R-1	UF	70	0	1070	60	1000	70
Exp. 52	UF	58.33	0	891.67	50	833.33	58.33
Exp. 53	UF	58.33	0	891.67	50	833.33	58.33
Exp. 54	UF	58.33	0	891.67	50	833.33	58.33
Exp. 55	UF	46.66	0	713.3	40	666.67	46.67
Exp. 56	UF	46.66	0	713.33	40	666.67	46.67
Exp. 57	UF	58.33	196.67	1088.33	50	833.33	255.00
Exp. 58	UF	58.33	7.87	899.53	50	833.33	66.20
Exp. 59	UF	58.33	3.93	895.60	50	833.33	62.26

Appendix I: Mass balance calculations across the gas liquid cylindrical hydrocyclone cont'd.

Exp. #	OF. Water Rate	OF. Air Rate	Σ Overflow Rate	UF. Water Rate	UF. Air Rate	UF. Air	Σ UF Flow Rate	Surf. Triton X100
No.	Qo.w cm3/s	Qo.A	Σqo cm3/s	Qu.w cm3	Qu.A	cm3	Σqu cm3	ppm
Exp. 24	40.10	75.81	115.92	1043.23	0.0019	0.0198	1043.25	
Exp. 24-R	40.08	75.82	115.92	1043.24	0.0004	0.0041	1043.25	
Exp. 25	40.08	75.83	115.92	1043.25	0	0	1043.25	
Exp. 25-R-1	40.08	75.83	115.92	1043.25	0	0	1043.25	
Exp. 25-R-2	40.08	75.83	115.92	1043.25	0.0002	0.0021	1043.25	
Exp. 26	-30.71	154.50	123.783	1114.05	0	0	1114.05	
Exp. 27	-30.71	154.50	123.783	1114.05	0	0	1114.05	
Exp. 27-R	-30.59	154.38	123.783	1113.93	0.010	0.12	1114.05	
Exp. 28	-29.80	153.58	123.783	1113.13	0.082	0.91	1114.05	
Exp. 28-R	-29.61	153.39	123.783	1112.94	0.099	1.11	1114.05	
Exp. 29	-13.96	137.74	123.783	1097.29	1.504	16.75	1114.05	
Exp. 29-R	-30.12	153.91	123.783	1113.46	0.052	0.58	1114.05	
Exp. 30	-3.82	127.61	123.783	1087.16	2.41	26.89	1114.05	
Exp. 30-R	21.36	102.42	123.783	1061.97	4.67	52.08	1114.05	
Exp. 31	-6.51	130.29	123.783	1089.84	2.17	24.20	1114.05	
Exp. 31-R	-9.38	133.16	123.783	1092.71	1.91	21.33	1114.05	
Exp. 32	-9.39	133.17	123.783	1092.72	1.91	21.32	1114.05	
Exp. 32-R	-25.04	148.82	123.783	1108.37	0.51	5.67	1114.05	
Exp. 33	29.66	60.29	89.95	803.67	0.73	5.90	809.58	30
Exp. 33-R	37.75	52.19	89.95	795.57	1.73	14.01	809.58	30

Appendix I: Mass balance calculations across the gas liquid cylindrical hydrocyclone cont'd.

Exp. # No.	OF. Water Rate Qo.w cm3/s	OF. Air Rate Qo.A	Σ Overflow Rate Σqo cm3/s	UF. Water Rate Qu.w cm3	UF. Air Rate Qu.A	UF. Air cm3	Σ UF Flow Rate Σqu cm3	Surf. Triton X100 ppm
Exp. 34	30.84	58.32	89.17	802.49	0.001	0.008025	802.5	30
Exp. 34-R	30.84	58.32	89.17	802.49	0.001	0.008025	802.5	30
Exp. 35	28.04	61.52	89.17	805.29	0.0929	0.75	806.04	30
Exp. 36	48.09	41.46	89.17	785.24	2.581	20.80	806.04	30
Exp. 36-R	47.90	41.66	89.17	785.43	2.557	20.61	806.04	30
Exp. 37	-19.84	161.46	141.67	1269.84	0.3692	4.70	1274.55	15
Exp. 37-R-1	19.22	122.39	141.67	1230.77	3.4346	43.77	1274.55	15
Exp. 37-R-2	5.56	136.06	141.67	1244.44	2.3624	30.11	1274.55	15
Exp. 38	-130.19	283.62	153.42	1380.19	0.0402	0.55	1380.75	15
Exp. 38-R-1	-111.91	265.33	153.42	1361.90	1.3647	18.84	1380.75	15

Appendix I: Mass balance calculations across the gas liquid cylindrical hydrocyclone cont'd.

Exp. #	OF. Water Rate	OF. Air Rate	Σ Overflow Rate	UF. Water Rate	UF. Air Rate	UF. Air	Σ UF Flow Rate	Surf. Triton X100
No.	Qo.w cm3/s	Qo.A	Σqo cm3/s	Qu.w cm3	Qu.A	cm3	Σqu cm3	ppm
Exp. 38-R-2	-111.22	264.63	153.41	1361.22	1.4143	19.52	1380.75	15
Exp. 39	37	70	107	963	0	0	963	
Exp. 39-R-1	75.35	31.65	107	924.65	3.99	38.35	963	
Exp. 39-R-2	48.45	58.54	107	951.54	1.19	11.46	963	
Exp. 40	33.47	55.69	89.17	799.85	0.33	2.64	802.5	
Exp. 40-R-1	-14.95	160.51	145.55	1264.95	3.44	44.99	1309.95	
Exp. 40-R-2	-48.78	194.33	145.55	1298.79	0.85	11.16	1309.95	
Exp. 40-R-3	46.25	87.5	133.75	1203.75	0	0	1203.75	
Exp. 41	40.09	75.82	115.92	1043.24	0.001	0.011	1043.25	25
Exp. 41-R-1	47.14	86.61	133.75	1202.86	0.074	0.89	1203.75	25
Exp. 41-R-2	46.26	87.49	133.75	1203.74	0.0006	0.007	1203.75	25
Exp. 41-R-3	54.84	61.078	115.92	1028.49	1.41	14.75	1043.25	
Exp. 42	40.083	75.83	115.92	1043.25	0	0	1043.25	25
Exp. 42-R-1	81.63	34.28	115.92	1001.70	3.98	41.54	1043.25	
Exp. 42-R-2	52.54	63.37	115.92	1030.79	1.19	12.45	1043.25	
Exp. 42-R-3	40.08	75.83	115.92	1043.25	0	0	1043.25	
Exp. 43	40.08	75.83	115.92	1043.25	0	0	1043.25	
Exp. 43-R-1	40.16	75.75	115.92	1043.17	0.0074	0.08	1043.25	
Exp. 44	37.06	69.93	107	962.94	0.0063	0.06	963	25
Exp. 44-R-1	37	70	107	963	0	0	963	25

Appendix I: Mass balance calculations across the gas liquid cylindrical hydrocyclone cont'd.

Exp. # No.	OF. Water Rate Qo.w cm3/s	OF. Air Rate Qo.A	Σ Overflow Rate Σqo cm3/s	UF. Water Rate Qu.w cm3	UF. Air Rate Qu.A	UF. Air cm3	Σ UF Flow Rate Σqu cm3	Surf. Triton X100 ppm
Exp. 45	43.18	81.65	124.83	1123.48	0.001	0.011	1123.5	
Exp. 45-R-1	43.17	81.65	124.83	1123.49	0.0008	0.009	1123.5	
Exp. 46	30.84	58.32	89.17	802.49	0.001	0.008	802.5	
Exp. 46-R-1	30.83	58.33	89.17	802.5	0	0	802.5	
Exp. 47	30.84	58.33	89.17	802.49	0.0009	0.007	802.5	50
Exp. 48	44.88	44.28	89.17	788.45	1.7505	14.05	802.5	50
Exp. 49	37.01	69.99	107	962.99	0.0014	0.014	963	50
Exp. 49-R-1	37.02	69.97	107	962.97	0.0028	0.026	963	
Exp. 49-R-2	37.03	69.97	107	962.97	0.0032	0.031	963	
Exp. 50	37	70	107	963	0	0	963	

Appendix I: Mass balance calculations across the gas liquid cylindrical hydrocyclone cont'd.

Exp. # No.	OF. Water Rate Qo.w cm3/s	OF. Air Rate Qo.A	Σ Overflow Rate Σqo cm3/s	UF. Water Rate Qu.w cm3	UF. Air Rate Qu.A	UF. Air cm3	Σ UF Flow Rate Σqu cm3	Surf. Triton X100 ppm
Exp. 50-R	37.071262	69.928738	107	962.928738	0.0074	0.071262	963	
Exp. 51	37.060669	69.939331	107	962.939331	0.0063	0.060669	963	
Exp. 51-R-1	37	70	107	963	0	0	963	
Exp. 52	45.72612833	43.44053833	89.16666667	787.607205	1.8558	14.892795	802.5	50
Exp. 53	30.84858083	58.31808583	89.16666667	802.4847525	0.0019	0.0152475	802.5	50
Exp. 54	30.87987833	58.28678833	89.16666667	802.453455	0.0058	0.046545	802.5	50
Exp. 55	24.67116067	46.66217267	71.33333333	641.995506	0.0007	0.004494	642	50
Exp. 56	24.67180267	46.66153067	71.33333333	641.994864	0.0008	0.005136	642	50
Exp. 57	-131.2185467	240.0518834	108.8333367	964.55188	1.5261	14.94814996	979.50003	50
Exp. 58	36.19981596	53.75351741	89.95333337	797.1335174	1.5374	12.44648292	809.5800003	50
Exp. 59	48.09722567	41.46277433	89.56000001	785.2361077	2.581	20.8038924	806.0400001	

Appendix O: Representative underflow stream bubble size class data and Rosin-Rammler predicted value (Exp. 23).

x_i.μm	$\%Pass$	$Cum.y_i$	$(x_i/\bar{x})^{\beta}$	$\hat{y}$	$(y-\hat{y})^2$	$y_i-\hat{y}$	$(y_i-\bar{y}_i)^2$	η^2	$\hat{y}_i(y_i-\hat{y}_i)$	x_iy_i
188	100	1	9.894736842	1	2.54414E-09	5.04395E-05	0.142293985	0.999999982	5.04369E-05	188
162	100	1	8.526315789	1	3.92768E-08	0.000198184	0.142293985	0.999999724	0.000198145	162
140	100	1	7.368421053	0.999	3.97989E-07	0.000630863	0.142293985	0.999997203	0.000630466	140
121	99.9	0.999	6.368421053	0.998	5.11032E-07	0.000714865	0.141540548	0.99999639	0.000713639	121
104	99.9	0.999	5.473684211	0.996	1.02128E-05	0.003195746	0.141540548	0.999927845	0.003182337	104
89.9	99.9	0.999	4.731578947	0.991	6.10359E-05	0.007812546	0.141540548	0.999568775	0.007743697	89.8
77.5	99.3	0.993	4.078947368	0.983	9.8511E-05	0.009925272	0.137061923	0.999281266	0.009757284	77
66.9	97.1	0.971	3.521052632	0.97	3.22958E-07	0.000568294	0.121256298	0.999997337	0.000551491	65
57.7	93.8	0.938	3.036842105	0.952	0.000196387	-	0.09936286	0.998023537	-0.013341345	54.1
49.8	89.6	0.896	2.621052632	0.927	0.000978046	-	0.074648485	0.986897976	-0.02899931	44.6
42.9	85.2	0.852	2.257894737	0.895	0.00188613	-	0.052541235	0.964101909	-0.038888148	36.6
37.1	81.5	0.815	1.952631579	0.858	0.001857596	-	0.036948048	0.9497241	-0.036983967	30.2
32	78.8	0.788	1.684210526	0.814	0.000697441	-	0.027297235	0.974450126	-0.021507817	25.2
27.6	76.6	0.766	1.452631579	0.766	2.13357E-09	-4.61906E-	0.02051161	0.999999896	-3.53842E-05	21.1
23.8	74	0.74	1.252631579	0.714	0.000663157	0.025751828	0.013740235	0.951736151	0.018393196	17.6
20.5	69.9	0.699	1.078947368	0.66	0.00151735	0.038953183	0.005809298	0.738806566	0.025710924	14.3
17.7	65.1	0.651	0.931578947	0.606	0.002018815	0.044931222	0.000796298	-1.53525078	0.027231411	11.5
15.3	62.1	0.621	0.805263158	0.553	0.00461996	0.067970287	3.17285E-06	-1455.0908	0.037589588	9.5
13.2	60.1	0.601	0.694736842	0.501	0.010041202	0.100205801	0.000474423	-20.1650903	0.050182484	7.93
11.4	56.3	0.563	0.6	0.451	0.012501842	0.111811636	0.003573798	-2.49819505	0.050448109	6.42
9.8	50.2	0.502	0.515789474	0.403	0.009806757	0.09902907	0.01458811	0.327756891	0.039905836	4.92
8.5	43.2	0.432	0.447368421	0.361	0.005084878	0.07130833	0.036397485	0.860295899	0.025720321	3.67
7.3	36.6	0.366	0.384210526	0.319	0.002207876	0.046988046	0.06593661	0.966515166	0.014989748	2.67
6.3	31.8	0.318	0.331578947	0.282	0.001280887	0.035789486	0.09289161	0.986210947	0.010100169	2
5.4	29.8	0.298	0.284210526	0.247	0.002561188	0.050608184	0.10548286	0.975719389	0.012520051	1.61
4.7	27.6	0.276	0.247368421	0.219	0.003232259	0.056852958	0.120257235	0.973122126	0.012459158	1.3
4.1	23	0.23	0.215789474	0.194	0.001289165	0.035904948	0.15427711	0.991643833	0.006968973	0.94
3.5	19	0.19	0.184210526	0.168	0.000473527	0.021760678	0.18729961	0.99747182	0.003661002	0.67
3	16.1	0.161	0.157894737	0.146	0.000223194	0.014939666	0.213241923	0.998953331	0.002182093	0.48
2.6	12.4	0.124	0.136842105	0.128	1.51483E-05	-	0.248782735	0.99993911	-0.000497767	0.32
2.2	8.6	0.086	0.115789474	0.109	0.000544629	-	0.28813411	0.998109807	-0.002551636	0.19
1.9	5.5	0.055	0.1	0.095	0.001613033	-	0.322375548	0.994996416	-0.003821975	0.1
	Ave =	**0.62278125**		**Σ =**	**0.065481504**					

Appendix P: Exp. 23. Underflow stream bubble size class data and Rosin-Rammler predicted value.

$x_i.\mu m$	$\%Pass$	$Cum.y_i$	$lanx_i\ y_i$	y_i	$(\ln x_i)^2$	y_i^2	$\ln x_i y_i$
188	100	1	5.236441963	2.292	27.42032443	5.253277677	12.0019406
162	100	1	5.087596335	2.143	25.88363647	4.593123453	10.90351951
140	100	1	4.941642423	1.997	24.41982983	3.988821595	9.869465263
121	99.9	0.999	4.795790546	1.851	22.99960696	3.427502623	8.878694339
104	99.9	0.999	4.644390899	1.7	21.57036682	2.88983653	7.895241226
89.9	99.9	0.999	4.498697941	1.554	20.23828317	2.415720922	6.992141594
77.5	99.3	0.993	4.350277936	1.406	18.92491812	1.976383174	6.115790198
66.9	97.1	0.971	4.203198967	1.259	17.66688156	1.584476707	5.290818681
57.7	93.8	0.938	4.055257174	1.111	16.44511074	1.233917061	4.504653451
49.8	89.6	0.896	3.908014984	0.964	15.27258112	0.928478717	3.765669465
42.9	85.2	0.852	3.758871826	0.814	14.1291174	0.663300862	3.061348682
37.1	81.5	0.815	3.61361697	0.669	13.0582276	0.447799183	2.418152942
32	78.8	0.788	3.465735903	0.521	12.01132535	0.271750483	1.806677464
27.6	76.6	0.766	3.317815773	0.373	11.0079015	0.13941023	1.238795415
23.8	74	0.74	3.169685581	0.225	10.04690668	0.050736031	0.713960905
20.5	69.9	0.699	3.020424886	0.076	9.122966493	0.005773858	0.229509724
17.7	65.1	0.651	2.87356464	-0.07	8.257373738	0.005023172	-0.203662
15.3	62.1	0.621	2.727852828	-0.22	7.441181053	0.046909561	-0.59081514
13.2	60.1	0.601	2.58021683	-0.36	6.657518888	0.132657774	-0.93977212
11.4	56.3	0.563	2.433613355	-0.51	5.922473964	0.260942818	-1.24315206
9.8	50.2	0.502	2.282382386	-0.66	5.209269354	0.438318933	-1.51106631
8.5	43.2	0.432	2.140066163	-0.8	4.579883184	0.647015627	-1.72141105
7.3	36.6	0.366	1.987874348	-0.96	3.951644424	0.915015893	-1.90153029
6.3	31.8	0.318	1.840549633	-1.1	3.387622953	1.218571688	-2.03176313
5.4	29.8	0.298	1.686398954	-1.26	2.843941431	1.582664706	-2.12155738
4.7	27.6	0.276	1.547562509	-1.4	2.394949718	1.951263874	-2.16175365
4.1	23	0.23	1.410986974	-1.53	1.99088424	2.351475053	-2.1636808
3.5	19	0.19	1.252762968	-1.69	1.569415055	2.861767725	-2.11926906
3	16.1	0.161	1.098612289	-1.85	1.206948961	3.407076171	-2.02784788
2.6	12.4	0.124	0.955511445	-1.99	0.913002122	3.955832736	-1.90044302
2.2	8.6	0.086	0.78845736	-2.16	0.621665009	4.648256741	-1.69989958
1.9	5.5	0.055	0.641853886	-2.3	0.411976411	5.30189811	-1.47792319

Appendix Q: Predicted fluid velocity in the hydrocyclone.

Exp. # No.	Sampling Point OF- UF	Wall Velocity m/s	Inlet Velocity m/s	Wall Axial Velocity m/s
Exp. 1	UF	3.91	9.72	3.60
Exp. 1-R	UF	3.91	9.72	3.60
Exp. 2	UF	3.91	9.72	3.60
Exp. 3	UF	3.91	9.72	3.60
Exp. 4	UF	3.91	9.72	3.60
Exp. 5	UF	3.91	9.72	3.60
Exp. 6	UF	3.91	9.72	3.60
Exp. 7	OF	3.91	9.72	3.60
Exp. 8	OF	3.91	9.72	3.60
Exp. 9	UF	3.91	9.72	3.60
Exp. 10	UF	3.91	9.72	3.60
Exp. 11	UF	3.91	9.72	3.60
Exp. 13	OF	3.91	9.72	3.60
Exp. 14	UF	3.91	9.72	3.60
Exp. 15	UF	3.91	9.72	3.60
Exp. 16	UF	3.91	9.72	3.60
Exp. 17	UF	3.91	9.72	3.60
Exp. 18	UF	3.91	9.72	3.60
Exp. 20	OF	3.91	9.72	3.60
Exp. 20-R-1	OF	3.91	9.72	3.60
Exp. 20-R-2	OF	3.91	9.72	3.60
Exp. 20-R-3	OF	3.91	9.72	3.60
Exp. 21	UF	3.91	9.72	3.60
Exp. 23	UF	3.91	9.72	3.60
Exp. 23-R	UF	3.91	9.72	3.60
Exp. 25	UF	4.23	10.54	3.90
Exp. 25-R-1	UF	4.23	10.54	3.90
Exp. 25-R-2	UF	4.23	10.54	3.90
Exp. 26	OF	4.23	11.25	4.17
Exp. 27	OF	4.23	11.25	4.17
Exp. 27-R	OF	4.23	11.25	4.17
Exp. 28	UF	4.23	11.25	4.17
Exp. 28-R	UF	4.23	11.25	4.17
Exp. 31	UF	4.23	11.25	4.17
Exp. 31-R	UF	4.23	11.25	4.17
Exp. 32	OF	4.23	11.25	4.17
Exp. 32-R	UF	4.23	11.25	4.17

Appendix L: Predicted fluid velocity in the hydrocyclone

Exp. # No.	Sampling Point UF-OF	Wall Velocity m/s	Inlet Velocity m/s	Wall Axial Velocity m/s
Exp. 33	UF	3.28	8.18	3.03
Exp. 33-R	UF	3.28	8.18	3.03
Exp. 34	UF	3.25	8.11	3.03
Exp. 34-R	UF	3.25	8.11	3.03
Exp. 35	UF	3.27	8.11	3.03
Exp. 37	OF	5.17	12.87	4.77
Exp. 37-R-1	OF	5.17	12.87	4.77
Exp. 37-R-2	OF	5.17	12.87	4.77
Exp. 38	UF	5.60	13.95	5.16
Exp. 38-R-1	UF	5.60	13.95	5.16
Exp. 38-R-2	UF	5.60	13.95	5.16
Exp. 40	UF	3.25	8.11	3.00
Exp. 40-R-1	OF	5.31	13.23	4.90
Exp. 40-R-2	UF	5.31	13.23	4.90
Exp. 40-R-3	UF	4.88	12.16	4.50
Exp. 41-R-3	UF	4.23	10.54	3.90
Exp. 42	UF	4.23	10.54	3.90
Exp. 42-R-3	UF	4.23	10.54	3.90
Exp. 43	UF	4.23	10.54	3.90
Exp. 43-R-1	UF	4.23	10.54	3.90
Exp. 45	UF	4.55	11.35	4.20
Exp. 45-R-1	UF	4.55	11.35	4.20
Exp. 47	UF	3.25	8.11	3.00
Exp. 49	UF	3.91	9.73	3.60
Exp. 49-R-1	UF	3.91	9.73	3.60
Exp. 49-R-2	UF	3.91	9.73	3.60
Exp. 50	UF	3.91	9.73	3.60
Exp. 50-R	UF	3.91	9.73	3.60
Exp. 53	OF	3.25	8.11	3.00
Exp. 54	OF	3.25	8.11	3.00
Exp. 55	UF	2.60	6.48	2.40
Exp. 56	UF	2.60	6.48	2.40
Exp. 57	UF	3.97	9.89	3.66
Exp. 58	UF	3.28	8.17	3.03

Appendix R: Reynolds number across the hydrocyclone and the feed inlet.

Exp. #	Sampling Point	Cyclone Body Re No.	Feed Reynolds No
No.	OF- UF	Re_R	Re
Exp. 1	UF	1145	53636
Exp. 1-R	UF	1145	53636
Exp. 2	UF	1145	53636
Exp. 3	UF	1145	53636
Exp. 4	UF	1145	53636
Exp. 5	UF	1145	53636
Exp. 6	UF	1145	53636
Exp. 7	OF	1145	53636
Exp. 8	OF	1145	53636
Exp. 9	UF	1145	53636
Exp. 10	UF	1145	53636
Exp. 11	UF	1145	53636
Exp. 13	OF	1145	53636
Exp. 14	UF	1145	53636
Exp. 15	UF	1145	53636
Exp. 16	UF	1145	53636
Exp. 17	UF	1145	53636
Exp. 18	UF	1145	53636
Exp. 20	OF	1145	53636
Exp. 20-R-1	OF	1145	53636
Exp. 20-R-2	OF	1145	53636
Exp. 20-R-3	OF	1145	53636
Exp. 21	UF	1145	53636
Exp. 23	UF	1145	53636
Exp. 23-R	UF	1145	53636
Exp. 25	UF	1241	58106
Exp. 25-R-1	UF	1241	58106
Exp. 25-R-2	UF	1241	58106
Exp. 26	OF	1325	62049
Exp. 27	OF	1325	62049
Exp. 27-R	OF	1325	62049
Exp. 28	UF	1325	62049
Exp. 28-R	UF	1325	62049

Appendix S: Reynolds number across the hydrocyclone and the feed inlet.

Exp. #	Sampling Point	Cyclone Body Re No.	Feed Reynolds No
No.	OF- UF	Re_R	Re
Exp. 31	UF	1325	62049
Exp. 31-R	UF	1325	62049
Exp. 32	OF	1325	62049
Exp. 32-R	UF	1325	62049
Exp. 33	UF	963	45091
Exp. 33-R	UF	963	45091
Exp. 34	UF	954	44697
Exp. 34-R	UF	954	44697
Exp. 35	UF	958	44894
Exp. 37	OF	1516	70988
Exp. 37-R-1	OF	1516	70988
Exp. 37-R-2	OF	1516	70988
Exp. 38	UF	1642	76904
Exp. 38-R-1	UF	1642	76904
Exp. 38-R-2	UF	1642	76904
Exp. 40	UF	954	44697
Exp. 40-R-1	OF	1558	72960
Exp. 40-R-2	UF	1558	72960
Exp. 40-R-3	UF	1431	67045
Exp. 41-R-3	UF	1240	58106
Exp. 42	UF	1240	58106
Exp. 42-R-3	UF	1240	58106
Exp. 43	UF	1240	58106
Exp. 43-R-1	UF	1240	58106
Exp. 45	UF	1336	62575
Exp. 45-R-1	UF	1336	62575
Exp. 47	UF	954	44697
Exp. 49	UF	1145	53636
Exp. 49-R-1	UF	1145	53636
Exp. 49-R-2	UF	1145	53636
Exp. 50	UF	1145	53636
Exp. 50-R	UF	1145	53636
Exp. 53	OF	954	44697
Exp. 54	OF	954	44697
Exp. 55	UF	763	35757
Exp. 56	UF	763	35757
Exp. 57	UF	1165	54555
Exp. 58	UF	963	45091

Appendix T: Flow velocity in vortex finder, inner core, characteristic velocity and total friction factor.

Exp. # No.	Vx m/s	Inner Core Velocity m/s	Characteristic velocity m/s	Total Friction Factor *f*
Exp. 1	1.44	5.55	2.11	0.0051386
Exp. 1-R	1.44	5.55	2.11	0.0051386
Exp. 2	1.44	5.55	2.11	0.0051386
Exp. 3	1.44	5.55	2.11	0.0051386
Exp. 4	1.44	5.55	2.11	0.0051386
Exp. 5	1.44	5.55	2.11	0.0051386
Exp. 6	1.44	5.55	2.11	0.0051386
Exp. 7	1.44	5.55	2.11	0.0051386
Exp. 8	1.44	5.55	2.11	0.0051386
Exp. 9	1.44	5.55	2.11	0.0051386
Exp. 10	1.44	5.55	2.11	0.0051386
Exp. 11	1.44	5.55	2.11	0.0051386
Exp. 13	1.44	5.55	2.11	0.0051386
Exp. 14	1.44	5.55	2.11	0.0051386
Exp. 15	1.44	5.55	2.11	0.0051386
Exp. 16	1.44	5.55	2.11	0.0051386
Exp. 17	1.44	5.55	2.11	0.0051386
Exp. 18	1.44	5.55	2.11	0.0051386
Exp. 20	1.44	5.55	2.11	0.0051386
Exp. 20-R-1	1.44	5.55	2.11	0.0051386
Exp. 20-R-2	1.44	5.55	2.11	0.0051386
Exp. 20-R-3	1.44	5.55	2.11	0.0051386
Exp. 21	1.44	5.55	2.11	0.0051386
Exp. 23	1.44	5.55	2.11	0.0051386
Exp. 23-R	1.44	5.55	2.11	0.0051386
Exp. 25	1.56	6.01	2.28	0.0051386
Exp. 25-R-1	1.56	6.01	2.28	0.0051386
Exp. 25-R-2	1.56	6.01	2.28	0.0051386
Exp. 26	2.19	6.40	2.44	0.0051979
Exp. 27	2.19	6.40	2.44	0.0051979
Exp. 27-R	2.19	6.40	2.44	0.0051979
Exp. 28	2.19	6.40	2.44	0.0051979
Exp. 28-R	2.19	6.40	2.44	0.0051979
Exp. 31	2.19	6.40	2.44	0.0051979
Exp. 31-R	2.19	6.40	2.44	0.0051979
Exp. 32	2.19	6.40	2.44	0.0051979
Exp. 32-R	2.19	6.40	2.44	0.0051979

Appendix U: Flow velocity in vortex finder, inner core, characteristic velocity and total friction factor cont.

Exp. # No.	Vx m/s	Inner Core Velocity m/s	Characteristic velocity m/s	Total Friction Factor *f*
Exp. 33	1.26	4.66	2.44	0.0051477
Exp. 33-R	1.26	4.66	1.77	0.0051477
Exp. 34	1.20	4.62	1.75	0.0051386
Exp. 34-R	1.20	4.62	1.76	0.0051386
Exp. 35	1.23	4.64	1.76	0.0051432
Exp. 37	2.42	7.32	2.79	0.005191
Exp. 37-R-1	2.43	7.32	2.79	0.005191
Exp. 37-R-2	2.43	7.32	2.79	0.005191
Exp. 38	3.36	7.90	3.02	0.0052498
Exp. 38-R-1	3.36	7.90	3.03	0.0052498
Exp. 38-R-2	3.36	7.90	3.0	0.0052498

Appendix N: Flow velocity in vortex finder, inner core, characteristic velocity and total friction factor.

Exp. # No.	Vx m/s	Inner Core Velocity m/s	Characteristic velocity m/s	Total Friction Factor *f*
Exp. 40	1.20	4.62	1.76	0.0051386
Exp. 40-R-1	2.74	7.51	2.87	0.0052124
Exp. 40-R-2	2.74	7.51	2.87	0.0052124
Exp. 40-R-3	1.80	6.94	2.63	0.0051386
Exp. 41-R-3	1.56	6.01	2.28	0.0051386
Exp. 42	1.56	6.01	2.28	0.0051386
Exp. 42-R-3	1.56	6.01	2.28	0.0051386
Exp. 43	1.56	6.01	2.28	0.0051386
Exp. 43-R-1	1.56	6.01	2.28	0.0051386
Exp. 45	1.68	6.47	2.46	0.0051386
Exp. 45-R-1	1.68	6.47	2.46	0.0051386
Exp. 47	1.20	4.62	1.76	0.0051386
Exp. 49	1.44	5.55	2.11	0.0051386
Exp. 49-R-1	1.44	5.55	2.11	0.0051386
Exp. 49-R-2	1.44	5.55	2.11	0.0051386
Exp. 50	1.44	5.55	2.11	0.0051386
Exp. 50-R	1.44	5.55	2.11	0.0051386
Exp. 53	1.20	4.62	1.76	0.0051386
Exp. 54	1.20	4.62	1.76	0.0051386
Exp. 55	0.96	3.70	1.41	0.0051386
Exp. 56	0.96	3.70	1.41	0.0051386
Exp. 57	2.76	5.59	2.15	0.0052898
Exp. 58	1.26	4.66	1.77	0.0051477

Appendix V: Comparison of Measured and model predicted cut-size (d_{50}) in underflow and overflow streams.

Exp. # No.	Sampling Point OF- UF	d50 (Measured) µm	d50 (Musch.) m	d50 (Musch.) µm	d50 (Barth) m	d50 (Barth) µm
Exp. 7	OF	59.2	0.000024	24	0.0000282	28.2
Exp. 8	OF	15.7	0.000024	24	0.0000282	28.2
Exp. 13	OF	72.1	0.000024	24	0.0000282	28.2
Exp. 20	OF	2.6	0.000024	24	0.0000282	28.2
Exp. 20-R-1	OF	8.1	0.000024	24	0.0000282	28.2
Exp. 20-R-2	OF	125.3	0.000024	24	0.0000282	28.2
Exp. 20-R-3	OF	125.3	0.000024	24	0.0000282	28.2
Exp. 26	OF	25.2	0.0000224	22.4	0.0000263	26.3
Exp. 27	OF	29.4	0.0000224	22.4	0.0000263	26.3
Exp. 27-R	OF	22.8	0.0000224	22.4	0.0000263	26.3
Exp. 32	OF	346.4	0.0000224	22.4	0.0000263	26.3
Exp. 37	OF	347.5	0.000021	21	0.0000246	24.6
Exp. 37-R-1	OF	229.1	0.000021	21	0.0000246	24.6
Exp. 37-R-2	OF	292.5	0.000021	21	0.0000246	24.6
Exp. 40-R-1	OF	229.1	0.0000207	20.7	0.0000243	24.3
Exp. 53	OF	2.4	0.0000263	26.3	0.0000309	30.9
Exp. 54	OF	62	0.0000263	26.3	0.0000309	30.9
Exp. 1	UF	45.1	0.000024	24	0.0000282	28.2
Exp. 1-R	UF	45.7	0.000024	24	0.0000282	28.2
Exp. 2	UF	39.7	0.000024	24	0.0000282	28.2
Exp. 3	UF	39.424	0.000024	24	0.0000282	28.2
Exp. 4	UF	44.1	0.000024	24	0.0000282	28.2
Exp. 5	UF	47.6	0.000024	24	0.0000282	28.2
Exp. 6	UF	45.1	0.000024	24	0.0000282	28.2
Exp. 9	UF	49.6	0.000024	24	0.0000282	28.2
Exp. 10	UF	40	0.000024	24	0.0000282	28.2
Exp. 11	UF	40	0.000024	24	0.0000282	28.2
Exp. 14	UF	44.2	0.000024	24	0.0000282	28.2
Exp. 15	UF	41.7	0.000024	24	0.0000282	28.2
Exp. 16	UF	42.1	0.000024	24	0.0000282	28.2
Exp. 17	UF	43.2	0.000024	24	0.0000282	28.2
Exp. 18	UF	43.4	0.000024	24	0.0000282	28.2
Exp. 21	UF	41.8	0.000024	24	0.0000282	28.2
Exp. 23	UF	49.8	0.000024	24	0.0000282	28.2

Appendix O: Comparison of Measured and model predicted cut-size (d_{50}) in underflow and overflow streams cont'd.

Exp. # No.	Sampling Point OF- UF	d50 (Measured) µm	d50 (Musch.) m	d50 (Musch.) µm	d50 (Barth) m	d50 (Barth) µm
Exp. 23-R	UF	40.2	0.000024	24	0.0000282	28.2
Exp. 25	UF	38.6	0.0000231	23.1	0.0000271	27.1
Exp. 25-R-1	UF	39.6	0.0000231	23.1	0.0000271	27.1
Exp. 25-R-2	UF	38.3	0.0000231	23.1	0.0000271	27.1
Exp. 28	UF	37.8	0.0000224	22.4	0.0000263	26.3
Exp. 28-R	UF	39.7	0.0000224	22.4	0.0000263	26.3
Exp. 31	UF	41.9	0.0000224	22.4	0.0000263	26.3
Exp. 31-R	UF	40.8	0.0000224	22.4	0.0000263	26.3
Exp. 32-R	UF	44.5	0.0000224	22.4	0.0000263	26.3
Exp. 33	UF	50.5	0.0000262	26.2	0.0000308	30.8
Exp. 33-R	UF	50.9	0.0000262	26.2	0.0000308	30.8
Exp. 34	UF	53	0.0000263	26.3	0.0000309	30.9
Exp. 34-R	UF	49.2	0.0000263	26.3	0.0000309	30.9
Exp. 35	UF	48.7	0.0000263	26.3	0.0000308	30.8
Exp. 38	UF	32.7	0.0000202	20.2	0.0000237	23.7
Exp. 38-R-1	UF	33	0.0000202	20.2	0.0000237	23.7
Exp. 38-R-2	UF	35	0.0000202	20.2	0.0000237	23.7
Exp. 40	UF	54.6	0.0000263	26.3	0.0000309	30.9
Exp. 40-R-2	UF	35.9	0.0000207	20.7	0.0000243	24.3
Exp. 40-R-3	UF	39.5	0.0000215	21.5	0.0000252	25.2
Exp. 41-R-3	UF	49.9	0.0000231	23.1	0.0000271	27.1
Exp. 42	UF	44.39	0.0000231	23.1	0.0000271	27.1
Exp. 42-R-3	UF	48	0.0000231	23.1	0.0000271	27.1
Exp. 43	UF	42.32	0.0000231	23.1	0.0000271	27.1
Exp. 43-R-1	UF	50.8	0.0000231	23.1	0.0000271	27.1
Exp. 45	UF	44.2	0.0000223	22.3	0.0000261	26.1
Exp. 45-R-1	UF	41.9	0.0000223	22.3	0.0000261	26.1
Exp. 47	UF	49.1	0.0000263	26.3	0.0000309	30.9
Exp. 49	UF	44	0.000024	24	0.0000282	28.2
Exp. 49-R-1	UF	43.5	0.000024	24	0.0000282	28.2
Exp. 49-R-2	UF	43.5	0.000024	24	0.0000282	28.2
Exp. 50	UF	43.7	0.000024	24	0.0000282	28.2
Exp. 50-R	UF	43.2	0.000024	24	0.0000282	28.2
Exp. 55	UF	44.8	0.0000294	29.4	0.0000345	34.5
Exp. 56	UF	52.4	0.0000294	29.4	0.0000345	34.5
Exp. 57	UF	59.2	0.0000241	24.1	0.0000282	28.2
Exp. 58	UF	45.5	0.0000262	26.2	0.0000308	30.8

Appendix W: Linearalized efficiency curve for underflow stream (Based on experimental data).

No.	Line Equation	Slope (a)	D (v, 0.5)	D (v, 0.9)	D (v, 0.1)	D (4, 3)	D (3, 2)	Triton,ppm	Injected Air m3/h
Exp. 1	y = 2.25x-10.535	2.25	45.1	149.7	4.3	55.1	34.2	10	0
Exp. 1-R	y = 1.1x-3.5408	1.1	45.7	70.9	3.6	23	8.4	10	0
Exp. 2	y = x-3.2189	1	39.7	80.9	3.6	23	8.4	10	0
Exp. 3	y = 2.55x-11.043	2.55	39.424	119.5	6.7	70.8	37.5	10	0
Exp. 4	y = 3.45x-13.055	3.45	44.1	61.4	5.7	41.9	34.2	0	0
Exp. 5	y = 2.25x-8.6144	2.25	47.6	78.2	4.9	45.4	31.5	0	0
Exp. 6	y = 3x-12.614	3	45.1	106.4	7.7	64.2	44.2	0	0
Exp. 9	y = 3.5x-13.323	3.5	49.6	60.6	5.6	42.6	36.7	0	0
Exp. 10	y = 3.4798x-14.48	3.4798	40	82.4	4.9	54.7	48.2	0	0
Exp. 11	y = 15.702x-72.927	15.702	40	110.2	9.1	98	45.1	0	0
Exp. 14	y = 2.25x-10.722	2.25	44.2	156.4	4.9	104.2	33.1	0	0
Exp. 15	y = 3.7x-15.149	3.7	41.7	83.8	7.7	52.9	21.7	5.55	0
Exp. 16	y = 4.6x-19.477	4.6	42.1	83.7	5.2	61.4	33.4	0	0
Exp. 17	y = 4.8x-20.393	4.8	43.2	87.5	5.5	61.2	49.6	0	0
Exp. 18	y = 3.1x-13.425	3.1	43.4	111.6	4.2	70.7	30.9	0	0
Exp. 21	y = 2.1x-9.4024	2.1	41.8	135	3.2	78.3	26.4	0	0
Exp. 23	y = x-2.9444	1	49.8	50.3	2.4	18.4	6.1	0	0
Exp. 23-R	y = 1.25x-5.4459	1.25	40.2	125.6	10.8	69.7	26.7	0	0
Exp. 25	y = 9.9991x-42.901	9.9991	38.6	79.9	5.8	69	38.2	0	0
Exp. 25-R-1	y = 1.85x-6.4116	1.85	39.6	44.8	7	27.7	38.2	0	0
Exp. 25-R-2	y = x-2.9957	1	38.3	46.4	2.7	16.4	26.1	0	0
Exp. 28	y = 6.4x-31.534	6.4	37.8	161.6	11.1	69.8	26	0	0.28317

Appendix X: Linearalized efficiency curve for underflow stream (Based on experimental data).

No.	Line Equation	Slope (a)	D (v, 0.5)	D (v, 0.9)	D (v, 0.1)	D (4, 3)	D (3, 2)	Triton,ppm	Injected Air m3/h
Exp. 28-R	y = 3.7x-17.039	3.7	39.7	114.9	6.28	92.9	31.7	0	0.28317
Exp. 31	y = 3x-12.283	3	41.9	112.8	3.5	72.3	40.9	0	0.28317
Exp. 31-R	y = 2.85x-11.669	2.85	40.8	113.7	3.6	70.9	43.5	0	0.28317
Exp. 32-R	y = 4.35x-25.863	4.35	44.5	118.4	5.1	41.8	39.6	0	0.28317
Exp. 33	y = 7.5x-32.075	7.5	50.5	74.6	5.4	62.8	35.9	30	0.028317
Exp. 33-R	y = 3x-11.795	3	50.9	74.6	2.93	46.5	33.5	30	0.028317
Exp. 34	y = 2.5x-11.862	2.5	53	59.1	8.8	73.9	32.2	30	0
Exp. 34-R	y = 0.7x-0.4852	0.7	49.2	75.5	7.7	32.1	21.2	30	0
Exp. 35	y = 3x-13.904	3	48.7	141	5.8	93	30.3	30	0.0141585
Exp. 38	y = 1.3x-7.2289	1.3	32.7	123.3	3.9	72.9	28.5	0	0.056634
Exp. 38-R-1	y = 5x-21.098	5	33	87.3	9.2	66.4	46	0	0.056634
Exp. 38-R-2	y = 4.65x-19.756	4.65	35	87.6	4.8	69.1	58.8	0	0
Exp. 40	y = 5x-29.894	5	54.6	113.5	3.7	54	39	0	0.424755
Exp. 40-R-2	y = 12x-52.433	12	35.9	83.4	8.8	71.1	18.3	0	0.56634
Exp. 40-R-3	y = 2x-11.408	2	39.5	127.5	13.8	62.8	38.2	0	0.424755
Exp. 41-R-3	y = 3x-12.788	3	49.9	87.6	48	69.1	38.8	0	0
Exp. 42	y = 12.998x-56.463	12.998	44.39	80.3	68	74.1	33.8	25	0
Exp. 43	y = 0.9x-1.4485	0.9	48	44.2	2.3	40.1	23.4	0	0

Appendix P: Linearalized efficiency curve for underflow stream (Based on experimental data) contd.

No.	Line Equation	Slope (a)	D (v, 0.5)	D (v, 0.9)	D (v, 0.1)	D (4, 3)	D (3, 2)	Triton,ppm	Injected Air m3/h
Exp. 38-R-1	y = 5x-21.098	5	33	87.3	9.2	66.4	46	0	0.056634
Exp. 38-R-2	y = 4.65x-19.756	4.65	35	87.6	4.8	69.1	58.8	0	0
Exp. 40	y = 5x-29.894	5	54.6	113.5	3.7	54	39	0	0.424755
Exp. 40-R-2	y = 12x-52.433	12	35.9	83.4	8.8	71.1	18.3	0	0.56634
Exp. 40-R-3	y = 2x-11.408	2	39.5	127.5	13.8	62.8	38.2	0	0.424755
Exp. 41-R-3	y = 3x-12.788	3	49.9	87.6	48	69.1	38.8	0	0
Exp. 42	y = 12.998x-56.463	12.99	44.39	80.3	68	74.1	33.8	25	0
Exp. 43	y = 0.9x-1.4485	0.9	48	44.2	2.3	40.1	23.4	0	0
Exp. 43-R-1	y = 1.25x-3.8137	1.25	42.32	72.5	6.8	39.6	25.9	0	0
Exp. 45	y = 1.25x-2.4325	1.25	50.8	90.8	3.9	46.1	32.6	0	0
Exp. 45-R-1	y = 0.6 x-3E-12	0.6	44.2	72.5	2.9	1.8	21.5	0	0
Exp. 47	y = 0.95x-4.2535	0.95	41.9	135.5	5.5	72.6	20.1	0	0
Exp. 49	y = 3.5x-16.899	3.5	49.1	105.3	3.3	62.3	16.3	50	0
Exp. 49-R-1	y = 3.4x-5.4721	3.4	44	65.4	3.2	3.9	13.7	50	0
Exp. 49-R-2	y = 0.85x-2.1122	0.85	43.5	55.1	3.1	17.6	25.2	50	0
Exp. 50	y =1.5x-4.7671	1.5	43.7	44.2	2.3	10.1	23.4	0	0
Exp. 50-R	y = 1.2x-3.8137	1.2	43.2	62.5	3.8	19.6	25.9	0	0
Exp. 55	y = 0.25x-0.4024	0.25	44.8	73	3.9	42.5	32	50	0
Exp. 56	y = 0.6x-1.9068	0.6	52.4	73.5	1.2	29.8	33.5	0	0
Exp. 57	y = 2.6x-9.6554	2.6	59.2	78	6.3	37.8	25	50	0.707925
Exp. 58	y = 2.8x-10.897	2.8	45.5	65.5	5.2	44.5	30.7	50	0

Appendix Y: Comparison of measured and models predicted efficiency of the 1" diameter hydrocyclone.

No.	D (3, 2)	D (v, 0.5)	Model 1 (d90)	Model 2 (d90)	Model 1 (d10)	Model 2 (d10)	Model 1 (d32)	Model 2 (d32)
	μm	μm	m	m	m	m	m	m
Exp. 1	34.2	45.1	0.71208728	0.929285612	0.114346651	0.002950468	0.471208981	0.418741794
Exp. 1-R	8.4	45.7	0.784793473	0.999462312	0.165204932	8.06386E-05	0.603487283	0.920102052
Exp. 2	8.4	39.7	0.764264264	0.999462312	0.186528497	8.06386E-05	0.594315245	0.920102052
Exp. 3	37.5	39.424	0.839816757	0.984608171	0.205297004	0.032387896	0.579823528	0.691742828
Exp. 4	34.2	44.1	0.838393699	0.954957121	0.204509358	0.074479728	0.581271895	0.647588945
Exp. 5	31.5	47.6	0.838566094	0.990865314	0.283471475	0.066752918	0.604474237	0.76967049
Exp. 6	44.2	45.1	0.878058049	0.985393257	0.24260159	0.081007696	0.612672627	0.726763296
Exp. 9	36.7	49.6	0.815947686	0.938369155	0.178458161	0.057762624	0.56355141	0.614758918
Exp. 10	48.2	40	0.859202111	0.965326708	0.234906119	0.102317639	0.594579363	0.669135539
Exp. 11	45.1	40	0.821285849	0.650584845	0.162882708	0.33912406	0.421352695	0.467720626
Exp. 14	33.1	44.2	0.669859008	0.88211152	0.099487789	0.001896005	0.448634816	0.357440461
Exp. 15	21.7	41.7	0.856560098	0.956521697	0.237135007	0.117004759	0.521211901	0.536647056
Exp. 16	33.4	42.1	0.797875342	0.871059039	0.188286157	0.115786254	0.486966376	0.481870106
Exp. 17	49.6	43.2	0.82658362	0.889155198	0.17118651	0.10880668	0.461487899	0.448729461
Exp. 18	30.9	43.4	0.852320379	0.973888628	0.218135989	0.066889404	0.583666541	0.667629474
Exp. 21	26.4	41.8	0.790164894	0.982722096	0.165232088	0.00712821	0.545372976	0.635212365
Exp. 23	6.1	49.8	0.836938436	0.999971569	0.196721311	0.000122872	0.65248227	0.982566887
Exp. 23-R	26.7	40.2	0.666428975	0.971898765	0.08510937	5.23928E-06	0.488989365	0.443854225
Exp. 25	38.2	38.6	0.821228942	0.726292585	0.176336487	0.271591217	0.514529525	0.509301279
Exp. 25-R-1	38.2	39.6	0.682807145	0.934157294	0.064921673	9.82467E-05	0.469355307	0.395419293

Appendix Z: Comparison of measured and models predicted efficiency of the 1" diameter hydrocyclone.

No.	D (3, 2)	D (v, 0.5)	Model 1 (d90)	Model 2 (d90)	Model 1 (d10)	Model 2 (d10)	Model 1 (d32)	Model 2 (d32)
	μm	μm	m	m	m	m	m	m
Exp. 25-R-2	26.1	38.3	0.531187123	0.689852145	0.103846154	1.02247E-06	0.413098237	0.095565245
Exp. 28	26	37.8	0.817844077	0.817844077	0.182443264	0.182443264	0.524824791	0.524824791
Exp. 28-R	31.7	39.7	0.831074815	0.940246591	0.225189318	0.105515691	0.553080844	0.591133015
Exp. 31	40.9	41.9	0.911241815	0.993093106	0.168712963	0.032227108	0.729978997	0.892988192
Exp. 31-R	43.5	40.8	0.908557771	0.994269862	0.205379229	0.045723935	0.721138531	0.894125726
Exp. 32-R	39.6	44.5	0.678505072	0.750054382	0.123842315	0.053222487	0.348926519	0.285423184
Exp. 33	35.9	50.5	0.154334839	0.189767882	0.147273649	0.182637683	0.342631315	0.364468044
Exp. 33-R	33.5	50.9	0.65799201	0.801542846	0.229174126	0.069934785	0.543046664	0.591034394
Exp. 34	32.2	53	0.727828848	0.92540135	5.27803E-06	3.08698E-14	0.302101342	0.104938581
Exp. 34-R	21.2	49.2	0.743778043	0.99994133	0.40677886	0.030781459	0.596699345	0.972920912
Exp. 35	30.3	48.7	0.800672054	0.9510329	0.174185968	0.034891689	0.535445147	0.575169244
Exp. 38	28.5	32.7	0.685212327	0.978737508	0.075561784	4.42364E-06	0.483093461	0.4174973
Exp. 38-R-1	46	33	0.85721919	0.908399725	0.254472129	0.201672545	0.604467743	0.632479435
Exp. 38-R-2	58.8	35	0.854144738	0.919284777	0.263111044	0.195062728	0.660244448	0.713903911
Exp. 40	39	54.6	0.796070436	0.851099235	0.201220523	0.146200821	0.476925904	0.47047854
Exp. 40-R-2	18.3	35.9	0.755982724	0.646361194	0.235312061	0.347836487	0.313468728	0.39696962
Exp. 40-R-3	38.2	39.5	0.730742933	0.960640563	0.161294417	0.005088803	0.506317956	0.520207521
Exp. 41-R-3	38.8	49.9	0.757737189	0.919284777	0.339745966	0.195062728	0.605547595	0.713903911
Exp. 42	33.8	44.39	0.746413017	0.629847694	0.253222225	0.369931012	0.508781535	0.504324219
Exp. 43	23.4	48	0.913963309	0.99999995	0.426237824	0.1077871	0.737776967	0.999361699
Exp. 43-R-1	25.9	42.32	0.583703535	0.84948112	0.036304935	5.1198E-08	0.426989992	0.181530841
Exp. 45	32.6	50.8	0.765051536	0.99763487	0.127243247	5.22798E-05	0.614556277	0.915946709
Exp. 45-R-1	21.5	44.2	0.541072766	0.852757686	0.38975822	0.008308177	0.491890628	0.414345413
Exp. 47	20.1	41.9	0.625121915	0.969077368	0.073599628	3.89038E-08	0.479646115	0.366145904
Exp. 49	16.3	49.1	0.746883808	0.878534596	1.58356E-07	3.67322E-13	0.406365523	0.333355338

Appendix Q: Comparison of measured and models predicted efficiency of the 1" diameter hydrocyclone.

No.	D (3, 2)	D (v, 0.5)	Model 1 (d90)	Model 2 (d90)	Model 1 (d10)	Model 2 (d10)	Model 1 (d32)	Model 2 (d32)
	μm	μm	m	m	m	m	m	m
Exp. 49-R-1	13.7	44	0.813719536	0.941324756	0.424413492	0.360425504	0.590957777	0.666537712
Exp. 49-R-2	25.2	43.5	0.871287197	0.999999442	0.462472929	0.243726473	0.790117061	0.999953742
Exp. 50	23.4	43.7	0.980892107	0.99999995	0.378631109	0.1077871	0.848653225	0.999361699
Exp. 50-R	25.9	43.2	0.580414631	0.84948112	0.041183249	5.1198E-08	0.429871143	0.181530841
Exp. 55	32	44.8	0.701352712	1	0.439003492	0.00187493	0.636339536	0.999999398
Exp. 56	33.5	52.4	0.635032998	0.997289605	0.128408049	1.34372E-09	0.503050915	0.532497618
Exp. 57	25	59.2	0.781830694	0.958585433	0.116731198	0.006816613	0.540714317	0.599112607
Exp. 58	30.7	45.5	0.776305608	0.945009543	0.114096481	0.009150838	0.54038553	0.591469913
Exp. 45	32.6	50.8	0.765051536	0.99763487	0.127243247	5.22798E-05	0.614556277	0.915946709
Exp. 45-R-1	21.5	44.2	0.541072766	0.852757686	0.38975822	0.008308177	0.491890628	0.414345413
Exp. 47	20.1	41.9	0.625121915	0.969077368	0.073599628	3.89038E-08	0.479646115	0.366145904
Exp. 49	16.3	49.1	0.746883808	0.878534596	1.58356E-07	3.67322E-13	0.406365523	0.333355338
Exp. 49-R-1	13.7	44	0.813719536	0.941324756	0.424413492	0.360425504	0.590957777	0.666537712
Exp. 49-R-2	25.2	43.5	0.871287197	0.999999442	0.462472929	0.243726473	0.790117061	0.999953742
Exp. 50	23.4	43.7	0.980892107	0.99999995	0.378631109	0.1077871	0.848653225	0.999361699
Exp. 50-R	25.9	43.2	0.580414631	0.84948112	0.041183249	5.1198E-08	0.429871143	0.181530841
Exp. 55	32	44.8	0.701352712	1	0.439003492	0.00187493	0.636339536	0.999999398
Exp. 56	33.5	52.4	0.635032998	0.997289605	0.128408049	1.34372E-09	0.503050915	0.532497618
Exp. 57	25	59.2	0.781830694	0.958585433	0.116731198	0.006816613	0.540714317	0.599112607
Exp. 58	30.7	45.5	0.776305608	0.945009543	0.114096481	0.009150838	0.54038553	0.591469913

Appendix AA: Comparison of the measured and models predicted pressure drop across the hydrocyclone.

Exp. # No.	Measured Δp kPa	Δp body (Musch.) kPa	Δp body (Barth) kPa	ΔPx (Musch.) kPa	ΔPx (Barth, k=3.9) kPa
Exp. 1	58.61	24.33	75.36	59.42	65.78
Exp. 1-R	79.29	24.33	75.36	59.42	65.78
Exp. 2	79.29	24.33	75.36	59.42	65.78
Exp. 3	93.08	24.33	75.36	59.42	65.78
Exp. 4	79.29	24.33	75.36	59.42	65.78
Exp. 5	93.08	24.33	75.36	59.42	65.78
Exp. 6	99.97	24.33	75.36	59.42	65.78
Exp. 7	93.08	24.33	75.36	59.42	65.78
Exp. 8	72.39	24.33	75.36	59.42	65.78
Exp. 9	86.18	24.33	75.36	59.42	65.78
Exp. 10	72.39	24.33	75.36	59.42	65.78
Exp. 11	79.29	24.33	75.36	59.42	65.78
Exp. 13	72.39	24.33	75.36	59.42	65.78
Exp. 14	79.29	24.33	75.36	59.42	65.78
Exp. 15	86.18	24.33	75.36	59.42	65.78
Exp. 16	106.87	24.33	75.36	59.42	65.78
Exp. 17	86.18	24.33	75.36	59.42	65.78
Exp. 18	51.71	24.33	75.36	59.42	65.78
Exp. 20	93.08	24.33	75.36	59.42	65.78
Exp. 20-R-1	113.76	24.33	75.36	59.42	65.78

Appendix BB: Comparison of the measured and models predicted pressure drop across the hydrocyclone.

Exp. # No.	Measured Δp kPa	Δp body (Musch.) kPa	Δp body (Barth) kPa	ΔPx (Musch.) kPa	ΔPx (Barth, k=3.9) kPa
Exp. 20-R-2	99.97	24.33	75.35	59.42	65.78
Exp. 20-R-3	99.97	24.33	75.35	59.42	65.78
Exp. 21	72.39	24.33	75.35	59.42	65.78
Exp. 23	58.61	24.33	75.35	59.42	65.78
Exp. 23-R	51.71	24.33	75.35	59.42	65.78
Exp. 25	51.71	24.33	75.35	59.42	65.78
Exp. 25-R-1	79.29	24.33	75.35	59.42	65.78
Exp. 25-R-2	86.18	24.33	75.35	59.42	65.78
Exp. 26	44.82	24.33	75.35	59.42	65.78
Exp. 27	58.61	24.33	75.35	59.42	65.78
Exp. 27-R	72.39	24.33	75.35	59.42	65.78
Exp. 28	44.82	24.33	75.35	59.42	65.78
Exp. 28-R	58.61	32.7085702	44.7927797	89.1802535	97.5278241
Exp. 31	72.39	32.7085702	44.7927797	89.1802535	97.5278241
Exp. 31-R	24.13	32.7085702	44.7927797	89.1802535	97.5278241
Exp. 32	44.82	32.7085702	44.7927797	89.1802535	97.5278241
Exp. 32-R	51.71	32.7085702	44.7927797	89.1802535	97.5278241
Exp. 33	44.82	17.2057879	45.8400862	42.6975335	47.2109427
Exp. 33-R	58.61	17.2057879	45.8400862	42.6975335	47.2109427
Exp. 34	37.92	16.8941247	52.331636	41.2638174	45.6832792

Appendix CC: Comparison of the measured and models predicted pressure drop across the hydrocyclone.

Exp. # No.	Measured Δp kPa	Δp body (Musch.) kPa	Δp body (Barth) kPa	ΔPx (Musch.) kPa	ΔPx (Barth, k=3.9) kPa
Exp. 34-R	51.71	16.89	52.33	41.26	45.68
Exp. 35	37.92	17.05	48.85	41.97	46.44
Exp. 37	58.61	42.789	63.26	115.13	126.15
Exp. 37-R-1	86.18	42.789	63.26	115.13	126.15
Exp. 37-R-2	44.82	42.789	63.26	115.13	126.15
Exp. 38	37.92	50.44	42.71	152.18	163.39
Exp. 38-R-1	24.13	50.44	42.71	152.18	163.39
Exp. 38-R-2	37.92	50.44	42.71	152.18	163.39
Exp. 40	58.61	16.89	52.33	41.26	45.68
Exp. 40-R-1	44.82	45.27	53.26	126.99	138.25
Exp. 40-R-2	37.92	45.27	53.26	126.99	138.25
Exp. 40-R-3	51.71	38.01	117.74	92.84	102.78
Exp. 41-R-3	31.03	28.55	88.44	69.73	77.20
Exp. 42	72.39	28.55	88.44	69.73	77.20
Exp. 42-R-3	58.61	28.55	88.44	69.73	77.20
Exp. 43	72.39	28.55	88.44	69.73	77.20
Exp. 43-R-1	65.5	28.55	88.44	69.73	77.20
Exp. 45	93.08	33.11	102.57	80.87	89.53
Exp. 45-R-1	72.39	33.11	102.57	80.87	89.53
Exp. 47	58.61	16.89	52.33	41.26	45.68

Appendix DD: Comparison of the measured and models predicted pressure drop across the hydrocyclone cont.

Exp. # No.	Measured Δp kPa	Δp body (Musch.) kPa	Δp body (Barth) kPa	ΔPx (Musch.) kPa	ΔPx (Barth, k=3.9) kPa
Exp. 49	58.61	24.3275396	75.3575559	59.4198971	65.783922
Exp. 49-R-1	65.5	24.3275396	75.3575559	59.4198971	65.783922
Exp. 49-R-2	93.08	24.3275396	75.3575559	59.4198971	65.783922
Exp. 50	51.71	24.3275396	75.3575559	59.4198971	65.783922
Exp. 50-R	72.39	24.3275396	75.3575559	59.4198971	65.783922
Exp. 53	58.61	16.8941247	52.331636	41.2638174	45.6832792
Exp. 54	24.13	16.8941247	52.331636	41.2638174	45.6832792
Exp. 55	37.92	10.8122398	33.4922471	26.4088431	29.2372987
Exp. 56	37.92	10.8122398	33.4922471	26.4088431	29.2372987
Exp. 57	44.82	25.4619394	16.3056102	82.9021284	87.4089271
Exp. 58	24.13	17.2057879	45.8400862	42.6975335	47.2109427

Appendix EE: Model predicted Euler number in inlet, body and vortex finder of the hydrocyclone.

Exp. # No.	Eu body (Musch.)	Eu body (Barth)	Eu_{in} (Musch.)	Eu_{in} (Barth)	Eu_X (Measured)	Eu_X (Musch.)	Eu_X Barth, k=3.9	Eu_{in} Shepherd-Lapple	Eu_{in} Casal Martinez-Benet
Exp. 1	8.943663	27.7040998	0.42	1.30	21.54	46.89	51.91	12.22	9.92
Exp. 1-R	8.943663	27.7040998	0.42	1.30	29.15	46.89	51.91	12.22	9.92
Exp. 2	8.943663	27.7040998	0.42	1.30	29.15	46.89	51.91	12.22	9.92
Exp. 3	8.943663	27.7040998	0.42	1.30	34.21	46.89	51.91	12.22	9.92
Exp. 4	8.943663	27.7040998	0.42	1.30	29.15	46.89	51.91	12.22	9.92
Exp. 5	8.943663	27.7040998	0.42	1.30	34.22	46.89	51.91	12.22	9.92
Exp. 6	8.943663	27.7040998	0.42	1.30	36.75	46.89	51.91	12.22	9.92
Exp. 7	8.943663	27.7040998	0.42	1.30	34.22	46.89	51.91	12.22	9.92
Exp. 8	8.943663	27.7040998	0.42	1.30	26.61	46.89	51.91	12.22	9.92
Exp. 9	8.943663	27.7040998	0.42	1.30	31.68	46.89	51.91	12.22	9.92
Exp. 10	8.943663	27.7040998	0.42	1.30	26.61	46.89	51.91	12.22	9.92
Exp. 11	8.943663	27.7040998	0.42	1.30	29.15	46.89	51.91	12.22	9.92
Exp. 13	8.943663	27.7040998	0.42	1.30	26.61	46.89	51.91	12.22	9.92
Exp. 14	8.943663	27.7040998	0.42	1.30	29.15	46.89	51.91	12.22	9.92
Exp. 15	8.943663	27.7040998	0.42	1.30	31.68	46.89	51.91	12.22	9.92
Exp. 16	8.943663	27.7040998	0.42	1.30	39.29	46.89	51.91	12.22	9.92
Exp. 17	8.943663	27.7040998	0.42	1.30	31.68	46.89	51.91	12.22	9.92
Exp. 18	8.943663	27.7040998	0.42	1.30	19.01	46.89	51.91	12.22	9.92
Exp. 20	8.943663	27.7040998	0.42	1.30	34.22	46.89	51.91	12.22	9.92
Exp.20-R1	8.943663	27.7040998	0.42	1.30	41.82	46.89	51.91	12.22	9.92

Appendix FF: Model predicted Euler number in inlet, body and vortex finder of the hydrocyclone.

Exp. # No.	Eu body (Musch.)	Eu body (Barth)	Eu_{in} (Musch.)	Eu_{in} (Barth)	Eu_X (Measured)	Eu_X (Musch.)	Eu_X Barth, k=3.9	Eu_{in} Shepherd-Lapple	Eu_{in} Casal Martinez-Benet
Exp.20-R2	8.943663	27.7040998	0.42	1.30	36.75	46.89	51.91	12.22	9.92
Exp20-R-3	8.943663	27.7040998	0.4214889	1.305614	36.7539672	46.8955462	51.9181807	12.2222222	9.9238465
Exp. 21	8.943663	27.7040998	0.4214889	1.305614	26.6149418	46.8955462	51.9181807	12.2222222	9.9238465
Exp. 23	8.943663	27.7040998	0.4214889	1.305614	21.5454291	46.8955462	51.9181807	12.2222222	9.9238465
Exp. 23-R	8.943663	27.7040998	0.4214889	1.305614	19.0106727	46.8955462	51.9181807	12.2222222	9.9238465
Exp. 25	8.943663	27.7040998	0.4214889	1.305614	16.198443	46.8955462	51.9181807	12.2222222	9.9238465
Exp25-R-1	8.943663	27.7040998	0.4214889	1.305614	24.8376126	46.8955462	51.9181807	12.2222222	9.9238465
Exp25-R-2	8.943663	27.7040998	0.4214889	1.305614	26.9974051	46.8955462	51.9181807	12.2222222	9.9238465
Exp. 26	8.9850812	12.3046272	0.4234408	0.5798814	12.3109845	30.5564382	33.4166233	12.2222222	9.9238465
Exp. 27	8.9850812	12.3046272	0.4234408	0.5798814	16.0989797	30.5564382	33.4166233	12.2222222	9.9238465
Exp. 27-R	8.9850812	12.3046272	0.4234408	0.5798814	19.886975	30.5564382	33.4166233	12.2222222	9.9238465
Exp. 28	8.9850812	12.3046272	0.4234408	0.5798814	12.3109845	30.5564382	33.4166233	12.2222222	9.9238465
Exp. 28-R	8.9850812	12.3046272	0.4234408	0.5798814	16.0989797	30.5564382	33.4166233	12.2222222	9.9238465
Exp. 31	8.9850812	12.3046272	0.4234408	0.5798814	19.886975	30.5564382	33.4166233	12.2222222	9.9238465
Exp. 31-R	8.9850812	12.3046272	0.4234408	0.5798814	6.6289917	30.5564382	33.4166233	12.2222222	9.9238465
Exp. 32	8.9850812	12.3046272	0.4234408	0.5798814	12.3109845	30.5564382	33.4166233	12.2222222	9.9238465
Exp. 32-R	8.9850812	12.3046272	0.4234408	0.5798814	14.2049821	30.5564382	33.4166233	12.2222222	9.9238465
Exp. 33	8.9500371	23.8449105	0.4217893	1.1237415	23.3121651	43.8361294	48.4698957	12.2222222	9.9238465
Exp. 33-R	8.9500371	23.8449105	0.4217893	1.1237415	30.485139	43.8361294	48.4698957	12.2222222	9.9238465
Exp. 34	8.943663	27.7040998	0.4214889	1.305614	20.0752704	46.8955462	51.9181807	12.2222222	9.9238465

Appendix S: Model predicted Euler number in inlet, body and vortex finder of the hydrocyclone cont.

Exp. # No.	Eu body (Musch.)	Eu body (Barth)	Eu_{in} (Musch.)	Eu_{in} (Barth)	Eu_X (Measured)	Eu_X (Musch.)	Eu_X Barth, k=3.9	Eu_{in} Shepherd-Lapple	Eu_{in} Casal Martinez-Benet
Exp. 34-R	8.943663	27.7040998	0.4214889	1.305614	27.3753687	46.8955462	51.9181807	12.2222222	9.9238465
Exp. 35	8.9469025	25.6352207	0.4216416	1.2081137	19.8993228	45.3149499	50.1374826	12.2222222	9.9238465
Exp. 37	8.9803389	13.2778847	0.4232174	0.6257482	12.2996843	32.0285399	35.0932954	12.2222222	9.9238465
Exp. 37-R-1	8.9803389	13.2778847	0.4232174	0.6257482	18.0877711	32.0285399	35.0932954	12.2222222	9.9238465
Exp. 37-R-2	8.9803389	13.2778847	0.4232174	0.6257482	9.4056409	32.0285399	35.0932954	12.2222222	9.9238465
Exp. 38	9.020824	7.6373556	0.4251253	0.3599264	6.7814312	22.0124793	23.6343614	12.2222222	9.9238465
Exp. 38-R-1	9.020824	7.6373556	0.4251253	0.3599264	4.3154562	22.0124793	23.6343614	12.2222222	9.9238465
Exp. 38-R-2	9.020824	7.6373556	0.4251253	0.3599264	6.7814312	22.0124793	23.6343614	12.2222222	9.9238465
Exp. 40	8.943663	27.7040998	0.4214889	1.305614	31.0254179	46.8955462	51.9181807	12.2222222	9.9238465
Exp. 40-R-1	8.9951634	10.5833774	0.423916	0.4987639	8.9041551	27.7182559	30.1773152	12.2222222	9.9238465
Exp. 40-R-2	8.9951634	10.5833774	0.423916	0.4987639	7.534285	27.7182559	30.1773152	12.2222222	9.9238465
Exp. 40-R-3	8.943663	27.7040998	0.4214889	1.305614	12.1668305	46.8955462	51.9181807	12.2222222	9.9238465
Exp. 41-R-3	8.943663	27.7040998	0.4214889	1.305614	9.7190658	46.8955462	51.9181807	12.2222222	9.9238465
Exp. 42	8.943663	27.7040998	0.4214889	1.305614	22.6778202	46.8955462	51.9181807	12.2222222	9.9238465
Exp. 42-R-3	8.943663	27.7040998	0.4214889	1.305614	18.3582354	46.8955462	51.9181807	12.2222222	9.9238465
Exp. 43	8.943663	27.7040998	0.4214889	1.305614	22.6778202	46.8955462	51.9181807	12.2222222	9.9238465
Exp. 43-R-1	8.943663	27.7040998	0.4214889	1.305614	20.5180278	46.8955462	51.9181807	12.2222222	9.9238465
Exp. 45	8.943663	27.7040998	0.4214889	1.305614	25.1406447	46.8955462	51.9181807	12.2222222	9.9238465
Exp. 45-R-1	8.943663	27.7040998	0.4214889	1.305614	19.5538348	46.8955462	51.9181807	12.2222222	9.9238465
Exp. 47	8.943663	27.7040998	0.4214889	1.305614	31.0254179	46.8955462	51.9181807	12.2222222	9.9238465

Appendix S: Model predicted Euler number in inlet, body and vortex finder of the hydrocyclone cont.

Exp. # No.	Eu body (Musch.)	Eu body (Barth)	Eu_{in} (Musch.)	Eu_{in} (Barth)	Eu_X (Measured)	Eu_X (Musch.)	Eu_X Barth, k=3.9	Eu_{in} Shepherd-Lapple	Eu_{in} Casal Martinez-Benet
Exp. 49	8.943663	27.7040998	0.4214889	1.305614	21.5454291	46.8955462	51.9181807	12.2222222	9.9238465
Exp. 49-R-1	8.943663	27.7040998	0.4214889	1.305614	24.0801854	46.8955462	51.9181807	12.2222222	9.9238465
Exp. 49-R-2	8.943663	27.7040998	0.4214889	1.305614	34.2192109	46.8955462	51.9181807	12.2222222	9.9238465
Exp. 50	8.943663	27.7040998	0.4214889	1.305614	19.0106727	46.8955462	51.9181807	12.2222222	9.9238465
Exp. 50-R	8.943663	27.7040998	0.4214889	1.305614	26.6149418	46.8955462	51.9181807	12.2222222	9.9238465
Exp. 53	8.943663	27.7040998	0.4214889	1.305614	31.0254179	46.8955462	51.9181807	12.2222222	9.9238465
Exp. 54	8.943663	27.7040998	0.4214889	1.305614	12.7751721	46.8955462	51.9181807	12.2222222	9.9238465
Exp. 55	8.943663	27.7040998	0.4214889	1.305614	31.36761	46.8955462	51.9181807	12.2222222	9.9238465
Exp. 56	8.943663	27.7040998	0.4214889	1.305614	31.36761	46.8955462	51.9181807	12.2222222	9.9238465
Exp. 57	9.0479957	5.7942598	0.4264058	0.2730667	15.9255062	17.7629243	18.7285681	12.2222222	9.9238465
Exp. 58	8.9500371	23.8449105	0.4217893	1.1237415	12.5527043	43.8361294	48.4698957	12.2222222	9.9238465

Appendix GG: Calculated some dimensionless numbers in hydrocyclone.

Exp. #	Froude Number	Stokes' 50 number	Stokes' 50 number	Stokes' 50 number	Swirl number	Swirl number
No.	F	Calc.	Musch.	Barth.	S_X	S_C
Exp. 1	4.20	0.046223	0.0018309	0.0025195	4.65	3.17
Exp. 1-R	4.20	0.0011371	0.0018309	0.0025195	4.65	3.17
Exp. 2	4.20	0.0011371	0.0018309	0.0025195	4.65	3.17
Exp. 3	4.20	0.0179622	0.0018309	0.0025195	4.65	3.17
Exp. 4	4.20	0.0066964	0.0018309	0.0025195	4.65	3.17
Exp. 5	4.20	0.0065218	0.0018309	0.0025195	4.65	3.17
Exp. 6	4.20	0.0140053	0.0018309	0.0025195	4.65	3.17
Exp. 7	4.20	0.0161672	0.0018309	0.0025195	4.65	3.17
Exp. 8	4.20	0.0011371	0.0018309	0.0025195	4.65	3.17
Exp. 9	4.20	0.007234	0.0018309	0.0025195	4.65	3.17
Exp. 10	4.20	0.011076	0.0018309	0.0025195	4.65	3.17
Exp. 11	4.20	0.0461307	0.0018309	0.0025195	4.65	3.17
Exp. 13	4.20	0.0239806	0.0018309	0.0025195	4.65	3.17
Exp. 14	4.20	0.060162	0.0018309	0.0025195	4.65	3.17
Exp. 15	4.20	0.0123302	0.0018309	0.0025195	4.65	3.17
Exp. 16	4.20	0.0177899	0.0018309	0.0025195	4.65	3.17
Exp. 17	4.20	0.0184257	0.0018309	0.0025195	4.65	3.17
Exp. 18	4.20	0.0185425	0.0018309	0.0025195	4.65	3.17
Exp. 20	4.20	0.0000312	0.0018309	0.0025195	4.65	3.17
Exp. 20-R-1	4.20	0.0003027	0.0018309	0.0025195	4.65	3.17
Exp. 20-R-2	4.20	0.0724256	0.0018309	0.0025195	4.65	3.17
Exp. 20-R-3	4.20	0.0724256	0.0018309	0.0025195	4.65	3.17
Exp. 21	4.20	0.0237815	0.0018309	0.0025195	4.65	3.17
Exp. 23	4.20	0.000443	0.0018309	0.0025195	4.65	3.17
Exp. 23-R	4.20	0.0240472	0.0018309	0.0025195	4.65	3.17
Exp. 25	4.55	0.023518	0.0018309	0.0025195	4.65	3.17
Exp. 25-R-1	4.55	0.0043786	0.0018309	0.0025195	4.65	3.17
Exp. 25-R-2	4.55	0.0027131	0.0018309	0.0025195	4.65	3.17
Exp. 26	6.37	0.003389	0.0018477	0.0025426	3.53	3.15
Exp. 27	6.37	0.0046128	0.0018477	0.0025426	3.53	3.15
Exp. 27-R	6.37	0.0027742	0.0018477	0.0025426	3.53	3.15
Exp. 28	6.37	0.0871626	0.0018477	0.0025426	3.53	3.15

Appendix HH: Calculated some dimensionless numbers in hydrocyclone.

Exp. # No.	Froude Number F	Stokes' 50 number Calc.	Stokes' 50 number Musch.	Stokes' 50 number Barth.	Swirl number S_X	Swirl number S_C
Exp. 28-R	6.3751872	0.0410457	0.0018477	0.0025426	3.5277936	3.16
Exp. 31	6.3751872	0.0143748	0.0018477	0.0025426	3.5277936	3.16
Exp. 31-R	6.3751872	0.013772	0.0018477	0.0025426	3.5277936	3.16
Exp. 32	6.3751872	0.6403601	0.0018477	0.0025426	3.5277936	3.16
Exp. 32-R	6.3751872	0.8305437	0.0018477	0.0025426	3.5277936	3.16
Exp. 33	3.6829451	0.0181972	0.0018334	0.002523	4.4548562	3.17
Exp. 33-R	3.6829451	0.007474	0.0018334	0.002523	4.4548562	3.17
Exp. 34	3.5004901	0.0410213	0.0018309	0.0025195	4.6493112	3.17
Exp. 34-R	3.5004901	0.0000055	0.0018309	0.0025195	4.6493112	3.17
Exp. 35	3.5917176	0.0303786	0.0018322	0.0025213	4.5495955	3.17
Exp. 37	7.0752852	0.7372763	0.0018457	0.0025399	3.6385842	3.16
Exp. 37-R-1	7.0752852	0.3204578	0.0018457	0.0025399	3.6385842	3.16
Exp. 37-R-2	7.0752852	0.522363	0.0018457	0.0025399	3.6385842	3.16
Exp. 38	9.8121109	0.3581555	0.0018624	0.0025629	2.82953	3.15
Exp. 38-R-1	9.8121109	0.0246115	0.0018624	0.0025629	2.82953	3.15
Exp. 38-R-2	9.8121109	0.0237319	0.0018624	0.0025629	2.82953	3.15
Exp. 40	3.5004901	0.4998737	0.0018309	0.0025195	4.6493112	3.17
Exp. 40-R-1	7.9875601	0.3293584	0.0018518	0.0025483	3.3070899	3.16
Exp. 40-R-2	7.9875601	0.0361495	0.0018518	0.0025483	3.3070899	3.16
Exp. 40-R-3	5.2507352	0.3883066	0.0018309	0.0025195	4.6493112	3.17
Exp. 41-R-3	4.5506372	0.0179311	0.0018309	0.0025195	4.6493112	3.17
Exp. 42	4.5506372	0.0272924	0.0018309	0.0025195	4.6493112	3.17
Exp. 42-R-3	4.5506372	0.0272924	0.0018309	0.0025195	4.6493112	3.17
Exp. 43	4.5506372	0.0000512	0.0018309	0.0025195	4.6493112	3.17
Exp. 43-R-1	4.5506372	0.0030737	0.0018309	0.0025195	4.6493112	3.17
Exp. 45	4.9006862	0.0000949	0.0018309	0.0025195	4.6493112	3.17
Exp. 45-R-1	4.9006862	0.0000194	0.0018309	0.0025195	4.6493112	3.17
Exp. 38-R-2	9.8121109	0.0237319	0.0018624	0.0025629	2.82953	3.1462023
Exp. 40	3.5004901	0.4998737	0.0018309	0.0025195	4.6493112	3.1731996
Exp. 40-R-1	7.9875601	0.3293584	0.0018518	0.0025483	3.3070899	3.1552253
Exp. 40-R-2	7.9875601	0.0361495	0.0018518	0.0025483	3.3070899	3.1552253
Exp. 40-R-3	5.2507352	0.3883066	0.0018309	0.0025195	4.6493112	3.1731996

Appendix T: Calculated some dimensionless numbers in hydrocyclone contd.

Exp. # No.	Froude Number F	Stokes' 50 number Calc.	Stokes' 50 number Musch.	Stokes' 50 number Barth.	Swirl number S_X	Swirl number S_C
Exp. 41-R-3	4.5506372	0.0179311	0.0018309	0.0025195	4.6493112	3.1731996
Exp. 42	4.5506372	0.0272924	0.0018309	0.0025195	4.6493112	3.1731996
Exp. 42-R-3	4.5506372		0.0018309	0.0025195	4.6493112	3.1731996
Exp. 43	4.5506372	0.0000512	0.0018309	0.0025195	4.6493112	3.1731996
Exp. 43-R-1	4.5506372	0.0030737	0.0018309	0.0025195	4.6493112	3.1731996
Exp. 45	4.9006862	0.0000949	0.0018309	0.0025195	4.6493112	3.1731996
Exp. 45-R-1	4.9006862	0.0000194	0.0018309	0.0025195	4.6493112	3.1731996
Exp. 47	3.5004901	0.0240526	0.0018309	0.0025195	4.6493112	3.1731996
Exp. 49	4.2005882	0.0599515	0.0018309	0.0025195	4.6493112	3.1731996
Exp. 49-R-1	4.2005882	0.0000565	0.0018309	0.0025195	4.6493112	3.1731996
Exp. 49-R-2	4.2005882	0.0000632	0.0018309	0.0025195	4.6493112	3.1731996
Exp. 50	4.2005882	0.0000472	0.0018309	0.0025195	4.6493112	3.1731996
Exp. 50-R	4.2005882	0.0028372	0.0018309	0.0025195	4.6493112	3.1731996
Exp. 53	3.5004901	0.0000221	0.0018309	0.0025195	4.6493112	3.1731996
Exp. 54	3.5004901	0.0147772	0.0018309	0.0025195	4.6493112	3.1731996
Exp. 55	2.8003921	0.0000177	0.0018309	0.0025195	4.6493112	3.1731996
Exp. 56	2.8003921	0.0026222	0.0018309	0.0025195	4.6493112	3.1731996
Exp. 57	8.0618658	0.0059132	0.0018739	0.0025786	2.4355823	3.136598
Exp. 58	3.6829451	0.006841	0.0018334	0.002523	4.4548562	3.1709845

Appendix II: Comparison of measured cut-size to models predicted cut-size.

Exp. #	d_{50}(Measured)	d_{50} (Musch.)	d_{50}(Barth)
No.	µm	µm	µm
Exp. 1	45.1	19.9	23.4
Exp. 1-R	45.7	19.9	23.4
Exp. 2	39.7	19.9	23.4
Exp. 3	39.424	19.9	23.4
Exp. 4	44.1	19.9	23.4
Exp. 5	47.6	19.9	23.4
Exp. 6	45.1	19.9	23.4
Exp. 9	49.6	19.9	23.4
Exp. 10	40	19.9	23.4
Exp. 11	40	19.9	23.4
Exp. 14	44.2	19.9	23.4
Exp. 15	41.7	19.9	23.4
Exp. 16	42.1	19.9	23.4
Exp. 17	43.2	19.9	23.4
Exp. 18	43.4	19.9	23.4
Exp. 21	41.8	19.9	23.4
Exp. 23	49.8	19.9	23.4
Exp. 23-R	40.2	19.9	23.4
Exp. 25	38.6	19.1	22.5
Exp. 25-R-1	39.6	19.1	22.5
Exp. 25-R-2	38.3	19.1	22.5
Exp. 28	37.8	18.6	21.8
Exp. 28-R	39.7	18.6	21.8
Exp. 31	41.9	18.6	21.8
Exp. 31-R	40.8	18.6	21.8
Exp. 32-R	44.5	18.6	21.8
Exp. 33	50.5	21.7	25.5
Exp. 33-R	50.9	21.7	25.5
Exp. 34	53	21.8	25.6
Exp. 34-R	49.2	21.8	25.6
Exp. 35	48.7	21.8	25.6
Exp. 38	32.7	16.8	19.7
Exp. 38-R-1	33	16.8	19.7

Appendix JJ: Comparison of measured cut-size to models predicted cut-size.

Exp. #	d_{50}(Measured)	d_{50} (Musch.)	d_{50}(Barth)
No.	µm	µm	µm
Exp. 40	54.6	21.8	25.6
Exp. 40-R-2	35.9	17.2	20.2
Exp. 40-R-3	39.5	17.8	20.9
Exp. 41-R-3	49.9	19.1	22.5
Exp. 42	44.39	19.1	22.5
Exp. 42-R-3	48	19.1	22.5
Exp. 43	42.32	19.1	22.5
Exp. 43-R-1	50.8	19.1	22.5
Exp. 45	44.2	18.4	21.6
Exp. 45-R-1	41.9	18.4	21.6
Exp. 47	49.1	21.8	25.6
Exp. 49	44	19.9	23.4
Exp. 49-R-1	43.5	19.9	23.4
Exp. 49-R-2	43.7	19.9	23.4
Exp. 50	43.2	19.9	23.4
Exp. 50-R	44.8	19.9	23.4
Exp. 55	52.4	24.4	28.6
Exp. 56	59.2	24.4	28.6
Exp. 57	45.5	20	23.4
Exp. 58	45	21.7	25.5

Model for computing constriction coefficient (α)

$$\alpha = \frac{1}{\xi}\left\{1-\sqrt{1+4\left[\left(\frac{\xi}{2}\right)^2-\frac{\xi}{2}\right]}\sqrt{1-\frac{\left(1-\xi^2\right)\left(2\xi-\xi^2\right)}{1+c_o}}\right\}$$ Equation 178

Where

$$\xi = b(\frac{1}{2}D) = \frac{b}{R}$$ Equation 179

C_o is the ratio of the mass of the incoming solids to mass of incoming gas in the stream feeding the cyclone.

b = width of the cyclone inlet.

D = Cyclone Diameter.

R= D/2 radius of the cyclone.

C_o = mass of the incoming solid to mass of incoming gas in the feed.

```
// (n) refer to equation numbers in "Model Programming.doc" (14/5/3)

class Model1
{
      // probably won't be modeling with
      // different values for gravity
      static final double g = 9.81;

//---------------------------------------------------------------------


      // Xi (2)
      // b - width of cyclone inlet
      // d - cyclone diameter

      static double xi(double b, double d)
      {
            return b / (0.5 * d);
      }

//---------------------------------------------------------------------
```

```
      // constriction coefficient (1)
      // b - width of cyclone inlet
      // d - cyclone diameter
      // c0 - ratio of mass of incoming solid to mass of incoming gas
in feed
      // Modified for fewer operations

      static double alpha(double b, double d, double c0)
      {
            double xi = b / (0.5 * d);   // (2)
            double xisq = xi * xi;
            return (1 -
                        Math.sqrt((1 + (xisq - 2 * xi))
                           * (1 - (1 - xisq) * xi * (2 - xi) / (1 +
c0)))) / xi;
      }


      // for use when Xi is already calculated

      static double alpha(double xi, double c0)
      {
            double xisq = xi * xi;
            return (1 -
                        Math.sqrt((1 + (xisq - 2 * xi))
                           * (1 - (1 - xisq) * xi * (2 - xi) / (1 +
c0)))) / xi;
      }
```

```
//-----------------------------------------------------------------------
```

Model for computing wall velocity ($v_{\theta w}$)

$$v_{\theta w} = \frac{v_{in} R_{in}}{\alpha R}$$ Equation 180

$v_{\theta w}$ = Wall Velocity.

v_{in}= Mean gas velocity inlet.

R_{in}= Inlet Radius.

```
//-----------------------------------------------------------------------

      // wall velocity (3)
      // r - radius of hydrocyclone
      // rin - radius of inlet
      // alpha - constriction coefficient
      // vin - mean gas velocity inlet
```

```
	static double vThetaW(double r, double rin, double alpha, double
vin)
	{
		return vin * rin / (alpha * r);
	}
//---------------------------------------------------------------------
```

Mean Gas Velocity Inlet (v_{in})

$$v_{in} = \frac{Q}{A_{in}} = \frac{Q}{a.b}$$ Equation 181

a and b are the height and wide of the cyclone inlet.

Q is the volumetric flow rates ms^{-1}.

$R_{in} = R\text{-}R_{in}$

```
//---------------------------------------------------------------------

	// mean gas velocity inlet (4)
	// a - height of cyclone inlet
	// b - width of cyclone inlet
	// q - volumetric flow rate

	static double vin(double a, double b, double q)
	{
		return q / (a * b);
	}


//---------------------------------------------------------------------
```

Geometric mean radius (R_m)

$$R_m = \sqrt{R_x.R}$$ Equation 182

R_x = Vortex diameter.

R= Cyclone Diameter.

```
// geometric mean radius (5)
	// r - cyclone radius
	// rx - vortex radius

	static double rm(double r, double rx)
	{
		return Math.sqrt(rx * r);
	}
```

Wall axial velocity (v_{zw})

$$V_{zw} = \frac{0.9Q}{\pi(R^2 - R_m^2)}$$ Equation 183

```
//-------------------------------------------------------------------------

      // wall axial velocity (6)
      // r - cyclone radius
      // rm - geometric mean radius
      // q - volumetric flow rate

      static double vzw(double r, double rm, double q)
      {
            return 0.9 * q / (Math.PI * (r * r - rm * rm));
      }

//-------------------------------------------------------------------------
```

Cyclone Body Reynolds Number Re_p (Muschelknautz and Trefz)

$$\mathrm{Re}_R = \frac{R_{in} R_m v_{zw} \rho}{H\mu\left(1 + \left(\frac{v_{zw}}{v_{\theta m}}\right)^2\right)}$$ Equation 184

This equation is good for Reynolds numbers greater than 2000.

ρ and μ are the gas phase density and absolute viscosity.

$v_{\theta m}$ geometrical mean rotational velocity based on the spin velocity near the wall $v_{\theta w}$

$v_{\theta CS}$ is internal spin velocity (inner vortex).

μ is absolute viscosity.

R_m is geometric mean radius.

H Cyclone length.

```
//-------------------------------------------------------------------------
      // cyclone body Reynolds number (7)
      // rin - inlet radius
      // rm - geometric mean radius
      // h - cyclone length
      // rho - gas phase density
      // mu - absolute viscosity
      // vzw - wall axial velocity
      // vThetaM - geometrical mean rotational velocity
```

```
      static double rer(double rin, double rm, double h,
                        double rho, double mu, double vzw, double
vThetaM)
      {
            return rin * rm * vzw * rho
                        / (h * mu * (1 + (vzw * vzw / (vThetaM *
vThetaM))));
      }

      // usually, (vzw/vThetaM)^2 << 1, so it can be ignored

      static double rer(double rin, double rm, double h,
                        double rho, double mu, double vzw)
      {
            return rin * rm * vzw * rho / (h * mu);
      }

//-----------------------------------------------------------------------
```

$v_{\theta m}$ Geometrical mean rotational velocity

$$v_{\theta m} = \sqrt{v_{\theta w} v_{\theta CS}}$$ Equation 185

```
//-----------------------------------------------------------------------

      // geometrical mean rotational velocity (8)
      // vThetaW - wall velocity
      // vThetaCS - inner cortex velocity

      static double vThetaM(double vThetaW, double vThetaCS)
      {
            return Math.sqrt(vThetaW * vThetaCS);
      }

//-----------------------------------------------------------------------
```

$v_{\theta CS}$ inner vortex velocity

$$v_{\theta cs} = \left(\frac{v_{zw}}{v_{\theta m}} \right)^2 \equiv nil$$ Equation 186

Total Friction Factor (f) Muschelknautz model

$$f = f_{air} + 0.25\left(\frac{R}{R_x}\right)^{-0.625}\sqrt{\frac{\eta c_o Fr_x \rho}{\rho_{str}}}$$ Equation 187

ρ_{str} density of the strand.

η Overall cyclone collection efficiency. (0.9-0.99).

Fr_x Froude number for the flow out the vortex tube.

C_o mass fraction of solids in incoming feed.

```
//-------------------------------------------------------------------------
      // total friction factor (10)
      // r - cyclone radius
      // rx - vortex radius
      // fAir - friction from air
      // rho - gas phase density
      // rhoStr - density of the strand
      // c0 - constriction coefficient
      // frx - Froude number
      // eta - overall cyclone collection efficiency (0.9-0.99)

      static double f(double r, double rx, double fAir, double rho,
                        double rhoStr, double c0, double frx, double
eta)
      {
            return fAir + 0.25 * Math.pow(r / rx, -0.625)
                  * Math.sqrt(eta * c0 * frx * rho / rhoStr);
      }

//-------------------------------------------------------------------------
```

$$f = f_{air} + f_{water} = 0.005\left(1 + 3\sqrt{c_o}\right)$$ Equation 188

```
//-------------------------------------------------------------------------

      // c0 for calculating f using (11)

      static double c0(double qInG, double rhoG, double qInL, double
rhoL)
      {
            return qInG * rhoG / (qInL * rhoL);
      }

      // total friction factor (11)

      static double f(double c0)
      {
```

```
            return 0.005 * (1 + 3 * Math.sqrt(c0));
      }

//---------------------------------------------------------------------
```

Froude Number (Fr)

$$Fr_x = \frac{v_x}{\sqrt{2R_x g}} \qquad \text{Equation 189}$$

v_x is superficial axial velocity through the inlet section of the vortex tube.

```
//---------------------------------------------------------------------

      // Froude number (12)
      // rx - vortex radius
      // vx - superficial axial velocity through inlet section of
vortex tube
      // g - gravity

      static double frx(double rx, double vx)
      {
            return vx / Math.sqrt(2 * rx * g);
      }
//---------------------------------------------------------------------

      // vx - superficial axial velocity through inlet section of
vortex tube
      // Ax - Vortex finder area

      static double vx(double Ax, double Q)
      {
            return Q / Ax;
      }

//---------------------------------------------------------------------
```

The Muschelknautz Cutpoint Models (d_{50}) 1972

In order to compute d_{50} we must first compute the tangential velocity of the gas at the inner core radius $R_{cs.}$

$$v_{\theta CS} = v_{\theta W} \frac{\left(\frac{R}{R_x}\right)}{\left[1 + \frac{fA_R v_{\theta W}\sqrt{\frac{R}{R_x}}}{2Q}\right]}$$

Equation 190

A_R is the total inside area of the cyclone.

$A_R = A_{roof} + A_{barrel} + A_{vt}$

A_{vt} = is the area of vortex tube.

```
//-------------------------------------------------------------------------

      // Muschelknautz Cutpoint Models
      // tangential velocity of gas at inner core radius Rcs (13)
      // r - radius of cyclone
      // rx - radius of vortex
      // ar - total area inside cyclone: aRoof + aBarrel + aVortexTube
      // q - volumetric flow rate
      // f - total friction factor
      // vThetaW - wall velocity

      static double vThetaCS(double r, double rx, double ar,
                             double q, double f, double vThetaW)

      {
            return vThetaW * (r / rx)
                        / (1 + f * ar * vThetaW * Math.sqrt(r / rx) /
(2 * q));
      }
// ------------------------------------------------------------------------------------------------------------------------
```

Modified the Muschelknautz Cut-point Models for Underflow Stream (d_{50})

$$d_{50underflow} = 1.093\sqrt{\frac{18\mu.0.9Q}{2\pi(\rho_l - \rho_g)v_{\theta CS}^2(H-S)}}$$

Equation 191

```
// Modified Muschelknautz Cutpoint model d50 (underflow stream) (14)
      // h - cyclone height (m)
      // s - length of vortex finder (m)
      // rho - gas phase density (kg/m^3)
      // rhop - density of liquid (kg/m^3)
      // mu - absolute viscosity
      // q - volumetric flow rate
      // vThetaCS - inner cortex velocity
      static double d50_modU(double h, double s, double rho, double
rhop,
                                 double mu, double q, double vThetaCS)
      {
            return 1.093 * Math.sqrt(18 * mu * 0.9 * q
                                                / (2 * Math.PI * (rhop
- rho)
                                                   * Math.pow(vThetaCS,
2) * (h - s)));
      }
// ----------------------------------------------------------------------------------------------------------------
```

Modified the Muschelknautz Cut-point Models for Overflow Stream(d_{50})

$$d_{50overflow} = 1.55\sqrt{\frac{18\mu.0.9Q}{2\pi(\rho_l - \rho_g)v_{\theta CS}^2(H-S)}}$$ Equation 192

```
// Modified Muschelknautz Cutpoint model d50 (overflow stream) (15)
      // h - cyclone height (m)
      // s - length of vortex finder (m)
      // rho - gas phase density (kg/m^3)
      // rhop - density of liquid (kg/m^3)
      // mu - absolute viscosity
      // q - volumetric flow rate
      // vThetaCS - inner cortex velocity
      static double d50_modO(double h, double s, double rho, double rhop,
                                 double mu, double q, double vThetaCS)
      {
            return 1.55* Math.sqrt(18 * mu * 0.9 * q
                                    / (2 * Math.PI * (rhop - rho)
                                       * Math.pow(vThetaCS, 2) * (h - s)));
      }
// ----------------------------------------------------------------------
```

The Muschelknautz Cut-point Models

$$d_{50} = x_{fact}\sqrt{\frac{18\mu(0.9Q)}{2\pi(\rho_p - \rho)v_{\theta CS}^2(H-S)}}$$ Equation 193

```
//-----------------------------------------------------------------------


      // Muschelknautz Cutpoint model d50 (16)
      // h - cyclone height
      // s - length of vortex finder
      // rho - gas phase density
      // rhop - density of ____
      // mu - absolute viscosity
      // q - volumetric flow rate
      // vThetaCS - inner cortex velocity
      // xFact - 'X' factor
      // Modified for fewer operations

      static double d50(double h, double s, double rho, double rhop,
                        double mu, double q, double vThetaCS, double
xFact)
      {
            return xFact * Math.sqrt(8.1 * mu * q
                                     / (Math.PI * (rhop - rho)
                                          * vThetaCS * vThetaCS * (h -
s)));
      }

//-----------------------------------------------------------------------
```

The Barth Cut-point Models (d_{50}) 1956

$$d_{50} = \sqrt{\frac{v_{rCS}9\mu D_x}{\rho_p v_{\theta CS}^2}}$$ Equation 194

```
//-----------------------------------------------------------------------

      // Barth Cutpoint model d50 (17)
      // dx - diameter of vortex finder
      // rhop - density of liquid
      // mu - absolute viscosity
      // vrcs - radial velocity
      // vThetaCS - inner cortex velocity

      static double d50(double dx, double rhop, double mu,
                        double vrcs, double vThetaCS)
      {
```

```
            return Math.sqrt(vrcs * 9 * mu * dx / (rhop * vThetaCS *
vThetaCS));
      }

//-----------------------------------------------------------------------
```

Modified The Barth Cut-point Models for the Underflow Stream (d_{50})

$$d_{50underflow} = 0.98\sqrt{\frac{v_{rcs}.\mu.9.D_x}{\rho_l v_{\theta CS}^2}}$$ Equation 195

```
// Modified Barth Cutpoint model d50 (underflow stream) (18)
        // dx - diameter of vortex finder
        // rhop - density of liquid
        // mu - absolute viscosity
        // vrcs - radial velocity
        // vThetaCS - inner cortex velocity
        static double d50_modU(double dx, double rhop, double mu, double vrcs, double vThetaCS)
        {
                return 0.98* Math.sqrt(vrcs * 9 * mu * dx / (rhop * Math.pow(vThetaCS, 2)));
        }

// ----------------------------------------------------------------------------------------------------------------------
```

Modified the Barth Cut-point Models for the Overflow Stream (d_{50})

$$d_{50overflow} = 1.22\sqrt{\frac{(v_{rcs}).\mu.9.D_x}{\rho_l v_{\theta CS}^2}}$$ Equation 196

```
        // Modified Barth Cutpoint model d50 (overflow stream) (19)
        // dx - diameter of vortex finder
        // rhop - density of liquid
        // mu - absolute viscosity
        // vrcs - radial velocity
```

```
// vThetaCS - inner cortex velocity
static double d50_modO(double dx, double rhop, double mu, double vrcs, double vThetaCS)
{
        return 1.22* Math.sqrt(vrcs * 9 * mu * dx / (rhop * Math.pow(vThetaCS, 2)));
}

//-----------------------------------------------------------------------
```

Radial Velocity

$$\left\|v_r\left(R_x\right)\right\| \equiv v_{rCS} = \frac{Q}{\pi D_x H_{cs}}$$ Equation 197

Q is the volumetric flowrate through the cyclone.

D_x is the diameter of the vortex finder.

Hcs is the height of the vortex finder.

```
//-----------------------------------------------------------------------

      // Barth Cutpoint Models
      // radial velocity (20)
      // dx - diameter of vortex finder
      // hcs - height of vortex finder
      // q - volumetric flowrate through cyclone

      static double vrcs(double dx, double hcs, double q)
      {
            return q / (Math.PI * dx * hcs);
      }

//-----------------------------------------------------------------------
```

Swirl velocity in the cyclone body (Alexander 1949)

$$v_\theta = \frac{C}{r^n}$$ Equation 198

n is 1 for less free and and -1 for solid body rotation (0.7-0.8). C is a constant.

```
//-----------------------------------------------------------------------

      // swirl velocity in cyclone body (21)
      // r - cyclone radius
      // n -
```

```
        // c - constant

        static double vTheta(double r, double n, double c)
        {
              return c / Math.pow(r, n);
        }

//---------------------------------------------------------------------
```

Empirical Expression for n (Alexander 1949)

$$n = 1 - \left(1 - 0.6D^{0.14}\right)\left(\frac{T}{T_o}\right)^{0.3} \qquad \text{Equation 199}$$

D body diameter. (m)

T degree Kelvin. T_o @ room temperature 283K

```
//---------------------------------------------------------------------
        // empirical expression for n (22)
        // d - body diameter in meters
        // t - temperature in degrees Kelvin
        // t0 - initial temperate in K

        static double n(double d, double t, double t0)
        {
              return 1 - (1 - 0.6 * Math.pow(d, 0.14)) * Math.pow(t / t0,
0.3);
        }

//---------------------------------------------------------------------
```

The Muschelknautz Hydrocyclone Efficiency Model

This model compute the efficiency curve (S shape curve) and overall separation efficiency at low inlet solids $C_o < C_{oL}$

$\eta \rightarrow 0$ as $d \rightarrow 0$

$\eta \rightarrow 1$ as $d >> d_{50}$

$\eta = 0.5$ for $d = d_{50}$

The efficiency curve η is normally defined with the use of just the two parameters.

1. The cut-size d_{50}
2. a slope (m)
3. a variety of equations have been proposed to represent $\eta(d_{50}, m)$.

$$\eta_i = \frac{1}{1+\left(\frac{d_{50}}{d_i}\right)^m}$$ Equation 200

```
//-----------------------------------------------------------------------

      // Muschelknautz Hydrocyclone Efficiency Model (23)
      // d50 - cut-size
      // d - particle size to calculate efficiency for
      // m - slope

      static double eta(double d50, double d, double m)
      {
            return 1 / (1 + Math.pow(d50 / d, m));
      }

//-----------------------------------------------------------------------
```

The Dirgo and Leith (1985) Hydrocyclone Efficiency Model

$$\eta(d) = \frac{1}{1+\left(\frac{d_{50}}{d}\right)^{6.4}}$$ Equation 201

```
// Dirgo and Leith (1985) Hydrocyclone Efficiency Model (24)

      // d50 - cut-size
      // d - particle size to calculate efficiency for

      static double eta(double d50, double d)
      {
            return 1 / (1 + Math.pow(d50 / d, 6.4));
      }
//-----------------------------------------------------------------------
```

Pressure Drop over the hydrocyclone

Pressure drop in total pressure (The sum of the static and dynamic pressures).

Pressure Drop

1. Losses in the entry (Negligible).
2. Losses in the separation space (the main space body, losses is high).
3. Losses in the vortex finder (the largest).

The pressure drop over a cyclone, Δp is proportional to the square of the volumetric flow rates.

Pressure drop is often reported in a dimensionless form known as the "Euler number".

$$E_u \equiv \frac{\Delta p}{\frac{1}{2}\rho < v_z >^2}$$ Equation 202

Where $<v_z>$ is the mean axial velocity in the cyclone body.

```
//-----------------------------------------------------------------------

      // Euler number for change in pressure across body (25)
      // deltaP - change in pressure across body
      // rho - liquid density
      // vz - axial velocity in hydrocyclone body

      static double euBody(double deltaP, double rho, double vz)
      {
            return deltaP / (0.5 * rho * vz * vz);
      }

//-----------------------------------------------------------------------
```

Pressure loss in the body of hydrocyclone: (Barth Model)

Barth stated that inlet losses could be effectively avoided by design. He estimated the pressure loss in the body as the decrease in dynamic pressure at this imagined friction surface, i.e. he considered the decrease in total pressure to rise from the loss of swirl velocity at the friction surface. This become is:

$$\frac{\Delta p_{body}}{\frac{1}{2}\rho v_x^2} = \frac{D_x}{D}\left[\frac{1}{\left[\frac{v_x}{v_{\theta cs}} - \frac{(H-S)}{0.5D_x}f\right]^2} - \left(\frac{v_{\theta cs}}{v_x}\right)^2\right]$$ Equation 203

$f = f_{air} + f_{water}$

D_x= Vortex Finder diameter

D = Body Diameter.

ρ = Gas density

V_x = velocity of gas in vortex finder.

θCS= tangential velocity in vortex finder.

v = tangential velocity.

H= cyclone height.

S = length of vortex finder.

f = Friction Factor.

$v_{\theta CS}$= internal spine velocity.

```
//-------------------------------------------------------------------------

      // Barth model for Pressure loss in body of hydrocyclone (26)
      // d - body diameter
      // dx - vortex finder diameter
      // h - cyclone height
      // s - length of vortex finder
      // rho - gas density
      // f - fAir + fWater
      // vx - velocity of gas in vortex finder
      // vThetaCS - tangential velocity in vortex finder

      static double deltaPBody(double d, double dx, double h,
                               double s, double rho, double f,
                               double vx, double vThetaCS)
      {
            return 0.5 * rho * vx * vx
                     * dx / d
                     * (1 / Math.pow(vx / vThetaCS - (h - s) * 2 / dx *
f, 2)
                        - Math.pow(vThetaCS / vx, 2));
      }

//-------------------------------------------------------------------------
```

Pressure Loss in Vortex Finder (Barth semi empirical approach).

Barth estimated the loss in the vortex finder by a semi-empirical approach, the reasoning behind which is somewhat cryptic.

$$\frac{\Delta p_x}{\frac{1}{2}\rho v_x^2} = \left(\frac{v_{\theta CS}}{v_x}\right)^2 + K\left(\frac{v_{\theta CS}}{v_x}\right)^{\frac{4}{3}}$$

Equation 204

K is an empirical value 3.41-4.4.

```
//-------------------------------------------------------------------

      // Pressure loss in vortex finder (Barth semi-empirical approach)
(27)
      // rho - density of gas
      // vx - velocity of gas in vortex finder
      // vThetaCS - tangential velocity in vortex finder
      // k - empirical value, 3.41 - 4.4

      static double deltaPx(double rho, double vx, double vThetaCS,
double k)
      {
            double v = vThetaCS / vx;
            return 0.5 * rho * vx * vx
                        * (Math.pow(v, 2) + k * Math.pow(v, 4.0 / 3));
      }
//-------------------------------------------------------------------
```

Modified Barth Pressure Drop Model

$$\frac{\Delta p_x}{\frac{1}{2}\rho v_x^2} = \left(\left(\frac{v_{\theta CS}}{v_x} \right)^{2.35} + 4 \left(\frac{v_{\theta CS}}{v_x} \right)^{\frac{4}{3}} \right)$$

Equation 205

```
// Pressure loss in vortex finder (modified Barth semi-empirical(28)
approach) (23)
      // rho - density of gas
      // vx - velocity of gas in vortex finder
      // vThetaCS - tangential velocity in vortex finder
      static double deltaPx_modB(double rho, double vx, double
vThetaCS)
      {
            double v = vThetaCS / vx;
            return 0.5 * rho * vx * vx * (Math.pow(v, 2.35) + 4 *
Math.pow(v, 4.0 / 3));
      }
```

Purely empirical models: Pressure Drop

Shepherd and Lapple (1940)

This model is valid for slot inlets hydrocyclones.

$$Eu_{in} = \frac{16ab}{D_x^2}$$

Equation 206

```
//-------------------------------------------------------------------
      // Shepherd and Lapple (1940) purely empirical model for pressure
drop
      // valid for slot inlets hydrocyclones (29)
      // Dx - vortex finder diameter
      // a - cyclone inlet height
      // b - cyclone inlet width

      static double euIn40(double dx, double a, double b)
      {
            return 16 * a * b / (dx * dx);
      }

//-------------------------------------------------------------------
```

Casal and Martinez-Benet (1983) Model.

$$Eu_{in} = 3.33 + 11.3\left(\frac{ab}{D_x^2}\right)^2 \qquad \text{Equation 207}$$

a is the inlet area

b is the outlet area

D_x diameter of the gas exit tube.

```
//-------------------------------------------------------------------

      // Casal and Martinez-Benet (1983) purely empirical model for
      //   pressure drop (30)
      // dx - diameter of gas exit tube
      // a - inlet area
      // b - outlet area

      static double euIn83(double dx, double a, double b)
      {
            return 3.33 + 11.3 * Math.pow(a * b / (dx * dx), 2);
      }
//-------------------------------------------------------------------
```

The Muschelknautz Hydrocyclone Pressure Drop Models

The wall loss, or the loss in the cyclone body, is given by,

$$\Delta p_{body} = \frac{f A_R \rho \left(v_{\theta w} v_{\theta CS}\right)^{1.5}}{2 \times 0.9 Q} \qquad \text{Equation 208}$$

```
//-------------------------------------------------------------------

      // Muschelknautz model for
```

```
      // pressure loss in cyclone body (31)
      // ar - total area inside cyclone: aRoof + aBarrel + aVortexTube
      // rho - gas phase density
      // f - total friction factor
      // q - volumetric flow rate
      // vThetaW - wall velocity
      // vThetaCS - inner cortex velocity

      static double deltaPBody(double ar, double rho, double f,
                               double q, double vThetaW, double
vThetaCS)
      {
            return f * ar * rho * Math.pow(vThetaW * vThetaCS, 1.5) /
(1.8 * q);
      }

//-----------------------------------------------------------------------
```

The loss in the core and in the vortex finder is given by,

$$\Delta p_x = \left[2 + \left(\frac{v_{\theta CS}}{v_x} \right)^2 + 3 \left(\frac{v_{\theta CS}}{v_x} \right)^{\frac{4}{3}} \right] \frac{1}{2} \rho v_x^2$$

Equation 209

```
// Muschelknautz model for
      // pressure loss in core and in vortex finder (32)
      // rho - gas phase density
      // vx - wall velocity
      // vThetaCS - inner cortex velocity

      static double deltaPx(double rho, double vx, double vThetaCS)
      {
            double v = vThetaCS / vx;
            return 0.5 * (2 + Math.pow(v, 2) + 3 * Math.pow(v, 4.0 /
3))
                        * rho * vx * vx;
      }
//-----------------------------------------------------------------------
```

Modified Muschelknautz Pressure Drop Model

$$\frac{\Delta p_x}{\frac{1}{2} \rho v_x^2} = \left(5 + \left(\frac{v_{\theta CS}}{v_x} \right)^{2.42} + 3 \left(\frac{v_{\theta CS}}{v_x} \right)^{\frac{4}{3}} \right)$$

Equation 210

```
// pressure loss in core and in vortex finder (33)
      // rho - gas phase density
```

```
	// vx - wall velocity
	// vThetaCS - inner cortex velocity
	static double deltaPx_modM(double rho, double vx, double
vThetaCS)
	{
		double v = vThetaCS / vx;
		return 0.5 * (5 + Math.pow(v, 2.42) + 3 * Math.pow(v, 4.0 /
3)) * rho * vx * vx;
```

```
//-----------------------------------------------------------------
```

Pressure Drop over inlet area Δp_{in}:

$$Eu_{in} = \frac{\Delta p}{\frac{1}{2}\rho v_{in}^2}$$ Equation 211

```
//-----------------------------------------------------------------

	// Euler number for pressure drop over inlet area (34)
	// deltaP - change in pressure across body
	// rho - liquid density
	// vin - inlet velocity

	static double euInlet(double deltaP, double rho, double vin)
	{
		return deltaP / (0.5 * rho * vin * vin);
	}

//-----------------------------------------------------------------
```

Pressure Drop over vortex finder Δ_x:

v_x predicted by the models.(m/s).

$$Eu_x = \frac{\Delta p}{\frac{1}{2}\rho v_x^2}$$ Equation 212

```
	// Euler number for pressure drop over vortex finder (35)
	// deltaP - change in pressure over vortex finder
	// rho - liquid density
	// vx - velocity inside vortex finder

	static double euX(double deltaP, double rho, double vx)
	{
		return deltaP / (0.5 * rho * vx * vx);
	}
```

```
//-------------------------------------------------------------------
```

Bernoulli's Equation

$$P_1 + \frac{1}{2}\rho_l V_1^2 = P_2 + \frac{1}{2}\rho_l V_2^2 = C \qquad \text{Equation 213}$$

```
// Calculate p2 using Bernoulli equation (36)
// p1 + 0.5 * rhoL * v1^2 = p2 + 0.5 * rhoL * v2^2

static double p2(double p1, double v1, double v2, double rhoL)
{
      return p1 + 0.5 * rhoL * (v1 * v1 - v2 * v2);
}

//-------------------------------------------------------------------
```

Swirl Number Calculation (S)

Swirl number represents the intensity of swirl in annular flow.

$$S = \frac{Tangential.momenta}{Axial.momenta} = \frac{Tangential.Velocity}{Axial.Velocity} = \frac{m/s}{m/s} \qquad \text{Equation 214}$$

```
//-------------------------------------------------------------------

      // Swirl number - represents intensity of swirl in annular flow
(37)
      // vtangential - tangential velocity
      // vaxial - axial velocity

      static double swirl(double vtangential, double vaxial)
      {
            return vtangential / vaxial;
      }

//-------------------------------------------------------------------
```

Characteristic velocity inside the cylindrical hydrocyclone

$$v = \frac{4Q}{\pi D_c^2} \qquad \text{Equation 215}$$

In this equation Q is volume inflow rate m^3/s.

Dc = Hydrocyclone inside diameter = 2.45 cm = 0.0245 m

v = is characteristic velocity across the hydrocyclone = m/s

```
//-----------------------------------------------------------------------
```

```
// Characteristic velocity (38)
// qIn - volume inflow rate
// D - diameter inside hydrocyclone

static double vChar(double qIn, double D)
{
      return 4 * qIn / (Math.PI * D * D);
}
```

```
//-----------------------------------------------------------------------
```

Stokes' number for cut-size d_{50} (StK_{50})

$$StK_{50} = \frac{d_{50}^2 (\rho_l - \rho_g) v}{18 \mu D_c} \qquad \text{Equation 216}$$

d_{50} = μm × 10^{-6} = m

μ = 0.001 Kg/m/s viscosity of water

ρ_l = 1000 kg/m^3 Density of water.

ρ_g =1.22 Kg/m^3 Density of air

v = m/s Characteristic velocity.

```
//-----------------------------------------------------------------------
```

```
// Stokes' number for cut-size d50 (StK50) (39)
// Dc - diameter inside hydrocyclone, m
// d50 - cut-size, m
// mu - viscosity of liquid, kg/s/m
// rhoL - density of liquid, kg/m^3
// rhoG - density of gas, kg/m^3
// v - characteristic velocity of hydrocyclone

static double stokes(double Dc, double d50, double mu,
                     double rhoL, double rhoG, double v)
{
      return d50 * d50 * (rhoL - rhoG) * v / (18 * mu * Dc);
}
```

```
//-----------------------------------------------------------------------
```

Reynolds Number Re

Reynolds number defines the flow

$$\mathrm{Re} = \frac{VD\rho}{\mu} \qquad \text{Equation 217}$$

V= Characteristic Velocity m/s.

D = Cyclone diameter = 0.0254 m

ρ = 1000 Kg/m^3

μ = water viscosity =0.001 kg/m/s

```
//---------------------------------------------------------------------------

      // Reynolds number(40)
      // D - cyclone diameter, m
      // rho - density, kg/m^3
      // mu - liquid viscosity, kg/s/m
      // v - characteristic velocity, m/s

      static double reynolds(double D, double rho, double mu, double v)
      {
            return v * D * rho / mu;
      }
}
//---------------------------------------------------------------------------
```

Test 2

```
import java.io.*;
import java.util.StringTokenizer;
import java.text.*;

class Test2
{
      public static void main(String args[])
      {
            // Constants
            double a = 0.022;                  // a:     HC inlet height,
meters
            double b = 0.005;                  // b:     HC inlet width,
meters
            double D = 0.0254;                 // D:     meters
            double Rin = 0.0102;               // Rin:   meters
            double Rx = 0.006;                 // Rx:    vortex finder
radius, meters
            double H = 0.28;                   // H:     cyclone length,
meters
            double S = 0.125;                  // S:     vortex finder
length, meters
            double Ar = 0.03585855269;         // Ar:    total area inside
cyclone

            double C0 = 0.0;                   // C0:    mass fraction of
solid, g/m^3
            double rho = 1.299;                // rho:   gas phase
density, kg/m^3
            double mu = 1.73 / 100000;         // mu:    viscosity, Ns/m^2
            double rhoA = 1.22;                // rhoA:  density of air
kg/m^3
            double rhoL = 1000;                // rhoL:  liquid density,
kg/m^3
            double muL = 0.001;                // muL:   viscosity of
liquid, Ns/m^2
            double xFact = 1.0;                // xFact: empirical
correction factor

            // Object to store the hydrocyclone properties
            // and do the calculations
            Hydrocyclone1 hc = new Hydrocyclone1(a, b, Rin, D, H, Rx,
S, Ar);

            try
            {
                  BufferedReader in = new BufferedReader(new
FileReader("Material Balance.txt"));
                  BufferedReader in2 = new BufferedReader(new
FileReader("deltap.txt"));
                  BufferedReader in3 = new BufferedReader(new
FileReader("Grade Efficiency1.txt"));

                  File outfile = new File("main.txt");
```

```
                PrintWriter out = new PrintWriter(new
BufferedWriter(new FileWriter(outfile)));

                // Temporary storage for the current line and
                // values that need to be parsed
                String s, qs;
                String expno;
                StringTokenizer tok, tok3;

                // Values to be retrieved in the loop
                double qInG, qInL, qo, d50, m = 1;
                double inlet = 1, underflow = 0, deltapc;

                String str2, str3, buffer;
                boolean keepstr2;
                boolean keepstr3;
                boolean over;

                Data1 data;
                NumberFormat fmt = NumberFormat.getNumberInstance();
                fmt.setMaximumFractionDigits(2);

                int i;

                // The first few lines of the spreadsheets are just
headers
                out.println(in.readLine());
                out.println(in.readLine());
                out.print(in.readLine().trim());
                out.println("\tInlet Pressure\tUnderflow
Pressure\tOverflow Pressure"
                                        + "\tConstriction Coefficient"
                                        + "\tInlet Velocity\tWall Velocity"
                                        + "\tWall Axial
Velocity\tVx\tFroude Number\tCyclone Body Reynolds Number"
                                        + "\tc0\tTotal Friction
Factor\tInner Core Velocity"
                                        + "\tCharacteristic velocity"
                                        + "\td50 (Measured)\td50
(Musch.)\td50 (Modified Musch.)\tRadial Velocity\td50 (Barth)\td50
(Modified Barth)"
                                        + "\tdPbody (Musch.)\tdPbody
(Barth)\tdPx (Musch.)\tdPx (Modified Musch.)\tdPx (Barth, k=3.3)\tdPx
(Modified Barth)"
                                        + "\t\tdPtotal (Musch.)\tdPtotal
(Modified Musch.)\tdPtotal (Barth, k=3.3)\tdPtotal (Modified Barth)"
                                        + "\tMeasured dPc\tMeasured dP
Ratio"
                                        + "\t\tEu body (Measured)\tEu body
(Musch.)\tEu body (Barth)"
                                        + "\t\tEu inlet (Measured)\tEu
inlet (Musch.)\tEu inlet (Barth)"
                                        + "\t\tEu x (Measured)\tEu x
(Musch.)\tEu x (Modified Musch.)\tEu x (Barth, k=3.3)\tEu x (Modified
Barth)"
                                        + "\t\tEuIn (Shepherd and
Lapple)\tEuIn (Casal and Martinez-Benet)"
```

```
                                        + "\t\tSwirl number (Vx)\tSwirl
number (vChar)"
                                        + "\t\tStokes' number (Measured
d50)\tStokes' number (Musch. d50)\tStokes' number (Modified Musch.)"
                                        + "\tStokes' number
(Barth)\tStokes' number (Modified Barth)"
                                        + "\t\tReynolds number");

                    out.print(in.readLine().trim());

      out.println("\tkPa\tkPa\tkPa\t\tm/s\tm/s\tm/s\tm/s\t\t\t\t\tm/s\t
m/s\tm\tm\tm/s\tm\tm"
                                        +
"\tkPa\tkPa\tkPa\tkPa\tkPa\tkPa\t\tkPa\tkPa\tkPa\tkPa\tkPa");

                    for(i = 0; i < 4; i++)
                          in2.readLine();

                    in3.readLine();
                    in3.readLine();

                    str2 = in2.readLine();
                    str3 = in3.readLine();

                    while((s = in.readLine()) != null &&
s.startsWith("Exp"))
                    {
                          tok = new StringTokenizer(s, "\t");

                          // Remember the Exp. No to match with other
file
                          expno = tok.nextToken().trim();
                          buffer = expno;

                          keepstr2 = str2 == null ||
!str2.startsWith(expno);
                          keepstr3 = !str3.startsWith(expno);

                          buffer = buffer + "\t" + tok.nextToken();
                          qs = tok.nextToken();
                          if(qs.equals("AO"))
                          {
                                str3 = in3.readLine();
                                continue;
                          }
                          else
                                over = qs.equals("OF");

                          out.print(buffer + "\t" + qs + "\t");

                          // qInL (total inlet liquid flow) comes from
column H
                          for(i = 3; i < 7; i++)
                                out.print(tok.nextToken() + "\t");

                          qs = tok.nextToken();
                          qInL = Double.parseDouble(qs) / 1000000;
```

```
                        out.print(qs);

                        // qInG (total inlet gas flow) comes from
column I
                        qs = tok.nextToken();
                        qInG = Double.parseDouble(qs) / 1000000;
                        out.print("\t" + qs);

                        // QO (total overflow rate) comes from column L
                        for(i = 0; i < 2; i++)
                              out.print("\t" + tok.nextToken());

                        qs = tok.nextToken();
                        qo = Double.parseDouble(qs) / 1000000;
                        out.print("\t" + qs);

                        i = 4;
                        while(tok.hasMoreTokens() && i > 0)
                        {
                              out.print("\t" + tok.nextToken());
                              i--;
                        }
                        for(; i > 0; i--)
                              out.print("\t");

                        // read measured pressures from the other file
                        if(!keepstr2)
                        {
                              tok = new StringTokenizer(str2, "\t");
                              for(i = 0; i < 9; i++)
                                    tok.nextToken();

                              qs = tok.nextToken();
                              inlet = (Double.parseDouble(qs) -
6.5)*6894.757293168 / 1000;

                              // exp 34, 34-R and 35 mess up, and get
the psi instead of kPa
                              /*    if(inlet > 300)
                              {
                                    qs = tok.nextToken();
                                    inlet = (Double.parseDouble(qs) -
6.5)*6894.757293168 / 1000;
                                    }*/
                              out.print("\t" + fmt.format(inlet));
                              tok.nextToken();
                              tok.nextToken();
                              out.print("\t" +
fmt.format(Double.parseDouble(tok.nextToken())));

                              tok.nextToken();
                              qs = tok.nextToken();
                              underflow = Double.parseDouble(qs);
                              out.print("\t" + fmt.format(underflow));
                        }
                        else
                        {
```

```
                        out.print("\t\t\t");
                  }

                  if(!keepstr3)
                  {
                        tok3 = new StringTokenizer(str3, "\t");
                        for(i = 0; i < 6; i++)
                              tok3.nextToken();
                        qs = tok3.nextToken();

                        d50 = Double.parseDouble(qs);
                        if(d50 > 1.0)
                              d50 = d50 / 1000000;

                        str3 = in3.readLine();
                  }
                  else
                  {
                        d50 = -1;
                  }

                  // Save and process the data
                  data = new Data1(C0, qInG, qInL, rho, mu, rhoA,
rhoL, muL, xFact, d50);
                  hc.process_Data(data);

                  // Output calculated values after last column
of data
                  out.print("\t" + data.getAlpha());
                  out.print("\t" + data.getVin());
                  out.print("\t" + data.getVthetaW());
                  out.print("\t" + data.getVzw());
                  out.print("\t" + data.getVx());
                  out.print("\t" + data.getFrx());
                  out.print("\t" + data.getRer());
                  out.print("\t" + data.getc0());
                  out.print("\t" + data.getF());
                  out.print("\t" + data.getVthetaCS());
                  out.print("\t" + data.getVchar());
                  out.print("\t" + data.getD50_meas());
                  out.print("\t" + data.getD50_m());

                  if(over)
                        out.print("\t" + data.getD50_mModO());
                  else
                        out.print("\t" + data.getD50_mModU());

                  out.print("\t" + data.getVrcs());
                  out.print("\t" + data.getD50_b());

                  if(over)
                        out.print("\t" + data.getD50_bModO());
                  else
                        out.print("\t" + data.getD50_bModU());

                  out.print("\t" + data.getDeltaPBody_m());
                  out.print("\t" + data.getDeltaPBody_b());
```

```
                        out.print("\t" + data.getDeltaPx_m());
                        out.print("\t" + data.getDeltaPx_mMod());
                        out.print("\t" + data.getDeltaPx_b());
                        out.print("\t" + data.getDeltaPx_bMod());
                        out.print("\t\t" +
Data1.fmt.format(data.deltaPBody_m

      + data.deltaPx_m));
                        out.print("\t" +
Data1.fmt.format(data.deltaPBody_m

+ data.deltaPx_mMod));
                        out.print("\t" +
Data1.fmt.format(data.deltaPBody_b

+ data.deltaPx_b));
                        out.print("\t" +
Data1.fmt.format(data.deltaPBody_b

+ data.deltaPx_bMod));

                        if(!keepstr2)
                        {
                              qs = tok.nextToken();
                              qs = tok.nextToken();
                              deltapc = (Double.parseDouble(qs) -
6.5)*6894.757293168 / 1000;
                              out.print("\t" + fmt.format(deltapc));
                              data.deltaPx_meas = deltapc;
                              hc.process_Data2(data);
                              //out.print("\t" +
fmt.format(Math.abs(deltapc - data.deltaPx_m)));

                              out.print("\t" + fmt.format(deltapc /
(inlet - underflow)));
                              //out.print("\t" +
fmt.format(Double.parseDouble(tok.nextToken())));
                              //out.print("\t" +
fmt.format(data.deltaPx_m / (inlet - underflow)));

                              //out.print("\t\t");

                              str2 = in2.readLine();
                        }
                        else
                        {
                              out.print("\t\t");
                        }

                        out.print("\t\t"/* + data.getEuBody_meas()*/);
                        out.print("\t" + data.getEuBody_Musch());
                        out.print("\t" + data.getEuBody_Barth());
                        out.print("\t\t"/* + data.getEuInlet_meas()*/);
                        out.print("\t" + data.getEuInlet_Musch());
                        out.print("\t" + data.getEuInlet_Barth());
                        out.print("\t\t" + data.getEuX_meas());
                        out.print("\t" + data.getEuX_Musch());
```

```
                        out.print("\t" + data.getEuX_MuschMod());
                        out.print("\t" + data.getEuX_Barth());
                        out.print("\t" + data.getEuX_BarthMod());
                        out.print("\t\t" + data.getEuIn_sl());
                        out.print("\t" + data.getEuIn_cmb());

                        out.print("\t\t" + data.getSwirl_x());
                        out.print("\t" + data.getSwirl_char());

                        out.print("\t\t" + data.getStokes_meas());
                        out.print("\t" + data.getStokes_m());

                        if(over)
                              out.print("\t" + data.getStokes_mModO());
                        else
                              out.print("\t" + data.getStokes_mModU());

                        out.print("\t" + data.getStokes_b());

                        if(over)
                              out.print("\t" + data.getStokes_bModO());
                        else
                              out.print("\t" + data.getStokes_bModU());

                        out.print("\t\t" + data.getReynolds());
                        out.println();
                  }

                  out.println();

                  in.close();
                  in2.close();
                  in3.close();
                  out.close();

                  double d90, d10, d32;

                  in = new BufferedReader(new FileReader("uf.txt"));
                  out = new PrintWriter(new BufferedWriter(new
FileWriter("uf2.txt")));

                  out.println(in.readLine());

                  s = in.readLine();
                  tok = new StringTokenizer(s, "\t");
                  for(i = 0; i < 14; i++)
                  {
                        out.print(tok.nextToken() + "\t");
                  }

                  out.print("E Model 1 (d90)\tE Model 2 (d90)\tE Model
1 (d10)\tE Model 2 (d10)\tE Model 1 (d32)\tE Model 2 (d32)\t");
                  tok.nextToken();
                  tok.nextToken();
                  out.println(tok.nextToken() + "\t" +
tok.nextToken());
```

```
                    while((s = in.readLine()) != null &&
s.startsWith("E"))
                    {
                          tok = new StringTokenizer(s, "\t");
                          for(i = 0; i < 4; i++)
                                out.print(tok.nextToken() + "\t");

                          qs = tok.nextToken();
                          m = Double.parseDouble(qs);
                          out.print(qs + "\t");

                          out.print(tok.nextToken() + "\t");

                          qs = tok.nextToken();
                          d50 = Double.parseDouble(qs);
                          out.print(qs + "\t");

                          qs = tok.nextToken();
                          d90 = Double.parseDouble(qs);
                          out.print(qs + "\t");

                          qs = tok.nextToken();
                          d10 = Double.parseDouble(qs);
                          out.print(qs + "\t");

                          qs = tok.nextToken();
                          d32 = Double.parseDouble(qs);
                          out.print(qs + "\t");

                          for(i = 0; i < 4; i++)
                                out.print(tok.nextToken() + "\t");

                          out.print(Model1.eta(d50, d90, m) + "\t");
                          out.print(Model1.eta(d50, d90) + "\t");
                          out.print(Model1.eta(d50, d10, m) + "\t");
                          out.print(Model1.eta(d50, d10) + "\t");
                          out.print(Model1.eta(d50, d32, m) + "\t");
                          out.print(Model1.eta(d50, d32) + "\t");

                          out.println(tok.nextToken() + "\t" +
tok.nextToken());
                    }

                    in.close();
                    out.close();

                    in = new BufferedReader(new FileReader("of.txt"));
                    out = new PrintWriter(new BufferedWriter(new
FileWriter("of2.txt")));

                    out.println(in.readLine());

                    s = in.readLine();
                    tok = new StringTokenizer(s, "\t");
                    for(i = 0; i < 14; i++)
                    {
                          out.print(tok.nextToken() + "\t");
```

```
                }

                out.print("E Model 1 (d90)\tE Model 2 (d90)\tE Model
1 (d10)\tE Model 2 (d10)\tE Model 1 (d32)\tE Model 2 (d32)\t");
                tok.nextToken();
                tok.nextToken();
                out.println(tok.nextToken() + "\t" +
tok.nextToken());

                while((s = in.readLine()) != null &&
s.startsWith("E"))
                {
                      tok = new StringTokenizer(s, "\t");
                      for(i = 0; i < 4; i++)
                            out.print(tok.nextToken() + "\t");

                      qs = tok.nextToken();
                      m = Double.parseDouble(qs);
                      out.print(qs + "\t");

                      out.print(tok.nextToken() + "\t");

                      qs = tok.nextToken();
                      d50 = Double.parseDouble(qs);
                      out.print(qs + "\t");

                      qs = tok.nextToken();
                      d90 = Double.parseDouble(qs);
                      out.print(qs + "\t");

                      qs = tok.nextToken();
                      d10 = Double.parseDouble(qs);
                      out.print(qs + "\t");

                      qs = tok.nextToken();
                      d32 = Double.parseDouble(qs);
                      out.print(qs + "\t");

                      for(i = 0; i < 4; i++)
                            out.print(tok.nextToken() + "\t");

                      out.print(Model1.eta(d50, d90, m) + "\t");
                      out.print(Model1.eta(d50, d90) + "\t");
                      out.print(Model1.eta(d50, d10, m) + "\t");
                      out.print(Model1.eta(d50, d10) + "\t");
                      out.print(Model1.eta(d50, d32, m) + "\t");
                      out.print(Model1.eta(d50, d32) + "\t");

                      out.println(tok.nextToken() + "\t" +
tok.nextToken());
                }
                in.close();
                out.close();

                pressure_drops();
          }
          catch(Exception e)
```

```
		{
			e.printStackTrace();
		}
	}

	static void pressure_drops() throws IOException
	{
		BufferedReader in = new BufferedReader(new
FileReader("Pressure Drops AO v1.txt"));
		PrintWriter out = new PrintWriter(new FileWriter("pressure
drops AO.txt"));

		NumberFormat fmt = Data1.fmt;

		out.println(in.readLine());
		out.println(in.readLine());

		double p1, p2, v1, v2;
		double rhoL = 1000;

		String str, t;
		StringTokenizer tok;

		int line = 1;
		while((str = in.readLine()) != null)
		{
			tok = new StringTokenizer(str, "\t");

			for(int i = 0; i < 11; i++)
			{
				t = tok.nextToken();
				if(i == 5 && Double.parseDouble(t) < 0.2)
				{
					i = i + 2;
					out.print("\t\t");
				}

				out.print(t + "\t");
			}

			t = tok.nextToken();
			p1 = Double.parseDouble(t);
			out.print(t + "\t");

			for(int i = 0; i < 6; i++)
			{
				out.print(tok.nextToken() + "\t");
			}

			t = tok.nextToken();
			v1 = Double.parseDouble(t);
			out.print(t + "\t");

			t = tok.nextToken();
			v2 = Double.parseDouble(t);
			out.print(t + "\t");
```

```
                p2 = Model1.p2(p1 * 1000, v1, v2, rhoL) / 1000;
                out.print(fmt.format(p2) + "\t");
                out.print(fmt.format(p1 - p2));

                while(tok.hasMoreTokens())
                {
                        out.print("\t" + tok.nextToken());
                }

                out.println();
            }
            in.close();
            out.close();
        }
}
```

Data 1

```
import java.text.NumberFormat;

class Data1
{
      // Static formatter for use by the string output functions
      static NumberFormat fmt = NumberFormat.getNumberInstance();
      static int maxDigits = 7;

      // Static initialization code
      // This gets run once, when the class is loaded
      {
            fmt.setMaximumFractionDigits(maxDigits);
      }

      // Given values
      final double C0;      // mass fraction of solid, g/m^3
      final double qInG;    // inlet gas flow, m^3/s
      final double qInL;    // inlet liquid flow, m^3/s
      final double qo;      // total overflow rate, m^3/s
      final double rho;     // gas phase density, kg/m^3
      final double mu;      // absolute viscosity, Ns/m^2
      final double rhoG;    // gas phase density, kg/m^3
      final double rhoL;    // liquid density, kg/m^3
      final double muL;     // liquid viscosity, Ns/m^2
      final double xFact;   // empirical correction factor
      double deltaPBody_meas;
      double deltaPx_meas;
      double d50_meas;
      //    final double m;       // slope of grade efficiency curve
      //  final double d10, d32, d90; // Sizes to calculate efficiency
at

      // Calculated values
      double alpha;         // constriction coefficient
      double qIn;           // total inlet flow rate, m^3/s
      double vin;           // mean gas velocity inlet, m/s
      double vThetaW;       // wall velocity, m/s
      double vzw;           // wall axial velocity, m/s
      double vx;            // superficial axial velocity through inlet
section of vortex tube, m/s
      double Frx;           // Froude number
      double Rer;           // Reynolds number
      double c0;            // ratio of mass of gas to mass of liquid in
inlet flow
      double f;             // total friction factor
      double vThetaCS;      // inner core velocity
      double d50_m;         // d50 according to Muschelknautz Cutpoint
Models
      double d50_mModU;     // d50 according to modified Muschelknautz
Cutpoint Model (underflow)
      double d50_mModO;     // d50 according to modified Muschelknautz
Cutpoint Model (overflow)
      double vrcs;          // radial velocity, m/s
      double d50_b;         // d50 according to Barth's Equilibrium
Orbit Model
```

```
      double d50_bModU;    // d50 according to modified Barth's
Equilibrium Orbit Model (underflow)
      double d50_bModO;    // d50 according to modified Barth's
Equilibrium Orbit Model (overflow)
      double deltaPBody_b; // pressure loss in hydrocyclone (Barth
model)
      double deltaPx_b;    // pressure loss in vortex finder (Barth
semi-empirical)
      double deltaPx_bMod; // pressure loss in vortex finder (modified
Barth semi-empirical)
      double deltaPBody_m; // pressure loss in hydrocyclone
(Muschelknautz)
      double deltaPx_m;    // pressure loss in vortex finder
(Muschelknautz)
      double deltaPx_mMod; // pressure loss in vortex finder (modified
Muschelknautz)
      double euBody_meas;
      double euBody_m;
      double euBody_b;
      double euInlet_meas;
      double euInlet_m;
      double euInlet_b;
      double euX_meas;
      double euX_m;
      double euX_mMod;
      double euX_b;
      double euX_bMod;
      double euIn_sl;
    double euIn_cmb;
      double swirlno_x;
      double swirlno_char;
      double vChar;
      double stokes_meas;
      double stokes_m;
      double stokes_b;
      double stokes_mModU;
      double stokes_mModO;
      double stokes_bModU;
      double stokes_bModO;
      double reynolds;

      Data1(double C0, double qInG, double qInL, double rho, double mu,
            double rhoG, double rhoL, double muL, double xFact,
double d50_meas)
      {
            this.C0 = C0;
            this.qInG = qInG;
            this.qInL = qInL;
            this.rho = rho;
            this.mu = mu;
            this.rhoG = rhoG;
            this.rhoL = rhoL;
            this.muL = muL;
            this.xFact = xFact;
            this.d50_meas = d50_meas;

            qIn = qInG + qInL;
```

```
        qo = qInG * 0.9 + qInL * 0.1;
}

// Functions for getting values for printing
// All the digits of precision supported by double
// usually don't need to be output
String getC0()
{
        return fmt.format(C0);
}

String getQInG()
{
        return fmt.format(qInG);
}

String getQinL()
{
        return fmt.format(qInL);
}

String getQo()
{
        return fmt.format(qo);
}

String getRhoG()
{
        return fmt.format(rhoG);
}

String getRhoL()
{
        return fmt.format(rhoL);
}

String getMu()
{
        return fmt.format(mu);
}

String getXfact()
{
        return fmt.format(xFact);
}

String getAlpha()
{
        return fmt.format(alpha);
}

String getQin()
{
        return fmt.format(qIn);
}

String getVin()
```

```
{
	return fmt.format(vin);
}

String getVthetaW()
{
	return fmt.format(vThetaW);
}

String getVzw()
{
	return fmt.format(vzw);
}

String getVx()
{
	return fmt.format(vx);
}

String getFrx()
{
	return fmt.format(Frx);
}

String getRer()
{
	return fmt.format(Rer);
}

String getc0()
{
	return fmt.format(c0);
}

String getF()
{
	return fmt.format(f);
}

String getVthetaCS()
{
	return fmt.format(vThetaCS);
}

String getD50_meas()
{
	if(d50_meas > 0)
		return fmt.format(d50_meas);
	else
		return "";
}

String getD50_m()
{
	return fmt.format(d50_m);
}
```

```
String getD50_mModU()
{
      return fmt.format(d50_mModU);
}

String getD50_mModO()
{
      return fmt.format(d50_mModO);
}

String getVrcs()
{
      return fmt.format(vrcs);
}

String getD50_b()
{
      return fmt.format(d50_b);
}

String getD50_bModU()
{
      return fmt.format(d50_bModU);
}

String getD50_bModO()
{
      return fmt.format(d50_bModO);
}

String getDeltaPBody_b()
{
      return fmt.format(deltaPBody_b);
}

String getDeltaPx_b()
{
      return fmt.format(deltaPx_b);
}

String getDeltaPx_bMod()
{
      return fmt.format(deltaPx_bMod);
}

String getDeltaPBody_m()
{
      return fmt.format(deltaPBody_m);
}

String getDeltaPx_m()
{
      return fmt.format(deltaPx_m);
}

String getDeltaPx_mMod()
{
```

```
        return fmt.format(deltaPx_mMod);
}

String getEuBody_meas()
{
        return fmt.format(euBody_meas);
}

String getEuBody_Musch()
{
        return fmt.format(euBody_m);
}

String getEuBody_Barth()
{
        return fmt.format(euBody_b);
}

String getEuInlet_meas()
{
        return fmt.format(euInlet_meas);
}

String getEuInlet_Musch()
{
        return fmt.format(euInlet_m);
}

String getEuInlet_Barth()
{
        return fmt.format(euInlet_b);
}

String getEuX_meas()
{
        return fmt.format(euX_meas);
}

String getEuX_Musch()
{
        return fmt.format(euX_m);
}

String getEuX_MuschMod()
{
        return fmt.format(euX_mMod);
}

String getEuX_Barth()
{
        return fmt.format(euX_b);
}

String getEuX_BarthMod()
{
        return fmt.format(euX_bMod);
}
```

```
String getSwirl_x()
{
	return fmt.format(swirlno_x);
}

String getVchar()
{
	return fmt.format(vChar);
}

String getSwirl_char()
{
	return fmt.format(swirlno_char);
}

String getStokes_meas()
{
	if(d50_meas > 0)
		return fmt.format(stokes_meas);
	else
		return "";
}

String getStokes_m()
{
	return fmt.format(stokes_m);
}

String getStokes_b()
{
	return fmt.format(stokes_b);
}

String getStokes_mModU()
{
	return fmt.format(stokes_mModU);
}

String getStokes_mModO()
{
	return fmt.format(stokes_mModO);
}

String getStokes_bModU()
{
	return fmt.format(stokes_bModU);
}

String getStokes_bModO()
{
	return fmt.format(stokes_bModO);
}

String getReynolds()
{
	return fmt.format(reynolds);
```

```
        }

        String getEuIn_sl()
        {
              return fmt.format(euIn_sl);
        }

        String getEuIn_cmb()
        {
              return fmt.format(euIn_cmb);
        }
}
```

```
// (n) refer to equation numbers in "Model Programming.doc" (14/5/3)

class Model1
{
	// probably won't be modelling with
	// different values for gravity
	static final double g = 9.81;

	// Xi (2)
	static double xi(double b, double d)
	{
		return b / (0.5 * d);
	}

	// constriction coefficient (1)
	// b - width of cyclone inlet
	// d - cyclone diameter
	// c0 - ratio of mass of incoming solid to mass of incoming gas
in feed
	// Modified for fewer operations
	static double alpha(double b, double d, double c0)
	{
		double xi = b / (0.5 * d);	// (2)
		double xisq = xi * xi;
		return (1 -
				Math.sqrt((1 + (xisq - 2 * xi))
					* (1 - (1 - xisq) * xi * (2 -
xi) / (1 + c0)))) / xi;
	}

	static double alpha(double xi, double c0)
	{
		double xisq = xi * xi;
		return (1 -
				Math.sqrt((1 + (xisq - 2 * xi))
					* (1 - (1 - xisq) * xi * (2 -
xi) / (1 + c0)))) / xi;
	}

	// mean gas velocity inlet (4)
	// a - height of cyclone inlet
	// b - width of cyclone inlet
	// q - volumetric flow rate
	static double vin(double a, double b, double q)
	{
		return q / (a * b);
	}

	// wall velocity (3)
	// r - radius of ___
	// rin - radius of inlet
	// alpha - constriction coefficient
	// vin - mean gas velocity inlet
```

```
	static double vThetaW(double r, double rin, double alpha, double
vin)
	{
		return vin * rin / (alpha * r);
	}

	// geometric mean radius (5)
	// r - cyclone radius
	// rx - vortex radius
	static double rm(double r, double rx)
	{
		return Math.sqrt(rx * r);
	}

	// wall axial velocity (6)
	// r - cyclone radius
	// rm - geometric mean radius
	// q - volumetric flow rate
	static double vzw(double r, double rm, double q)
	{
		return 0.9 * q / (Math.PI * (r * r - rm * rm));
	}

	// geometrical mean rotational velocity (8)
	// vThetaW - wall velocity
	// vThetaCS - inner cortex velocity
	static double vThetaM(double vThetaW, double vThetaCS)
	{
		return Math.sqrt(vThetaW * vThetaCS);
	}

	// cyclone body Reynolds number (7)
	// rin - inlet radius
	// rm - geometric mean radius
	// h - cyclone length
	// rho - gas phase density
	// mu - absolute viscosity
	// vzw - wall axial velocity
	// vThetaM - geometrical mean rotational velocity
	static double rer(double rin, double rm, double h, double rho,
double mu, double vzw, double vThetaM)
	{
		return rin * rm * vzw * rho / (h * mu * (1 + (vzw * vzw /
(vThetaM * vThetaM))));
	}

	// usually, (vzw/vThetaM)^2 << 1, so it can be ignored
	static double rer(double rin, double rm, double h, double rho,
double mu, double vzw)
	{
		return rin * rm * vzw * rho / (h * mu);
	}

	// vx - superficial axial velocity through inlet section of
vortex tube
	// Ax - Vortex finder area
	static double vx(double Ax, double Q)
```

```
	{
		return Q / Ax;
	}

	// Froude number (12)
	// rx - vortex radius
	// vx - superficial axial velocity through inlet section of
vortex tube
	// g - gravity
	static double frx(double rx, double vx)
	{
		return vx / Math.sqrt(2 * rx * g);
	}

	// total friction factor (10)
	// r - cyclone radius
	// rx - vortex radius
	// fAir - friction from air
	// rho - gas phase density
	// rhoStr - density of the strand
	// c0 - constriction coefficient
	// frx - Froude number
	// eta - overall cyclone collection efficiency (0.9-0.99)
	static double f(double r, double rx, double fAir, double rho,
double rhoStr,
				double c0, double frx, double eta)
	{
		return fAir + 0.25 * Math.pow(r / rx, -0.625)
			* Math.sqrt(eta * c0 * frx * rho / rhoStr);
	}

	// c0 for calculating f using (11)
	static double c0(double qInG, double rhoG, double qInL, double
rhoL)
	{
		return qInG * rhoG / (qInL * rhoL);
	}

	// total friction factor (11)
	static double f(double c0)
	{
		return 0.005 * (1 + 3 * Math.sqrt(c0));
	}

	static double vThetaCS(double vzw, double vThetaM)
	{
		return Math.pow(vzw / vThetaM, 2);
	}

	// Muschelknautz Cutpoint Models
	// tangential velocity of gas at inner core radius Rcs (13)
	// r - radius of cyclone
	// rx - radius of vortex
	// ar - total area inside cyclone: aRoof + aBarrel + aVortexTube
	// q - volumetric flow rate
	// f - total friction factor
	// vThetaW - wall velocity
```

```
      static double vThetaCS(double r, double rx, double ar, double q,
double f, double vThetaW)
      {
            return vThetaW * (r / rx) / (1 + f * ar * vThetaW *
Math.sqrt(r / rx) / (2 * q));
      }

      // Muschelknautz Cutpoint model d50 (14)
      // h - cyclone height
      // s - length of vortex finder
      // rho - gas phase density
      // rhop - density of liquid
      // mu - absolute viscosity
      // q - volumetric flow rate
      // vThetaCS - inner cortex velocity
      // xFact - 'X' factor
      // Modified for fewer operations
      static double d50(double h, double s, double rho, double rhop,
                              double mu, double q, double vThetaCS,
double xFact)
      {
            return xFact * Math.sqrt(8.1 * mu * q
                                                / (Math.PI * (rhop -
rho) * vThetaCS * vThetaCS * (h - s)));
      }

      // Modified Muschelknautz Cutpoint model d50 (underflow stream)
      // h - cyclone height (m)
      // s - length of vortex finder (m)
      // rho - gas phase density (kg/m^3)
      // rhop - density of liquid (kg/m^3)
      // mu - absolute viscosity
      // q - volumetric flow rate
      // vThetaCS - inner cortex velocity
      static double d50_modU(double h, double s, double rho, double
rhop,
                              double mu, double q, double vThetaCS)
      {
            return 0.98 * Math.sqrt(18 * mu * 0.9 * q
                                                / (2 * Math.PI * (rhop
- rho)
                                                   * Math.pow(vThetaCS,
1.9) * (h - s)));
      }

      // Modified Muschelknautz Cutpoint model d50 (overflow stream)
      // h - cyclone height (m)
      // s - length of vortex finder (m)
      // rho - gas phase density (kg/m^3)
      // rhop - density of liquid (kg/m^3)
      // mu - absolute viscosity
      // q - volumetric flow rate
      // vThetaCS - inner cortex velocity
      static double d50_modO(double h, double s, double rho, double
rhop,
                              double mu, double q, double vThetaCS)
      {
```

```
            return Math.sqrt(18 * mu * 0.9 * q
                                    / (2 * Math.PI * (rhop - rho)
                                        * Math.pow(vThetaCS, 1.55) *
(h - s)));
      }

      // Barth Cutpoint Models
      // radial velocity (16)
      // dx - diameter of vortex finder
      // hcs - height of vortex finder
      // q - volumetric flowrate through cyclone
      static double vrcs(double dx, double hcs, double q)
      {
            return q / (Math.PI * dx * hcs);
      }

      // Barth Cutpoint model d50 (15)
      // dx - diameter of vortex finder
      // rhop - density of liquid
      // mu - absolute viscosity
      // vrcs - radial velocity
      // vThetaCS - inner cortex velocity
      static double d50(double dx, double rhop, double mu, double vrcs,
double vThetaCS)
      {
            return Math.sqrt(vrcs * 9 * mu * dx / (rhop * vThetaCS *
vThetaCS));
      }

      // Modified Barth Cutpoint model d50 (underflow stream)
      // dx - diameter of vortex finder
      // rhop - density of liquid
      // mu - absolute viscosity
      // vrcs - radial velocity
      // vThetaCS - inner cortex velocity
      static double d50_modU(double dx, double rhop, double mu, double
vrcs, double vThetaCS)
      {
            return Math.sqrt(vrcs * 9 * mu * dx / (rhop *
Math.pow(vThetaCS, 2.02)));
      }

      // Modified Barth Cutpoint model d50 (overflow stream)
      // dx - diameter of vortex finder
      // rhop - density of liquid
      // mu - absolute viscosity
      // vrcs - radial velocity
      // vThetaCS - inner cortex velocity
      static double d50_modO(double dx, double rhop, double mu, double
vrcs, double vThetaCS)
      {
            return Math.sqrt(Math.pow(vrcs, 0.88) * 9 * mu * dx / (rhop
* Math.pow(vThetaCS, 1.8)));
      }

      // empirical expression for n (18)
      // d - body diameter in meters
```

```
	// t - temperature in degrees Kelvin
	// t0 - initial temperate in K
	static double n(double d, double t, double t0)
	{
		return 1 - (1 - 0.6 * Math.pow(d, 0.14)) * Math.pow(t / t0,
0.3);
	}

	// swirl velocity in cyclone body (17)
	// r - cyclone radius
	// n -
	// c - constant
	static double vTheta(double r, double n, double c)
	{
		return c / Math.pow(r, n);
	}

	// Muschelknautz Hydrocyclone Efficiency Model (19)
	// d50 - cut-size
	// d - particle size to calculate efficiency for
	// m - slope
	static double eta(double d50, double d, double m)
	{
		return 1 / (1 + Math.pow(d50 / d, m));
	}

	// Dirgo and Leith (1985) Hydrocyclone Efficiency Model (20)
	// d50 - cut-size
	// d - particle size to calculate efficiency for
	static double eta(double d50, double d)
	{
		return 1 / (1 + Math.pow(d50 / d, 6.4));
	}

	// Pressure loss in body of hydrocyclone (Barth) (22)
	// d - body diameter
	// dx - vortex finder diameter
	// h - cyclone height
	// s - length of vortex finder
	// rho - gas density
	// f - fAir + fWater
	// vx - velocity of gas in vortex finder
	// vThetaCS - tangential velocity in vortex finder
	static double deltaPBody(double d, double dx, double h,
                                        double s, double rho, double
f, double vx, double vThetaCS)
	{
		return 0.5 * rho * vx * vx
                * dx / d * (1 / Math.pow(vx / vThetaCS - (h - s) *
2 / dx * f, 2)
                                        - Math.pow(vThetaCS / vx, 2));
	}

	// Pressure loss in vortex finder (Barth semi-empirical approach)
(23)
	// rho - density of gas
	// vx - velocity of gas in vortex finder
```

```
	// vThetaCS - tangential velocity in vortex finder
	// k - empirical value, 3.41 - 4.4
	static double deltaPx(double rho, double vx, double vThetaCS,
double k)
	{
		double v = vThetaCS / vx;
		return 0.5 * rho * vx * vx * (Math.pow(v, 2) + k *
Math.pow(v, 4.0 / 3));
	}

	// Pressure loss in vortex finder (modified Barth semi-empirical
approach) (23)
	// rho - density of gas
	// vx - velocity of gas in vortex finder
	// vThetaCS - tangential velocity in vortex finder
	static double deltaPx_modB(double rho, double vx, double
vThetaCS)
	{
		double v = vThetaCS / vx;
		return 0.5 * rho * vx * vx * (Math.pow(v, 2.35) + 4 *
Math.pow(v, 4.0 / 3));
	}

	// Purely empirical models for pressure drop:
	// Shepherd and Lapple (1940) - valid for slot inlets
hydrocyclones (24)
	// Dx - vortex finder diameter
	// a - cyclone inlet height
	// b - cyclone inlet width
	static double euIn40(double dx, double a, double b)
	{
		return 16 * a * b / (dx * dx);
	}

	// Casal and Martinez-Benet (1983) Model
	// dx - diameter of gas exit tube
	// a - inlet area
	// b - outlet area
	static double euIn83(double dx, double a, double b)
	{
		return 3.33 + 11.3 * Math.pow(a * b / (dx * dx), 2);
	}

	// Muschelknautz Hydrocyclone Pressure Drop Models
	// pressure loss in cyclone body (25)
	// ar - total area inside cyclone: aRoof + aBarrel + aVortexTube
	// rho - gas phase density
	// f - total friction factor
	// q - volumetric flow rate
	// vThetaW - wall velocity
	// vThetaCS - inner cortex velocity
	static double deltaPBody(double ar, double rho, double f, double
q, double vThetaW, double vThetaCS)
	{
		return f * ar * rho * Math.pow(vThetaW * vThetaCS, 1.5) /
(1.8 * q);
	}
```

```
	// pressure loss in core and in vortex finder (26)
	// rho - gas phase density
	// vx - wall velocity
	// vThetaCS - inner cortex velocity
	static double deltaPx(double rho, double vx, double vThetaCS)
	{
		double v = vThetaCS / vx;
		return 0.5 * (2 + Math.pow(v, 2) + 3 * Math.pow(v, 4.0 /
3)) * rho * vx * vx;
	}

	// pressure loss in core and in vortex finder (modified from 26)
	// rho - gas phase density
	// vx - wall velocity
	// vThetaCS - inner cortex velocity
	static double deltaPx_modM(double rho, double vx, double
vThetaCS)
	{
		double v = vThetaCS / vx;
		return 0.5 * (5 + Math.pow(v, 2.42) + 3 * Math.pow(v, 4.0 /
3)) * rho * vx * vx;
	}

	// Euler number for change in pressure across body
	// deltaP - change in pressure across body
	// rho - liquid density
	// vz - axial velocity in hydrocyclone body
	static double euBody(double deltaP, double rho, double vz)
	{
		return deltaP / (0.5 * rho * vz * vz);
	}

	// Euler number for pressure drop over inlet area
	// deltaP - change in pressure across body
	// rho - liquid density
	// vin - inlet velocity
	static double euInlet(double deltaP, double rho, double vin)
	{
		return deltaP / (0.5 * rho * vin * vin);
	}

	// Euler number for pressure drop over vortex finder
	// deltaP - change in pressure over vortex finder
	// rho - liquid density
	// vx - velocity inside vortex finder
	static double euX(double deltaP, double rho, double vx)
	{
		return deltaP / (0.5 * rho * vx * vx);
	}

	static double p2(double p1, double v1, double v2, double rhoL)
	{
		return p1 + 0.5 * rhoL * (v1 * v1 - v2 * v2);
	}

	// Swirl number - represents intensity of swirl in annular flow
```

```
	// vtangential - tangential velocity
	// vaxial - axial velocity
	static double swirl(double vtangential, double vaxial)
	{
		return vtangential / vaxial;
	}

	// Characteristic velocity
	// qIn - volume inflow rate
	// D - diameter inside hydrocyclone
	static double vChar(double qIn, double D)
	{
		return 4 * qIn / (Math.PI * D * D);
	}

	// Stokes' number for cut-size d50 (StK50)
	// Dc - diameter inside hydrocyclone, m
	// d50 - cut-size, m
	// mu - viscosity of liquid, kg/s/m
	// rhoL - density of liquid, kg/m^3
	// rhoG - density of gas, kg/m^3
	// v - characteristic velocity of hydrocyclone
	static double stokes(double Dc, double d50, double mu, double
rhoL, double rhoG, double v)
	{
		return d50 * d50 * (rhoL - rhoG) * v / (18 * mu * Dc);
	}

	// Reynolds number
	// D - cyclone diameter, m
	// rho - density, kg/m^3
	// mu - liquid viscosity, kg/s/m
	// v - characteristic velocity, m/s
	static double reynolds(double D, double rho, double mu, double v)
	{
		return v* D * rho / mu;
	}
}
```

```
class Hydrocyclone1
{
	// Given Hydrocyclone properties
	final double a;		// a:	HC inlet height, meters
	final double b;		// b:	HC inlet width, meters
	final double Rin;	// Rin: meters
	final double D;		// D:	meters
	final double H;		// H:	HC length, meters
	final double Rx;	// Rx:	Vortex finder radius, meters
	final double S;		// S:	Vortex finder length, meters
	final double Ar;	// Ar:	total area inside cyclone

	// Calculated properties
	final double R;		// 1/2 D
	final double Ax;	// Ax:	Vortex finder area, m^2
	final double Ac;	// Ac:	cross sectional area of hc
	final double xi;	// b*D/2, used to calculate alpha
	final double Rm;	// Geometric mean radius, meters

	Hydrocyclone1(double a, double b, double Rin, double D, double H,
double Rx, double S, double Ar)
	{
		this.a = a;
		this.b = b;
		this.Rin = Rin;
		this.D = D;
		this.H = H;
		this.Rx = Rx;
		this.S = S;
		this.Ar = Ar;

		R = D / 2;
		Ax = Math.PI * Rx * Rx;
		Ac = Math.PI * R * R;
		xi = Model1.xi(b, D);
		Rm = Model1.rm(R, Rx);
	}

	void process_Data(Data1 data)
	{
		data.alpha = Model1.alpha(xi, data.C0);
		data.vin = Model1.vin(a, b, data.qIn);
		data.vThetaW = Model1.vThetaW(R, Rin, data.alpha,
data.vin);
		data.vzw = Model1.vzw(R, Rm, data.qIn);
		data.vx = Model1.vx(Ax, data.qo);
		data.Frx = Model1.frx(Rx, data.vx);
		data.Rer = Model1.rer(Rin, Rm, H, data.rho, data.mu,
data.vzw);
		data.c0 = Model1.c0(data.qInG, data.rhoG, data.qInL,
data.rhoL);
		data.f = Model1.f(data.c0);
```

```
            data.vThetaCS = Model1.vThetaCS(R, Rx, Ar, data.qIn,
data.f, data.vThetaW);
            data.d50_m = Model1.d50(H, S, data.rhoG, data.rhoL,
data.muL, data.qIn, data.vThetaCS, data.xFact);
            data.d50_mModU = Model1.d50_modU(H, S, data.rhoG,
data.rhoL, data.muL, data.qIn, data.vThetaCS);
            data.d50_mModO = Model1.d50_modO(H, S, data.rhoG,
data.rhoL, data.muL, data.qIn, data.vThetaCS);
            data.vrcs = Model1.vrcs(Rx * 2, S, data.qIn);
            data.d50_b = Model1.d50(Rx * 2, data.rhoL, data.muL,
data.vrcs, data.vThetaCS);
            data.d50_bModU = Model1.d50_modU(Rx * 2, data.rhoL,
data.muL, data.vrcs, data.vThetaCS);
            data.d50_bModO = Model1.d50_modO(Rx * 2, data.rhoL,
data.muL, data.vrcs, data.vThetaCS);
            data.deltaPBody_b = Model1.deltaPBody(D, Rx * 2, H, S,
data.rhoG, data.f, data.vx, data.vThetaCS);
            data.deltaPx_b = Model1.deltaPx(data.rhoG, data.vx,
data.vThetaCS, 3.3);
            data.deltaPx_bMod = Model1.deltaPx_modB(data.rhoG, data.vx,
data.vThetaCS);
            data.deltaPBody_m = Model1.deltaPBody(Ar, data.rhoG,
data.f, data.qIn, data.vThetaW, data.vThetaCS);
            data.deltaPx_m = Model1.deltaPx(data.rhoG, data.vx,
data.vThetaCS);
            data.deltaPx_mMod = Model1.deltaPx_modM(data.rhoG, data.vx,
data.vThetaCS);
            data.swirlno_x = Model1.swirl(data.vThetaCS, data.vx);
            data.vChar = Model1.vChar(data.qIn, D);
            data.swirlno_char = Model1.swirl(data.vThetaCS,
data.vChar);

            data.stokes_meas = Model1.stokes(D, data.d50_meas,
data.muL, data.rhoL, data.rhoG, data.vChar);
            data.stokes_m = Model1.stokes(D, data.d50_m, data.muL,
data.rhoL, data.rhoG, data.vChar);
            data.stokes_mModU = Model1.stokes(D, data.d50_mModU,
data.muL, data.rhoL, data.rhoG, data.vChar);
            data.stokes_mModO = Model1.stokes(D, data.d50_mModO,
data.muL, data.rhoL, data.rhoG, data.vChar);
            data.stokes_b = Model1.stokes(D, data.d50_b, data.muL,
data.rhoL, data.rhoG, data.vChar);
            data.stokes_bModU = Model1.stokes(D, data.d50_bModU,
data.muL, data.rhoL, data.rhoG, data.vChar);
            data.stokes_bModO = Model1.stokes(D, data.d50_bModO,
data.muL, data.rhoL, data.rhoG, data.vChar);
            data.reynolds = Model1.reynolds(D, data.rhoL, data.muL,
data.vChar);

            data.euIn_sl = Model1.euIn40(Rx * 2, a, b);
            data.euIn_cmb = Model1.euIn83(Rx * 2, a, b);
      }

      void process_Data2(Data1 data)
      {
            //data.euBody_meas = Model1.euBody(data.deltaPBody_meas *
1000, data.rhoG, data.qIn / Ac);
```

```
            data.euBody_m = Model1.euBody(data.deltaPBody_m, data.rhoG,
data.qIn / Ac);
            data.euBody_b = Model1.euBody(data.deltaPBody_b, data.rhoG,
data.qIn / Ac);
            //data.euInlet_meas = Model1.euInlet(data.deltaPBody_meas *
1000, data.rhoG, data.vin);
            data.euInlet_m = Model1.euInlet(data.deltaPBody_m,
data.rhoG, data.vin);
            data.euInlet_b = Model1.euInlet(data.deltaPBody_b,
data.rhoG, data.vin);
            data.euX_meas = Model1.euBody(data.deltaPx_meas, data.rhoG,
data.vChar);
            data.euX_m = Model1.euBody(data.deltaPx_m, data.rhoG,
data.vx);
            data.euX_mMod = Model1.euBody(data.deltaPx_mMod, data.rhoG,
data.vx);
            data.euX_b = Model1.euBody(data.deltaPx_b, data.rhoG,
data.vx);
            data.euX_bMod = Model1.euBody(data.deltaPx_bMod, data.rhoG,
data.vx);
      }
                                    }
```

Appendix W: De-Watering Hydrocyclone

Data on hydro-cyclonic dehydration of crude oil is limited in the literature. Less success with hydrocyclones has been achieved for the treatment of water-in-oil emulsions. De-hydration or the removal of water from oil, by hydrocyclones has been unsuccessful in industry. This separation is physically difficult to perform for a number of reasons:

- The continuous phase viscosity reduces water droplet migration velocity.
- Water droplets are more likely to break-up, especially in the inlet region of the hydrocyclone as compared with oil droplets in water.
- Phase inversion is likely.
- The combination of these factors, plus low residence time, may cause poor de-hydration hydrocyclone performance.

For more information on water from oil separations see the following citations.

Welker, J.R., et al. (1974) experimented with the separation of W/O emulsions in conventional geometry de-oiling hydrocyclones (**Figure 91**). They did not achieve reasonable separation results even for water in kerosene dispersions. They state that the separation of water or brine from the organic phase becomes less successful as the oil viscosity approaches five times that of water.

A. B. Sinker and M. T. Thew (1996b) reported that correctly matched demulsifiers could improve separation of water from oil by ~ 30% by enhancing oil droplet coalescence.

K. Nezhati and I. C. Smyth (1989) studied de-watering of water-in-oil (w/o) dispersions using an especially designed hydrocyclone. The feed to this system comes from the reject flow of a de-oiling hydrocyclone. He did not succeed in removing water from oil with this system.

A. B. Sinker and M. T. Thew (1996a) studied the effect of demulsifiers on water droplet removal from w/o dispersions using a hydrocyclone. They reported that removal performance depends on the feed, dispersed component, size distribution. They also studied the effect of operating parameters (split ratio) on performance for a given feed size distribution.

A. Belaidi et al. (2000) studied the effect of droplet size using a typical de-oiling hydrocyclone with a reference diameter of 15.2-mm **(Figure 91)**. The body material was cast polyurethane with a head machined from a PVC block. It had twin tangential inlets that produced a swirl number of 12 and a main taper angel of 1.2°

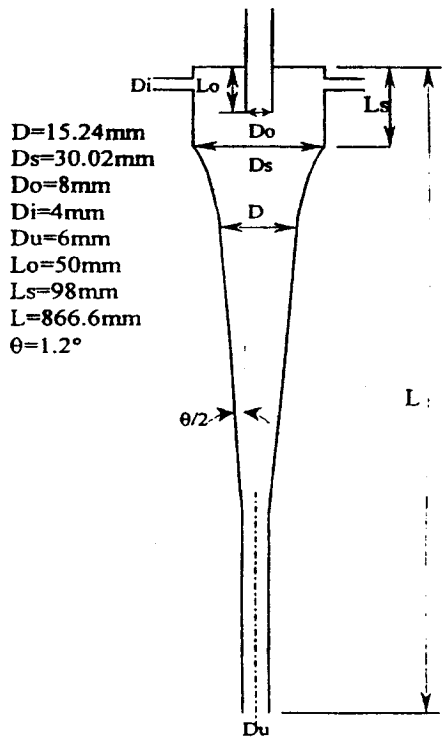

Figure 91: Internal geometry of a de-oiling types hydrocyclone, from Belaidi A., et al. (2000)

A. Belaidi et al. (2000) used water (10%) in gas-oil (density = 854.2 kg/m^3, surface tension of 28.9 mN/m at 20° C, and viscosity of 4.69 C.P. @ 20° C). The oil was

transparent enough to allow optical droplet sizing. Their findings are summarized in sections 2.4.1 through 2.4.5.

Effect of Feed Droplet Size on Overflow Size Distribution

Coalescence takes place over a range of feed droplet sizes. The effect is maximum at about 50 μm (**Figure 92**). Droplet growth in the underflow stream was determined to be much larger than in the overflow.

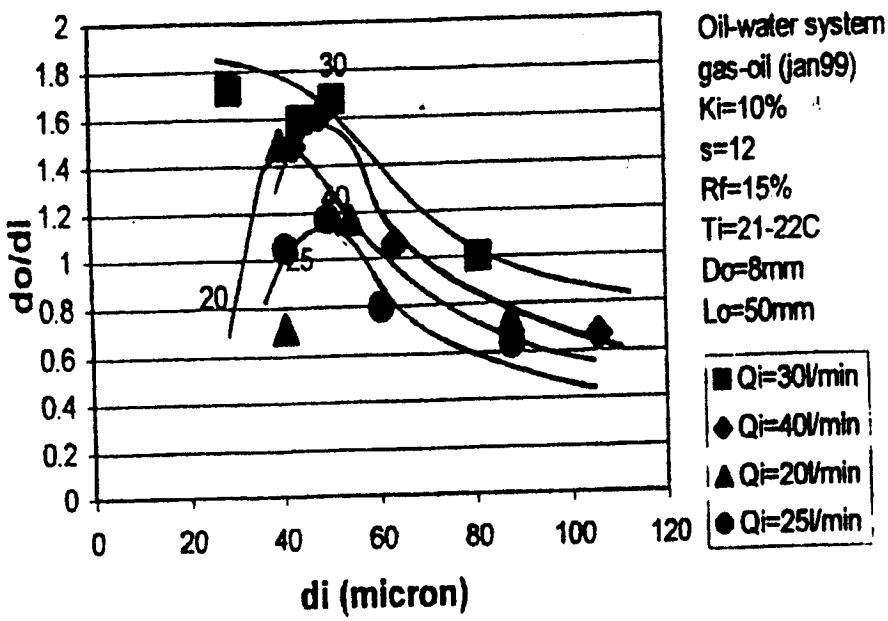

Figure 92: Effect of feed droplet size and flow rate on overflow drop size, from Belaidi A., et al. (2000).

In **Figure 92**, d_o is over-flow droplet size, d_i is inflow droplet size, K_i feed water concentration, s is swirl number and Rf is split ratio.

Effect of Feed Droplet Size on Hydrocyclone Performance.

De-watering hydrocyclone separation efficiency is based on the ability to remove water from oil (**Figure 93**). This figure shows an increase in separation efficiency with increasing feed droplet size.

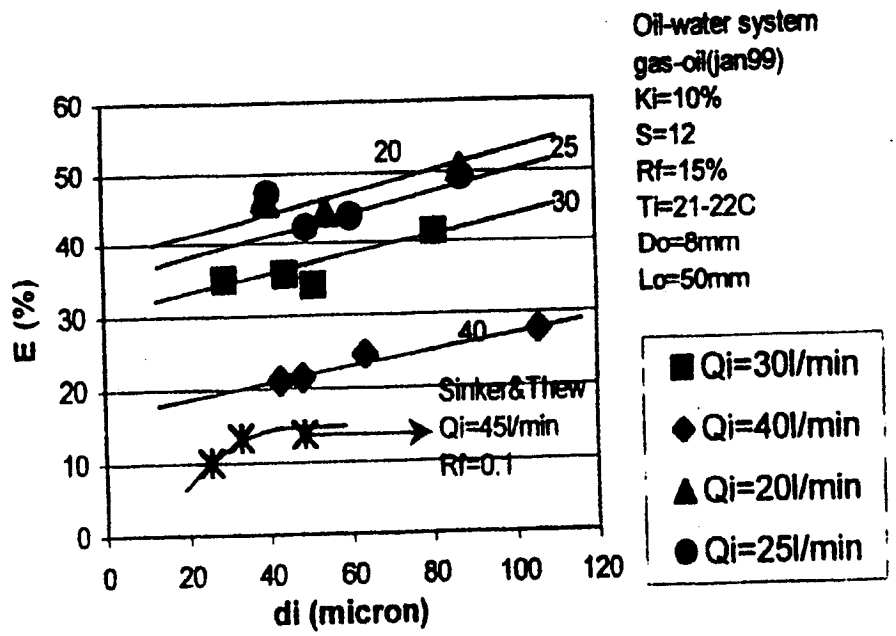

Figure 93: Effect of droplet size at feed on hydrocyclone performance, from Belaidi A., et al. (2000).

A. Belaidi et al. (2000) defined this efficiency, E as **Equation 218.**

$$E = \frac{(K_i - K_o)}{K_i} \qquad \text{Equation 218}$$

In **Equation 218**, K_i is feed water volume concentration (Volume Based %) and K_o is overflow water concentration.

These authors state that:

- A high value of efficiency; "E", can be obtained even though the overflow stream contained less than half of the oil present in the feed.
- "E" is sensitive to a relatively small amount of water in the overflow.

Separation efficiency increases with feed droplet size. Larger droplets settle near the wall faster than smaller ones. Computational fluid dynamics (CFD) predictions

indicate that the small droplets get trapped in a strong axial pressure gradient that is directed toward the cyclone vortex.

Effect of Flow Rate on Hydrocyclone Performance.

Separation efficiency decreases as feed flow increases (**Figure 94**). **Belaidi A., et al. (2000)** emphasize that higher flows are less effective in spite of a larger acceleration field. High shear stress can cause droplet breakage -- this problem may arise because of unsatisfactory hydrocyclone design or operation.

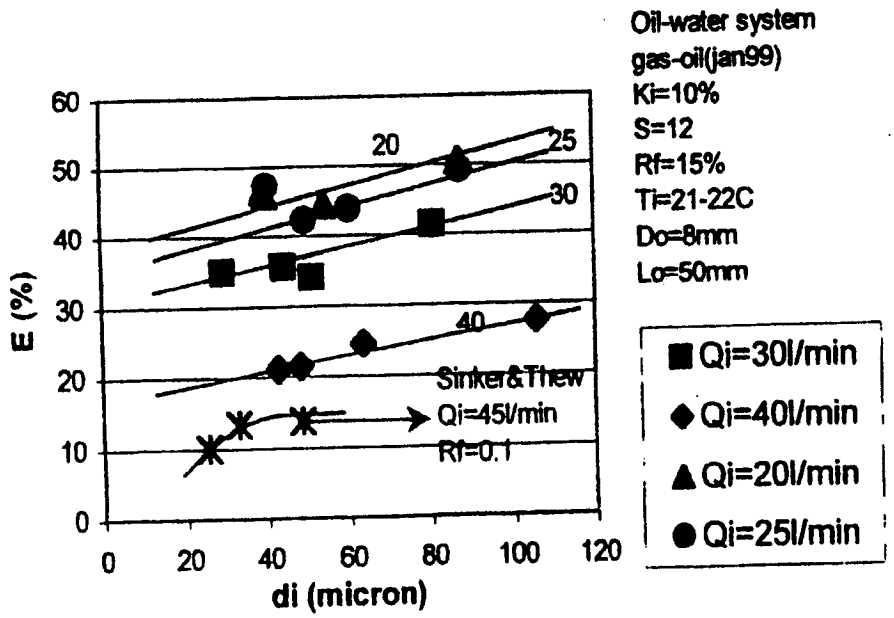

Figure 94: Effect of flow rate on hydrocyclone performance, from Belaidi A., et al. (2000).

Effect of Split Ratio

Poor hydrocyclone de-watering performance is partly related to operational conditions. Separation efficiency, "E", can be improved as the ratio R_f/K_i increases as shown in **Figure 95**. In **Figure 95**, R_f is split ratio.

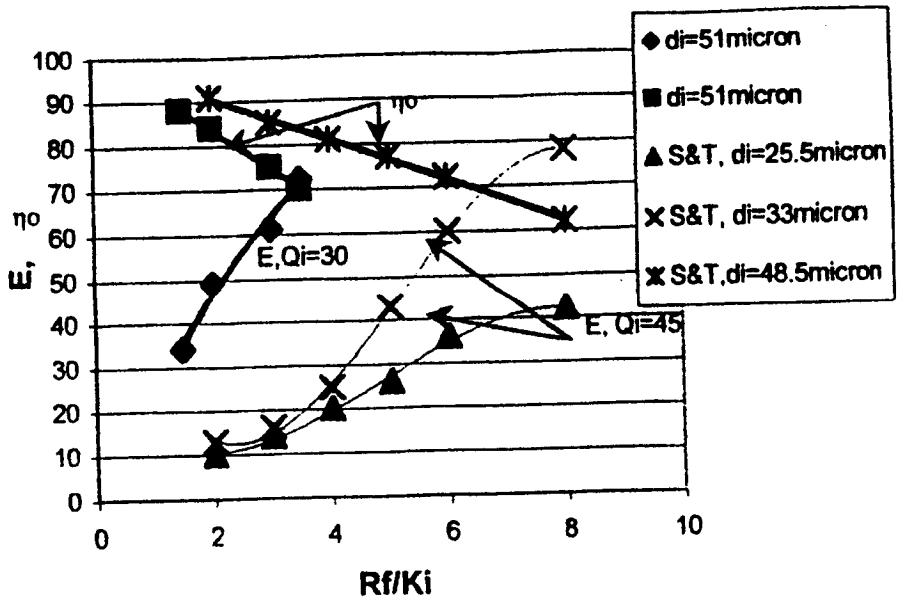

Figure 95: Variation in separation efficiency, from Belaidi A., et al. (2000).

Effect of Pressure Drop and Energy Dissipation

Sinker and Thew have reported that Reynolds number is a function of flow rate at constant temperature. Dimensionless pressure drop is given by the Euler number; "Eu", as shown in **Equation 219**.

$$Eu = \frac{2\Delta p_l}{\rho_l u^2} \qquad \text{Equation 219}$$

In Equation 219, "u" is a reference velocity; Δp is pressure drop and ρ_l is liquid density.

The split pressure drop ratio (P.D.R) is proportional to Reynolds number as shown in **Equation 220**.

$$PDR = \frac{p_i - p_o}{p_i - p_u} \propto \mathrm{Re}^{0.02} \qquad \text{Equation 220}$$

In **Equation 220**, P_i is inflow pressure, P_o is overflow pressure and P_u is underflow pressure.

These investigators also report that for a doubling of flow rate energy dissipation rate increases eight-fold.

The Electric Double Layer

Most substances acquire a surface electric charge when brought into contact with a polar aqueous medium. Possible charging mechanisms are ionization, ion adsorption and ion dissolution. This surface charge influences the distribution of nearby ions in the polar medium. Ions of opposite charge are attracted toward the surface and ions of like charge are repelled (D. Shaw 1980). This, together with the mixing tendency of thermal motion leads to the formation of an electric double layer made-up of a charged surface and an excess of neutralizing counter-ions over co-ions distributed in a diffuse manner in the polar medium (**Figure 96**).

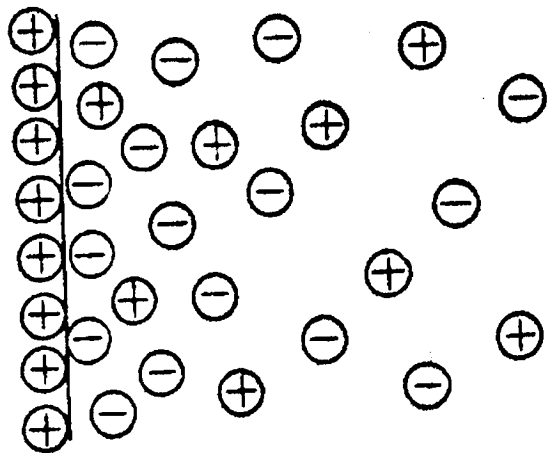

Figure 96: Schematic diagram of a diffuse electric double layer by Shaw. D. J (1980).

Origin of the Charge at Surfaces

The electric double layer effect plays an important role in determining the physical properties of the system as a whole. D. Shaw (1980) states that the electrical potential: ψ_0, at a flat surface and ψ at the distance x from the surface in the electrolyte solution taking the surface to be positively charged (**Figure 96**). In **Figure 97**, n_0 is the corresponding bulk concentration of each ionic species.

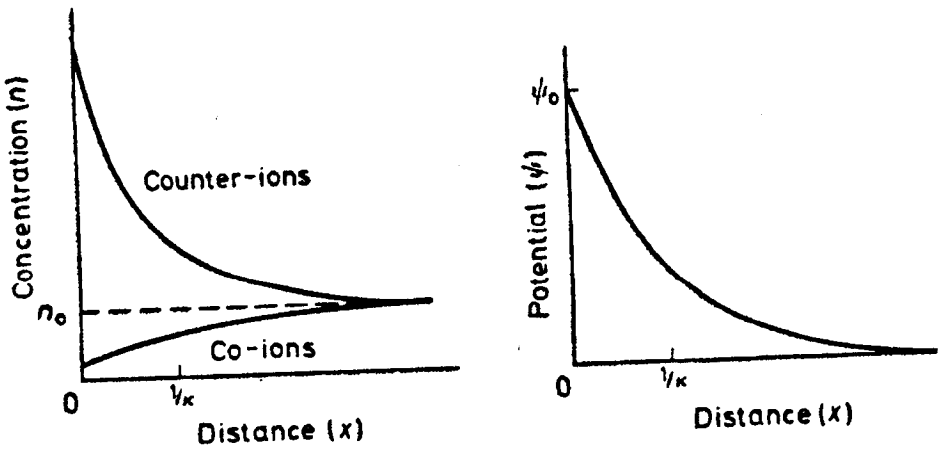

Figure 97: Schematic diagram of a diffuse electric double layer by Shaw. D. J (1980).

Colloid Stability

An important physical property of colloidal dispersions is the tendency of particles to aggregate. Molecules may attract each other at moderate distances but repel each other at close range. The attractive forces between particles or droplets are collectively called "Van der Waals forces". These forces are much weaker than chemical bonds and random thermal motion may disrupt them. They operate only when molecules are close to each other: during collisions or near misses. Opposing this are the repulsive interactions between similarly charged electric double layers. Bubble stability is somehow like a droplet stability and is necessary for successful phase separation.

N. D. Sylvester and J. J. Byeseda (1980) reported that oil removal during flotation of a burner fuel emulsion increased from 55 to 75% upon addition of a cationic polyelectrolyte. This kind of surfactant changes the droplet interfacial characteristics.

K. Okada et al. (1988) studied the effect of oil droplet and bubbles surface charge in oil-in-water flotation processes by measuring the zeta potential (ξ). They reported that increased flotation performance was achieved by reducing or reversing the negative charge on oil droplets by the addition of salt rather than polyelectrolytes. The salt altered the oil droplet electrical charge without affecting the sign of the bubble charge. (The

authors added various electrolytes such as NaCl, $CaCl_2$, and $Al_2(SO_4)_3$ to the solution to vary the surface charge of the oil droplets and bubbles just before the flotation experiment). In addition, they found that the separation efficiency; η, of flotation was strongly dependent on the zeta potentials of both the oil droplets and bubbles. η Increased as the zeta potentials of both the oil droplets and bubble decreased. η Was as largest when the oil droplets were negatively charged and the bubbles were positively charged.

G. Rios et al. (1998) studied the influence of inorganic salts on zeta potentials of cutting-oil water emulsions using light scattering techniques. They added $AlCl_3$, $MgCl_2$, $CaCl_2$ and NaCl (10^{-4} mol/dm^3 to 10^{-1} mol/dm^3) to the oil-in-water emulsions in order to study the influence of electrolyte concentration and cation charge on emulsion zeta potential. They found a decrease in the absolute value of the zeta potential when electrolytes were added to the emulsion -- the effect of added electrolytes followed the Schulze-Hardy rule that states that critical coagulation concentration values (c.c.c) are determined by the counter ion valency (D. J. Shaw 1980).

- Similar electrolytes have similar critical coagulation concentration values (c.c.c).
- Effectiveness of the electrolyte in coagulating the dispersion increases when multivalent ions are contained.
- Counter ion valency is the important factor in determining critical coagulation concentration values (c.c.c).

The empirical Schulze-Hardy rule states that effectiveness of counter ions in inducing coagulation is approximately proportional to the sixth power of the counter ion charge.

C. W. Farrell (1991) states that coagulation and removal of solid particles and oil droplets from stable suspensions and emulsions can be achieved by alternating current electrocoagulation techniques (**Figure 98**) In this technique particles, including oil droplets, move toward a positively charged electrode and collision is not only likely between positive and negative droplets (particles) moving in opposite directions, but also between discharged particles of different sizes, once the stabilizing charges are eliminated.

The author used electrical current for charge neutralization and aluminium hydroxide for electroflocculation and achieved rapid settling and improved de-watering without the use of expensive polyelectrolytes, chemicals (Alum) or sophisticated filtration systems and reduced the difficult to de-water and handle hydrous sludge volume. These two steps (electrical current for charge neutralization and aluminium hydroxide for electro flocculation) enhance particle growth as a result of electro coagulation.

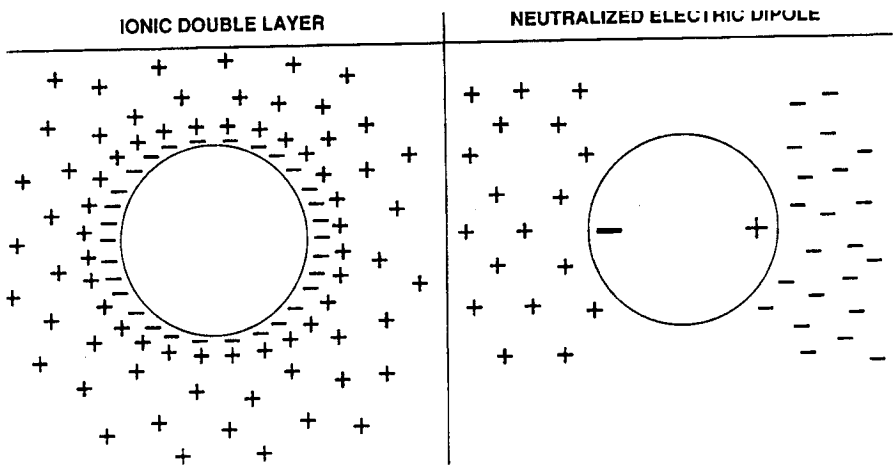

Figure 98: Surface charge distribution, Farrell, C. W (1991).

The End